Exotic Ordered and Disordered Many-Particle Systems with Novel Properties

Ge Zhang

A Dissertation
Presented to the Faculty
of Princeton University
in Candidacy for the Degree
of Doctor of Philosophy

Recommended for Acceptance
by the Department of
Chemistry
Adviser: Professor Salvatore Torquato

September 2017

Abstract

This dissertation presents studies on several statistical-mechanical problems, many of which involve exotic many-particle systems. In Chapter 2, we present an algorithm to generate Random Sequential Addition (RSA) packings of hard hyperspheres at the infinite-time saturation limit, and investigate this limit with unprecedented precision. In Chapter 3, we study the problem of devising smooth, short-ranged isotropic pair potentials such that their ground state is an unusual targeted crystalline structure. We present a new algorithm to do so, and demonstrate its capability by targeting several singular structures that were not known to be achievable as ground states with isotropic interactions.

A substantial portion of this dissertation examines exotic many-particle systems with so-called "collective-coordinate" interactions. They include "stealthy" potentials, which are isotropic pair potentials with disordered and infinitely degenerate ground states as well as "perfect-glass" interactions, which have up to four-body contributions, and possess disordered and *unique* ground states, up to trivial symmetry operations. Chapters 4-7 study the classical ground states of "stealthy" potentials. We establish a numerical means to sample these infinitely-degenerate ground states in Chapter 4 and study exotic "stacked-slider" phases that arise at suitable low densities in Chapter 5. In Chapters 6 and 7, we investigate several geometrical and physical properties of stealthy systems. Chapter 8 studies lattice-gas systems with the same stealthy potentials. Chapter 9 is concerned with the introduction and study of the perfect-glass paradigm. Chapter 10 demonstrates that perfect-glass interactions indeed possess disordered and unique classical ground states – a highly counterintuitive proposition.

In Chapter 11, we use statistical-mechanical methods to characterize the spatial distribution of the prime numbers. We show that the primes are much more ordered than anyone previously thought via the structure factor. Indeed, they are charac-

terized by infinitely many Bragg peaks in any non-zero interval of wave vectors, yet unlike quasicrystals, the ratio between the heights or locations of any two Bragg peaks is always rational. We analytically explain the locations and heights of all such peaks.

Acknowledgements

I am very grateful to Prof. Salvatore Torquato, who is an extremely responsible advisor. He devoted constant, close attention to my research, even in his busiest times, and provided numerous insightful guidance. I am also very grateful to Dr. Frank Stillinger, who devoted similarly close attention to my research, providing insightful ideas. I would like to also thank Prof. Roberto Car, Prof. Robert DiStasio Jr., and Prof. Annabella Selloni, who have also helped me in my previous research.

I would like to thank past and present group members, including Yang Jiao, Adam Hopkins, Étienne Marcotte, Steven Atkinson, Duyu Chen, Jaeuk Kim, and Zheng Ma. In our numerous discussions I learned lots of fascinating knowledge and ideas. Additionally, many of them had carefully read drafts of my previous papers and provided great suggestions.

I would like to thank my parents, who have spent enormous amount of energy and resources in educating me, equipping me with knowledge and abilities that enabled me to thrive in Princeton University.

Finally, I would like to thank Princeton University for providing such an ideal environment for doing research. Here, I was astonished to find out how nice every person is. Such a warm community allowed me to easily relax and focus on my studies.

To my parents.

Contents

List of Tables

List of Figures

8.8 (*Upper left*) Vectorial representation of a stealthy pattern comprised of $N = 2$ particles. The corresponding structure factor, $S(\mathbf{k}) = \frac{1}{N}|\sum_{j=1}^{N}\exp[i\mathbf{k}\cdot\mathbf{r}_j]|^2$, will vanish at a given pair of $\mathbf{k}$-vectors, $\mathbf{k}_1$ and $\mathbf{k}_2$, when $\mathbf{r}_1$ and $\mathbf{r}_2$ satisfy the following equations: (1) $\exp[i\mathbf{k}_1\cdot\mathbf{r}_1] + \exp[i\mathbf{k}_1\cdot\mathbf{r}_2] = 0$ and (2) $\exp[i\mathbf{k}_2\cdot\mathbf{r}_1] + \exp[i\mathbf{k}_2\cdot\mathbf{r}_2] = 0$. Any set of $N = 2$ particles whose coordinates satisfy these constraints constitutes a *doublet* (D). (*Lower left*) Graphical depiction of a series of stealthy patterns discretized on a periodic 6×6 square lattice that were constructed *via* superposition of multiple doublets (*i.e.*, $D_2 = D \oplus D$ and $D_9 = D \oplus D \oplus \cdots \oplus D$). Since *each* doublet constitutes a stealthy pattern, the superposition of multiple doublets (without overlap) constitutes a stealthy (or multi-stealthy) hyperuniform pattern as well. (*Upper right*) Vectorial representation of a stealthy pattern comprised of $N = 4$ particles. The corresponding structure factor will vanish at a given pair of $\mathbf{k}$-vectors, $\mathbf{k}_1$ and $\mathbf{k}_2$, when $\mathbf{r}_1$, $\mathbf{r}_2$, $\mathbf{r}_3$, and $\mathbf{r}_4$ satisfy the following equations: (1) $\exp[i\mathbf{k}_1\cdot\mathbf{r}_1] + \exp[i\mathbf{k}_1\cdot\mathbf{r}_2] = 0$, (2) $\exp[i\mathbf{k}_1\cdot\mathbf{r}_3] + \exp[i\mathbf{k}_1\cdot\mathbf{r}_4] = 0$, (3) $\exp[i\mathbf{k}_2\cdot\mathbf{r}_1] + \exp[i\mathbf{k}_2\cdot\mathbf{r}_3] = 0$, and (4) $\exp[i\mathbf{k}_2\cdot\mathbf{r}_2] + \exp[i\mathbf{k}_2\cdot\mathbf{r}_4] = 0$. Any set of $N = 4$ particles whose coordinates satisfy these constraints constitutes a *quartet* (Q). Note here that a quartet is not simply a pair of doublets, *i.e.*, $Q \neq D_2 = D \oplus D$. (*Lower right*) Graphical depiction of a series of stealthy patterns discretized on a periodic 6×6 square lattice that were constructed *via* superposition of multiple doublets and quartets (*i.e.*, $QD = Q \oplus D$, $Q_2 = Q \oplus Q$, and $Q_3D_3 = Q \oplus Q \oplus Q \oplus D \oplus D \oplus D$). Since *each* doublet and *each* quartet constitutes a stealthy pattern, the superposition of multiple doublets and quartets (without overlap) constitutes a stealthy (or multi-stealthy) hyperuniform pattern as well. Hence, this superposition technique can be utilized to directly generate stealthy patterns with both large L and N. 226

Chapter 1

Introduction

This dissertation reports results on the statistical mechanics of a variety of ordered and disordered many-particle systems. Particular focus has been directed toward exotic systems that are often endowed with novel structural and physical properties. Many of the results were obtained using numerical simulation techniques, but in some cases, theoretical analysis was brought to bear to interpret the numerical results. In what follows, summaries of the individual chapters of the dissertation are provided.

In Chapter 2, we study the random sequential addition (RSA) time-dependent packing process, in which congruent hard hyperspheres are randomly and sequentially placed into a system without interparticle overlap. This is a useful packing model to study disorder in high dimensions. Of particular interest is the infinite-time *saturation* limit in which the available space for another sphere tends to zero. However, the associated saturation density has been determined in all previous investigations by extrapolating the density results for near-saturation configurations to the saturation limit, which necessarily introduces numerical uncertainties. We have refined an algorithm described in [323] to generate RSA packings of identical hyperspheres. The improved algorithm produce such packings that are guaranteed to reach the saturation limit with heretofore unattained precision and across the widest

range of dimensions ($2 \leq d \leq 8$). We have also calculated the packing and covering densities, pair correlation function $g_2(r)$ and structure factor $S(k)$ of the saturated RSA configurations. As the space dimension increases, we find that pair correlations markedly diminish, consistent with a recently proposed "decorrelation" principle, and the degree of "hyperuniformity" (suppression of infinite-wavelength density fluctuations) increases. We have also calculated the void exclusion probability in order to compute the so-called quantizer error of the RSA packings, which is related to the second moment of inertia of the average Voronoi cell. Finally, we discuss the possibility of generalizing this algorithm to generate saturated RSA packings of nonspherical particles. The work in this chapter has been published previously as:

- G. Zhang and S. Torquato, *Precise Algorithm to Generate Random Sequential Addition of Hard Hyperspheres at Saturation*, Physical Review E, **88**, 053312 (2013).

In Chapter 3, we test the fundamental limitations of radial pair potentials by applying inverse statistical-mechanical methods. Such methods can be employed to design optimized short-ranged radial (isotropic) pair potentials that robustly produce targeted classical ground-state many-particle configurations. All of the previous studies targeted low-coordinated crystals with a high degree of symmetry. We target crystal structures with appreciably less symmetry, including those in which the particles have different local structural environments. These challenging target configurations demanded that we modify previous inverse optimization techniques. In particular, we first find local minima of a candidate enthalpy surface and determine the enthalpy difference ΔH between such inherent structures and the target structure. Then we determine the lowest positive eigenvalue λ_0 of the Hessian matrix of the enthalpy surface at the target configuration. Finally, we maximize $\lambda_0 \Delta H$ so that the target structure is both locally stable and globally stable with respect to the inherent structures. Using this modified optimization technique, we have de-

signed short-ranged radial pair potentials that stabilize the two-dimensional kagome crystal, the rectangular kagome crystal, and rectangular lattices, as well as the three-dimensional structure of CaF_2 crystal inhabited by a single particle species. We verify our results by cooling liquid configurations to absolute zero temperature via simulated annealing and ensuring that such states have stable phonon spectra. Except for the rectangular kagome structure, all of the target structures can be stabilized with monotonic repulsive potentials. Our work demonstrates that single-component systems with short-ranged radial pair potentials can counterintuitively self-assemble into crystal ground states with low symmetry and different local structural environments. Finally, we present general principles that offer guidance in determining whether certain target structures can be achieved as ground states by radial pair potentials. The work in this chapter has been published previously as:

- G. Zhang, F. H. Stillinger, and S. Torquato, *Probing the Limitations of Isotropic Pair Potentials to Produce Ground-State Structural Extremes via Inverse Statistical Mechanics*, Physical Review E, **88**, 042309 (2013).

They have also been presented in short talks at the 109th Statistical Mechanics Conference at Rutgers University in May, 2013; and at the 11th Mid-Atlantic Soft Matter workshop in July, 2013.

In Chapters 4-7, we study systems of particles interacting with "stealthy" pair potentials. They have been shown to possess infinitely degenerate disordered hyperuniform classical ground states. Thus, one can have different ways to sample the infinitely degenerate ground states, which assign different weights to different parts of the ground state manifold. To sample the ground states, previous studies used energy minimization techniques. However, in Chapter 4, we demonstrate that such techniques introduce algorithmic dependence that is artificial in nature. We therefore argue that a physically more meaningful way is to perform molecular dynamics simulations at sufficiently low temperatures and minimizing the energy of the

snapshots. Such sampling method correspond to the zero-temperature limit of the canonical ensemble (*i.e.*, define the probability measure $P(\mathbf{r}^N) \propto \exp[-\Phi_s(\mathbf{r}^N)/k_BT]$, where $\Phi_s(\mathbf{r}^N)$ is the potential energy, k_B is the Boltzmann constant, and T is the temperature; and then take the $T \to 0$ limit). We report results for the pair correlation functions, structure factors, and Voronoi cell statistics. In the high-density regime, we verify the theoretical ansatz that stealthy disordered ground states behave like "pseudo" disordered equilibrium hard-sphere systems in Fourier space. The pair statistics obey certain exact integral conditions with very high accuracy. These results show that as the density decreases from the high-density limit, the disordered ground states in the canonical ensemble are characterized by an increasing degree of short-range order and eventually the system undergoes a phase transition to crystalline ground states. In the crystalline regime (low densities), there exist aperiodic structures that are part of the ground-state manifold, but yet are not entropically favored. We also provide numerical evidence suggesting that different forms of stealthy pair potentials produce the same ground-state ensemble in the zero-temperature limit. Our techniques may be applied to sample the zero-temperature limit of the canonical ensemble of other potentials with highly degenerate ground states. The work in Chapter 4 has been published previously as:

- G. Zhang, F. H. Stillinger, and S. Torquato, *Ground States of Stealthy Hyperuniform Potentials: I. Entropically Favored Configurations*, Physical Review E, **92**,022119 (2015).

They have also been presented in a short talk at the 111th Statistical Mechanics Conference at Rutgers University in May, 2014.

In Chapter 5, we investigate using both numerical and analytical techniques metastable stacked-slider phases, which are part of the ground-state manifold of stealthy potentials at low densities. Our numerical results enable us to devise analytical models of this phase in two, three and higher dimensions. Utilizing this model,

we estimated the size of the feasible region in configuration space of the stacked-slider phase, finding it to be smaller than that of crystal structures in the infinite-system-size limit, which is consistent with previous chapter's finding that crystals are entropically favored. In two dimensions, we also determine exact expressions for the pair correlation function and structure factor of the analytical model of stacked-slider phases and analyze the connectedness of the ground-state manifold of stealthy potentials in this density regime. We demonstrate that stacked-slider phases are distinguishable states of matter; they are nonperiodic, statistically anisotropic structures that possess long-range orientational order but have zero shear modulus. We outline some possible future avenues of research to elucidate our understanding of this unusual phase of matter. The work in this chapter has been published previously as:

- G. Zhang, F. H. Stillinger, and S. Torquato, *Ground States of Stealthy Hyperuniform Potentials: II. Stacked-Slider Phases*, Physical Review E, **92**,022120 (2015).

They have also been presented in a short talk at the 113th Statistical Mechanics Conference at Rutgers University in May, 2015.

In Chapter 6, we map these stealthy disordered hyperuniform point configurations to two-phase media by circumscribing each point with a possibly overlapping sphere of a common radius a: the "particle" and "void" phases are taken to be the space interior and exterior to the spheres, respectively. The hyperuniformity of such two-phase media depend on the sphere sizes: While it was previously analytically proven that the resulting two-phase media maintain hyperuniformity if spheres do not overlap, here we show numerically that they lose hyperuniformity whenever the spheres overlap. We study certain transport properties of these systems, including the effective diffusion coefficient of point particles diffusing in the void phase as well as static and time-dependent characteristics associated with diffusion-controlled reactions. Besides these effective transport properties, we also investigate several related

structural properties, including pore-size functions, quantizer error, an order metric denoted τ, and percolation thresholds. We show that these transport, geometrical and topological properties of our two-phase media derived from decorated stealthy ground states are distinctly different from those of equilibrium hard-sphere systems and spatially uncorrelated overlapping spheres. As the extent of short-range order increases, stealthy disordered two-phase media can attain nearly maximal effective diffusion coefficients over a broad range of volume fractions while also maintaining isotropy, and therefore may have practical applications in situations where ease of transport is desirable. We also show that the percolation threshold and the order metric are positively correlated with each other, while both of them are negatively correlated with the quantizer error. In the highly disordered regime ($\chi \to 0$), stealthy point-particle configurations are weakly-perturbed ideal gases. Nevertheless, reactants of diffusion-controlled reactions decay much faster in our two-phase media than in equilibrium hard-sphere systems of similar degrees of order, and hence indicate that the formation of large holes is strongly suppressed in the former systems, which inspires the next chapter. The work in this chapter has been published previously as:

- G. Zhang, F. H. Stillinger, and S. Torquato, *Transport, Geometrical, and Topological Properties of Stealthy Disordered Hyperuniform Two-phase Systems*, Journal of Chemical Physics, **145**, 244109 (2016).

In Chapter 7, we study the probability of finding a spherical cavity or "hole" of arbitrarily large size in stealthy systems. Such "hole" statistics are intimately linked to the thermodynamic and nonequilibrium physical properties of the system. We provide strong numerical evidence that disordered stealthy configurations across the first three space dimensions cannot tolerate arbitrarily large holes in the infinite-system-size limit, *i.e.*, the hole probability has compact support. This structural "rigidity" property apparently endows disordered stealthy systems with novel thermodynamic and physical properties, including desirable band-gap, optical and transport charac-

teristics. We also determine the maximum hole size that any stealthy system can possess across the first three space dimensions. The work in this chapter has been accepted for publication in Soft Matter as:

- G. Zhang, F. H. Stillinger, and S. Torquato, *Can exotic disordered "stealthy" particle configurations tolerate arbitrarily large holes?*, (2017).

In Chapter 8, we change our focus to study stealthy spin systems (or equivalently, lattice gas systems). We define and analyze the order metric τ, which ranks such systems by providing an *unbiased* estimate of the order contained within a given discretized pattern by *equally* accounting for contributions across short-, intermediate-, and long-range distances. To demonstrate that τ is consistent with our intuitive perception of order, we first apply it to a digitized representation of the Mona Lisa, which is arguably one of the most easily recognizable and well-known images in existence to date, and compare our findings with the most ordered and most disordered configurations of the same resolution. This is followed by a detailed analysis of τ for a series of stealthy hyperuniform patterns, which are characterized by the presence of hidden long-range order. We then showcase several new algorithms that allow for the systematic identification and generation of digitized stealthy hyperuniform patterns, paving the way towards the rational design of such configurations with a tunable degree of order. The work in this chapter has been submitted to Science Advances as:

- R. A. Distasio, Jr., G. Zhang, F. H. Stillinger, and S. Torquato, *Rational Design of Stealthy Hyperuniform Patterns with Tunable Order*, (2017).

They have also been presented in a short talk at the 115th Statistical Mechanics Conference at Rutgers University in May, 2016.

In Chapters 9 and 10, we devise and study a many-particle model which we call "perfect glasses," since it is a soft-interaction analog of the maximally random jammed

(MRJ) packings of hard particles. These latter states can be regarded as the epitome of a glass since they are out of equilibrium, maximally disordered, hyperuniform, mechanically rigid with infinite bulk and shear moduli, and can never crystallize due to configuration-space trapping. In Chapter 9, we devise the model perfect glass utilizing two-, three-, and four-body soft interactions. The work in Chapter 9 has been published previously as:

- G. Zhang, F. H. Stillinger, and S. Torquato, *The Perfect Glass Paradigm: Disordered Hyperuniform Glasses Down to Absolute Zero*, Scientific Reports, **6**, 36963 (2016).

They have also been presented in a short talk at the 116th Statistical Mechanics Conference at Rutgers University in December, 2016.

In Chapter 10, we show that this model possesses unique disordered classical ground states. This is a highly counterintuitive situation, since classical ground states (global energy-minimizing configurations) of many-particle systems are typically unique but crystalline structures. By contrast, the few previously known disordered classical ground states of many-particle systems are all highly degenerate. For all of the system sizes, parameters, and space dimensions that we have numerically investigated, the disordered ground states are unique such that they can always be superposed onto each other or their mirror image. At low energies, the density of states calculated from harmonic approximations near a single ground state matches numerical results with high precision, further confirming ground-state uniqueness. Such ground states would have zero "enumeration entropy," defined as the natural logarithm of the number of *distinct* accessible structures. Thus, this discovery provides singular examples in which entropy and disorder are at odds with one another. It also impinges on the famous Kauzmann glass paradox. We expect that our disordered unique patterns to be of value in cryptography as pseudo-random functions

with tunable computational complexity. The work in this chapter has been submitted to Physical Review Letters as:

- G. Zhang, F. H. Stillinger, and S. Torquato, *Classical many-particle systems with unique disordered ground states*, (2017).

They have also been presented in a short talk at the 117th Statistical Mechanics Conference at Rutgers University in May, 2017.

In Chapter 11, we study the spacial distribution of prime numbers using statistical-mechanical methods. Although the primes are deterministic, they can be viewed, by some measures, as pseudo-random numbers. We study prime numbers in the interval $[M, M + L)$, where M and L are large integers, and treat such configurations as (correlated) lattice gases. We find that the structure factor of such systems consists of Bragg peaks in a small, noisy background, which we call the "diffuse part". Using a stronger form of Dirichlet's theorem on arithmetic progressions, we were able to analytically explain the location and height of all peaks. The Bragg peaks are dense in the sense that one can find infinitely many peaks in any non-zero interval, similar to quasicrystals. However, primes differ from quasicrystals in that the ratio between the location of any two Bragg peaks is rational. We also numerically observed that the diffuse part decays slowly as M or L increases. With such analytical understandings of the structure factor, we were able to reconstruct the real-space configuration, *i.e.,* predict prime numbers in the interval, with high accuracy in certain cases. This chapter is based on materials of two papers under preparation:

- G. Zhang, F. Martelli, and S. Torquato, *Structure Factor of the Primes*, (2017).

- S. Torquato, G. Zhang, and M. De Courcy-Ireland, *Hidden Multiscale Order in the Primes*, (2017).

Chapter 2

Precise Algorithm to Generate Random Sequential Addition of Hard Hyperspheres at Saturation

2.1 Introduction

In d-dimensional Euclidean space $\mathbb{R}^d$, a hard hypersphere (i.e. d-dimensional sphere) packing is an arrangement of hyperspheres in which no two hyperspheres overlap. The *packing density* or *packing fraction* ϕ is the fraction of space in $\mathbb{R}^d$ covered by the spheres, which for identical spheres of radius R, the focus of this chapter, is given by:

$$\phi = \rho v_1(R), \tag{2.1}$$

where ρ is the number density and

$$v_1(R) = \frac{\pi^{d/2}}{\Gamma(1+d/2)} R^d \tag{2.2}$$

is the volume of a d-dimensional sphere of radius R and $\Gamma(x)$ is the gamma function. Sphere packings are of importance in a variety of contexts in the physical and mathematical sciences. Dense sphere packings have been used to model a variety of many-particle systems, including liquids [127], amorphous materials and glassy states of matter [31, 102, 222, 316, 223, 224, 321], granular media [301], suspensions and composites [40, 361, 201], and crystals [45]. The densest sphere packings are intimately related to the ground states of matter [45, 303] and the optimal way of sending digital signals over noisy channels [61]. Finding the densest sphere packing in $\mathbb{R}^d$ for $d \geq 3$ is generally a notoriously difficult problem [61]. Kepler's conjecture, which states that there is no other three-dimensional arrangement of identical spheres with a density greater than that of face-centered cubic lattice, was only recently proved [125]. The densest sphere packing problem in the case of congruent spheres has not been rigorously solved for $d \geq 4$ [61, 56], although for $d = 8$ and $d = 24$ the E_8 and Leech lattices, respectively, are almost surely the optimal solutions [58].

Understanding the high-dimensional behavior of disordered sphere packings is a fundamentally important problem, especially in light of the recent conjecture that the densest packings in sufficiently high dimensions may be disordered rather than ordered [319]. Indeed, Ref. [319] provides a putative exponential improvement on Minkowski's lower bound on the maximal density ϕ_{max} among all Bravais lattices [206]:

$$\phi_{max} \geq \frac{\zeta(d)}{2^{d-1}}, \tag{2.3}$$

where $\zeta(d) = \sum_{k=1}^{\infty} k^{-d}$ is the Riemann zeta function. For large values of d, the asymptotic behavior of the Minkowski's lower bound is controlled by 2^{-d}. Interestingly, any saturated packing density satisfies the following so-called "greedy" lower bound:

$$\phi \geq \frac{1}{2^d}. \tag{2.4}$$

A saturated packing of congruent spheres of unit diameter and density ϕ in $\mathbb{R}^d$ has the property that each point in space lies within a unit distance from the center of some sphere. Thus, a covering of the space is achieved if each center is encompassed by a sphere of unit radius and the density of this covering is

$$\theta = 2^d \phi \geq 1, \tag{2.5}$$

which proves the lower bound (2.4). Note that it has the same dominant exponential term as in inequality (2.3). The packing density of 2^{-d} can also be exactly achieved by *ghost random sequential addition* packings [318], an unsaturated packing less dense than the standard random sequential addition (RSA) packing [339] in some fixed dimension d, implying that the latter will have a superior dimensional scaling. Additionally, the effect of dimensionality on the behavior of equilibrium hard-sphere liquids [93, 275, 253, 330, 186] and of maximally random jammed spheres [275, 224, 321] have been investigated.

Sphere packings are linked to a variety of fundamental characteristics of point configurations in $\mathbb{R}^d$, including the *covering radius* R_c and the *quantizer error* $\mathcal{G}$, which are related to properties of the underlying Voronoi cells [61]. The covering and quantizer problems have relevance in numerous applications, including wireless communication network layouts, the search of high-dimensional data parameter spaces, stereotactic radiation therapy, data compression, digital communications, meshing of space for numerical analysis, coding, and cryptography [303, 61]. It has recently been shown [303] that both of these quantities can be extracted from the *void exclusion probability* $E_V(R)$, which is defined to be the probability of finding a randomly placed spherical cavity of radius R empty of any points. It immediately follows that $E_V(R)$ is the expected fraction of space not covered by circumscribing spheres of radius R centered at each point. Thus, if $E_V(R)$ is identically zero for $R \geq R_c$ for a point

process, then there is a covering associated with the point process with covering radius R_c. Finally, for a point configuration with positions $\mathbf{r}_1, \mathbf{r}_2, \ldots$, a quantizer is a device that takes as an input a position $\mathbf{x}$ in $\mathbb{R}^d$ and outputs the nearest point $\mathbf{r}_i$ of the configuration to $\mathbf{x}$. Assuming $\mathbf{x}$ is uniformly distributed, one can define a mean square error, called the *scaled dimensionless quantizer error*, which can be obtained from the void exclusion probability via the relation [303]:

$$\mathcal{G} = \frac{2\rho^{\frac{2}{d}}}{d} \int_0^\infty R E_V(R) dR. \tag{2.6}$$

It is noteworthy that the optimal covering and quantizer solutions are the ground states of many-body interactions derived from $E_V(R)$ [303].[1]

The RSA procedure, which is the focus of the present chapter, is a time-dependent process to generate disordered hard-hypersphere packings in $\mathbb{R}^d$ [323, 339, 227, 288, 84, 62, 293, 247]. Starting with a large, empty region of $\mathbb{R}^d$ of volume V, spheres are randomly and sequentially placed into the volume subject to a nonoverlap constraint: if a new sphere does not overlap with any existing spheres, it will be added to the configuration; otherwise, the attempt is discarded. One can stop the addition process at any time t, obtaining RSA configurations with various densities $\phi(t)$ up to the maximal saturation density $\phi_s = \phi(\infty)$ that occurs in the infinite-time limit. Besides identical d-dimensional spheres, the RSA packing process has also been investigated for polydisperse spheres [6, 113] and other particle shapes, including squares [38], rectangles [331, 332], ellipses [291, 273], spheroids [272], superdisks [119], sphere dimers [54], and sphere polymers [52] in $\mathbb{R}^d$, and for different shapes on lattices [41] and fractals [53, 55]. The RSA packing process in the first three space dimensions has been widely used to model the structure of cement paste [344], ion implantation in semiconductors [254], protein adsorption [85], polymer oxidation [96], and particles in cell

[1] In Ref. [303], Eq. (75) is presented for unit density and hence does not contain the pre-factor $\rho^{2/d}$ indicated in Eq. (2.6).

membranes [92]. The one-dimensional case, also known as the "car-parking" problem, has been solved analytically and its saturation density is $\phi = 0.7475979202...$ [247]. However, for $d \geq 2$, the saturation density of RSA spheres has only been estimated through numerical simulations.

In general, generating exactly saturated (infinite-time limit) RSA configurations in $\mathbb{R}^d$ is particularly difficult because infinite computational time is not available. The long-time limit of RSA density behaves as [84, 227, 288]:

$$\phi(\infty) - \phi(t) \sim t^{-1/d}. \tag{2.7}$$

Previous investigators have attempted to ascertain the saturation densities of RSA configurations by extrapolating the densities obtained at large, finite times using the asymptotic formula (2.7) [62, 293, 323].

In order to describe more efficient ways of generating nearly-saturated and fully-saturated RSA configurations, we first need to define two important concepts: the *exclusion sphere* and the *available space*. The *exclusion sphere* associated with a hard sphere of diameter D (equal to $2R$) is the volume excluded to another hard sphere's center due to the impenetrability constraint, and thus an exclusion sphere of radius D circumscribes a hard sphere. The *available space* is the space exterior to the union of the exclusion spheres of radius D centered at each sphere in the packing. A more general notion of the available space is a fundamental ingredient in the formulation of a general canonical n-point distribution function [296].

An efficient algorithm to generate nearly-saturated RSA configurations was introduced in Ref. [323]. This procedure exploited an economical procedure to ascertain the available space (as explained in the subsequent section). Although a huge improvement in efficiency can be achieved, this and all other previous algorithms still

require extrapolation of the density of nearly-saturated configurations to estimate the saturation limit.

In this chapter, we present an improvement of the algorithm described in Ref. [323] in order to generate saturated (i.e., infinite-time limit) RSA packings of identical spheres in a finite amount of computational time. Using this algorithm, we improve upon previous calculations of the saturation packing and covering densities, pair correlation function, structure factor, void exclusion probability, and quantizer error in dimensions 2 through 8.

The rest of the chapter is organized as follows: In Sec. 2.2, we describe the improved algorithm; in Sec. 2.3, we present the packing and covering densities, pair correlation function, structure factor, void exclusion probability, and quantizer error of saturated RSA configurations; and in Sec. 2.4, we conclude with some discussions of extending this method to generate saturated RSA packings of objects other than congruent spheres.

2.2 Improved Algorithm to Generate Saturated RSA Packings in $\mathbb{R}^d$

Reference [323] introduced an efficient algorithm to generate nearly saturated RSA configurations of hard d-dimensional spheres. Specifically, a hypercubic simulation box is divided into small hypercubic "voxels" with side lengths much smaller than the diameter of the spheres. At any instant of time, spheres are sequentially added to the simulation box whenever there is available space for that sphere. Each voxel can be probed to determine whether it may contain any available space or not to add another sphere. By tracking all of the voxels that can contain some portion of the available space, one can make insertion attempts only inside these "available voxels" and save computational time. This enables one to achieve a huge improvement in

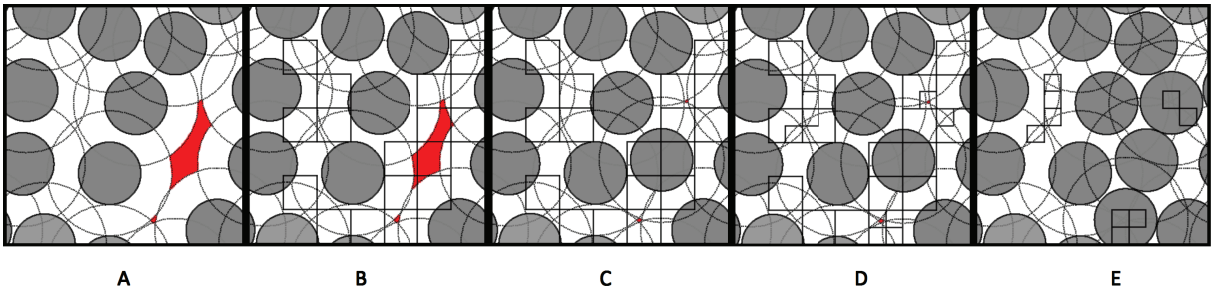

Figure 2.1 A description of the key steps involved to generate two-dimensional saturated RSA packings in a square box under periodic boundary conditions. Gray circles are RSA disks and dotted circles are their corresponding exclusion disks. The shaded region (red region in colored version) is the available space. Black squares are voxels in the available voxel list. A: Configuration after the first step. B: Same configuration with the available voxel list generated in the second step. C: A new disk is inserted in the third step, reducing the available space. D: In the fourth step, each available voxel is subdivided into 2^2 sub-voxels. The available ones constitute a new voxel list. E: Return to the third step with the new available voxel list and two additional disks are inserted. The program then subdivides each voxel into four subvoxels and all subvoxels can be identified as unavailable. Thus the program finishes.

computational efficiency over previous methods. However, this and all other previous algorithms still require extrapolation of the density of nearly-saturated configurations to estimate the saturation limit.

The improved algorithm reported in the present chapter differs from the original voxel method [323] by dividing the undetermined voxels (voxels that are not included in any exclusion sphere after certain amount of insertion trials) into smaller subvoxels. Repeating this voxel subdivision process with progressively greater resolution enables us to track the available space more and more precisely. Eventually, this allows us to discover *all* of the available space at any point in time and completely consume it in order to arrive at saturated configurations.

The improved algorithm consists of the following steps, which are illustrated in Figure 2.1:

1. Starting from an empty simulation box in $\mathbb{R}^d$, the Cartesian coordinates of a sphere of radius R are randomly generated. This sphere is added if it does not overlap with any existing sphere in the packing at that point in time; otherwise,

the attempt is discarded. This addition process is repeated until the success rate is sufficiently low [2]. The acceptance ratio of this step equals to the volume fraction of the available space inside the simulation box:

$$P_{acceptance} = \Phi_{available} = \frac{V_{available}}{L^d}, \tag{2.8}$$

where $P_{acceptance}$ is the acceptance ratio of this step, $\Phi_{available}$ is the volume fraction of the available space, $V_{available}$ is the volume of the available space and L^d is the volume of the simulation box with side length L.

2. When the fraction of the available space is low, we improve the acceptance ratio by avoiding insertion attempts in the unavailable space. To do this, the simulation box is divided into hypercubic voxels, with side lengths comparable to the sphere radius. Each voxel is probed to determine whether it is completely included in any of the exclusion spheres or not. If not, the voxel is added to the available voxel list. Thus we obtain an "available voxel list". A voxel in this list may or may not contain available space, but the voxels not included in this list are guaranteed to contain no available space.

3. Since some unavailable space is excluded from the voxel list, we can achieve a higher success rate of insertion by selecting a voxel randomly from the available voxel list, generate a random point inside it, attempt to insert a sphere and repeat this step. The acceptance ratio of this step is equal to the volume fraction of the available space inside voxels from the available voxel list:

$$P_{acceptance} = \Phi_{available} = \frac{V_{available}}{N_{voxel} V_{voxel}}, \tag{2.9}$$

[2] In the implementation of our algorithm, the criteria for "sufficiently low" is less than 3 spheres inserted in N trials. The optimal choice of N depends on the dimension d, ranging from $N = 500$ for $d = 2$ to $N = 2 \times 10^8$ for $d = 8$.

where $P_{acceptance}$ is the acceptance ratio of this step, $\Phi_{available}$ is the volume fraction of the available space inside the voxel list, $V_{available}$ is the volume of the available space, N_{voxel} is the number of voxels in the available voxel list and V_{voxel} is the volume of a voxel.

4. In the previous step, spheres were inserted into the system, thus the volume of the available space will decrease. Eventually, $V_{available}$ is very low and $P_{acceptance}$ is also low. Thus we improve the efficiency again by dividing each voxel in the voxel list into 2^d sub-voxels, each with side length equal to a half of that of the original voxel. Each sub-voxel is checked for availability according to the rule described in step 2. The available ones constitute the new voxel list.

5. Return to step 3 with the new voxel list and repeat steps 3 to 5 until the number of voxels in the latest voxel list is zero. Since we only exclude a voxel from the voxel list when we are absolutely sure that it does not contain any available space, we know at this stage that the entire simulation box does not contain any available space and thus the configuration is saturated.

2.3 Results

2.3.1 Saturation density

We have used the method described in Sec. 2.2 to generate saturated configurations of RSA packings of hyperspheres in dimensions two through eight in a hypercubic (d-dimensional cubic) box of side length L under periodic boundary conditions. In each dimension, multiple sphere sizes are chosen. The relative sphere volume is represented by the ratio of a sphere's volume to the simulation box's volume $v_1(R)/L^d$, where R is the sphere radius and L^d is the volume of the hypercubic simulation box. For each sphere size, multiple configurations are generated. The number of

spheres N contained in these configurations fluctuate around some average value inversely proportional to $v_1(R)/L^d$. The relative sphere volume $v_1(R)/L^d$ and number of configurations n_c generated for each sphere radius R in each dimension is given in Table 2.1. The mean density and its standard error for each sphere radius R is calculated. Subsequently, we plot the mean density ϕ_s and its standard error σ versus a quantity proportional to $N^{-1/2}$, namely $[v_1(R)/L^d]^{1/2}$. We then perform a weighted linear least squares fit [285] to this function in each dimension in order to extrapolate to the infinite-system-size $[v_1(R)/L^d \to 0]$ limit. The weight is given by

$$W(R) = \frac{1}{\sigma^2(R)}, \tag{2.10}$$

where $\sigma(R)$ is the standard error of the mean density for spheres with radius R.

Table 2.1 Dimensionless sphere size $v_1(R)/L^d$ and number of configurations n_c generated for each dimension d.

$d=2$	$v_1(R)/L^d$	1.0884×10^{-7}	5.4420×10^{-8}	2.7210×10^{-8}	1.3605×10^{-8}
	n_c	250	250	250	250
$d=3$	$v_1(R)/L^d$	3.82925×10^{-7}	1.91462×10^{-7}	7.65850×10^{-8}	3.82925×10^{-8}
	n_c	250	250	250	250
	$v_1(R)/L^d$	1.91462×10^{-8}			
	n_c	250			
$d=4$	$v_1(R)/L^d$	5.20225×10^{-6}	2.60112×10^{-6}	1.30056×10^{-6}	5.20225×10^{-7}
	n_c	250	250	250	250
	$v_1(R)/L^d$	2.60112×10^{-7}	1.30056×10^{-7}		
	n_c	250	250		
$d=5$	$v_1(R)/L^d$	1.71000×10^{-5}	8.55000×10^{-6}	3.42000×10^{-6}	1.71000×10^{-6}
	n_c	250	250	250	250
	$v_1(R)/L^d$	8.55000×10^{-7}	3.42000×10^{-7}		
	n_c	250	250		
$d=6$	$v_1(R)/L^d$	2.22500×10^{-5}	1.11250×10^{-5}	5.56250×10^{-6}	2.78125×10^{-6}
	n_c	50	50	50	50
	$v_1(R)/L^d$	1.39062×10^{-6}			
	n_c	50			
$d=7$	$v_1(R)/L^d$	2.72744×10^{-5}	1.36372×10^{-5}	6.81859×10^{-6}	4.54573×10^{-6}
	n_c	70	30	20	20
	$v_1(R)/L^d$	3.40930×10^{-6}	1.94817×10^{-6}	1.36372×10^{-6}	
	n_c	20	20	15	
$d=8$	$v_1(R)/L^d$	4.16930×10^{-5}	2.08465×10^{-5}	1.38977×10^{-5}	
	n_c	11	7	5	

The mean densities and the associated standard errors for different sphere radii R are shown in Fig. 2.2, while the extrapolated infinite-system-size densities are shown in Table 2.2. These density estimates for $2 \leq d \leq 8$ have been determined with heretofore unattained accuracy, including in the most previously studied dimensions of $d = 2$ and $d = 3$. For $d = 2$, several previous studies produced the following density estimates 0.547 ± 0.002 [84], 0.547 ± 0.003 [137], and 0.54700 ± 0.000063 [323]. For $d = 3$, several previous investigations yielded the following density estimates $0.37 - 0.40$ [62], 0.385 ± 0.010 [63], 0.382 ± 0.0005 [290], and 0.38278 ± 0.000046 [323]. Compared with previous results of saturation densities for $2 \leq d \leq 6$ [323], our corresponding results are only slightly higher for two dimensions, but the discrepancy increases as dimension increases. This suggests that the previous attempts did not generate fully saturated configurations, especially in high dimensions. Table 2.2 also includes corresponding RSA covering densities. A RSA covering is obtained by replacing each sphere in a saturated RSA packing in $\mathbb{R}^d$ with its exclusion sphere, and thus its covering density is given by

$$\theta = 2^d \phi_s. \tag{2.11}$$

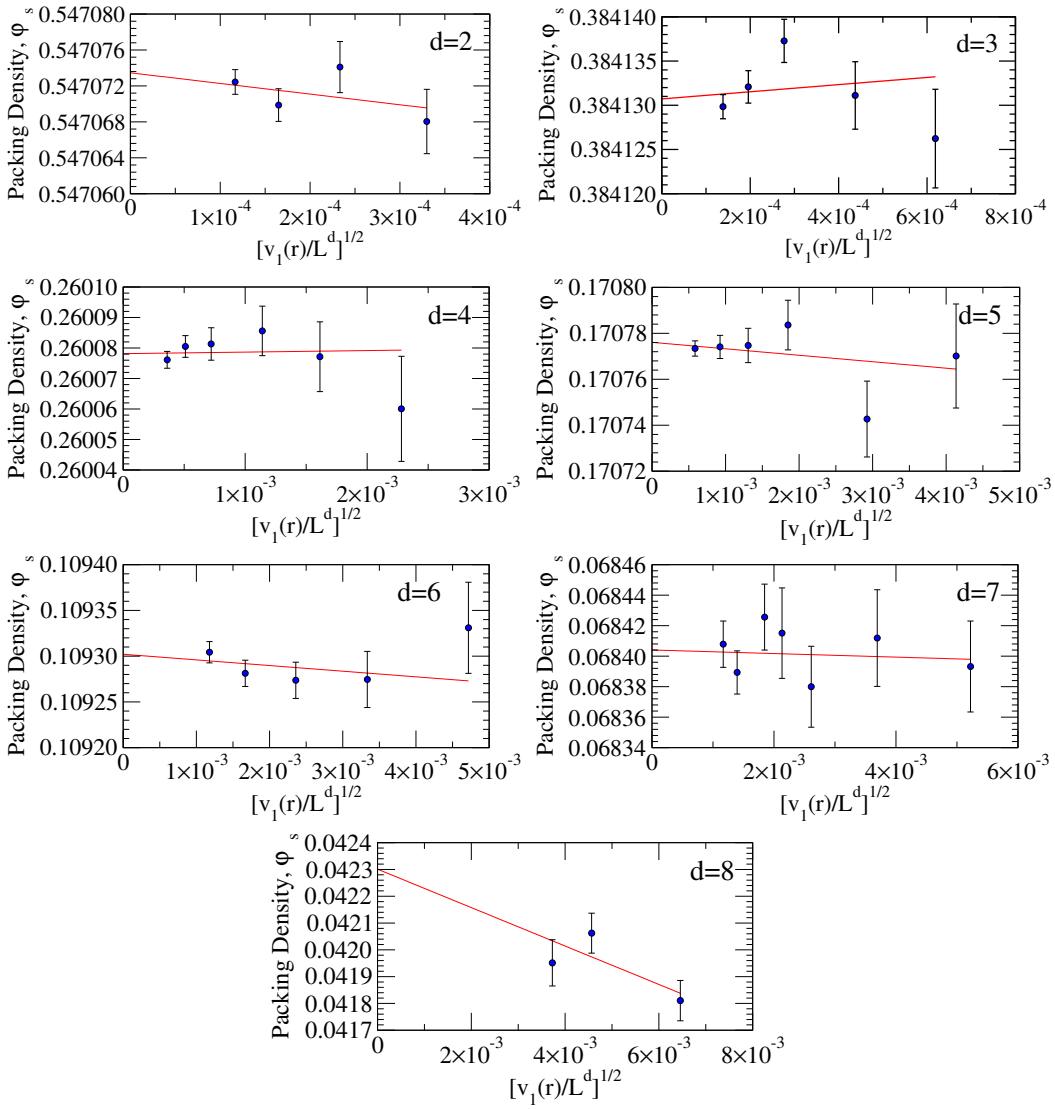

Figure 2.2 RSA saturation packing density, ϕ_s, (filled circles) of different system sizes as measured by a quantity proportional to $N^{-1/2}$, namely $[v_1(R)/L^d]^{1/2}$, in different dimensions d. Included are the associated linear fits. Error bars associated with filled circles are the standard error of the mean as obtained from averaging multiple configurations.

2.3.2 Pair correlation function and structure factor

We have used the methods described in Ref. [323] to calculate the pair correlation function $g_2(r)$ and structure factor $S(k)$ of the saturated RSA configurations for $2 \leq d \leq 7$. [For $d = 8$, we can only generate relatively small configurations, which are

Table 2.2 RSA saturation densities and covering densities in different dimensions, extrapolated to the infinite system size limit. Here ϕ_s is saturation packing density and θ is the corresponding covering density.

Dimension	ϕ_s [Present Work]	ϕ_s [Ref. [323]]	θ [Present Work]
2	0.5470735 ± 0.0000028	0.54700 ± 0.000063	2.188294 ± 0.000011
3	0.3841307 ± 0.0000021	0.38278 ± 0.000046	3.073046 ± 0.000017
4	0.2600781 ± 0.0000037	0.25454 ± 0.000091	4.161250 ± 0.000060
5	0.1707761 ± 0.0000046	0.16102 ± 0.000036	5.46483 ± 0.00015
6	0.109302 ± 0.000019	0.09394 ± 0.000048	6.9953 ± 0.00012
7	0.068404 ± 0.000016		8.75572 ± 0.0020
8	0.04230 ± 0.00021		10.829 ± 0.053

not suitable to calculate $g_2(r)$ and $S(k)$ accurately.] The structure factor is calculated using the collective density variables approach, i.e.,

$$S(\mathbf{k}) = \frac{\langle|\tilde{\rho}(\mathbf{k})^2|\rangle}{N}, \tag{2.12}$$

where N is the number of spheres in the periodic hypercubic box of side length L,

$$\tilde{\rho}(\mathbf{k}) = \sum_{j=1}^{N} \exp(i\mathbf{k} \cdot \mathbf{r}_j) \tag{2.13}$$

is the complex collective density variable and

$$\mathbf{k} = (\frac{2\pi n_1}{L}, \frac{2\pi n_2}{L}, ..., \frac{2\pi n_d}{L}), \tag{2.14}$$

where $\mathbf{k}$ is a wave vector and where n_i $(i = 1, 2, \ldots, d)$ are the integers. In presenting the structure factor, we will omit the forward scattering contribution ($\mathbf{k} = \mathbf{0}$); see Ref. [323] for additional details.

These pair statistics are shown in Figure 2.3 for dimensions two through seven. The decorrelation exhibited with increasing dimension was also observed in Ref. [323]. These trends are clearly consistent with a recently proposed "decorrelation" principle, which states that *unconstrained* spatial correlations diminish as the dimension

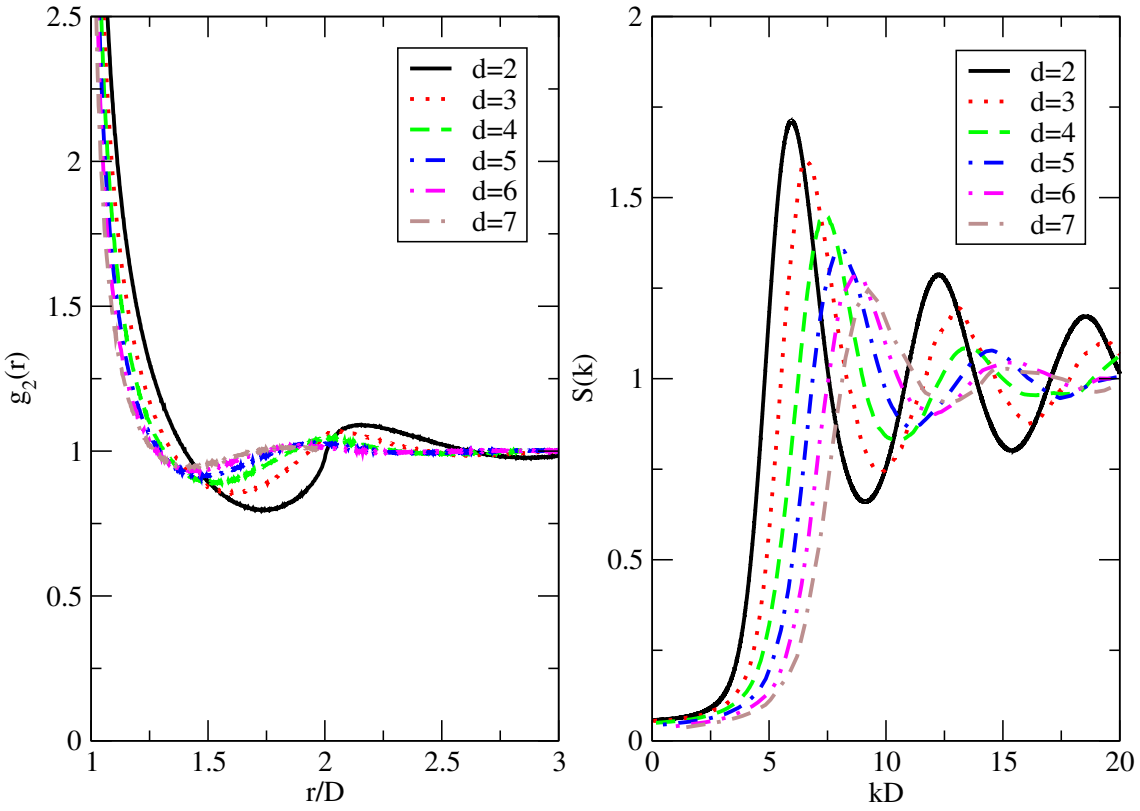

Figure 2.3 Pair correlation function and structure factor of saturated RSA configurations, in two through seven dimensions. It is clearly seen that these pair statistics indicate that the packings become more decorrelated as the dimension increases.

increases and vanish in the $d \to \infty$ limit [318, 319]. It is noteworthy that decorrelation is already exhibited in these low dimensions, which has been observed for other types of hard-sphere packings [318, 275].

The pair correlation function $g_2(r)$ of saturated RSA configurations has a logarithmic singularity when r approaches the sphere diameter, D [227, 288] :

$$g_2(r) \sim -\ln(r/D-1),\ r \to D^+. \tag{2.15}$$

Based on this analytical form, we have fit our pair correlation functions at $D < r < 1.018D$ to the following formula:

$$g_2(r) = a_0 \ln(r/D-1) + a_1. \tag{2.16}$$

Our results are shown in Table 2.3. The absolute value of a_0 in each dimension are significantly higher than previous results [323], which means that our $g_2(r)$'s are much sharper near $r = D$. This is due to the fact that our algorithm is capable of finding even the smallest fragments of the available space. Finding those pieces enables us to insert spheres that are very close to other spheres, substantially increasing $g_2(r)$ near $r = D$.

It is of interest to see to what extent RSA packings are hyperuniform. A packing is *hyperuniform* if the structure factor in the zero-wavenumber limit, $S_0 \equiv \lim_{k\to 0} S(k)$, is zero [317, 349]. Thus, the magnitude of S_0 quantifies the "distance" from hyperuniformity. It was reported in Ref. [323] that S_0 of saturated RSA packings decreases with dimension but because these simulations were not as precise in higher dimensions, the high-d asymptotic behavior of S_0 was difficult to ascertain. We fit the structure factors that we have determined in this chapter to a function of the form $S(k) = S_0 + S_2k^2 + S_4k^4$ in each dimension near $k = 0$ in order to estimate S_0. This form is the exact behavior of the structure factor as k goes to zero, as shown in Ref. [323]. The results for S_0 are summarized in Table 2.4. It is seen that as d increases, S_0 decreases, i.e., the "degree of hyperuniformity" (the ability to suppress infinite-wavelength density fluctuations) increases. The data indicates that S_0 tends to the perfect hyperuniformity limit of zero as $d \to \infty$. As we will show in Sec. 2.3.3, in the $d \to \infty$ limit, the void exclusion probability of RSA packings tends to a step function [303]. This indicates that the vacancies in infinite-dimensional RSA packings are spherically-shaped with similar sizes. Thus, S_0 tends to zero in the $d \to \infty$ limit. This also explains why RSA packings become more stealthy [$S(k)$ is nearly zero for larger range of k near $k = 0$] [29] as d increases.

Table 2.3 Results from fitting data to $g_2(r) = a_0 \ln(r/D - 1) + a_1$ in the near-contact range $D < r < 1.018D$

Dimension	a_0	a_1
2	-1.562 ± 0.031	-2.155 ± 0.155
3	-1.603 ± 0.026	-2.709 ± 0.133
4	-1.488 ± 0.028	-2.582 ± 0.116
5	-1.396 ± 0.030	-2.565 ± 0.155
6	-1.200 ± 0.039	-1.984 ± 0.206
7	-1.169 ± 0.055	-2.116 ± 0.269

Table 2.4 Structure factor $S(k)$ at $k = 0$, obtained by fitting data to $S(k) = S_0 + S_2k^2 + S_4k^4$ at $0 < kD < 3$, where S_0, S_2, and S_4 are fitting parameters.

Dimension	S_0
2	0.05869 ± 0.00004
3	0.05581 ± 0.00005
4	0.05082 ± 0.00007
5	0.04544 ± 0.00029
6	0.03834 ± 0.00072
7	0.03140 ± 0.00173

2.3.3 Void exclusion probability and quantizer error

We have calculated the void exclusion probability $E_V(r)$ (discussed in the Introduction) of saturated RSA configurations for $2 \leq d \leq 8$ and findings are summarized in Figure 2.4. The void exclusion probability in all dimensions vanishes at $r \to D^-$, confirming that the exclusion spheres with radius $R_c = D$ cover the space and that our RSA configurations are saturated. Our results are similar to previously reported results [303] and strongly supports the theory that the void exclusion probability of RSA packings tend to a step function in the infinite-dimensional limit [303], i.e.,

$$E_V(r) \to \Theta(r - D) \qquad (d \to \infty), \tag{2.17}$$

where

$$\Theta(x) = \begin{cases} 0, & x < 0 \\ 1, & x \geq 0 \end{cases} \tag{2.18}$$

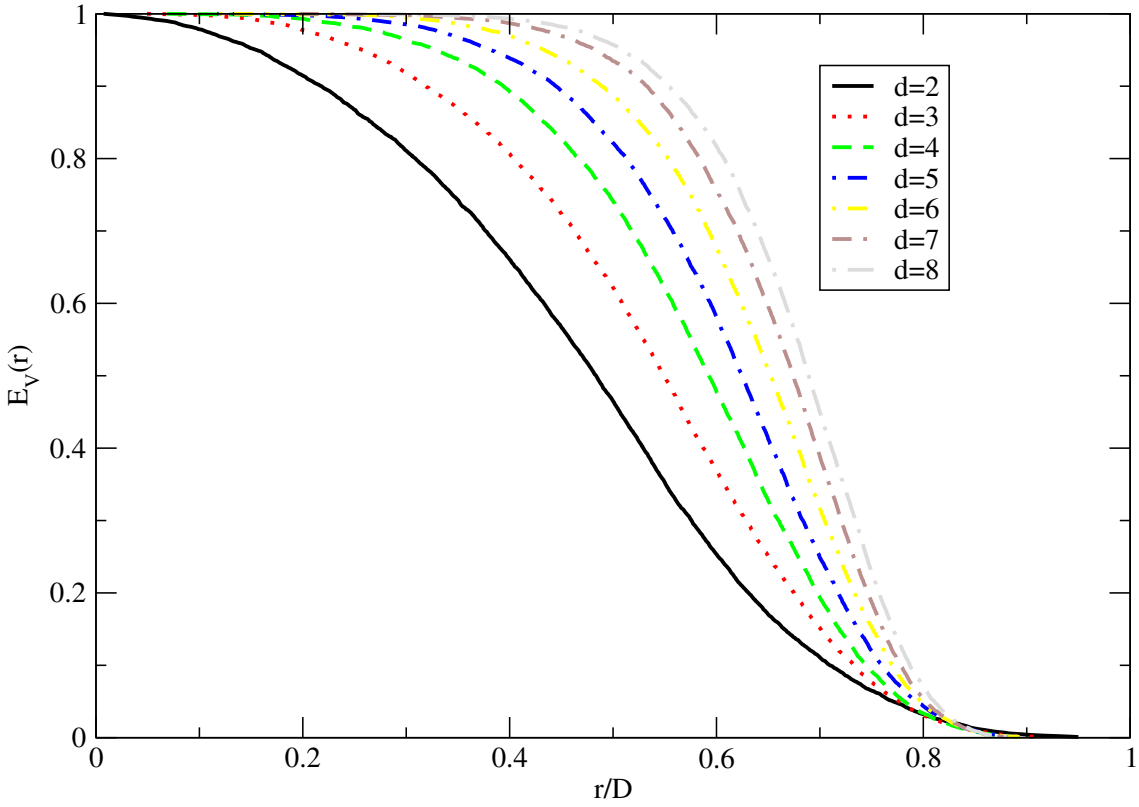

Figure 2.4 Void exclusion probability of saturated RSA configurations, in two through eight dimensions.

is the Heaviside step function. This indicates that the "holes" in RSA packings become spherically-shaped with similar sizes as d tends to infinity. It is interesting to note that the void exclusion probability of fermionic systems have similar behavior in the high-dimensional limit [315].

We have calculated the quantizer error $\mathcal{G}$ for saturated RSA configurations for $2 \leq d \leq 8$. These results are summarized in Table 2.5. Compared with results in Ref. [303] for $2 \leq d \leq 6$, our corresponding results for $\mathcal{G}$ are somewhat lower.

2.4 Conclusions and Discussion

We have devised an efficient algorithm to generate exactly saturated, infinite-time limit RSA configurations in finite computational time across Euclidean space dimen-

Table 2.5 Scaled dimensionless quantizer error $\mathcal{G}$.

Dimension	$\mathcal{G}$ [Present Work]	$\mathcal{G}$ [Ref. [303]]
2	0.08848 ± 0.00018	0.09900
3	0.08441 ± 0.00013	0.09232
4	0.08154 ± 0.00011	0.08410
5	0.07936 ± 0.00009	0.07960
6	0.07765 ± 0.00007	0.07799
7	0.07623 ± 0.00007	
8	0.07508 ± 0.00009	

sions. With the algorithm, we have improved previous results of the saturation density and extended them to a wider range of dimensions, i.e., up through dimension eight. The associated covering density, pair correlation function, structure factor, void exclusion probability, and quantizer error have also been improved. In particular, we found appreciable improvement for $g_2(r)$ near contact and $S(k)$ in the $k \to 0$ limit, which are especially sensitive to whether or not very small fragments of the available space are truly eliminated as the saturation state is approached. We observed that as d increases, the degree of "hyperuniformity" (the magnitude of the suppression of infinite-wavelength density fluctuations) increases and appears to be consistent with $\lim_{d\to\infty} S(0) = 0$. Our results also supports the "decorrelation principle", which in turns lends further credence to a conjectural lower bound on the maximal sphere packing density that provides the putative exponential improvement on Minkowski's lower bound [319].

It is noteworthy that the RSA packing in $\mathbb{R}^d$ has relevance in the study of high-dimensional scaling of packing densities. For example, Ref. [323] suggested that since RSA packing densities appear to have a similar scaling in high dimensions as the best lower bound on Bravais lattice packings densities, the density of disordered packings might eventually surpass that of the densest lattice packing beyond some large but finite dimension. Our improvements to the saturation densities, as well as a previous investigation [319], support this conjecture. Converting a packing into

a covering by replacing each sphere with its exclusion sphere is rigorous only if the packing is exactly saturated. By guaranteeing that the packings that we generated are saturated, we rigorously met this condition (in a large finite simulation box). Although the best known lattice covering and lattice quantizer perform better than their RSA counterparts in low dimensions, RSA packings may outperform lattices in sufficiently high dimensions, as suggested in Ref. [303].

It is useful here to comment on the ability to ascertain the high-dimensional scaling of RSA packing densities from low-dimensional data [303, 323]. We have fitted our data of the saturation densities as a function of d for $2 \leq d \leq 8$ using a variety of different functions. The best fit we find is the following form:

$$\phi_s = \frac{a_1 + a_2 d + a_3 d^2}{2^d}, \tag{2.19}$$

where $a_1 = 1.0801$, $a_2 = 0.32565$, and $a_3 = 0.11056$ are parameters. However, it is not clear how accurate this form is for $d \geq 9$. In fact, this form is likely not correct in high dimensions, where it has been suggested from theoretical considerations [303] that high-dimensional scaling may be given by the asymptotic form

$$\phi_s = \frac{b_1 + b_2 d + b_3 d \ln(d)}{2^d}, \tag{2.20}$$

where b_1, b_2, and b_3 are constants. It is noteworthy that (2.20) provides a fit that is very nearly as good as (2.19). Nonetheless, for $d = 15$, the estimates of the saturation densities obtained from (2.19) and (2.20) differ by about 20%, which is a substantial discrepancy and indicates the uncertainties involved in applying such dimensional scalings for even moderately-sized dimensions. When d is very large, extrapolations based on fits of low-dimensional data is even more problematic. In this limit, Eq. (2.19) is dominated by the $a_3 d^2/2^d$ term, which can be significantly larger than the $a_3 d \ln(d)/2^d$ dominating term in Eq. (2.20), although it is safe to say

that the saturation density grows at least as fast as $d2^{-d}$. Therefore, caution should be exercised in attempting to ascertain the precise high-d asymptotic behavior of RSA saturation densities from our data in relatively low dimensions. The same level of caution should be employed in attempting to determine high-d scaling behavior by extrapolating low-dimensional packing densities for other types of sphere packings. For example, it may useful to revisit the high-dimensional scalings that have been ascertained or tested for the maximally random jammed densities [224, 48]. In summary, it is nontrivial to ascertain high-d scalings of packing densities from low-dimensional information. In contrast, in the study of the dimensional dependence of continuum percolation thresholds, it is possible to obtain exact high-d asymptotics and tight upper and lower bounds that apply across all dimensions [304, 310].

RSA packings of spheres with a polydispersity in size have also been investigated previously [6, 113]. Our algorithm can easily be extended to generate saturated RSA packings of polydisperse spheres in $\mathbb{R}^d$ by constructing a $(d+1)$-dimensional auxiliary space for the associated radius-dependent available space and voxels, where the additional dimension is used to represent the radius of a sphere that could be added in the RSA process. RSA packings of nonspherical particles have also been studied, including squares [38], rectangles [331, 332], ellipses [291, 273], spheroids [272], and superdisks [119]. While packings of polyhedra have received recent attention [40, 311], RSA packings of such shapes have not been considered to our knowledge. Our algorithm can also be extended to treat these situations by constructing auxiliary spaces for the associated orientation-dependent available space and voxels. The dimension of such an auxiliary space is determined by the total number of degrees of freedom associated with a particle, i.e., translational and rotational degrees of freedom. The extensions of the methods devised here to generate saturated packings of polydisperse spheres and nonspherical particles is an interesting direction for future research.

Chapter 3

Inverse Statistical Mechanics: Probing the Limitations of Isotropic Pair Potentials to Produce Ground-State Structural Extremes

3.1 Introduction

A fundamental problem of statistical mechanics is the determination of the phase diagram of interacting many-particle systems in the absence of an external field. For a single-component system of N particles in a large region of volume V in d-dimensional Euclidean space $\mathbb{R}^d$, the interaction is represented by the potential energy $\Phi(\mathbf{r}^N)$, where $\mathbf{r}^N = \mathbf{r}_1, \mathbf{r}_2, ..., \mathbf{r}_N$ denotes the configurational coordinates. A theoretically simple and computationally widely used form of the potential energy is the following

pairwise form:

$$\Phi(\mathbf{r}^N) = \sum_{i<j} u_2(r_{ij}), \tag{3.1}$$

where $u_2(r)$ is a suitably stable isotropic pair potential and r_{ij} is the distance between the ith and jth particles.

Even for this simple class of potentials, our understanding of the phase diagram, including the $T = 0$ ground state, is still far from complete. Two approaches have been used to study phase diagrams of isotropic pair potentials. In the *forward* approach, one first specifies the isotropic pair potential $u_2(r)$ and then probes the structures in its phase diagram. This venerable approach has identified a variety of structures with varying degrees of complexity and order [338, 71, 337, 132, 236, 139, 217, 230, 357, 246, 25, 144, 43, 359]. In the *inverse* approach, a target many-particle configuration or physical property is first specified and then one attempts to determine an isotropic pair potential $u_2(r)$ under certain constraints that achieves the targeted behavior [302]. The target behavior can be ground state configurations [239, 240, 241, 243, 191, 192, 193, 143] or excited-state properties, such as negative thermal expansion [242] and negative Poisson ratio [244].

This chapter focuses on the use of inverse statistical mechanics to determine isotropic pair potentials that produce unusual targeted crystalline structures as unique ground states, as in multiple previous works [239, 240, 241, 243, 191, 192, 193, 143]. Contrary to the conventional view that low-coordinated crystal structures require directional bonds as in chemical covalency, earlier works employing the inverse approach have found optimized isotropic pair potentials (under certain constraints) stabilizing a variety of low-coordinated crystal structures as ground states. Target structures that have successfully been stabilized include the square lattice [240, 191, 192], honeycomb crystal [239, 240, 191, 192], and kagomé crystal [80] in two dimensions, and the simple cubic lattice [241, 143], diamond crystal [243, 193, 143], and wurtzite crystal [243] in three dimensions. These isotropic pair potentials have been designed using the follow-

ing steps [239, 240, 191, 192, 241, 243, 193, 143]: A functional form was chosen for the isotropic pair potential in terms of some parameters. One then optimized an objective function that is related to the stability of the target structure over competitors (for example, energy difference [240] or the target structure's stable pressure range [193]). Subsequently, the validity of the optimized potential was verified by cooling liquid configurations to absolute zero temperature via simulated annealing and by establishing that the target structure contains no phonon instabilities [240]. These results provide good counterexamples to the aforementioned intuition that low-coordinated structures require directional bonding. However, all of these target structures are globally highly symmetric, and the local environments around each of the particles in these structures are identical up to spatial inversions or rotations.

Here, we further probe the limitations of isotropic pair potentials to produce ground-state structural extremes using inverse statistical-mechanical techniques. Doing so has required us to improve upon previous optimization algorithms devised for inverse statistical mechanics for reasons that we will elaborate below. Our improved optimization algorithm not only allows each competitor structure to deform to become more competitive during the optimization, but also incorporates the local mechanical stability of the target structure (i.e. enthalpy cost to deform the target structure) into our objective function. We test our improved optimization algorithm by targeting the standard kagomé crystal, rectangular lattices, the rectangular kagomé crystal, and the three dimensional CaF_2 crystal inhabited by a single particle species. Compared to previous target structures, these new targets have lower symmetry, and particles in some cases have different local structural environments. We restrict ourselves to short-ranged potentials (i.e. $u_2(r) \equiv 0$ for $r > r_c$, where r_c is a constant) because they are both computationally easier to treat and experimentally simpler to realize. For all of our targets, except for the rectangular kagomé crystal, we are able to stabilize them with smooth short-ranged monotonic repulsive potentials, which would be

easier to produce experimentally. For the rectangular kagomé crystal, we found that a potential with a shallow well is needed for the class of functions considered.

In contrast to some previous inverse statistical mechanical approaches [239, 240, 241, 243, 191, 192], in which the specific volume $v = V/N$ (N is the number of particles and V is the volume) is fixed and the classical ground state is achieved by the global minimum of the potential energy $\Phi(\mathbf{r}^N)$, we fix the pressure p rather than the specific volume. At constant pressure p and number of particles N, the classical ground state is achieved by the global minimum of the configurational enthalpy per particle:

$$h(\mathbf{r}^N) = \Phi(\mathbf{r}^N)/N + pv. \tag{3.2}$$

There are two advantages in fixing the pressure rather than the specific volume. First, at zero temperature, phase separation (coexistence) only occurs at a unique pressure for a given potential, while it can occur at a nontrivial range of densities. By fixing the pressure rather than the density during simulations, we minimize our risk of encountering phase separation. Second, allowing the volume to change will enable us to fully deform the simulation box, thus minimizing the boundary effect during simulations.

The rest of the chapter is organized as follows: In Sec. 3.2, we describe the new algorithm. In Sec. 3.3, we present our designed isotropic pair potentials for the two-dimensional (2D) kagomé crystal, rectangular lattices, and the rectangular kagomé crystal, and the three-dimensional (3D) structure of the CaF_2 crystal inhabited by a single particle species. We close with conclusions and discussion in Sec. 3.4.

3.2 Extended Optimization Technique

3.2.1 Basic definitions

A *lattice* in $\mathbb{R}^d$ is an infinite periodic structure in which the space $\mathbb{R}^d$ is divided into identical regions called *fundamental cells*, each of which contains the just one point specified by the *lattice vector*

$$\mathbf{R} = n_1\mathbf{a}_1 + n_2\mathbf{a}_2 + \cdots + n_d\mathbf{a}_d, \tag{3.3}$$

where $\mathbf{a}_i$ are the lattice vectors and n_i spans all the integers for $i = 1, 2, \ldots, d$. A *crystal* is a more general notion than a lattice because it is obtained by placing a fixed configuration of N points (where $N \geq 1$), located at $\mathbf{r}_1, \mathbf{r}_2, ..., \mathbf{r}_N$, within one fundamental cell. The coordination structure of a crystal can be represented by the theta series [61], which is the generating function of squared distances of the vector displacements between any two particles of the crystal structure and has the following form:

$$\theta(q) = 1 + \sum_{j=1}^{\infty} Z_j q^{r_j^2}, \tag{3.4}$$

where r_j is the distance from a particle at the origin (measured in units of the nearest neighbor distance) and Z_j is the associated average coordination number (average number of particles at a radial distance r_j). See Appendix A for the vectors that specify the particle locations and lattice vectors of the crystal as well as the first few terms of the corresponding theta series of our target structures. For the special case of periodic structures, Eq. (3.2) can be written more explicitly in terms of coordination structure:

$$h(\mathbf{r}^N; \mathbf{A}) = \frac{1}{2}\sum_j u_2(r_j)Z_j + pv(\mathbf{A}), \tag{3.5}$$

where $\mathbf{A} = [\mathbf{a}_1, \mathbf{a}_2, ..., \mathbf{a}_d]^T$ is the generator matrix [61] (a matrix whose rows consist of the lattice vectors) and $v(\mathbf{A})$ is the specific volume, which depends on $\mathbf{A}$. The ground state is achieved by the global minimum of enthalpy per particle $h(\mathbf{r}^N; \mathbf{A})$.

For each target crystal structure, we use the following steps to attempt to find an isotropic pair potential $u_2(r)$ and a pressure p such that the target is the ground state.

3.2.2 Search for degenerate ground states

A target configuration cannot possibly be the unique ground state if a different structure has exactly the same coordination structure up to the range of the potential and the same specific volume v. In this degeneracy searching step, we start from a random configuration and minimize the "difference" between the coordination structure of the configuration and that of the target structure; see Appendix C for a detailed description. After minimizing the "difference", if there is no difference between the two coordination structures and specific volumes, we check if the resulting configuration is equivalent to the target structure. Two structures are considered to be "equivalent" if they are related to each other through translations, rotations, inversions, uniform scalings, or combinations of the above transformations [148, 110]. If the resulting configuration is different from the target structure, then we have found a degenerate structure and thus have proven that the target structure cannot be the unique ground state of any isotropic pair potential. If after trying minimizing the "difference" multiple times (often thousands of times) no degenerate structure is found, we tentatively assume that the target structure is unique and continue to the next step. In this step, we visually inspect the configurations to determine whether two structures are identical. However, in the upcoming optimization and verification steps, since we have already assumed that the target structure has a unique coordination structure, we

can test whether another structure is identical to the target structure by comparing their coordination structures using the computer.

3.2.3 Optimization

If the target structure has a unique coordination structure, it might be stabilized by an isotropic pair potential with finite range. We can specify a family of potential functions and optimize for the target structure's stability. Since extremely long-ranged potentials are both computationally inefficient and experimentally challenging to realize, we restrict ourselves to potential functions with compact support of the following form:

$$u_2(r) = \begin{cases} \left(\frac{b}{r^{12}} + c_0 + c_1 r + c_2 r^2 + ... \right) \exp(-\alpha r^2)(r - r_c)^2, & \text{if } r < r_c, \\ 0, & \text{otherwise,} \end{cases} \tag{3.6}$$

where b, c_n $(n = 0, 1, 2, ...)$, r_c, and α are parameters. This form is realistic because it contains a stiff core b/r^{12} and smoothly approaches 0 as r approaches r_c. If this form does not work well, we will add additional terms of different type, for example, Gaussian wells centered at some $r > 0$. Since the energy and length scale of the pair potential is arbitrary, we fix these scales so that:

1. The nearest neighbor distance of the target structure is 1.

2. The absolute value of the pair potential at the nearest neighbor distance of the target structure, $|u_2(1)|$, is 1.

We also require that $\alpha \geq 0$ so that the effect of the Gaussian core is to decrease the $u_2(r)$ as r increases rather than to increase $u_2(r)$. We further require that $r_c \leq 6.4$ in order to ensure that the potential is relatively short-ranged.

After the potential form is chosen, we optimize the parameters. Although previous objective functions worked for previous target structures with high symmetry, they must be modified for less symmetric and more complex target structures. The result of maximizing the energy difference or enthalpy difference is very sensitive to structurally close competitors (i.e. a slight deformation of the target structure) because they are not differentiated from structurally remote competitors (competitors that are not structurally close competitors). Figure 3.1 illustrates the close-competitor problem schematically.

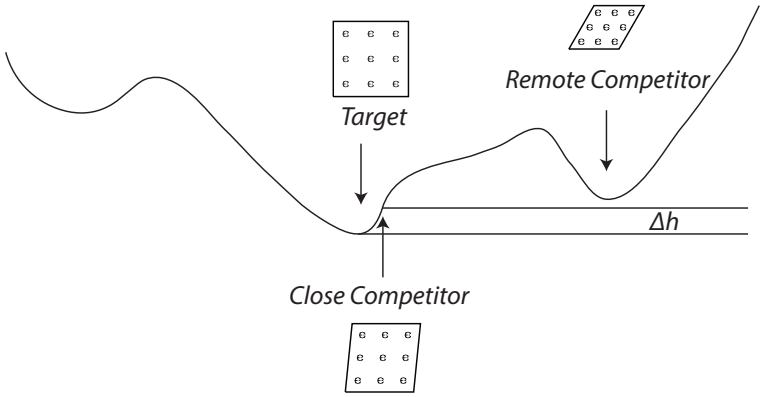

Figure 3.1 A schematic plot of the enthalpy surface (equivalent of potential energy surface at constant pressure). If we simply define Δh as the enthalpy difference between the target and the lowest competitor and maximize it, we will encounter the "close competitor problem". If the competitor list contains structurally close competitors, Δh will be controlled by a structurally close competitor, causing an abnormal lifting of the enthalpy of structurally close competitors.

Optimization over a pressure range solves the close competitor problem [193], but introduces its own problems. First, some structures with lower symmetry do not naturally have a stable pressure range. For example, consider the rectangular lattice with aspect ratio $b/a \neq 1$. (A precise definition of rectangular lattices and their aspect ratio is given in Appendix A.) Since the structure is anisotropic, it is expected to have different elastic constants in different directions; see Appendix D for an example. Thus when the pressure is changed by a small amount, the aspect

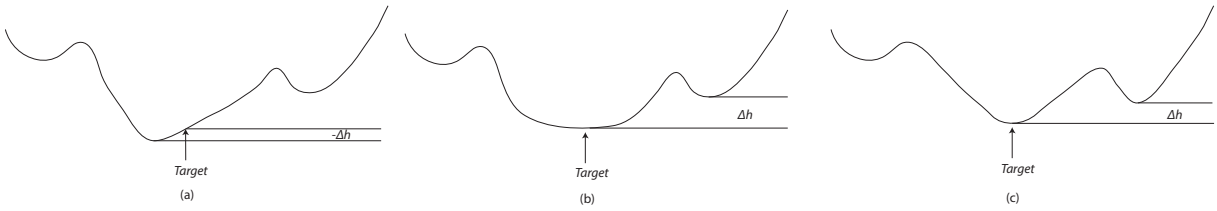

Figure 3.2 A schematic plot of the enthalpy surface, illustrating our definition of Δh. (a): If the target structure is not a local minimum of the enthalpy surface, the inherent structure of the target will not be identical to the target and will have a lower enthalpy. Δh becomes negative. (b) and (c): If the target structure is a local minimum of the enthalpy surface, the inherent structure of the target will be identical to the target. Δh becomes the enthalpy difference between the target and a different inherent structure. Thus Δh might be positive. (b): However, after maximizing Δh, the curvature near the target structure might be very small, leading to an undesirable phonon spectrum. (c): By maximizing $\lambda_0 \Delta h/(1 + r_c^d)$, we sacrifice some Δh to increase the curvature near the target structure while favoring short-ranged potentials. Note that we usually cannot find all inherent structures in the complex, multi-dimensional enthalpy surface. If we miss a inherent structure that has a lower enthalpy than our target, that inherent structure will be discovered in the latter verification step by simulated annealing.

ratio will also change. Second, after the optimization, there will be many competitors that are enthalpically close to the target. However, these competitor structures can be very different from the target and converting from one to another may require crossing a large enthalpy barrier. This makes it especially hard to find the ground state in the latter simulated annealing step.

In this chapter, we introduce an improved objective function that removes these shortcomings, enabling us to target ground-state structures with considerably greater complexity than previous targets. The improved objective function of the optimization is calculated by the following steps:

1. Given a set of potential function parameters, a isotropic pair potential $u_2(r)$ is determined. Using this potential function, we calculate the pressure of the target structure (knowing that the nearest neighbor distance of the target structure is 1). For this pressure, we find the inherent structure of the target structure and each competitor structures. The inherent structures are obtained by min-

imizing the enthalpy per particle $h(\mathbf{r}^N; \mathbf{A})$ in the isobaric ensemble, changing particle positions $\mathbf{r}^N$ and lattice vectors $\mathbf{A}$. In the current implementation, the minimizations are performed with the MINOP algorithm [69].

2. Then, we compare each of the inherent structures with the target structure to test if they are structurally identical.

3. For each inherent structure that is not identical to the target, we calculate its enthalpy per particle h_c. After calculating all the h_c's, we find their minimum value, h_{c0}. The difference between h_{c0} and the enthalpy per particle of the target structure is:

$$\Delta h = h_{c0} - h_{target}. \tag{3.7}$$

4. Having $\Delta h > 0$ will establish the target as the ground state. However, as illustrated in Fig. 3.2, Δh does not reflect the enthalpy cost to deform the target structure. Thus, optimizing for Δh can lead to undesirable phonon spectra. To overcome this problem, we incorporate quantities that enable us to modify the second derivative of the enthalpy around the target structure. For a fixed N, the enthalpy per particle $h(\mathbf{r}^N; \mathbf{A})$ is a function of particle positions and lattice vectors. The Hessian matrix of this function is calculated and its lowest non-zero eigenvalue, λ_0, is calculated. (In d dimensions, the matrix has $d(d+1)/2$ zero-valued eigenvalues corresponding to the translation of particles and the rotation of the fundamental cell.) Maximizing λ_0 will improve phonon stability. We also want to favor the smallest possible potential cut-off distance r_c. Therefore, we choose to maximize the objective function $\lambda_0 \Delta h/(1 + r_c^d)$, where r_c^d is proportional to the volume of the influence sphere of the potential. To sum up, the optimization problem is specified by the following description:

$$\text{maximize } \frac{\lambda_0 \Delta h}{1 + r_c^d}, \text{ subject to } \Delta h > 0,\ \lambda_0 > 0, \text{ and } r_c > 0. \tag{3.8}$$

Having defined the objective function, we use an optimizer to maximize it. We employ the optimizer to evaluate this objective function thousands of times using different parameters. Note that each objective function evaluation requires multiple inherent structure calculations. When optimizing for this objective function, the success rate can be low. This is partially due to the fact that the objective function is neither differentiable nor continuous. We found that the nonlinear "Subplex" optimization algorithm [256] is relatively robust in optimizing this objective function. However, we usually still need to implement the optimization hundreds of times starting from different, random sets of parameters to ensure that we obtain the best solution in a computationally feasible way. To relieve the problem, we optimize for the local stability of the target structure before optimizing for the above mentioned objective function. More precisely, we find target structure's inherent structure (which is the target structure itself if the target structure is locally stable), calculate the coordination structures of the target structure and its inherent structure, and minimize the difference between the two coordination structures.

3.2.4 Verification of the ground state

After the optimization step, we cool, via simulated annealing, liquid configurations of particles interacting with the putative optimized potential to absolute zero temperature to verify that the target is indeed the ground state. To increase computational efficiency, we use relatively small systems (1 to 24 particles) in a fully deformable simulation box under periodic boundary conditions. We also use the thermodynamic cooling schedule, which is given by Eq. (6) of Ref. [215].

In this step, if we discover new structures that are more stable (i.e., have a lower enthalpy) than the target structure, we add them to the competitor list and return to Step C. If we cannot find any competitor and can find the target structure multiple times (10 times in the current implementation), then the target structure is deemed

to be the ground state of the optimized potential. We finally check the result by calculating the target structure's phonon spectrum and ensure that all of the phonon frequencies are real. When calculating the phonon spectrum, we assume that each particle has a unit mass. We calculate the phonon frequency squared ω^2 along some trajectories between points of high symmetry in the Brillouin zone and ensure the nonnegativity condition $\omega^2 \geq 0$ for all wavevectors. The choice of the high symmetry points for each target structure are given in Appendix B.

3.3 Results

In this section, we report optimized potentials for our target structures. To test the validity of each potential, we have also performed Monte Carlo or molecular-dynamics based simulated annealing on relatively large systems, as explained in detail below. We have also calculated the elastic constants of our target structures, which are presented in Appendix D. The rectangular lattices and the rectangular kagomé crystal are elastically anisotropic structures.

3.3.1 Kagomé crystal

The kagomé crystal, as shown in Fig. 3.3, is a 2D crystal structure obtained by removing one one-fourth of the particles in the triangle lattice. The vacancies form a larger triangle lattice. Each fundamental cell contains 3 particles and each particle has 4 nearest neighbors. The local environment of each particle is equivalent up to rotations and translations. At pressure $p = 2.83709$, the kagomé crystal is the ground state of the following potential:

$$u_2(r) = \begin{cases} \left(\dfrac{b}{r^{12}} + c_0 + c_1 r\right)(r - r_c)^2, & \text{if } r < r_c, \\ 0, & \text{otherwise,} \end{cases} \tag{3.9}$$

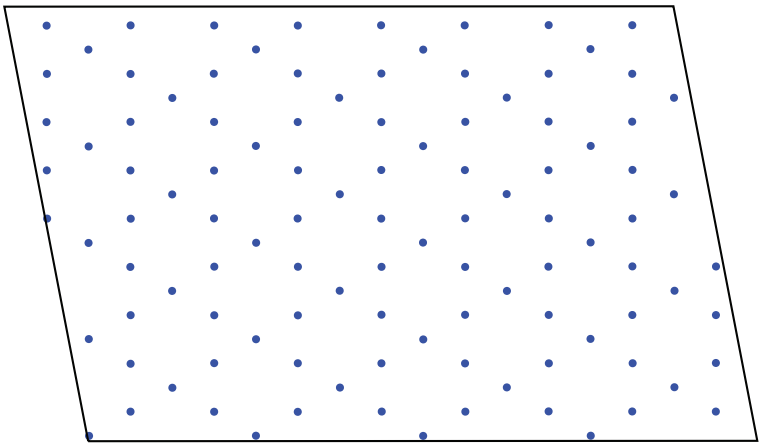

Figure 3.3 Result of a 108-particle simulated annealing for the potential given by Eq. (3.9). This is a perfect kagomé crystal.

where $b = 5.9860 \times 10^{-2}$, $c_0 = -1.2811$, $c_1 = 2.1521$, and $r_c = 2.0364$. The potential and the phonon spectrum of the kagomé crystal are shown in Fig. 3.4. The ending configuration of a 108-particle simulated annealing run is shown in Fig. 3.3 and is seen to be the perfect kagomé crystal.

3.3.2 Rectangular lattices

Rectangular lattices are 2D Bravais lattices [164] in which the two lattice vectors are perpendicular but not equal in length. Let the lengths of two lattice vectors be a and b; we call b/a the *aspect ratio*. When $b/a \neq 1$, the rectangular lattice generally does not retain its aspect ratio when the pressure is perturbed. However, as shown in Appendix E, for a specific class of potentials, a rectangular lattice does retain its aspect ratio in a nontrivial pressure range.

We undertook to stabilize the rectangular lattice with aspect ratio $b/a = 2$ using the potential form in Eq. (3.6). We found that this target structure can indeed be

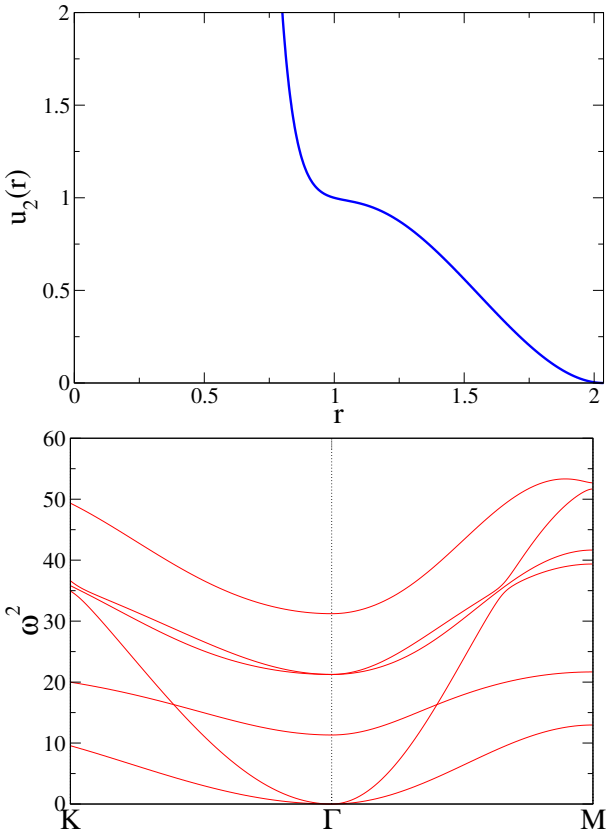

Figure 3.4 Top panel: The kagomé potential $u_2(r)$ versus distance corresponding to Eq. (3.9). Bottom panel: The phonon frequency squared ω^2 versus wavevector of kagomé crystal.

stabilized by the following potential at pressure $p = 1.81198$:

$$u_2(r) = \begin{cases} \left(\dfrac{b}{r^{12}} + c_0 + c_1 r\right) \exp(-\alpha r^2)(r - r_c)^2, & \text{if } r < r_c, \\ 0, & \text{otherwise,} \end{cases} \tag{3.10}$$

where $b = 2.1639 \times 10^{-2}$, $c_0 = -0.26107$, $c_1 = 0.31488$, $\alpha = 0.78857$, and $r_c = 6.4$. The potential and the phonon spectrum of the rectangular lattice with aspect ratio $b/a = 2$ are shown in Fig. 3.5. In the phonon spectrum, there is a very low branch between Γ and Y points (defined in Appendix B), indicating that there is a way to deform the target structure with very low energy cost. The final configuration of a 108-particle simulated annealing run is shown in Fig. 3.6. Although the particles

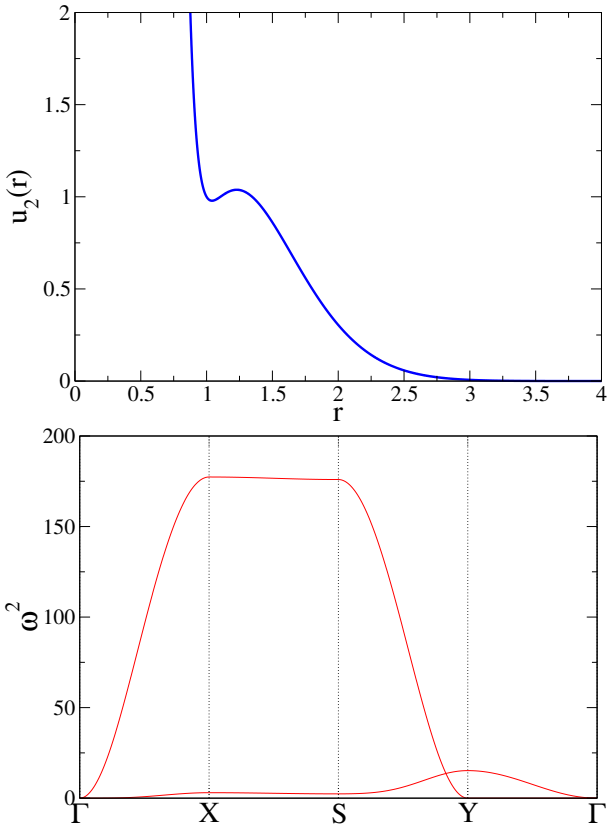

Figure 3.5 Top panel: Lower-order potential $u_2(r)$ versus distance for rectangular lattice with aspect ratio $b/a = 2$, corresponding to Eq. (3.10). Bottom panel: The phonon frequency squared ω^2 versus wavevector of the target.

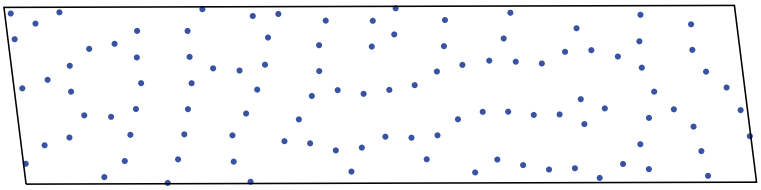

Figure 3.6 Result of a 108-particle simulated annealing for the potential given by Eq. (3.10). The particles show a tendency to self-assemble into the rectangular lattice with aspect ratio $b/a = 2$, but many defects exist in the resulting configuration.

show a tendency to self-assemble to the target lattice, the ending configuration is clearly disordered, revealing the difficulty to crystallize particles interacting with this potential.

These results can be improved when we increase the order of the polynomial in Eq. (3.6). We found that the target can be well stabilized using the following potential

at pressure $p = 1.12901$:

$$u_2(r) = \begin{cases} \left(\dfrac{b}{r^{12}} + c_0 + c_1 r + c_2 r^2 + c_3 r^3 + c_4 r^4 + c_5 r^5 \right) \exp(-\alpha r^2)(r - r_c)^2, & \text{if } r < r_c, \\ 0, & \text{otherwise,} \end{cases} \tag{3.11}$$

where $b = 3.0058 \times 10^{-3}$, $c_0 = 0.69293$, $c_1 = -0.30361$, $c_2 = 9.3960 \times 10^{-2}$, $c_3 = -0.36154$, $c_4 = 0.82231$, $c_5 = 4.3741 \times 10^{-2}$, $\alpha = 0.44095$, and $r_c = 2.2524$. The potential and the phonon spectrum of the rectangular lattice with aspect ratio $b/a = 2$ are shown in Fig. 3.7. The branch between Γ and Y points has been lifted, suggesting that it is harder to deform the target structure. The final configuration of a 108-particle simulated annealing run is shown in Fig. 3.8. The result is a perfect rectangular lattice with aspect ratio $b/a = 2$.

Using the new optimization technique, we can also stabilize rectangular lattices with unusually large aspect ratios. For example, at pressure $p = 1.04006$, the rectangular lattice with aspect ratio $b/a = \pi$ is the ground state of the following potential:

$$u_2(r) = \begin{cases} \left(\dfrac{b}{r^{12}} + c_0 + c_1 r + c_2 r^2 + c_3 r^3 + c_4 r^4 \right) \exp(-\alpha r^2)(r - r_c)^2, & \text{if } r < r_c, \\ 0, & \text{otherwise,} \end{cases} \tag{3.12}$$

where $b = 1.1416 \times 10^{-2}$, $c_0 = -1.1117$, $c_1 = 3.3164$, $c_2 = -3.1330$, $c_3 = 1.2578$, $c_4 = -0.16340$, $\alpha = 0.0309012$, and $r_c = 3.4103$. The potential and the phonon spectrum of the rectangular lattice with aspect ratio $b/a = \pi$ are shown in Fig. 3.9. The branch between Γ and Y points is low, because when the aspect ratio increases, it becomes increasingly difficult to prevent the target structure from deforming. Obtaining the target structure as a ground state using simulated annealing is also not easy. In fact, we were only able to achieve the ground state with a system of 24 particles. The

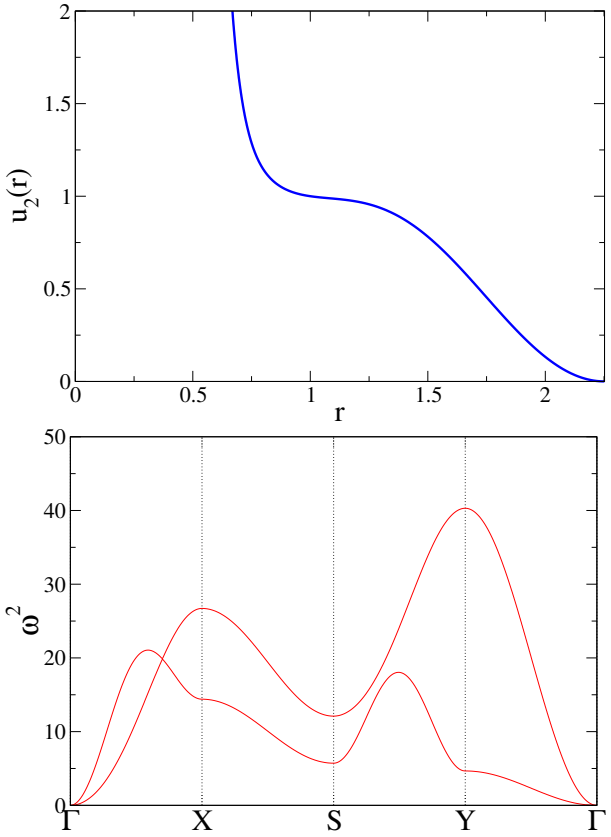

Figure 3.7 Top panel: Higher-order potential $u_2(r)$ versus distance for rectangular lattice with aspect ratio $b/a = 2$, corresponding to Eq. (3.11). Bottom panel: The phonon frequency squared ω^2 versus wavevector of the target.

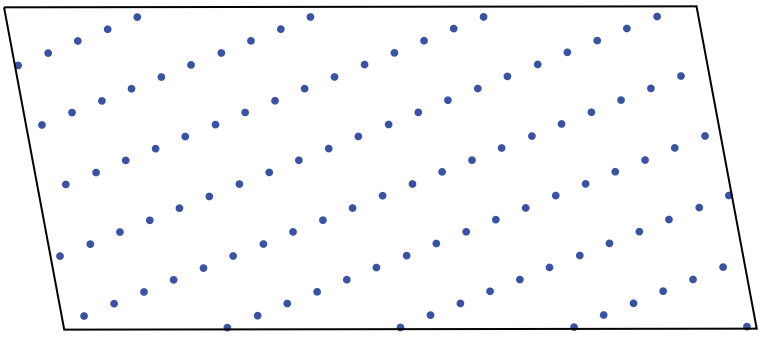

Figure 3.8 Result of a 108-particle simulated annealing for the potential given by Eq. (3.11). This is a perfect rectangular lattice with aspect ratio $b/a = 2$.

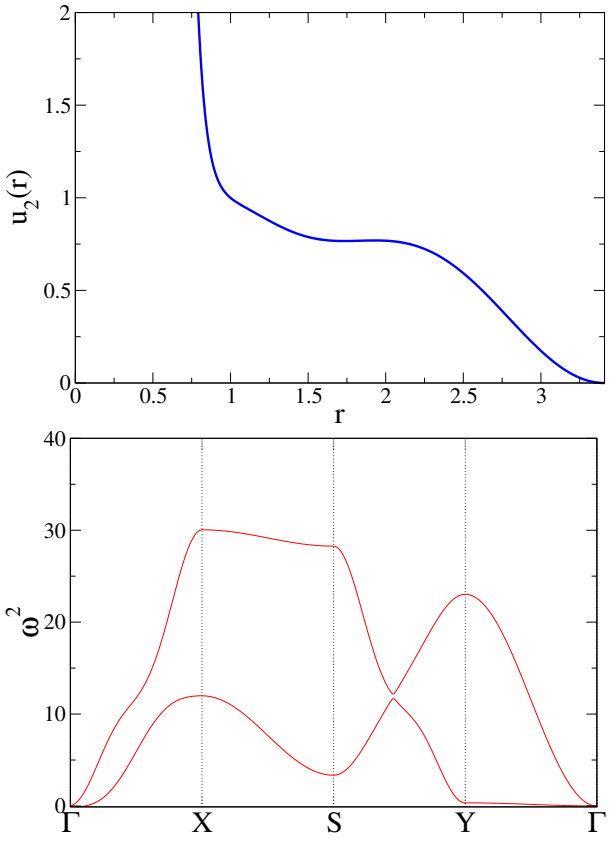

Figure 3.9 Top panel: The potential $u_2(r)$ versus distance for rectangular lattice with aspect ratio $b/a = \pi$, corresponding to Eq. (3.12). Bottom panel: The phonon frequency squared ω^2 versus wavevector of the target.

ending configuration of an 24-particle simulated annealing run is shown in Fig. 3.10. The result is perfect rectangular lattice with aspect ratio $b/a = \pi$.

3.3.3 Rectangular kagomé crystal

The rectangular kagomé crystal is shown in Fig. 3.11. This crystal is similar to kagomé crystal because they are both triangle lattices with vacancies, and each particle has 4 nearest neighbors. However, unlike the kagomé crystal, where the vacancies are arranged in a triangle lattice, in the rectangular kagomé crystal the vacancies are arranged in a rectangular lattice. Unlike all previous targets, where symmetry guarantees that the total force on each particle is zero, the local stability of some particles

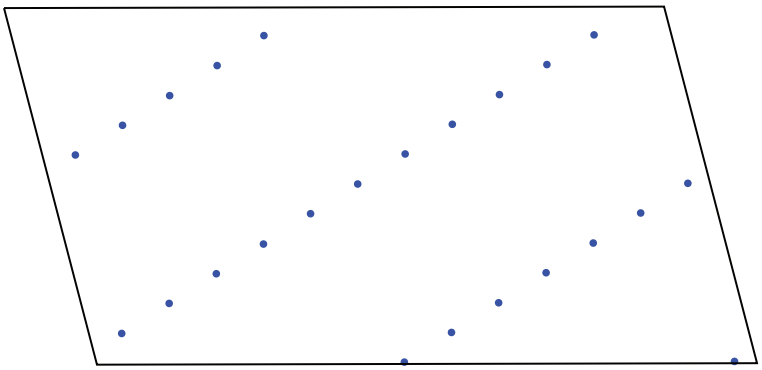

Figure 3.10 Result of a 24-particle simulated annealing for the potential given by Eq. (3.12). This is a perfect rectangular lattice with aspect ratio $b/a = \pi$.

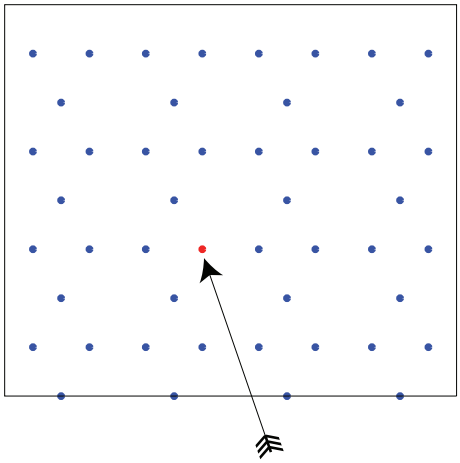

Figure 3.11 The rectangular kagomé crystal structure. The particle indicated by an arrow (the red particle in colored version) has 3 nearest neighbors on the left and 1 nearest neighbor on the right, thus it is very hard to be stabilized.

in the rectangular kagomé crystal is not guaranteed by the symmetry. For example, the particle indicated by an arrow in Fig. 3.11 has 3 nearest neighbors on the left and 1 nearest neighbor on the right, and thus it is not necessarily in force equilibrium. Accordingly, the rectangular kagomé crystal is a very challenging target structure. In fact, we were unable to stabilize this structure using the previous potential form, which produces smooth decaying functions. By exploring different potential forms, we found that the rectangular kagomé crystal is the ground state of the following potential at pressure $p = 3.97107$:

$$u_2(r) = \begin{cases} (0.012352r + 0.27370)\exp(-0.086364r^2)(r - 3.050295)^2 \\ +\dfrac{3.8032 \times 10^{-4}}{r^{12}} - \dfrac{1.0430 \times 10^{-2}}{r^6} \\ -0.092965\exp[-(\dfrac{r - 0.99953}{0.024893})^2] + 1.2956 \times 10^{-5}, & \text{if } r < 3.050295, \\ 0, & \text{otherwise.} \end{cases} \tag{3.13}$$

The potential and the phonon spectrum of the rectangular kagomé crystal are shown in Fig. 3.12. The potential contains a small Gaussian well, which is very helpful in stabilizing the particles with asymmetrical environments and forcing them to stay in the correct position. However, this narrow well in the potential greatly increases the frequency of some phonon modes, while it is not helpful for other phonon modes. Thus in the phonon spectrum, some branches are negligibly low compared to other branches. Using this potential, we were able to get rectangular kagomé crystal with simulated annealing, as shown in Fig. 3.13. The presence of a small Gaussian well indicates that this isotropic pair potential is experimentally unattainable. Consequently it would be scientifically useful to determine if 3-body interaction would enhance stability.

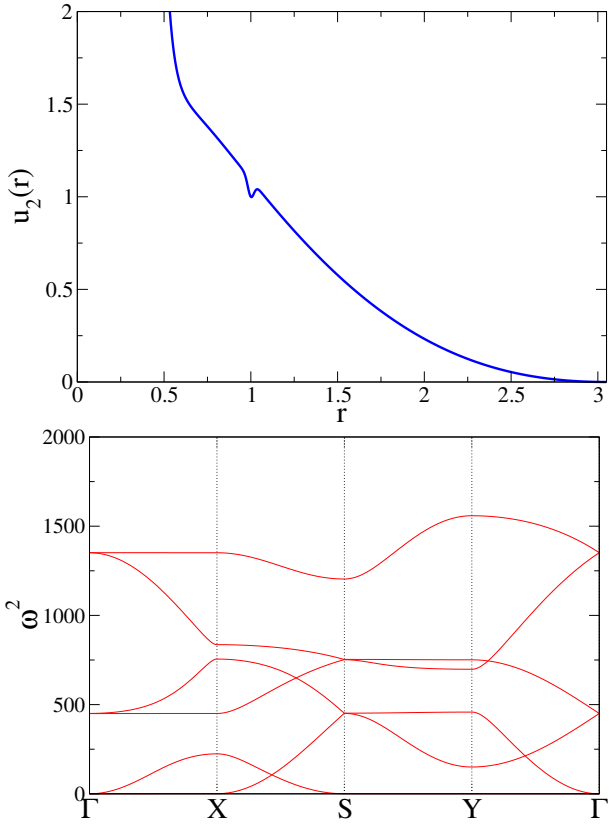

Figure 3.12 Top panel: The rectangular kagomé potential $u_2(r)$ versus distance corresponding to Eq. (3.13). Bottom panel: The phonon frequency squared ω^2 versus wavevector of the rectangular kagomé crystal.

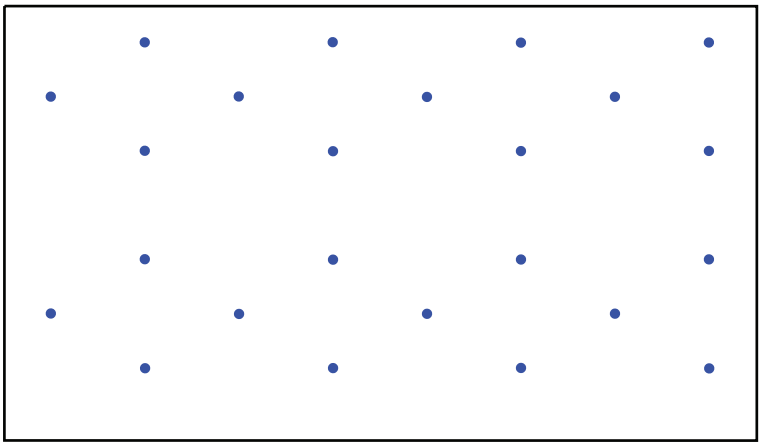

Figure 3.13 Result of a 24-particle simulated annealing for the potential given by Eq. (3.13). This is a perfect rectangular kagomé crystal.

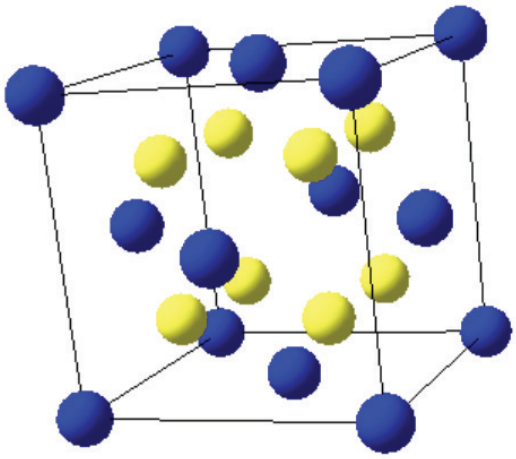

Figure 3.14 The conventional unit cell of CaF_2 crystal. Blue (dark gray) spheres are Ca^{2+} ions, yellow (light gray) spheres are F^- ions. Particle radii is drawn proportionally to their crystal ionic radii [268] $r(Ca^{2+})$=126pm, $r(F^-)$=117pm.

3.3.4 CaF_2 crystal inhabited by a single particle species

In the CaF_2 crystal, Ca^{2+} ions are located in a face-centered cubic lattice, F^- ions fills in all the tetrahedral voids. A conventional unit cell of the CaF_2 crystal is shown in Fig. 3.14. Unlike previous target structures, the CaF_2 crystal apparently contains 2 kinds of particles: Each Ca^{2+} ion has 8 nearest neighbors while each F^- ion has 4 nearest neighbors. However, we found that this structure can counterintuitively be the ground state of a single-component system with the following potential at pressure $p = 6.19610$:

$$u_2(r) = \begin{cases} \left(\dfrac{b}{r^{12}} + c_0 + c_1 r + c_2 r^2 + c_3 r^3 + c_4 r^4\right) \exp(-\alpha r^2)(r - r_c)^2, & \text{if } r < r_c, \\ 0, & \text{otherwise,} \end{cases} \tag{3.14}$$

where $b = 2.9340 \times 10^{-3}$, $c_0 = 0.83963$, $c_1 = 0.36976$, $c_2 = -0.13150$, $c_3 = -2.1869 \times 10^{-3}$, $c_4 = 1.5010 \times 10^{-3}$, $\alpha = 0.18682$, and $r_c = 2.0564$.

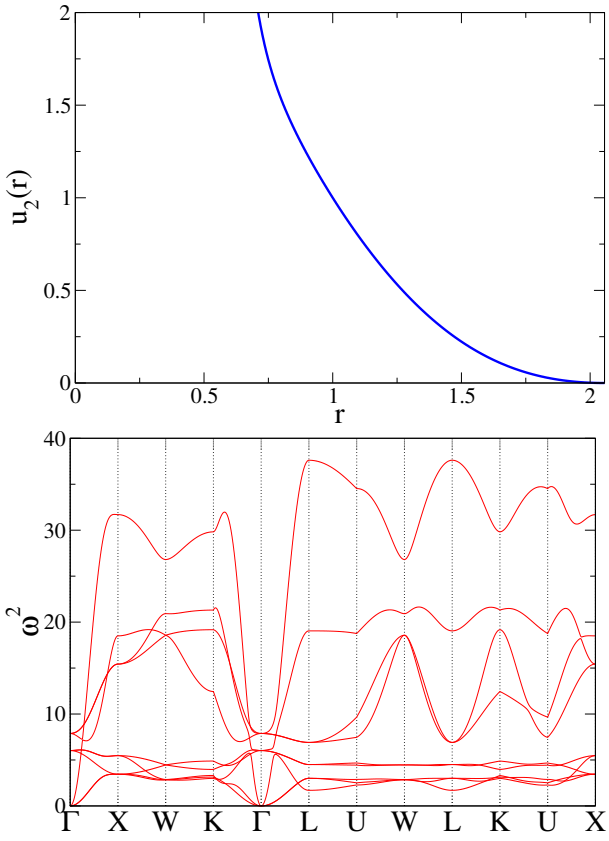

Figure 3.15 Top panel: The CaF_2 potential $u_2(r)$ versus distance corresponding to Eq. (3.14). Bottom panel: The phonon frequency squared ω^2 versus wavevector of the CaF_2 crystal inhabited by a single particle species.

The potential and the phonon spectrum of the target crystal are shown in Fig. 3.15. When we do simulated annealing using this potential, we rarely get the target structure when the system contains 3 or 6 particles. We were not able to achieve the ground state with larger systems. However, since we have tried simulated annealing using 1 to 18 particles and have never found any competitor structures with lower enthalpy, we still believe the target structure is the ground state of this potential.

To further test the validity of this potential, we have performed a molecular dynamics (MD) based simulated annealing running on GPU [1, 10] of 12000 particles in a fixed cubic box. The side length of the box is 10 times the side length of a CaF_2 conventional unit cell. Imitating the work by Rechtsman et al. [243], we fix 1200 particles into a layer of CaF_2 conventional unit cells, and let the rest 10800 particles

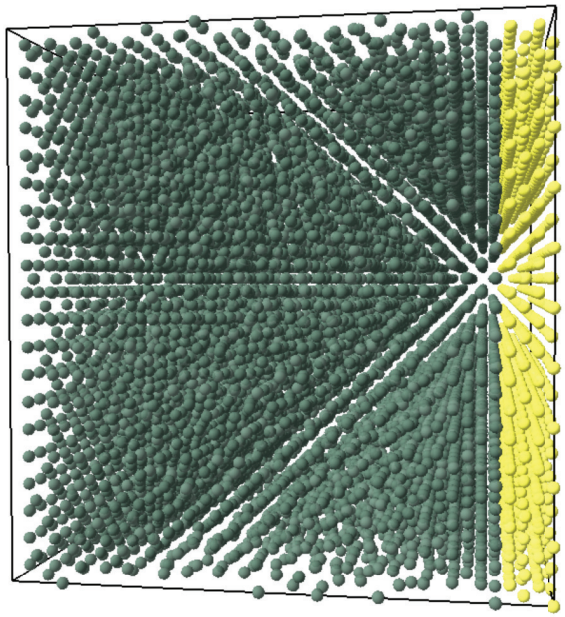

Figure 3.16 Result of a 12000-particle MD based simulated annealing for the potential given by Eq. (3.14). Yellow (light gray) particles are fixed into the CaF_2 structure during the simulation. Green (dark gray) particles self-assemble into the same structure.

move starting from a random sequential addition configuration with collision radius $r = 0.7$. Upon slow cooling, we find that the CaF_2 epitaxially grow from the fixed layer. The ending configuration is given in Fig. 3.16.

3.4 Conclusions and Discussion

To summarize, we have improved upon previous inverse statistical mechanical optimization techniques. By finding the inherent structures of each competitor structure, we are able to define a new objective function for optimization, thus overcoming difficulties involved in previous energy difference optimizations or pressure range optimizations. With this optimization technique, we have designed isotropic pair potentials so that the kagomé crystal, rectangular lattices with aspect ratio 2 and π, the rectangular kagomé crystal, and the structure of the CaF_2 crystal inhabited by a single particle species become the unique ground states.

By finding potentials that can stabilize these target structures as unique ground states, we have demonstrated the robustness of our method. Our potential which stabilizes the kagomé crystal showcases our improvement over previous inverse work [80] by being comparably simple to a potential found using the forward approach [25]. Moreover, by being able to design isotropic pair potentials for the rectangular kagomé crystal and CaF_2 crystal inhabited by a single particle species, we have also demonstrated that the new method can handle target structures that contain particles in different or asymmetrical local environments.

The rectangular lattices are very simple examples of a much broader family of crystal structures with lower elastic symmetry. Their low elastic symmetries make them spatially scale differently in different directions when the pressure changes. To our knowledge, none of the target structures in this family have been stabilized with pressure range optimization. One structure in this family, the 3D simple hexagonal lattice, has been stabilized previously [241] using energy difference optimization. However, since the result of energy difference optimization is sensitive to structurally close competitors (e.g. other rectangular lattices with slightly different aspect ratios), one cannot precisely control the aspect ratio. In contrast, our new method allows us to precisely specify large unusual aspect ratios (for example, π) when targeting this family of structures.

All of our target structures are stabilized as unique ground states. In the application of inverse statistical mechanics to spin systems [73], the possible outcomes for a given target configuration was organized into the following three solution classes: unique (nondegenerate) ground state (Class I), degenerate ground states with the same two-point correlation functions (Class II), and solutions not contained in the previous two classes (Class III). All of the target structures considered in this chapter fall within Class I. A simple thought experiment yields an example of Class III solutions. Since the face-centered cubic (FCC) and hexagonal close-packed (HCP)

crystals have different coordination structures, they cannot fall within Class II. If we limit the range of the pair potential to be between the nearest and next nearest neighbors, we will not be able to distinguish these target pairs from one another and thus they cannot belong to Class I. Therefore they will fall within Class III. It would be interesting to see if one can stabilize any Class II solutions for many particle system.

If a target crystal structure falls within Class I, then what are necessary functional characteristics of the potential? For example, can we stabilize a particular target with monotonic pair potential? What is the minimum range (cut-off) of the pair potential? While rigorous answers to these questions are beyond the scope of the present chapter, we can offer some general principles that may provide guidance in determining whether certain target structures can be achieved as ground states by a particular class of radial pair potentials. Let us consider the first question. Our experience is that, there are target structures where the symmetry does not guarantee that the total force on each particle is zero (for example, rectangular kagomé crystal). Target structures of this kind cannot be stabilized with monotonic radial pair potentials. Other target structures can be stabilized with either monotonic potentials or potentials with wells. For example, the diamond crystal has been stabilized with both a monotonic potential [193] and a potential with wells [243].

Concerning the second question, the minimum range of the pair potential varies for different targets, but is usually comparable to the longest diagonal length of the fundamental cell l_{dia} of the target crystal. It seems that in order for the particles to self-assemble into the target crystal, the pair potential only needs to encode coordination information within a range comparable in size to the fundamental cell (since the crystal is the replication of the fundamental cell under periodic boundary conditions). For certain relatively symmetric target structures, the fundamental cell consists of particle subsets that differ only by translations, rotations, and inversions. Thus, the pair potentials for these targets may only require a cut-off distance r_c that

is shorter than the longest diagonal of the fundamental cell. Examples include our kagomé and CaF_2 potentials, a previously designed body-centered-cubic potential [241], and a kagomé potential found by forward approach [25]. For certain relatively challenging target such as the rectangular kagomé crystal (it is challenging because of the reasons explained in Sec. 3.3.3), the range of the potential can be somewhat longer than the longest diagonal of the fundamental cell. In fact, the length and symmetry of the fundamental cell is the most important factor determining the required range of the potential. This is demonstrated by the CaF_2 crystal inhabited by a single particle species, which is symmetric but challenging (because it contains particles in different local environments). The optimized potential that we have obtained here contains a relatively high-order polynomial, but its range is surprisingly short. Table 3.1 summarizes the minimal cut-off distance r_c that we found for the targets considered in this chapter. To further support the notion that the minimal potential cut-off distance r_c need only be comparable in size to the longest diagonal of the fundamental cell, we have also generated short-ranged isotropic pair potentials using our algorithm for several other simpler targets. Except for the FCC crystal, all of them have been stabilized before, including the 2D honeycomb crystal [239, 240, 191, 192], 2D square lattice [240, 191, 192] 3D body-centered cubic (BCC) lattice [241], 3D simple cubic lattice [241], 3D diamond crystal [243, 193], and 3D FCC lattice. We see in Table 3.2 that the potential cut-off distances are indeed comparable in size to the longest diagonal of the fundamental cell, which is consistent with our results for more complicated targets listed in Table 3.1.

What are the limitations of isotropic pair potentials in achieving targeted ground states? In other words, given a target structure, how can we tell whether an isotropic pair potential can stabilize it or not? We are aware of a theorem that partially answers this question: Since the enthalpy per particle is determined by the coordination numbers Z_j and specific volume v in Eq. (3.5), a target structure cannot be stabilized

Table 3.1 Isotropic pair potential cut-off r_c, longest diagonal length of the fundamental cell l_{dia}, and their ratio of targets reported in Sec. 3.3. The nearest neighbor distance is 1.

Target Structure	r_c	l_{dia}	r_c/l_{dia}
Kagomé	2.04	$2\sqrt{3}$	0.59
Rectangular lattice $b/a = 2$	2.25	$\sqrt{5}$	1.00
Rectangular lattice $b/a = \pi$	3.41	$\sqrt{\pi^2 + 1}$	1.03
CaF_2 single species	2.06	4	0.52
Rectangular kagomé	3.05	$\sqrt{7}$	1.15

Table 3.2 Application of our current optimization scheme to stabilize simpler targets with potentials having a minimal cut-off distance r_c for the family of potential functions indicated in Eq. (3.6). Except for the FCC lattice, all of the targets have been stabilized before [239, 240, 191, 192, 241, 243, 193]. Isotropic pair potential cut-off r_c, longest diagonal length of the fundamental cell l_{dia}, and their ratio are listed. The nearest neighbor distance is 1.

Target Structure	r_c	l_{dia}	r_c/l_{dia}
Honeycomb	2.53	3	0.84
Square	1.87	$\sqrt{2}$	1.32
BCC	1.24	$\sqrt{11/3}$	0.65
Simple Cubic	1.54	$\sqrt{3}$	0.89
Diamond	2.46	4	0.62
FCC	1.77	$\sqrt{6}$	0.72

by isotropic pair potentials as unique ground state if its coordination numbers and specific volume is identical to that of another structure, or is a weighted average of other structures [57]. One example of this theorem is that chiral targets with only one type of handedness cannot be stabilized by isotropic pair interactions [302]. Besides the target structures that are disproved by this theorem, are all other structures realizable by isotropic pair interactions? Seeking a full answer to this question will be a direction of future research.

The entire set of possible target structures extends far beyond what has been examined. Specifically, this includes challenging structures such as "tunneled" crystals [320] characterized by a high concentration of chains of vacancies as well as the graphite crystal, to mention a few examples. A direction for future research is to either stabilize them with simplest possible radial potentials or to prove that they

cannot be stabilized with such interactions, which may require us to improve the current algorithm. We are also interested in expanding our method to stabilize multicomponent systems and systems containing particles with anisotropic interactions [302].

3.5 Appendix A: Crystal Structure and Theta Series of Target Structures

In this appendix, we provide the vectors that specify the target crystal structure as well as the corresponding partial theta series defined generally by Eq. (3.4).

3.5.1 Kagomé crystal

The kagomé crystal is a 2D crystal whose fundamental lattice vectors can be specified as follows:

$$\mathbf{a}_1 = 2\mathbf{i} \text{ and } \mathbf{a}_2 = \mathbf{i} + \sqrt{3}\mathbf{j}. \tag{3.15}$$

Its reciprocal lattice vectors are

$$\mathbf{b}_1 = \pi\mathbf{i} - \frac{\pi}{\sqrt{3}}\mathbf{j} \text{ and } \mathbf{b}_2 = \frac{2\pi}{\sqrt{3}}\mathbf{j}. \tag{3.16}$$

Each fundamental cell contains 3 particles, located at the positions

$$\begin{aligned} \mathbf{r}_1 &= \frac{1}{2}\mathbf{a}_1 = \mathbf{i}, \\ \mathbf{r}_2 &= \frac{1}{2}\mathbf{a}_2 = \frac{1}{2}\mathbf{i} + \frac{\sqrt{3}}{2}\mathbf{j}, \text{ and} \\ \mathbf{r}_3 &= \frac{1}{2}\mathbf{a}_1 + \frac{1}{2}\mathbf{a}_2 = \frac{3}{2}\mathbf{i} + \frac{\sqrt{3}}{2}\mathbf{j}. \end{aligned} \tag{3.17}$$

The first few terms of its theta series are

$$\theta(q) = 1 + 4q + 4q^3 + 6q^4 + 8q^7 + 4q^9 + \cdots . \tag{3.18}$$

3.5.2 Rectangular lattice with aspect ratio t

Rectangular lattices are 2D crystals whose fundamental lattice vectors can be specified as follows:

$$\mathbf{a}_1 = \mathbf{i} \text{ and } \mathbf{a}_2 = t\mathbf{j}. \tag{3.19}$$

Its reciprocal lattice vectors are

$$\mathbf{b}_1 = 2\pi\mathbf{i} \text{ and } \mathbf{b}_2 = \frac{2\pi}{t}\mathbf{j}. \tag{3.20}$$

Each fundamental cell contains 1 particle, located at the positions

$$\mathbf{r}_1 = \mathbf{0} \tag{3.21}$$

The first few terms of its theta series are

$$\theta(q) = 1 + 2q + 2q^4 + 2q^9 + \cdots + 2q^{t^2} + 4q^{t^2+1} + 4q^{t^2+4} + \cdots . \tag{3.22}$$

3.5.3 Rectangular kagomé crystal

The rectangular kagomé crystal is a 2D crystal whose fundamental lattice vectors can be specified as follows:

$$\mathbf{a}_1 = 2\mathbf{i} \text{ and } \mathbf{a}_2 = \sqrt{3}\mathbf{j}. \tag{3.23}$$

Its reciprocal lattice vectors are

$$\mathbf{b}_1 = \pi\mathbf{i} \text{ and } \mathbf{b}_2 = \frac{2\pi}{\sqrt{3}}\mathbf{j}. \tag{3.24}$$

Each fundamental cell contains 3 particles, located at the positions

$$\begin{aligned} \mathbf{r}_1 &= \frac{1}{2}\mathbf{a}_1 = \mathbf{i}, \\ \mathbf{r}_2 &= \frac{1}{4}\mathbf{a}_1 + \frac{1}{2}\mathbf{a}_2 = \frac{1}{2}\mathbf{i} + \frac{\sqrt{3}}{2}\mathbf{j}, \text{ and} \\ \mathbf{r}_3 &= \frac{3}{4}\mathbf{a}_1 + \frac{1}{2}\mathbf{a}_2 = \frac{3}{2}\mathbf{i} + \frac{\sqrt{3}}{2}\mathbf{j}. \end{aligned} \tag{3.25}$$

The first few terms of its theta series are

$$\theta(q) = 1 + 4q + \frac{14}{3}q^3 + \frac{14}{3}q^4 + \frac{28}{3}q^7 + 4q^9 + \cdots. \tag{3.26}$$

3.5.4 CaF_2 crystal inhabited by a single particle species

The CaF_2 crystal inhabited by a single particle species is a 3D crystal whose fundamental lattice vectors can be specified as follows:

$$\mathbf{a}_1 = \frac{2}{\sqrt{3}}(\mathbf{i}+\mathbf{j}),\ \mathbf{a}_2 = \frac{2}{\sqrt{3}}(\mathbf{i}+\mathbf{k}), \text{ and } \mathbf{a}_3 = \frac{2}{\sqrt{3}}(\mathbf{j}+\mathbf{k}). \tag{3.27}$$

Its reciprocal lattice vectors are

$$\mathbf{b}_1 = \sqrt{\frac{3}{4}}\pi(\mathbf{i}+\mathbf{j}-\mathbf{k}),\ \mathbf{b}_2 = \sqrt{\frac{3}{4}}\pi(-\mathbf{i}+\mathbf{j}+\mathbf{k}), \text{ and } \mathbf{b}_3 = \sqrt{\frac{3}{4}}\pi(\mathbf{i}-\mathbf{j}+\mathbf{k}). \tag{3.28}$$

Each fundamental cell contains 3 particles, located at the positions

$$\begin{aligned}\mathbf{r}_1 &= \mathbf{0},\\ \mathbf{r}_2 &= \frac{\mathbf{a}_1+\mathbf{a}_2+\mathbf{a}_3}{4} = \frac{\mathbf{i}+\mathbf{j}+\mathbf{k}}{\sqrt{3}}, \text{ and}\\ \mathbf{r}_3 &= \frac{3(\mathbf{a}_1+\mathbf{a}_2+\mathbf{a}_3)}{4} = \sqrt{3}(\mathbf{i}+\mathbf{j}+\mathbf{k}).\end{aligned} \tag{3.29}$$

The first several terms of its theta series are

$$\theta(q) = 1+\frac{16}{3}q+4q^{4/3}+12q^{8/3}+16q^{11/3}+\frac{16}{3}q^4+6q^{16/3}+16q^{19/3}+16q^{20/3}+24q^8+\frac{64}{3}q^9+\cdots. \tag{3.30}$$

3.6 Appendix B: Definition of High-Symmetry Points in the Brillouin Zone

When ascertaining the phonon spectrum of a crystal, we calculate the phonon frequency squared ω^2 along certain trajectories between points of high symmetry in the Brillouin zone. For different crystals, the points of high symmetry are described below.

3.6.1 2D kagomé crystal

The points of high symmetry of 2D kagomé crystal are

$$K = \frac{1}{2}\mathbf{b}_1,\ \Gamma = \mathbf{0},\text{ and } M = \frac{1}{3}(\mathbf{b}_1+\mathbf{b}_2), \tag{3.31}$$

where $\mathbf{b}_1$ and $\mathbf{b}_2$ are reciprocal lattice vectors.

3.6.2 2D rectangular lattices and rectangular kagomé crystal

The points of high symmetry of 2D rectangular lattices and rectangular kagomé crystal are

$$\Gamma = \mathbf{0},\ X = \frac{1}{2}\mathbf{b}_1,\ S = \frac{1}{2}(\mathbf{b}_1 + \mathbf{b}_2),\ \text{and}\ Y = \frac{1}{2}\mathbf{b}_2, \tag{3.32}$$

where $\mathbf{b}_1$ and $\mathbf{b}_2$ are reciprocal lattice vectors.

3.6.3 CaF_2 crystal inhabited by a single particle species

The points of high symmetry of CaF_2 crystal inhabited by a single particle species are

$$\begin{aligned}
&\Gamma = \mathbf{0},\\
&X = \frac{1}{2}(\mathbf{b}_1 + \mathbf{b}_3),\\
&W = \frac{1}{4}(2\mathbf{b}_1 + \mathbf{b}_2 + 3\mathbf{b}_3),\\
&K = \frac{3}{8}(\mathbf{b}_1 + \mathbf{b}_2 + 2\mathbf{b}_3),\\
&L = \frac{1}{2}(\mathbf{b}_1 + \mathbf{b}_2 + \mathbf{b}_3),\ \text{and}\\
&U = \frac{1}{8}(5\mathbf{b}_1 + 4\mathbf{b}_2 + 5\mathbf{b}_3),
\end{aligned} \tag{3.33}$$

where $\mathbf{b}_1$, $\mathbf{b}_2$, and $\mathbf{b}_3$ are reciprocal lattice vectors.

3.7 Appendix C: Definition of the "Difference" Between Two Coordination Structures

The coordination structure of a crystal is characterized by coordination numbers Z_j for different distances r_j, as defined in Sec. 3.2. As shown in Appendix A, the coordination numbers and distances of a crystal structure can be summarized into an infinite table, which consists of infinite number of "rows". Each row contains a distance r and the average number of neighbors Z at that distance. We have defined a

"difference" between two coordination structures. To calculate it, we use the following steps:

1. Rows of the two coordination structures, $\{r, Z\}$, are combined into pairs by the following rules:

   (a) The first unpaired rows of the two coordination structures are paired if their coordination numbers are equal.

   (b) If their coordination numbers are not equal, let the row with larger coordination number be $\{r_{large}, Z_{large}\}$ and the row with smaller coordination number be $\{r_{small}, Z_{small}\}$. The row with the larger coordination number, $\{r_{large}, Z_{large}\}$, is split into two rows: A row $\{r_{large}, Z_{small}\}$ and another row $\{r_{large}, Z_{large} - Z_{small}\}$. The former row is paired with $\{r_{small}, Z_{small}\}$. The latter row will be paired later.

   (c) Return to step (a) unless enough pairs are obtained.

   For example, to combine the coordination structure of rectangular kagomé crystal and that of kagomé crystal into pairs of rows, we do the following. To illustrate the process, let us denote a row from the rectangular kagomé crystal as $\{r, Z\}_r$, and a row from the kagomé crystal as $\{r, Z\}_k$

   (a) The first row of the coordination structure of rectangular kagomé crystal, $\{1, 4\}_r$, is paired with the first row of the coordination structure of kagomé crystal, $\{1, 4\}_k$.

   (b) The second row of the coordination structure of rectangular kagomé crystal, $\{\sqrt{3}, 14/3\}_r$, is split into two rows: a row $\{\sqrt{3}, 4\}_r$ will be paired with the second row from the kagomé crystal ($\{\sqrt{3}, 4\}_k$), the other row $\{\sqrt{3}, 2/3\}_r$ will be paired later.

(c) The next row from the kagomé crystal, $\{2, 6\}_k$, is split into two rows: a row $\{2, 2/3\}_k$ to be paired with the remaining row from the rectangular kagomé crystal, $\{\sqrt{3}, 2/3\}_r$, and another row $\{2, 16/3\}_k$ to be paired later.

(d) The remaining row from the kagomé crystal, $\{2, 16/3\}_k$, is split into two rows: $\{2, 14/3\}_k$ and $\{2, 2/3\}_k$. The former is paired with the third row from the rectangular kagomé crystal, $\{2, 14/3\}_r$. The latter remains to be paired.

(e) continue this process until enough pairs are obtained. The first several obtained pairs are:

$\{1, 4\}_r$	$\{1, 4\}_k$
$\{\sqrt{3}, 4\}_r$	$\{\sqrt{3}, 4\}_k$
$\{\sqrt{3}, 2/3\}_r$	$\{2, 2/3\}_k$
$\{2, 14/3\}_r$	$\{2, 14/3\}_k$
$\{\sqrt{7}, 2/3\}_r$	$\{2, 2/3\}_k$
$\{\sqrt{7}, 8\}_r$	$\{\sqrt{7}, 8\}_k$
$\{\sqrt{7}, 2/3\}_r$	$\{3, 2/3\}_k$
.....	

2. The distance between two coordination structures is given by:

$$D = \sum_{\text{all pairs } \{r_a, Z_a\} \text{ and } \{r_b, Z_b\}} Z_a (r_a - r_b)^2 \exp(-r_a) \tag{3.34}$$

In our implementation, the summation is truncated at $r = 5$.

This definition of distance D has the following properties:

1. $D \geq 0$. $D = 0$ if and only if the two coordination structures are identical.

2. A infinitesimally distorted structure of an original structure has a coordination structure which has an infinitesimal distance to the coordination structure of the original structure.

3.8 Appendix D: Elastic Properties of Target Structures

We have also calculated the elastic constants of our target structures. To illustrate the concept of elastic constants, consider a small, affine deformation of the target structure:

$$\mathbf{x} = (\mathbf{I} + \epsilon)\mathbf{x}_0, \tag{3.35}$$

where $\mathbf{x}_0$ is the original location, $\mathbf{x}$ is the new location, $\mathbf{I}$ is a unit second-order tensor, and ϵ is a small second-order tensor, called "strain tensor". The elastic constants C_{ijkl} are defined as:

$$C_{ijkl} = \frac{\partial^2 H}{\partial \epsilon_{ij} \partial \epsilon_{kl}}. \tag{3.36}$$

The elastic constants of our target structures are presented below.

3.8.1 2D isotropic target

The kagomé crystal is a 2D isotropic crystal. Its elastic constants are determined by two independent constants, e.g., its Young's modulus E and Poisson's ratio ν:

$$\begin{pmatrix} C_{1111} & C_{1122} & C_{1112} \\ C_{2211} & C_{2222} & C_{2212} \\ C_{1211} & C_{1222} & C_{1212} \end{pmatrix} = \frac{E}{1-\nu^2} \begin{pmatrix} 1 & \nu & 0 \\ \nu & 1 & 0 \\ 0 & 0 & \frac{1-\nu}{2} \end{pmatrix}. \tag{3.37}$$

With the pair potential in Eq. (3.9), under pressure $p = 2.83709$, the kagomé crystal has elastic constants $E = 23.61$ and $\nu = 0.4594$.

3.8.2 2D orthotropic targets

The rectangular lattices and the rectangular kagomé crystal are 2D orthotropic crystals. Their elastic constants are determined by four independent constants, E_x, E_y, G, and ν_{xy}:

$$\begin{pmatrix} C_{1111} & C_{1122} & C_{1112} \\ C_{2211} & C_{2222} & C_{2212} \\ C_{1211} & C_{1222} & C_{1212} \end{pmatrix} = \frac{1}{1-\nu_{xy}\nu_{yx}} \begin{pmatrix} E_x & \nu_{yx}E_x & 0 \\ \nu_{xy}E_y & E_y & 0 \\ 0 & 0 & G(1-\nu_{xy}\nu_{yx}) \end{pmatrix}, \quad (3.38)$$

where $\nu_{yx} = \nu_{xy}E_y/E_x$.

With the pair potential in Eq. (3.10), under pressure $p = 1.81198$, the rectangular lattice with aspect ratio 2 has elastic constants $E_x = 27.31$, $E_y = 7.17$, $G = 0.01$, and $\nu_{xy} = 0.4751$.

With the pair potential in Eq. (3.11), under pressure $p = 1.12901$, the rectangular lattice with aspect ratio 2 has elastic constants $E_x = 7.19$, $E_y = 17.60$, $G = 2.33$, and $\nu_{xy} = 0.2277$.

With the pair potential in Eq. (3.12), under pressure $p = 1.04006$, the rectangular lattice with aspect ratio π has elastic constants $E_x = 3.98$, $E_y = 16.91$, $G = 0.27$, and $\nu_{xy} = 0.1296$.

With the pair potential in Eq. (3.13), under pressure $p = 3.97107$, the rectangular kagomé crystal has elastic constants $E_x = 177.9$, $E_y = 177.5$, $G = 65.3$, and $\nu_{xy} = 0.3596$.

3.8.3 3D isotropic target

The CaF_2 crystal inhabited by a single particle species is a 3D cubic crystal. Its elastic constants are determined by three independent constants, E, ν, and A:

$$\begin{pmatrix} C_{1111} & C_{1122} & C_{1133} & C_{1123} & C_{1131} & C_{1112} \\ C_{2211} & C_{2222} & C_{2233} & C_{2223} & C_{2231} & C_{2212} \\ C_{3311} & C_{3322} & C_{3333} & C_{3323} & C_{3331} & C_{3312} \\ C_{2311} & C_{2322} & C_{2333} & C_{2323} & C_{2331} & C_{2312} \\ C_{3111} & C_{3122} & C_{3133} & C_{3123} & C_{3131} & C_{3112} \\ C_{1211} & C_{1222} & C_{1233} & C_{1223} & C_{1231} & C_{1212} \end{pmatrix} =$$

$$\frac{E}{(1+\nu)(1-2\nu)} \begin{pmatrix} 1-\nu & \nu & \nu & 0 & 0 & 0 \\ \nu & 1-\nu & \nu & 0 & 0 & 0 \\ \nu & \nu & 1-\nu & 0 & 0 & 0 \\ 0 & 0 & 0 & A(1-2\nu)/2 & 0 & 0 \\ 0 & 0 & 0 & 0 & A(1-2\nu)/2 & 0 \\ 0 & 0 & 0 & 0 & 0 & A(1-2\nu)/2 \end{pmatrix}. \tag{3.39}$$

With the pair potential in Eq. (3.14), under pressure $p = 6.19610$, the CaF_2 crystal inhabited by a single particle species has elastic constants $E = 2.1835$, $\nu = 0.4753$, and $A = 2.51$.

3.9 Appendix E: Stabilizing a Rectangular Lattice Over a Pressure Range

The rectangular lattices do not naturally have a stable pressure range because of their anisotropic elastic property. When the pressure changes, the two sides of the

rectangular unit cell may change disproportionally, thus the aspect ratio may also change and the structure changes according to our definition. However, we can make "corrections" to the potential to make sure that the aspect ratio does not change over a pressure range. Imagine a rectangular lattice with one side length a and the other side length $b = at$, thus the aspect ratio is t. In order for the rectangular lattice with aspect ratio t to be stable in a pressure range, when pressure p changes in the range, a or b can change while the aspect ratio t must not change. The enthalpy of the target is given by:

$$H = \sum_{(i,j)\neq(0,0)} u_2\left(\sqrt{i^2+(jt)^2}a\right) + pa^2t. \tag{3.40}$$

When the structure is stable, the partial derivatives of enthalpy are zero. Thus:

$$\frac{\partial H}{\partial a} = \sum_{(i,j)\neq(0,0)} u_2'\left(\sqrt{i^2+(jt)^2}a\right)\sqrt{i^2+(jt)^2} + 2pat = 0, \tag{3.41}$$

and:

$$\frac{\partial H}{\partial t} = \sum_{(i,j)\neq(0,0)} u_2'\left(\sqrt{i^2+(jt)^2}a\right)\frac{j^2t}{\sqrt{i^2+(jt)^2}} + pa = 0. \tag{3.42}$$

Eliminate variable p from Eq. (3.41) and Eq. (3.42), we get:

$$\sum_{(i,j)\neq(0,0)} u_2'\left(\sqrt{i^2+(jt)^2}a\right)\frac{i^2-(jt)^2}{\sqrt{i^2+(jt)^2}} = 0. \tag{3.43}$$

Integrating Eq. (3.43) over a will simplify it and give:

$$\sum_{(i,j)\neq(0,0)} u_2\left(\sqrt{i^2+(jt)^2}a\right)\frac{i^2-(jt)^2}{i^2+(jt)^2} = C, \tag{3.44}$$

where C is an arbitrary constant. Eq. (3.44) is a necessary condition for stability. Generally, a potential function does not satisfy this condition over a range of a.

However, for any potential function $u_2^0(r)$, let:

$$u_2^1(r) = -\frac{1}{2} \sum_{(i,j)\neq(0,0)} u_2^0\left(r\sqrt{i^2+(jt)^2}\right) \frac{i^2-(jt)^2}{i^2+(jt)^2} + C \ (0.9 < r < 1.1), \qquad (3.45)$$

Then, the potential $u_2(r) = u_2^0(r) + u_2^1(r)$ satisfies Eq. (3.44) over the range $0.9 < a < 1.1$. Constant C in Eq. (3.45) is chosen so that $u_2^1(1) = 0$. The "correction" $u_2^1(r)$ is usually much smaller than $u_2^0(r)$.

We have applied this correction to our higher-order potential for the rectangular lattice with aspect ratio $b/a = 2$ (Eq. (3.11)). After that, we do simulated annealing using the corrected potential at different pressures. We found that the rectangular lattice with aspect ratio $b/a = 2$ is indeed the ground state of the corrected potential over the pressure range $0.98 < p < 1.87$.

Chapter 4

Ground States of Stealthy Hyperuniform Potentials: I. Entropically Favored Configurations

4.1 Introduction

There has been long-standing interest in the phase behavior of many-particle systems in d-dimensional Euclidean spaces $\mathbb{R}^d$ in which the particles interact with soft, bounded pair potentials [281, 185, 121, 182, 181, 209, 208, 170, 25, 359, 44, 325]. Considerable attention has been devoted to the determination of the classical ground states (global energy minima) of such interactions [121, 209, 44, 325]. While typical interactions lead to unique classical ground states, certain special pair potentials are characterized by degenerate classical ground states—a phenomenon that has attracted recent attention [325, 83, 328, 286, 287, 329, 26, 27, 29, 350, 199].

One family of such pair interactions are the "stealthy potentials" because their ground states correspond to configurations that completely suppress single scattering for a range of wave numbers. The Fourier transforms of these potentials are bounded and non-negative and have compact support [325], and hence they have corresponding direct-space potentials that are bounded and long ranged. Because of their special construction in Fourier space, finding the ground states of stealthy potentials is equivalent to constraining the structure factor to be zero for wave vectors $\mathbf{k}$ contained within the support of the Fourier transformed potential [325], as will be summarized in Sec. 4.2. In the case when the constrained wave vectors lie in the radial interval $0 < |\mathbf{k}| \leq K$, the stealthy ground states fall within the class of hyperuniform states of matter [317] and can be tuned to have varying degrees of disorder. Disordered hyperuniform systems in general are of current interest because they are characterized by an anomalously large suppression of long-wavelength density fluctuations and can exist as equilibrium or nonequilibrium states, either classically or quantum mechanically [74, 347, 149, 50, 33, 173, 77, 177, 142, 66, 68, 346, 145, 315]. Moreover, because disordered hyperuniform states of matter have characteristics that lie between a crystal and a liquid [325], they are endowed with novel physical properties [26, 27, 95, 94, 189, 188, 123, 174, 131, 341, 37].

When a dimensionless parameter χ, inversely proportional to the number density ρ and proportional to K^d (size of the constrained region) is sufficiently small, the hyperuniform ground states are infinitely degenerate and counterintuitively disordered (i.e., isotropic without any Bragg peaks) [325]. However, when χ is large enough (ρ is sufficiently small), there is a phase transition to a regime in which the ground states are crystalline or highly ordered [83, 328, 286, 27]. For each spatial dimension d, there is a special value of χ, χ^*_{max}, at which the ground state is unique [1]. The unique ground state is the dual (reciprocal lattice) of the densest Bravais lattice packing in

[1]The ground state is unique if all ground state configurations can be transformed to each other using translation, rotation, inversion, particle permutation, or a combination of these operations.

each dimension [325]. In two and higher dimensions, as soon as χ drops below $\chi^*_{\max}$, the set of the ground states become uncountably infinite and gradually includes progressively less ordered structures [325]. Similarly to stealthy potentials, a family of two-, three-, and four-body potentials that lead to disordered ground states has also been defined in Fourier space and studied [329, 26, 350].

Due to the complexity of the problem, almost all previous investigations of the ground states employed computer simulations. Such numerical studies were carried out in one, two and three dimensions [83, 328, 329, 26, 27]. The ground states were sampled by minimization of potential energy at fixed densities starting from random initial conditions in a d-dimensional cubic simulation box under periodic boundary conditions. A few optimization techniques were employed to find the global energy minima with very high precision [328, 329].

Generally, a numerically obtained ground-state configuration depends on the number of particles N within the fundamental cell, initial particle configuration, shape of the fundamental cell, and particular optimization technique used [325]. Adding to the complexity of the problem is that the disordered ground states are highly degenerate with a configurational dimensionality that depends on the density, and there are an infinite number of distinct ways to sample this complex ground-state manifold, each with its own probability measure. These nontrivial aspects had made the task of formulating a statistical-mechanical theory of stealthy degenerate ground states a daunting one. Recently, we have formulated such an ensemble theory that yields analytical predictions of the structural characteristics and other properties of stealthy degenerate ground states [325]. A number of exact results for the thermodynamic and structural properties of these ground states were derived that applied to *general* ensembles. We then specialized our results to the canonical ensemble (in the zero-temperature limit) by exploiting an ansatz that stealthy disordered ground states (for sufficiently small χ) behave remarkably like "pseudo" disordered equilib-

rium hard-sphere systems in Fourier space. Our theoretical predictions for the pair correlation function $g_2(r)$ and structure factor $S(k)$ of these entropically favored disordered ground states were shown to be in agreement with corresponding computer simulations across the first three space dimensions. We also made predictions for the corresponding excited states for sufficiently small temperatures that were in agreement with simulations.

Because the focus of that previous investigation was the development of ensemble theories, few simulation details were presented about how the canonical ensemble was sampled to produce stealthy disordered ground states. One aim of this chapter is to provide a comprehensive description of the numerical procedure that we used to produce the simulation results in Ref. [325]. Moreover, here we also extend those results by applying the simulation procedure to study numerically the ground states in the canonical ensemble for all allowable values of χ and thus investigate the entire phase diagram for the entropically favored states across the first three space dimensions. In the next chapter, we will study the exotic aperiodic "wavy phases" identified in previous numerical work [328] (or "stacked-slider phases," as called in the next chapter, a special part of the ground-state manifold. An analytical model will enable an even more detailed study of this phase.

As a justification of sampling the canonical ensemble instead of minimizing energy, we also demonstrate here how a variety of different optimization techniques affect the ground states that are sampled, which was not previously investigated [328, 329, 26]. This investigation reveals that the pair statistics of the ground-state configurations indeed generally depend on the algorithm. Moreover, we show here that the energy minimization results depend on the initial conditions as well. We also provide the reason why the simulations in Ref. [325] and this chapter employ noncubic, possibly deforming, simulation boxes for $d \geq 2$. Because almost all previous numerical simulations were performed using some specific form of stealthy potentials, we show here

that different forms of stealthy potentials produce identical pair correlation functions, suggesting that the specific choice of the potential form does not affect the ensemble being sampled.

Among our major findings, we show that energy minimizations starting from random initial conditions may lead to clustering of particles, the degree of which depends on the algorithm for a finite range of χ below $1/2$ across the first three space dimensions. When minimizing the energy starting from configurations equilibrated at some temperature T_E, the ground-state configurations discovered depend on T_E. However, the algorithm dependence diminishes in the $T_E \to 0$ limit. We also demonstrate that the pair statistics [$g_2(r)$ and $S(k)$] in this limit do not depend on the particular form of the stealthy potential. The similarity between the structure factor in this limit and the pair correlation function of an equilibrium hard-sphere system in direct space [325] is valid for χ up to some dimension-dependent values between 0.25 and 0.33 in the first three space dimensions. Beyond this range of χ, the hard-sphere analogy in Fourier space undergoes modification. As χ increases further (to the value of about 0.4 in two dimensions, for example), the first peak in the structure factor diminishes while second peak in the structure factor grows and engulfs the first peak. Our simulated pair statistics obey certain exact integral conditions in Ref. [325] with very high accuracy, indicating the high fidelity of the numerical results. In the infinite-system-size limit, at $\chi = 0.5$, the entropically favored ground states undergo a transition from disordered states to crystalline states. Depending on the dimension, this phase transition can occur when aperiodic structures still are part of the ground state manifold, demonstrating that crystalline (ordered) structures can have a higher entropy than disordered structures.

The rest of the chapter is organized as follows: In Sec. 4.2, we briefly summarize the numerical collective-coordinate procedure and other details of the simulation that we employ in this chapter with justifications. In Sec. 4.3, we study the dependence

of the results on a variety of energy minimization algorithms, initial conditions, and the forms of the stealthy potentials. In Sec. 4.4, we provide pair correlation function, structure factor, Voronoi cell-volume distribution, and configuration snapshots of the stealthy hyperuniform ground states obtained from the canonical ensemble in the zero-temperature limit. We provide concluding remarks and discussion in Sec. 4.5, including suggestions for sampling the canonical ensemble in the zero-temperature limit of other potentials with degenerate disordered ground states.

4.2 Mathematical Relations and Simulation Procedure

As detailed in Sec. II of Ref. [325], we simulate point processes in periodic fundamental cells (i.e. simulation boxes) with a pairwise additive potential $v(\mathbf{r})$ such that its Fourier transform exists. Under nearest image convention, the total potential energy can be calculated by summing over all pairs of particles:

$$\Phi(\mathbf{r}^N) = \sum_{i<j} v(\mathbf{r}_{ij}), \tag{4.1}$$

where N is the number of particles, $\mathbf{r}^N \equiv \mathbf{r}_1, \mathbf{r}_2, ..., \mathbf{r}_N$ is the locations of the particles in d-dimensional Euclidean space, and $\mathbf{r}_{ij} = \mathbf{r}_i - \mathbf{r}_j$. Instead of summing over all pairwise contributions in the real space, the potential energy can also be represented in Fourier space:

$$\Phi(\mathbf{r}^N) = \frac{1}{2v_F}\left[\sum_{\mathbf{k}} \tilde{v}(\mathbf{k})|\tilde{n}(\mathbf{k})|^2 - N\sum_{\mathbf{k}} \tilde{v}(\mathbf{k})\right], \tag{4.2}$$

where v_F is the volume of the fundamental cell, $\tilde{v}(\mathbf{k}) = \int_{v_F} v(\mathbf{r}) \exp(-i\mathbf{k}\cdot\mathbf{r})d\mathbf{r}$ is the Fourier transform of the pair potential, $\tilde{n}(\mathbf{k}) = \sum_{j=1}^{N} \exp(-i\mathbf{k}\cdot\mathbf{r}_j)$ is the complex

collective density variable [with $\tilde{n}(\mathbf{k}=0)=N$], and both summations are over all reciprocal lattice vector $\mathbf{k}$'s appropriate to the fundamental cell. For every $\mathbf{k}\neq\mathbf{0}$, $\tilde{n}(\mathbf{k})$ is related to the structure factor, $S(\mathbf{k})$, via

$$S(\mathbf{k})=\frac{|\tilde{n}(\mathbf{k})|^2}{N}. \tag{4.3}$$

Given a $\tilde{v}(\mathbf{k})$, the corresponding real-space pair potential is

$$v(\mathbf{r})=\frac{1}{v_F}\sum_{\mathbf{k}}\tilde{v}(\mathbf{k})\exp(i\mathbf{k}\cdot\mathbf{r}). \tag{4.4}$$

In a finite-sized system, the real-space pair potential has the same periodicity as the fundamental cell. Therefore, in the infinite-volume limit, the cell periodicity disappears.

A family of "stealthy" potentials, which completely suppress single scattering for all wave vectors within a specific cutoff in their ground states, are defined as [83, 328, 329, 26, 27, 29]:

$$\tilde{v}(\mathbf{k})=\begin{cases}V(k), & \text{if } |\mathbf{k}|\leq K,\\ 0, & \text{otherwise,}\end{cases} \tag{4.5}$$

where $V(k)$ is a positive isotropic function and K is a constant. In this chapter we always take $K=1$, which sets the length scale. We will also use $V(k)=1$ unless otherwise specified. In the infinite-system-size limit, the isotropic $\tilde{v}(\mathbf{k})$ correspond to an isotropic real-space pair potential $v(\mathbf{r})$ [325]. However, for finite systems, the corresponding $v(\mathbf{r})$ is anisotropic. In Appendix A, we compare the infinite-system-size limit $v(\mathbf{r})$ with the finite-size $v(\mathbf{r})$'s in different-shaped simulation boxes and select the simulation box shape to be used in this chapter based on which $v(\mathbf{r})$ is closest to the infinite-size-limit $v(\mathbf{r})$.

From Eqs. (4.2) and (4.5), one can see that a configuration is a stealthy ground state if $\tilde{n}(\mathbf{k}) = 0$ for all $\mathbf{k}$ points such that $0 < |\mathbf{k}| \leq K$. Therefore, finding a ground state of a stealthy potential is equivalent to constraining $\tilde{n}(\mathbf{k}) = 0$ for all of those $\mathbf{k}$ points. However, in a simulation, one does not need to check all of the constraints. As detailed in Ref. [325], if there are $(2M+1)$ $\mathbf{k}$ points within the constrained radius, only M of them are independent and needed to be constrained to zero. Equation (4.2) can be simplified as [2]:

$$\Phi(\mathbf{r}^N) = \frac{1}{v_F} \sum_{\mathbf{k}} \tilde{v}(\mathbf{k}) |\tilde{n}(\mathbf{k})|^2 + \Phi_0, \tag{4.6}$$

where the sum is over all *independent* constraints, and

$$\Phi_0 = [N(N-1) - 2N \sum_{\mathbf{k}} \tilde{v}(\mathbf{k})]/(2v_F) \tag{4.7}$$

is a constant independent of the particle positions $\mathbf{r}^N$. We now introduce a parameter

$$\chi = \frac{M}{d(N-1)}, \tag{4.8}$$

which determines the degree to which the ground states are constrained, and therefore the degeneracy and disorder of the ground states [328]. Note that the constraints depend on K and the fundamental cell but are independent of the specific shape of $\tilde{v}(\mathbf{k})$ as long as $\tilde{v}(\mathbf{k}) > 0$ for all $0 < |\mathbf{k}| \leq K$. Therefore, changing $\tilde{v}(\mathbf{k})$ does not change the set of the ground states. However, there is no proof that changing $\tilde{v}(\mathbf{k})$ does not change the relative sampling weights of the ground states.

In this chapter we study various systems with different χ's and N's. One numerical complication is that these numbers cannot be chosen arbitrarily, since $M = \chi d(N-1)$ must be an integer consistent with the specific shape of the simulation box. (For

[2] Compared to Eq. (4.2), a factor of 2 in the denominator of Eq. (4.6) is removed because each independent constraint corresponds to two constrained $\mathbf{k}$ points.

example, a list of the allowed M values for a two-dimensional square box is given in Table II of Ref. [328].) This constraint is especially hard to meet when simulating multiple systems at the same χ value across dimensions. In fact, both χ and N in Table 4.1 (see Appendix C) had to be chosen carefully to meet this constraint.

Taking the gradient of Eq. (4.6) yields the forces on particles:

$$\mathbf{F}_j = -\bigtriangledown_j \Phi(\mathbf{r}^N) = \frac{2}{v_F} \sum_{\mathbf{k}} \mathbf{k}\, \tilde{v}(\mathbf{k})\, \mathrm{Im}[\tilde{n}(\mathbf{k}) \exp(i\mathbf{k} \cdot \mathbf{r}_j)], \tag{4.9}$$

where the sum is also over all independent constraints. This equation enables us to perform both energy minimizations and molecular dynamics (MD) simulations. In an energy minimization, a derivative-based algorithm is used. The first term on the right side of Eq. (4.6) is provided to the algorithm as the objective function and the negative of the force in Eq. (4.9) is provided as the derivative. In order to minimize energy, we have tried different algorithms including the MINOP algorithm [69], the steepest descent algorithm allowing large steps [4], the low-storage BFGS (L-BFGS) algorithm [214, 183, 150], the Polak-Ribiere conjugate gradient algorithm [118, 4], and our "local gradient descent" algorithm described in Appendix B. When $\chi < 0.5$, the objective function always ends up being very close to zero (the minimum). The maximum ending objective function for different algorithms varies from as high as 10^{-7} for a conjugate gradient algorithm to 10^{-17} for the local gradient descent and steepest descent algorithms to 10^{-20} for the L-BFGS algorithm, and to as low as 10^{-25} for the MINOP algorithm. From our practical point of view, all of these algorithms are precise enough, since an error of 10^{-7} or lower is indiscernible from any results presented below. Because the L-BFGS algorithm is the fastest, we will use it unless otherwise specified.

The energy minimizations, if started from random initial configurations, will sample an algorithm-dependent, nonequilibrium ensemble. To sample the canonical en-

semble at a given equilibrium temperature T_E we use MD simulations. One important parameter in MD simulations is the integration time step. Since the optimal choice of the time step depends on the temperature, and the latter varies across several orders of magnitude in this chapter, we desire a systematic way to determine the optimal time step. Starting from an energy minimized configuration and a very small time step (0.01 in dimensionless units), we repeat the following steps 10^4 times to equilibrate the system and find a suitable time step:

- Assign a random velocity from Boltzmann distribution at T_E to each particle.
- Calculate the total (kinetic and potential) energy of the system E_1.
- Evolve the system 1500 time steps using the velocity Verlet algorithm [101].
- Calculate the total energy of the system E_2.
- If $|\ln \frac{E_1}{E_2}| > 1 \times 10^{-5}$, then the time step is too large and errors will build up quickly. Therefore, we decrease the time step by 5%. On the other hand, if $|\ln \frac{E_1}{E_2}| < 4 \times 10^{-6}$, there is still some room to increase the time step. Since increasing the time step increases the efficiency of MD simulations, we increase the time step by 5%.

After the system is equilibrated and the time step is chosen, we perform constant temperature MD simulations with particle velocity resetting [9]. A randomly chosen particle is assigned a random velocity, drawn from Maxwell-Boltzmann distribution, every 100 steps. We take a sample configuration every 3000 time steps until we have sampled 20 000 configurations unless otherwise specified. This amounts to an implementation of the generation of configurations in the canonical ensemble.

The above MD procedure works well for $\chi < 0.5$. However, two new features arise when it is applied to $\chi \geq 0.5$ in all dimensions. First, the potential energy surface develops local minima and energy barriers that can trap the system if T_E is too small.

We address this problem by using simulated annealing, employing a thermodynamic cooling schedule [215] which starts at $T = 2 \times 10^{-3}$ and ends at 10^{-6}. Note that, by adopting a cooling schedule, we concede that we may only take one sample at the end of each MD trajectory, whereas a fixed-temperature MD trajectory produces multiple samples.

The second new feature is that the entropically favored ground states are crystalline for $\chi \geq 0.5$. Unlike disordered structures, a crystalline structure has long-range order and may not "fit" in simulation boxes with certain shapes. To overcome the second problem, we simulate an isothermal-isobaric ensemble with a deformable simulation box. Every 20 MD time steps, 10 Monte Carlo trial moves to deform the simulation box are attempted. The pressure is calculated from Eq. (41) of Ref. [325].

We employed the Wang-Landau Monte Carlo [335] to attempt to determine the entropically favored ground states for $\chi > 0.5$ in two and three dimensions. The Wang-Landau Monte Carlo is used to calculate the microcanonical entropy $\mathscr{S}(\Phi)$ as a function of the potential energy Φ. We limit our simulations to the energy range $3 \times 10^{-10} < \Phi - \Phi_0 < 10^{-9}$ (in dimensionless units), where Φ_0 is the ground state energy, by rejecting any trial move that violates this energy tolerance. This energy range is evenly divided into 1000 bins. Starting from a perfect crystal structure in a simulation box shaped like a fundamental cell, small perturbations are introduced so the energy is within the range. After that, 60 stages of Monte Carlo simulations are performed, each stage containing 3×10^7 trial moves. The "modification factor" in Ref. [335] is $f = \exp[5/(n + 10)]$, where n is the number of stages.

4.3 Dependence on Energy Minimization Algorithm, MD Temperature, and $\tilde{v}(\mathbf{k})$

In this section, we present numerical simulation results demonstrating that:

- Energy minimizations starting from Poisson initial configurations using different algorithms can yield ground states with different pair correlation functions.
- Energy minimizations starting from MD snapshots at different temperatures can yield ground states with different pair correlation functions.
- For configurations obtained by minimizing energy starting from MD snapshots at sufficiently small temperature, pair correlation functions do not depend on the minimization algorithm and the form of the stealthy potential.

These results motivate the reason why we ultimately study and report results in Sec. 4.4 in the canonical ensemble in the zero-temperature limit. For concreteness and visual clarity, we present results here in two dimensions. However, we have verified that all of the conclusions here also apply to one and three dimensions.

We performed energy minimizations starting from Poisson initial configurations (i.e., $T_E \to \infty$ state at fixed density) using each of the five numerical algorithms mentioned in Sec. 4.2 at $\chi = 0.2$ and $\chi = 0.4$. The results are shown in Figs. 4.1 and 4.2. At $\chi = 0.2$, the pair correlation functions produced by the MINOP algorithm and the L-BFGS algorithm are almost identical. However, the pair correlation function produced by the conjugate gradient algorithm noticeably differs. The steepest descent algorithm and our local gradient descent algorithm produce a significantly different pair correlation function with a much weaker peak at $r = 0$. The pair correlation functions produced by some algorithms appear to have $g_2(r) \propto \log(r)$ divergence near the origin. Since this divergence means particles have a tendency to form clusters, we call it a "clustering effect." At $\chi = 0.4$, the clustering effect disappears, but the pair statistics produced by different algorithms still differs. The fact that different optimization algorithms produce different pair statistics means that they sample the ground-state manifold with different weights. In other words, different optimization algorithms are sampling different ground-state ensembles.

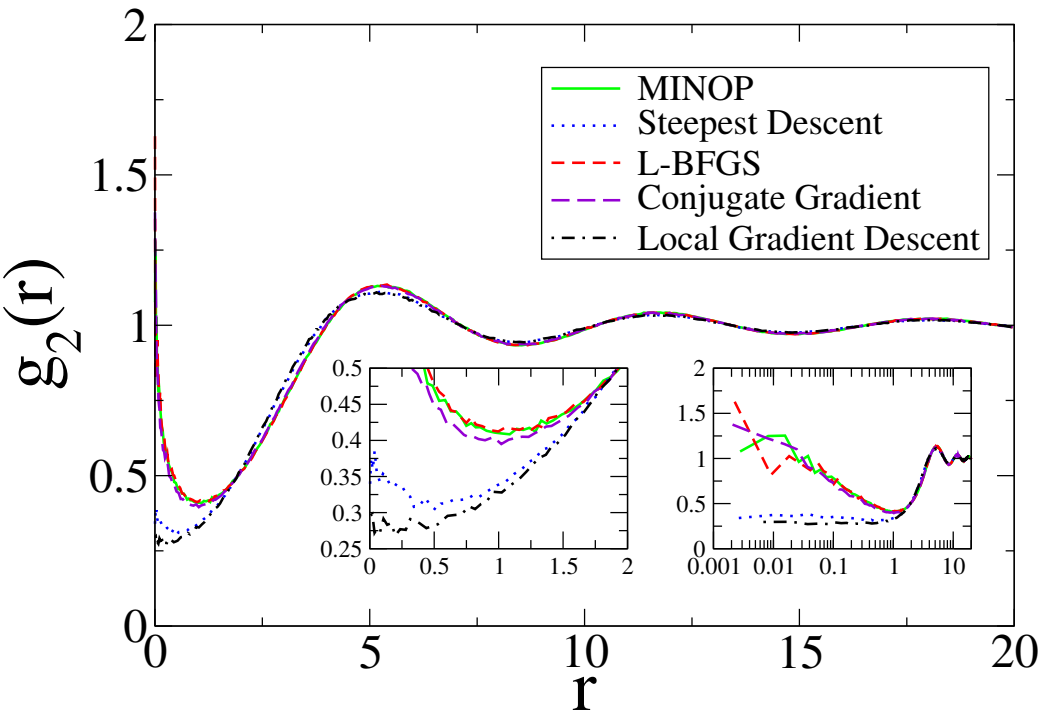

Figure 4.1 Pair correlation function as obtained from different optimization algorithms (as described in the legend) starting from Poisson initial configurations in two dimensions at $\chi = 0.2$. Each curve is averaged over 20 000 configurations of 136 particles each. The left inset zooms in near the origin, showing the differences between the five algorithms more clearly. The right inset uses a semilogarithmic scale to show $g_2(r) \propto \log(r)$ near the origin.

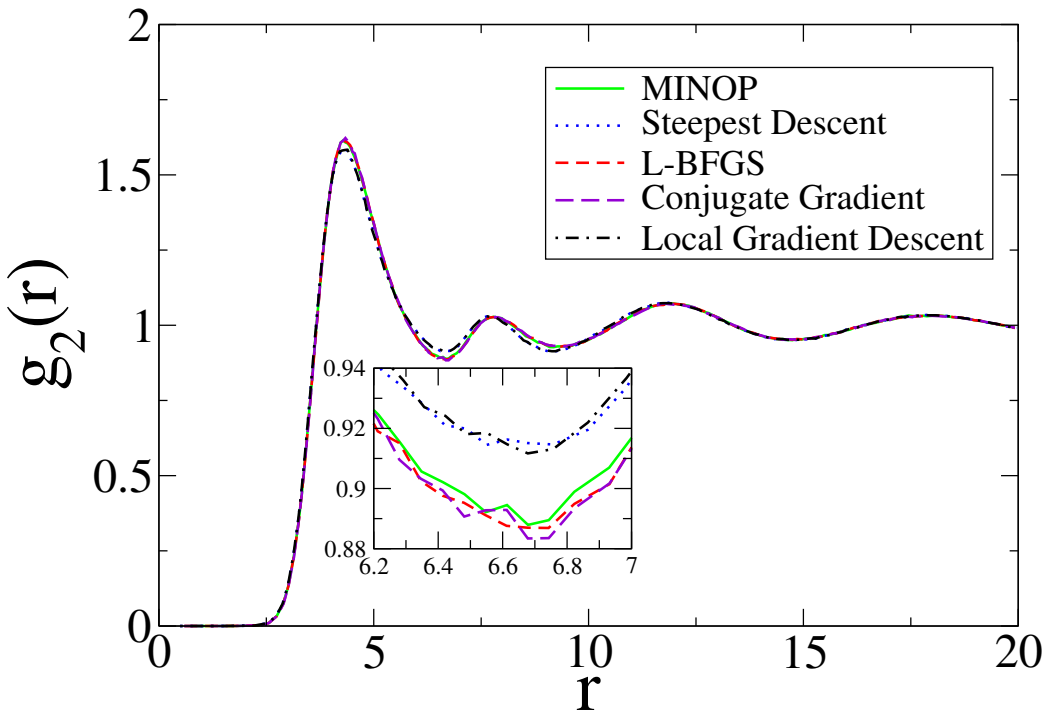

Figure 4.2 As in Fig. 4.1, except that $\chi = 0.4$ and each curve is averaged over 20 000 configurations of 151 particles each. The inset zooms in near the first well, showing the differences between the five algorithms more clearly.

In order to avoid the complexity caused by the details of various optimization algorithms, we turn our interest to the canonical ensemble in the $T \to 0$ limit. To sample this ensemble, we perform MD simulations at sufficiently small temperature T_E, periodically take "snapshots," and then use a minimization algorithm to bring each snapshot to a ground state. To determine a "sufficiently small" T_E, we calculated the pair correlation functions at various T_E's and present them in Fig. 4.3. The energy minimization result starting from $T_E \to \infty$ initial configurations clearly display the "clustering effect" at $\chi = 0.2$. When T_E goes to zero, the "clustering effect" also diminishes. At $\chi = 0.4$, particles develop hard cores [$g_2(0) = 0$], therefore there is no clustering even if T_E is large or infinite. However, the peak height of $g_2(r)$ becomes dependent on T_E at this χ value. For both χ values, the pair correlation functions of the two lowest T_E's are almost identical, verifying that the $T_E \to 0$ limit exists. These

results show that $T_E = 2 \times 10^{-6}$ is sufficiently small in two dimensions. Similarly, we have found that $T_E = 2 \times 10^{-4}$ and $T_E = 1 \times 10^{-6}$ are sufficiently small in one and three dimensions, respectively. These temperatures are used in generating all of the results presented in Sec. 4.4.1.

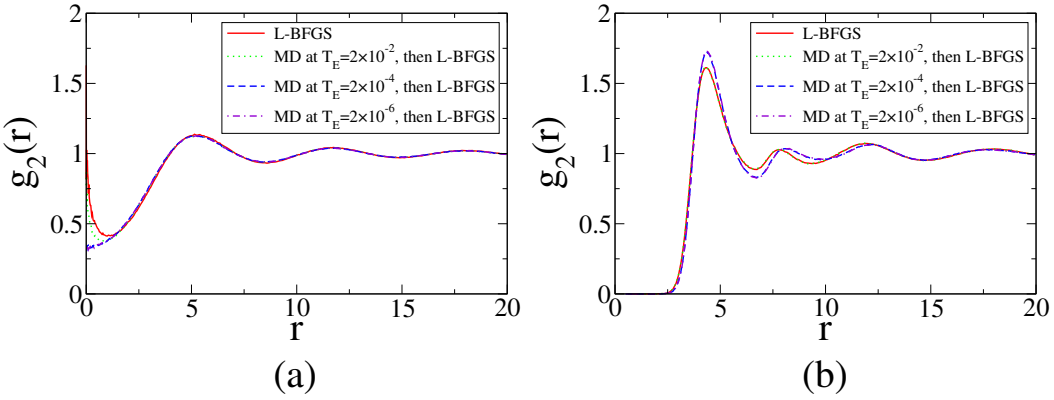

Figure 4.3 Pair correlation function produced by L-BFGS algorithm starting from snapshots of MD at different equilibration temperatures T_E, (a) $\chi = 0.2$ and (b) $\chi = 0.4$. Each curve is averaged over 20 000 configurations of 136 particles each or 151 particles each.

The energy minimization result starting from Poisson initial configurations differs for different algorithms, but the canonical ensemble in the $T \to 0$ limit should not depend on any particular algorithm. After finding that $T_E = 2 \times 10^{-6}$ is sufficiently small, we confirm the disappearing of algorithmic dependence by calculating the pair correlation function produced by different energy minimization algorithms starting from MD snapshots at $T_E = 2 \times 10^{-6}$. Figure 4.4 shows the results. The curves for all algorithms almost coincide.

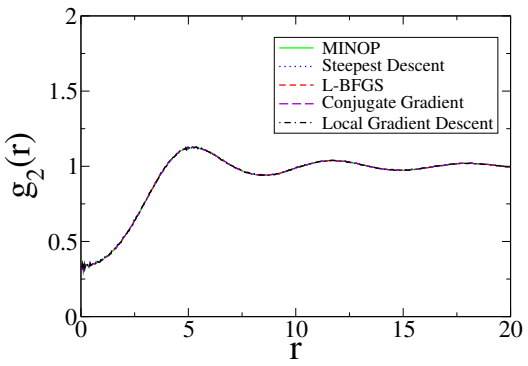

Figure 4.4 Pair correlation function produced by the five different algorithms starting from snapshots of MD at equilibration temperature $T_E = 2 \times 10^{-6}$ at $\chi = 0.2$. Each curve is averaged over 20 000 configurations of 136 particles each.

Last, the function $V(k)$ in Eq. (4.5) can have different forms. This chapter mainly use $V(k) = 1$ but we also want to know if the results obtained using this form are equivalent to those generated using other positive isotropic forms of $V(k)$ as well. In principle, stealthy potentials of any form should have the same set of ground-state configurations, but the form of the stealthy potential could theoretically affect the curvature of the potential energy surface near each ground-state configurations and thus also affect their relative weights. Figure (4.5) shows the pair correlation function produced by different $V(k)$'s. The pair correlation functions for $V(k) = 1$ and $V(k) = (1-k)^2$ at $T_E = 2 \times 10^{-6}$ are almost identical. For $V(k) = (1-k)^6$, we initially tried $T_E = 2 \times 10^{-6}$ but found that the "clustering effect" is still noticeable. We further lowered the temperature to $T_E = 2 \times 10^{-10}$ to completely suppress the "clustering effect" to produce a pair correlation function identical to that of $V(k) = 1$ and $V(k) = (1-k)^2$ potentials. This result suggests that the functional form of $V(k)$ does not produce noticeable differences in the ground-state ensembles in the $T \to 0$ limit of the canonical ensemble.

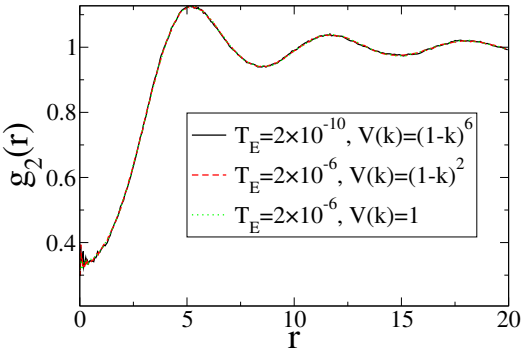

Figure 4.5 Pair correlation function produced by different potentials starting from snapshots of MD at sufficiently low temperature at $\chi = 0.2$. Each curve is averaged over 20 000 configurations of 136 particles each.

4.4 Canonical Ensemble in the $T \to 0$ Limit

We will show here that the entropically favored ground states in the canonical ensemble in the $T \to 0$ limit for the first three space dimensions differ markedly below and above $\chi = 0.5$. For $\chi < 0.5$, the entropically favored ground states are disordered while for $\chi \geq 0.5$ the entropically favored ground states are crystalline. Therefore, we will characterize them differently. For $\chi < 0.5$, we will report the pair correlation function, structure factor, and Voronoi cell statistics. For sufficiently small χ, we will show that the simulation results agree well with theory [325]. For $\chi \geq 0.5$, we will report the crystal structures. The numbers of particles in all of the systems reported in this section are collected in Appendix C.

4.4.1 $\chi < 0.5$ region

Representative entropically favored stealthy ground states in the first three space dimensions at $\chi = 0.1$ and $\chi = 0.4$ are shown in Figs. 4.6-4.8. As χ increases from 0.1 to 0.4, the stealthiness increases, accompanied with a visually perceptible increase in short-range order. This trend in short-range order is consistent with previous studies [328, 329, 26].

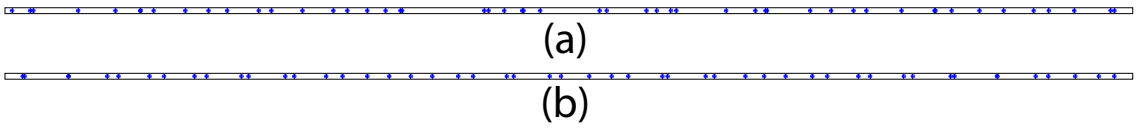

Figure 4.6 Representative one-dimensional entropically favored stealthy ground states at (a) $\chi = 0.1$ and (b) $\chi = 0.4$.

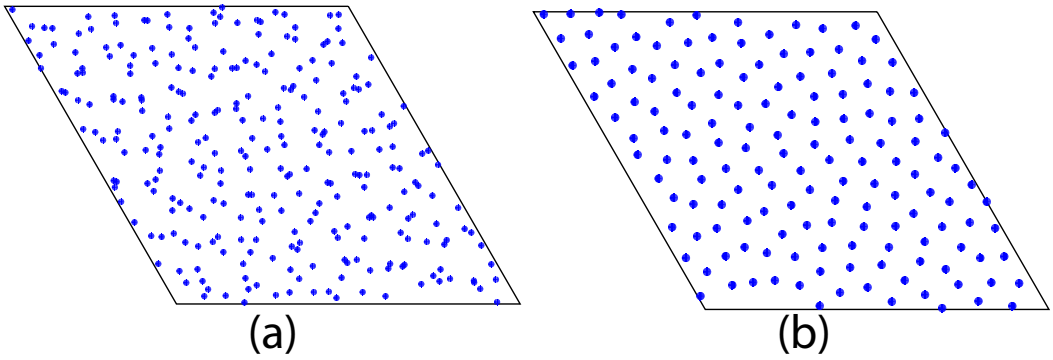

Figure 4.7 Representative two-dimensional entropically favored stealthy ground states at (a) $\chi = 0.1$ and (b) $\chi = 0.4$.

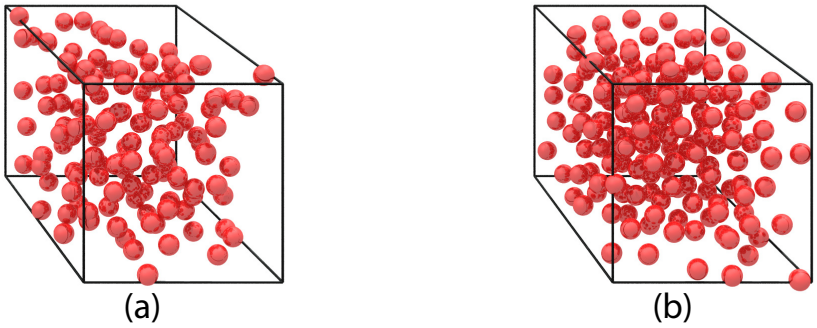

Figure 4.8 Representative three-dimensional entropically favored stealthy ground states at (a) $\chi = 0.1$ and (b) $\chi = 0.4$.

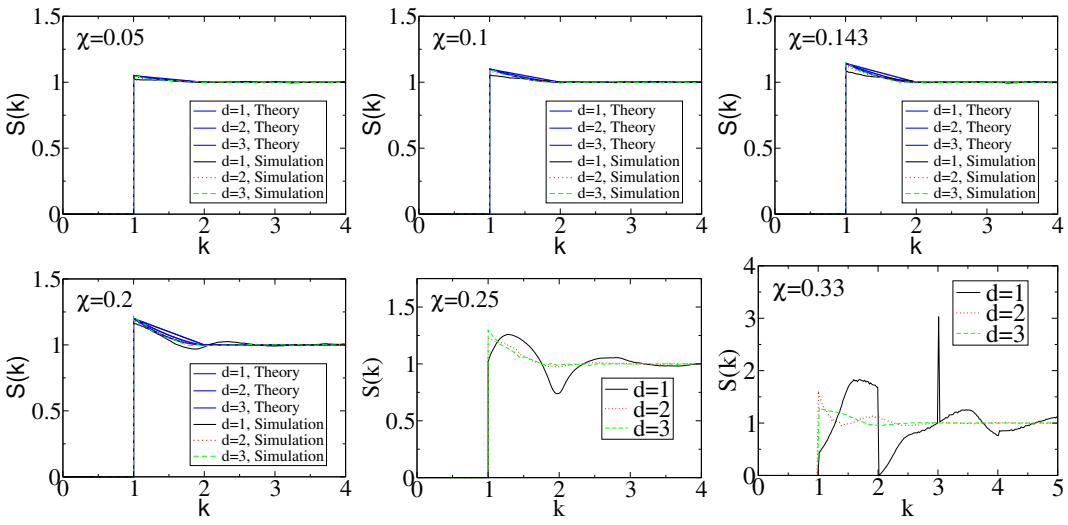

Figure 4.9 Structure factors for $1 \leq d \leq 3$ for $0.05 \leq \chi \leq 0.33$ from simulations and theory [325]. The smaller χ simulation results are also compared with the theoretical results in the infinite-volume limit [325]. For $\chi \leq 0.1$, the theoretical and simulation curves are almost indistinguishable, and the structure factor is almost independent of the space dimension. However, simulated $S(k)$ in different dimensions become very different at larger χ. Theoretical results for $\chi \geq 0.25$ are not presented because they are not valid in this regime.

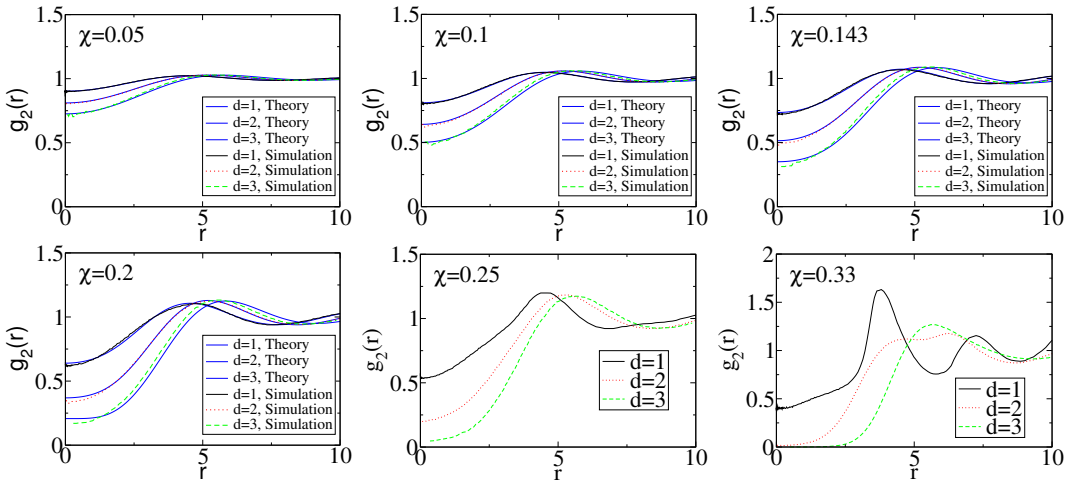

Figure 4.10 Pair correlation functions for $1 \leq d \leq 3$ for $0.05 \leq \chi \leq 0.33$ from simulations and theory [325]. The smaller χ simulation results are also compared with the theoretical results in the infinite-volume limit [325]. For $\chi \leq 0.1$, the theoretical and simulation curves are almost indistinguishable. Theoretical results for $\chi \geq 0.25$ are not presented because they are not valid in this regime.

We have calculated the pair correlation functions and the structure factors for various χ values. Results for $0.05 \leq \chi \leq 0.33$ are shown in Figs. 4.9 and 4.10. The $\chi < 0.2$ results are in excellent agreement with the "pseudo-hard-sphere ansatz," which states that the structure factor behaves like pseudo equilibrium hard-sphere systems in Fourier space [325]. However, the theory gradually becomes invalid as χ increases.

The pair correlation functions of the entropically favored stealthy ground states are shown in Fig. 4.10. When $\chi \leq 0.2$, since the structure factor is similar to the pair correlation function of the hard-sphere system, inversely the pair correlation function is also similar to the structure factor of the hard-sphere system. As χ grows larger, the pseudo hard-sphere ansatz gradually deviates from the simulation result.

We have checked that these pair statistics are consistent with four theoretical integral conditions of the pair statistics in the infinite-volume limit [325]. The first three conditions are Eqs. (58), (59), and (63) of Ref. [325], which are

$$\int_{\mathbb{R}^d} P(r) d\mathbf{r} = 0, \tag{4.10}$$

$$\int_{\mathbb{R}^d} P(r) v(r) d\mathbf{r} = 0, \tag{4.11}$$

and

$$g_2(0) = 1 - 2d\chi + 2d^2\chi \int_K^\infty k^{d-1} \tilde{Q}(k) dk, \tag{4.12}$$

where $P(r)$ is the inverse Fourier transform of $\Theta(k-1)\tilde{Q}(k)$, $\Theta(x)$ is the Heaviside step function, and $\tilde{Q}(k) = S(k) - 1$.

The fourth condition is that the pressure calculated from the "virial equation" [325] has to be either nonconvergent or convergent to the pressure calculated from the energy route [325]. All pair statistics in Figs. 4.9 and 4.10 were generated using the step-function potential [the $V(k) = 1$ case of Eq. (4.5)], but this potential does

not lead to a convergent virial pressure. However, as we have shown earlier, the stealthy ground states that we generated here are also the ground states of other stealthy functional forms $\tilde{v}(\mathbf{k})$. In one dimension, to test our simulation procedure, we used the potential form $V(k) = (1-k)$ to calculate the pressure from both the virial equation (Eq. (43) of Ref. [325]) and the energy equation (Eq. (41) of Ref. [325]). The pressure from the virial equation converges and agrees with the exact pressure from the energy equation, thus confirming the accuracy of our numerical results. These checks involve integrals of $g_2(r)$ and $S(k)$ that are only slowly converging. Therefore, passing them demonstrates that our results have very high precision.

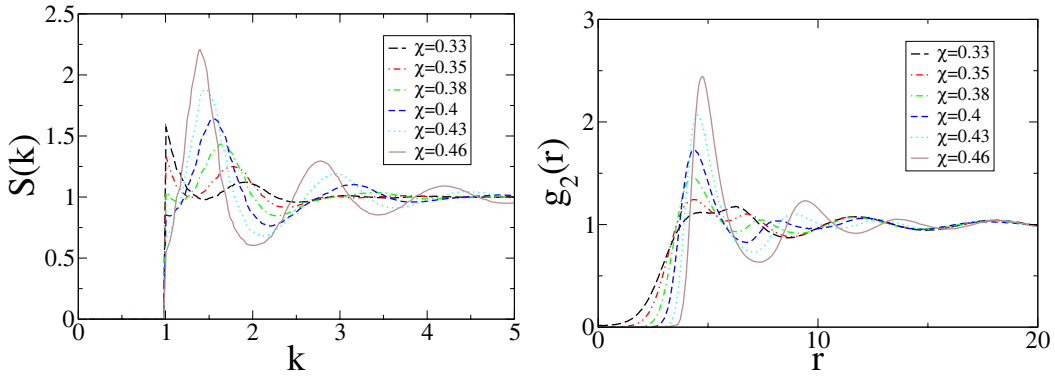

Figure 4.11 Structure factor and pair correlation function for $d = 2$ for $0.33 \leq \chi \leq 0.46$, as obtained from simulations.

For smaller χ values, the maximum of the structure factor is at the constraint cutoff $k = K^+$. However, for higher χ values, the maximum of $S(k)$ is no longer at $k = 1^+$. To probe this transition we have calculated the structure factor in two dimensions for $0.33 \leq \chi \leq 0.46$. The results are shown in Fig. 4.11. As χ increases, the peak at $k = 1^+$ gradually decreases its height, while the subsequent peak gradually grows and engulfs the first peak.

Besides pair statistics, other widely used characterization of point patterns include certain statistics of the Voronoi cells [328, 103, 218, 165]. A Voronoi cell is the region consisting of all of the points closer to a specific particle than to any other. We have

computed the Voronoi tessellation of the entropically favored stealthy ground states using the dD Convex Hulls and Delaunay Triangulations package [134] of the Computational Geometry Algorithms Library [5]. Since the number density of the stealthy ground states depends on the dimension and χ, we rescaled each configuration to unity density for comparison of the Voronoi cell volumes. The probability distribution function $p(v_c)$ of the Voronoi cell volumes (where v_c is the volume of a Voronoi cell) are shown in Fig. 4.12. In the same dimension, as χ increases, the distribution of Voronoi cell volumes narrows. This is expected because the system becomes more ordered as χ increases. For the same χ, the distribution also narrows as the dimension increases, consistent with theoretical results that at fixed χ, the nearest-neighbor distance distribution narrows as dimension increases [325]. In Fig. 4.12, we additionally show the Voronoi cell-volume distribution of saturated random sequential addition (RSA) [356, 323, 339] packings, the sphere packings generated by randomly and sequentially placing spheres into a large volume subject to the nonoverlap constraint until no additional spheres can be placed. Saturated RSA packings are neither stealthy nor hyperuniform [356, 323]. However, the Voronoi cell-volume distributions of saturated RSA packings look similar to that of the entropically favored stealthy ground states. This is not unexpected because Voronoi cell statistics are *local* characteristics, and hence are not sensitive to the stealthiness, which is a large-scale property.

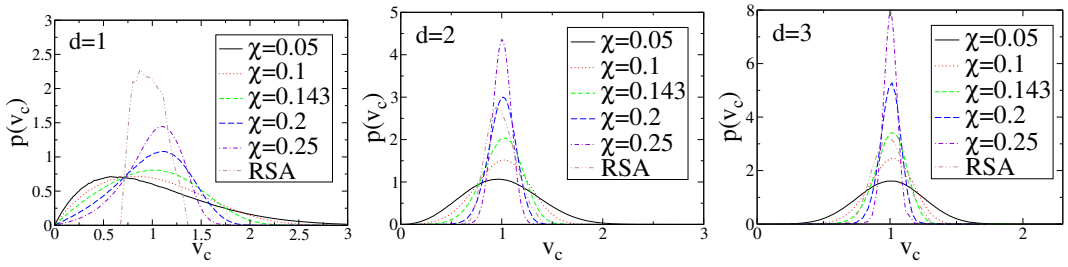

Figure 4.12 Voronoi cell-volume distribution for $1 \leq d \leq 3$ for $0.05 \leq \chi \leq 0.25$. For the same dimension, the Voronoi cell-volume distribution becomes narrower when χ increases. For the same χ, the Voronoi cell-volume distribution also becomes narrower when dimension increases. We also present Voronoi cell-volume distributions of RSA packings at saturation here.

One interesting phenomenon is that as χ increases and approaches 1/2, systems that are not sufficiently large can become crystalline. In Fig. 4.13, we show two snapshots of MD simulations at $\chi = 0.48$. The smaller configuration is crystalline. However, systems that are 4 times larger remain disordered at the same χ and temperature. Therefore, this strongly indicates that crystallization is a finite-size effect for χ tending to 1/2 from below.

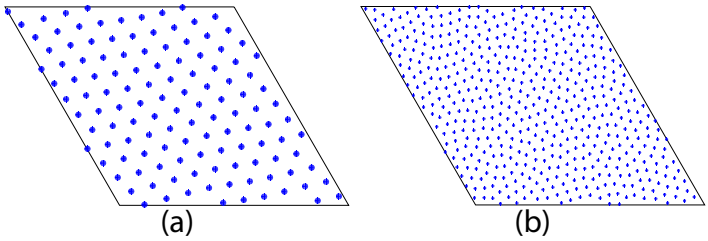

Figure 4.13 (a) Low-temperature MD snapshot of a 126-particle system at $\chi = 0.48$; the ground-state configuration is crystalline. (b) MD snapshot of a 504-particle system at the same T_E and χ; the system does not crystallize and is indeed disordered without any Bragg peaks.

4.4.2 $\chi \geq 0.5$ region

As explained in Sec. 4.2, we perform MD-based simulated annealing with Monte Carlo moves of the simulation box for $\chi > 0.5$, since this method works better with rough potential energy surface and can mitigate the finite-size effect. We performed this simulation at $\chi = 0.55$, $\chi = 0.73$, and $\chi = 0.81$ in two dimensions. The results are shown in Fig. 4.14. The resulting configuration is always triangular lattice. Even though the ground-state manifold in this χ regime contains aperiodic "wavy" phases discovered previously [328] [but which are called "stacked-slider" phases in the next chapter, since they are aperiodic configurations with a high degree of order in which rows (in two dimensions) or planes (in three dimensions) of particles can slide past each other] as well as crystals other than the triangular lattice, the entropically favored ground state is always a triangular lattice. This means that the triangular lattice has

a higher entropy than stacked-slider phases, although the latter appear to be more disordered [3].

Although we will show analytically that crystals are more entropically favored than stacked-slider phases in the next chapter, we still need simulation results to determine which crystal structure has the highest entropy. The results of MD-based simulated annealing with Monte Carlo moves of the simulation box suggest that triangular lattice has the highest entropy in two dimensions. It seems natural to apply the same technique to three dimensions to determine the entropically favored crystal structure. However, we were unable to crystallize the system in three dimensions. Even the longest cooling schedule that we tried resulted in stacked-slider phases.

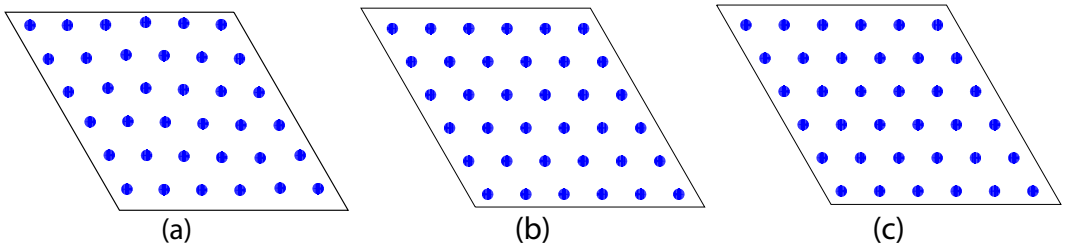

Figure 4.14 MD-based simulated annealing result at (a) $\chi = 0.55$, (b) $\chi = 0.73$, and (c) $\chi = 0.81$. The ending configuration is triangular lattice except for small deformations in the $\chi = 0.55$ case.

Another way to find the entropically favored crystal is to use Wang-Landau Monte Carlo to directly calculate the entropy of different crystal structures as a function of the potential energy. We have performed this simulation on two-dimensional triangular lattice, square lattice, and three-dimensional body-centered cubic (BCC) lattice, face-centered cubic (FCC) lattice, and simple cubic (SC) lattice. The results are shown in Figs. 4.15 and 4.16. In all cases the entropy decreases as the energy decreases. In two dimensions, the entropy of the square lattice clearly decreases faster

[3] In Fig. 4.13, we show that crystallization for $\chi < 0.5$ is a finite-size effect. So is crystallization for $\chi \geq 0.5$ also a finite-size effect? In the next chapter, we will present an analytical model of so-called "stacked-slider" phases for $\chi \geq 0.5$, which are relatively ordered but aperiodic configurations. Using the model, we will show that the entropy of stacked-slider phases is smaller than that of the crystalline structures. Therefore, crystallization for $\chi \geq 0.5$ is not a finite-size effect.

than that of the triangular lattice at every χ value, confirming that the triangular lattice is entropically favored over the square lattice in the zero-temperature limit. In three dimensions at $\chi = 0.58$, the entropy of the FCC lattice decreases more slowly than that of the BCC and SC lattice, suggesting that the entropically favored ground state in three dimensions at $\chi = 0.58$ is the FCC lattice. At higher χ values, the scaling of the entropy of the FCC lattice and the BCC lattice become very close to each other, preventing us from determining the entropically favored ground state at these χ values.

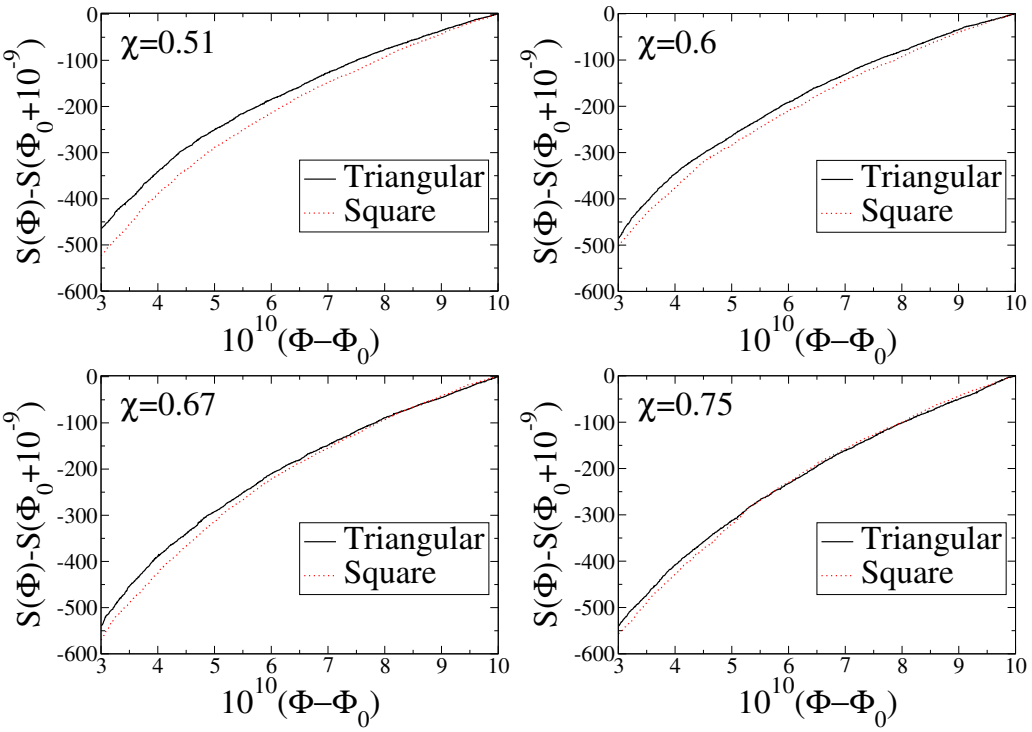

Figure 4.15 Microcanonical entropy as a function of energy $\mathscr{S}(\Phi)$ calculated from Wang-Landau Monte Carlo of triangular lattice and square lattice at various χ's. Here Φ_0 denotes the ground-state energy.

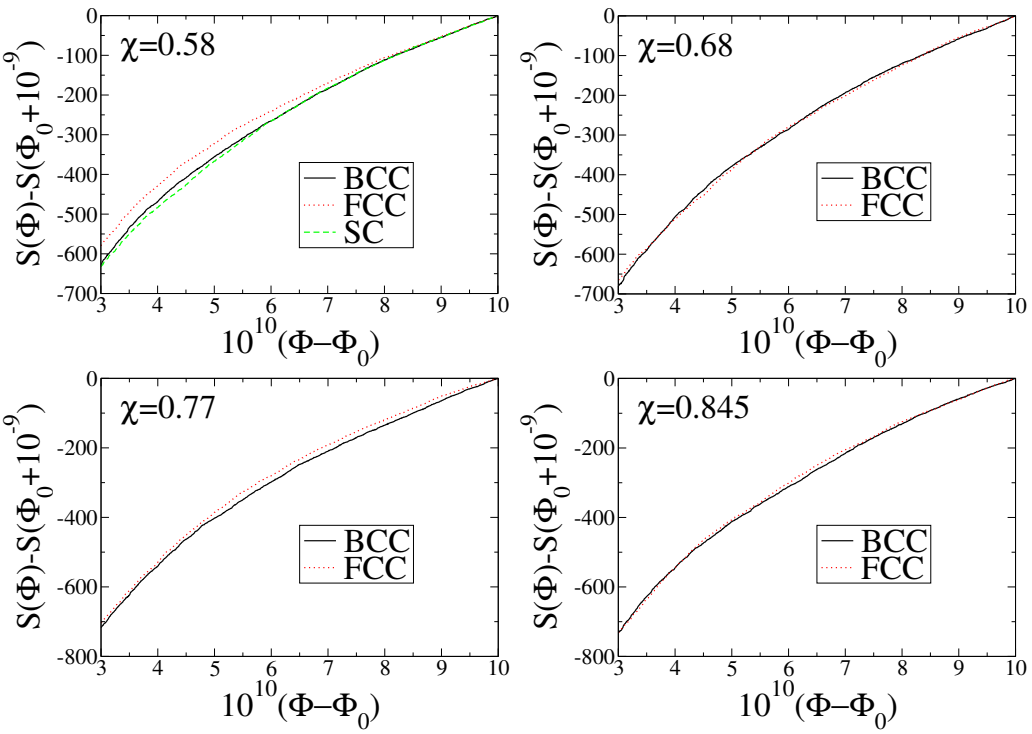

Figure 4.16 Microcanonical entropy as a function of energy $\mathscr{S}(\Phi)$ calculated from Wang-Landau Monte Carlo of BCC lattice, FCC lattice, and SC lattice at various χ's. A curve for SC lattice is not presented for $\chi \geq 0.68$ because the latter is not a ground state at such high χ values. Here Φ_0 denotes the ground-state energy.

4.5 Conclusions and Discussion

The uncountably infinitely degenerate classical ground states of the stealthy potentials have been sampled previously using energy minimizations. We demonstrate here that this way of sampling the ground states to produce ensembles of configurations introduces dependencies on the energy minimization algorithm and the initial configuration. Such artificial dependencies are avoided in studying the canonical ensemble in the $T \to 0$ limit. We sample this ensemble by performing MD simulations at sufficiently low temperatures, periodically taking snapshots, and minimizing the energy of the snapshots.

The configurations in this ensemble become more ordered as χ increases and obey certain theoretical conditions on their pair statistics [325], similarly to previous energy minimization results. However, other properties of this ensemble are unique. First, our numerical results demonstrate that the pair statistics of this ensemble displays no "clustering effect" [divergence of $g_2(r)$ as $r \to 0$] for any χ value, and is independent of the functional form of the stealthy potential. Second, we numerically verify the theoretical ansatz [325] that for sufficiently small χ stealthy disordered ground states behave like "pseudo" disordered equilibrium hard-sphere systems in Fourier space, i.e., $S(k)$ has the same functional form as the pair correlation function for equilibrium hard spheres for sufficiently small densities. Third, when χ is above the critical value of 0.5, our results strongly indicate that crystal structures are entropically favored in both two and three dimensions in the infinite-volume limit. Our numerical evidence suggests that the entropically favored crystal in two dimensions is the triangular lattice. However, we could not determine the entropically favored crystal structure in three dimensions. For finite systems, the disordered-to-crystal phase transition can happen at a slightly lower χ. A theoretical explanation of this phenomenon remains an open problem.

Besides ground states of stealthy potentials, other disordered degenerate ground states of many-particle systems have been studied using energy minimizations. Specifically, previous researchers have constrained the structure factor to have some targeted functional form other than zero for prescribed wave vectors [329, 26, 350]. Finding the configurations corresponding to such targeted structure factors amounts to finding the ground states of two-, three- and four-body potentials, in contrast to the two-body stealthy potential studied in this chapter. This situation is the most general application of the collective-coordinate approach. It will be interesting to study the resulting pair statistics of the ground states for these more general interactions in the zero-temperature limit of the canonical ensemble.

The collective-coordinate approach is an independent and fruitful addition to the basic statistical mechanics problem of connecting local interactions to macroscopic observables. One important feature of collective-coordinate interactions is that it has uncountably infinitely degenerate classical ground states [325]. In the case of isotropic pair interactions, the only other system that we know with this feature is the hard-sphere system. However, there are two important differences between hard-sphere systems and collective-coordinate ground states. First, while the dimensionality of the configuration space of equilibrium hard-sphere systems consisting of N particles within a periodic box is fixed [simply determined by the nontrivial number of degrees of freedom, $d(N-1)$], the dimensionality of the collective-coordinate ground-state configuration space decreases as χ increases and, on a per particle basis, eventually vanishes [325]. The decreased dimensionality of the ground-state configuration space creates challenges for accurate sampling of the entropically favored ground states using numerical simulations and hence the development of better sampling methods is a fertile ground for future research.

Second, while the probability measure of the equilibrium hard-sphere system is uniform over its entire ground-state manifold, that of the stealthy ground states is not uniform. To illustrate this point, imagine a one-dimensional energy landscape that has a double-well potential behavior in a portion of the configuration space, as shown in Fig. 4.17. Each minimum represents a degenerate ground state (as we find with stealthy potentials) and therefore the well depths of the minima are the same. Let us now consider harmonic approximations of the two wells in the vicinity of x_1 and x_2, respectively,

$$V_1(x) = a_1(x - x_1)^2,$$

and

$$V_2(x) = a_2(x - x_2)^2,$$

where x is the configurational coordinate. At very low temperature, to a good approximation, the system can only visit the part of the configuration space with energy less than ε, and $\varepsilon \to 0$ as $T \to 0$. Solving $V_i(x) < \varepsilon$, where $i = 1, 2$, one finds the feasible region of configuration space associated with both wells:

$$x_1 - \sqrt{\varepsilon/a_1} < x < x_1 + \sqrt{\varepsilon/a_1},$$

and

$$x_2 - \sqrt{\varepsilon/a_2} < x < x_2 + \sqrt{\varepsilon/a_2}.$$

When $a_1 \neq a_2$, we see that the feasible regions associated with the two potential wells have different ranges. Therefore, the weights associated with the two minima, i.e., the relative probabilities for finding the system in the vicinity of those minima, will also differ. Similarly, in the stealthy multidimensional configuration space that we are studying, the magnitude of the eigenvalues of the Hessian matrix will determine the relative weights. Therefore, the probability measure of the stealthy ground states is not uniform over the ground-state manifold, unlike the degenerate ground states of classical hard spheres. Our low-temperature MD simulations sample ground states with this nonuniform probability measure. It would be useful to devise theories to estimate the weights of different portions of the ground-state manifold. However, a feature that complicates the problem is that the Hessian matrix has zero eigenvalues. In the associated directions of the eigenvectors of the configuration space, the energy scales more slowly than quadratically (harmonically) but we do not know the specific form.

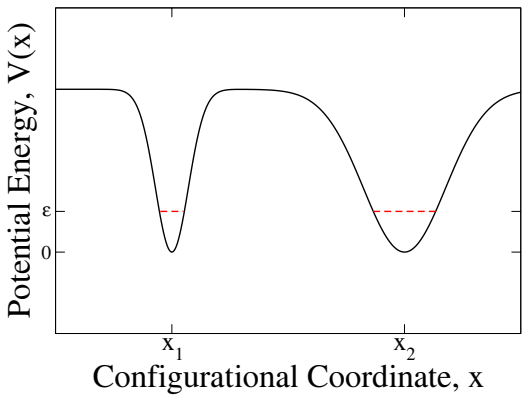

Figure 4.17 A model one-dimensional energy landscape with two wells located at x_1 and x_2 of the same depth but different curvatures. The "feasible regions," i.e., regions where $V(x) < \varepsilon$, is marked by red dashed lines.

This chapter, which investigates the entropically favored ground states, is the first of a two-chapter series. In the next chapter, we will study aspects of the ground-state manifold with an emphasis on configurations that are not entropically favored for χ above 1/2 (the ordered regime). In particular, we will more fully investigate the nature of so-called "wavy" crystals or "stacked-slider" phases, discovered in Ref. [328]. Using an analytical description of such states, we will demonstrate that they are part of the ground state but are not entropically favored. Our analytical model will also demonstrate that stacked-slider phases exist in three and higher dimensions.

4.6 Appendix A: Real-space Potential in Finite Systems

In the infinite-system-size limit, an isotropic $\tilde{v}(\mathbf{k})$ correspond to an isotropic real-space pair potential $v(\mathbf{r})$. However, for finite systems, the corresponding $v(\mathbf{r})$ is anisotropic. To illustrate the finite-size effect, we compare the two-dimensional real-space potential $v(\mathbf{r})$ in the infinite-system-size limit to corresponding potentials associated with finite-sized fundamental cells of square and rhombic shapes of different volumes in Fig. 4.18.

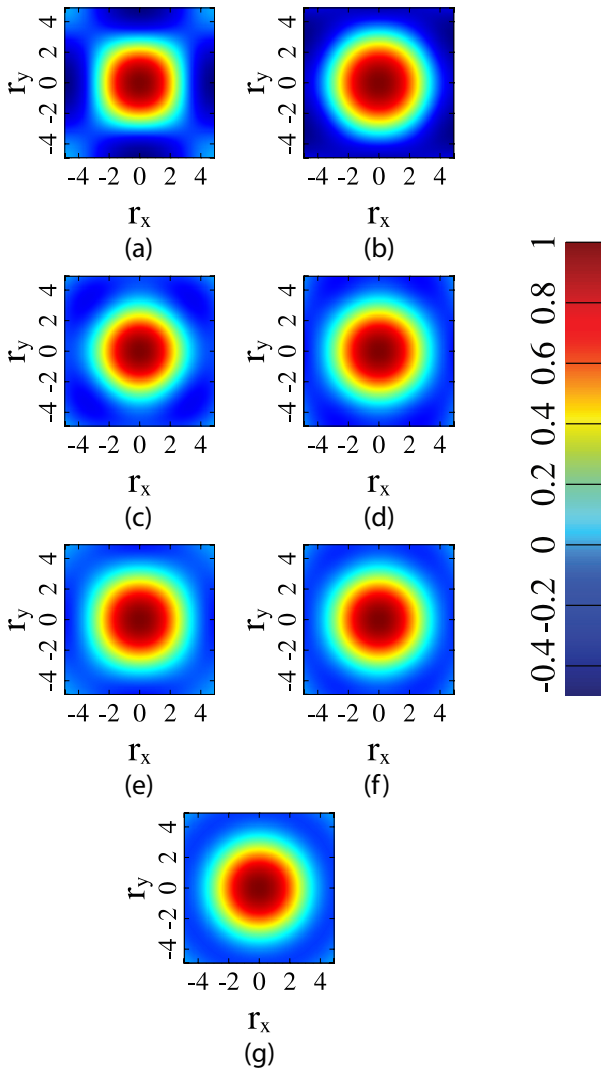

Figure 4.18 A portion of the real-space potential $v(\mathbf{r})$ around the origin for the stealthy potential (4.5) with $K = 1$ and $V(k) = 1$. (a)-(f) Real-space potential in a periodic simulation box that is [(a), (c), and (e)] square or [(b), (d), and (f)] rhombic in shape; the latter has a 60° interior angle. The volumes of the simulation boxes, v_F, are [(a) and (b)] 100, [(c) and (d)] 400, and [(e) and (f)] 1385. Panels (a)-(d) use unrealistically small simulation boxes and is intended to illustrate finite-size effect only. (g) The real-space potential in the infinite-system-size limit. All potentials are normalized by their respective values at the origin since scaling does not affect the ground state. Note that, starting from the center, the dark (red) region indicates the highest values of the potential, whereas towards the edge of the box, the dark (blue) region indicates the lowest values of the potential.

The real-space potential in the rhombic simulation box with a 60° interior angle is appreciably more isotropic than the real-space potential in a square simulation box. Therefore, in this chapter, we will henceforth use rhombic fundamental cells in two dimensions. Similarly, in three dimensions, we always use a simulation box shaped like a fundamental cell of a body-centered cubic (BCC) lattice since BCC lattice is the unique ground state at $\chi^*_{\max}$.

4.7 Appendix B: Local Gradient Descent Algorithm

Most optimization algorithms are designed for efficiency. They use complex rules to determine the direction of the next step and take as large steps as possible. These features make their path less obvious. To minimize energy in the path following the gradient vector, we designed a "local gradient descent algorithm" with the following steps:

1. Start from an initial guess, $\mathbf{x}$, and find the function value $f(\mathbf{x})$ and derivative $f'(\mathbf{x})$.

2. Start from a relatively large (10^{-3} times the simulation box side length) step size, s, and calculate the vector to the next step $\Delta\mathbf{x} = -s\frac{f'(\mathbf{x})}{|f'(\mathbf{x})|}$. Find the function value at the next step $f(\mathbf{x}+\Delta\mathbf{x})$. Calculate the change of function value $\Delta f = f(\mathbf{x}+\Delta\mathbf{x}) - f(\mathbf{x})$.

3. If we are following the path of steepest descent accurately, the change of the function value should be close to $f'(\mathbf{x})\cdot\Delta\mathbf{x}$. If the difference between Δf and $f'(\mathbf{x})\cdot\Delta\mathbf{x}$ is less than 1%, we accept this move. Otherwise, we abort this move and half the step size s.

4. Repeat the above steps until a minimum is found with enough precision.

4.8 Appendix C: Number of Particles of Every System in Sec. 4.4

Table 4.1 The number of particles N of each systems shown in Figs. 4.9 and 4.10.

χ	N for $d = 1$	N for $d = 2$	N for $d = 3$
0.05	1001	541	261
0.1	501	270	131
0.143	351	190	92
0.2	251	136	66
0.25	201	109	53
0.33	151	181	191

Table 4.2 The number of particles N of each systems shown in Fig. 4.11.

χ	N
0.33	181
0.35	171
0.38	161
0.4	151
0.43	141
0.46	131

Table 4.3 The number of particles N of each systems shown in Fig. 4.12.

χ	N for $d = 1$	N for $d = 2$	N for $d = 3$
0.05	1001	541	261
0.1	501	270	131
0.143	351	190	92
0.2	251	136	66
0.25	201	109	53

In this appendix we report the number of particles N in each system in Sec. 4.4. Both configurations in Fig. 4.6 consist of 51 particles. Configurations (a) and (b) in Fig. 4.7 consist of 271 and 151 particles, respectively. Those in Fig. 4.8 consist of 131 and 161 particles, respectively.

The number of particles of each system in Figs. 4.9, 4.10, 4.11, and 4.12 are shown in Tables 4.1, 4.2, and 4.3, respectively. Each configuration in Figs. 4.14, 4.15, and 4.16 consist of 36, 400, and 343 particles, respectively.

Chapter 5

Ground states of stealthy hyperuniform potentials: II. Stacked-slider phases

5.1 Introduction

A fundamental problem of statistical mechanics is the determination of the phase diagram of interacting many-particle systems. A substantial variety of pair interactions can produce a dramatic diversity of macroscopic phases, including crystals [262], quasicrystals [269, 179, 180, 34, 76], liquid crystals [47], hexatic phases [168, 32, 229, 154], disordered hyperuniform systems [317, 74, 329, 315, 349, 145, 325], and liquids [289]. While crystals and liquids are the most common condensed states of matter, there are other states in between. For example, quasicrystals and liquid crystals both have anisotropy and long-range orientational order, like crystals, but lack long-range translational order, similar to liquids. Other phases with features that lie between crystals and liquids include disordered hyperuniform systems, which are disordered

but behave more like crystals in the way in which they suppress long-range density fluctuations [317, 145].

A family of long-range isotropic pair potentials, called stealthy potentials, produces infinitely degenerate disordered hyperuniform classical ground states at high densities in d-dimensional Euclidean space $\mathbb{R}^d$ [329, 325, 328, 26, 27, 29, 352]. Stealthy potentials are often specially constructed such that finding a ground state is equivalent to constraining the structure factor $S(\mathbf{k})$ to be zero for all wave vectors $\mathbf{k}$ such that $0 < |\mathbf{k}| \leq K$, where K is some radial cutoff value. A dimensionless measure of the relative fraction of constrained degrees of freedom (proportional to K^d) compared to the total number of degrees of freedom, χ, controls the degree of order and degeneracy of the ground states of these potentials.

In the preceding chapter [352], we numerically studied the entropically favored ground states, i.e., configurations most likely to appear in the canonical ensemble in the zero-temperature limit, of stealthy potentials. We found that entropically favored ground states are disordered for $\chi < 1/2$, and crystalline for $\chi > 1/2$ up to a certain critical value [325].

The main focus of this chapter is the investigation of stacked-slider phases, which are metastable states that are part of the ground-state manifold for some χ above $1/2$, although not entropically favored. Stacked-slider phases were first discovered in two dimensions in Ref. [328] and were originally called wavy crystals because they were observed to consist of particle columns that display a meandering displacement away from linearity. However, we will see that "stacked-slider phases" for arbitrary dimensions is a more suitable name for this phase and this designation will be used henceforth.

The authors of Ref. [328] easily distinguished stacked-slider phases from crystal phases by a lack of periodicity in direct space and a lack of Bragg peaks in its diffraction pattern. Distinguishing stacked-slider phases and disordered phases, on

the other hand, was based on a different property. In disordered phases, all $\mathbf{k}$'s such that $|\mathbf{k}| > K$ have positive structure factors. However, in stacked-slider phases, the structure factor at some $\mathbf{k}$'s such that $|\mathbf{k}| > K$ are implicitly constrained to vanish identically [328], i.e., they are induced to be zero by the constraints inside the radius K. The existence of implicit constraints was used to distinguish stacked-slider phases from disordered phases in Ref. [328].

There are still many outstanding questions concerning stacked-slider phases. Can a theoretical model of stacked phases in the thermodynamic limit be devised to elucidate previous numerical studies? One disadvantage of numerical studies is that finite-size effects make it difficult to conclude anything definitive about the large system limit. For example, are stacked-slider phases isotropic or anisotropic in this limit? Moreover, to what extent does the choice of the simulation box shape affect the results? Were any important features of stacked-slider phases overlooked by studying finite-precision simulation results? Finally, because Ref. [328] studied two dimensions only, we do not know whether stacked-slider phases exist in other dimensions. This chapter provides additional insights into these unanswered questions.

The rest of the chapter is organized as follows. In Sec. 5.2 we perform numerical studies with much higher precision than previously. The numerical results enabled us to find an analytical model of two-dimensional stacked-slider phases, presented in Sec. 5.3. We generalize this model to higher dimensions in Sec. 5.4. We demonstrate that stacked-slider phases are distinguishable states of matter; they are nonperiodic, statistically anisotropic structures that possess long-range orientational order but have zero shear modulus. The model also shows that implicit constraints exist. In Sec. 5.5 we use this analytical model to show that stacked-slider phases are not entropically favored in the zero-temperature limit of the canonical ensemble. In Sec. 5.6 we postulate that the transition between stacked-slider phases and disordered phases occurs at a slightly lower χ than that reported in Ref. [328] from energy minimiza-

tions from high-temperature limit (Poisson) initial configurations. In Sec. 5.7 we make concluding remarks and draw comparisons to other common phases of matter.

5.2 Numerical Study of 2D Stacked-Slider Phases

In this section we numerically study the ground states of a stealthy potential at a variety of χ's (or densities) in two dimensions. We begin with the mathematical relations and simulation procedure in Sec. 5.2.1, and then present our results in Sec. 5.2.2. These results will suggest an analytical model of two-dimensional stacked-slider phases in Sec. 5.3.

5.2.1 Mathematical Relations and Simulation Procedure

As detailed in the preceding chapter and other references [325, 328, 329, 26, 27, 29], we simulate systems consisting of N point particles, located at $\mathbf{r}^N \equiv \mathbf{r}_1, \mathbf{r}_2, ..., \mathbf{r}_N$, in a simulation box in $\mathbb{R}^d$ under periodic boundary conditions. The number density is $\rho = N/v_F$, where v_F is the volume of the simulation box. The particles interact with a pairwise additive potential $v(\mathbf{r})$ such that its Fourier transform is:

$$\tilde{v}(\mathbf{k}) = \begin{cases} V(|\mathbf{k}|) & \text{if } |\mathbf{k}| \leq K \\ 0 & \text{otherwise,} \end{cases} \tag{5.1}$$

where $\tilde{v}(\mathbf{k}) = \int_{v_F} v(\mathbf{r}) \exp(-i\mathbf{k}\cdot\mathbf{r}) d\mathbf{r}$ is the Fourier transform of the pair potential $v(\mathbf{r})$, $V(k)$ is a positive function, and K is a constant.

Under such potential, the total potential energy of the system can be calculated in the Fourier space

$$\Phi(\mathbf{r}^N) = \frac{1}{2v_F} \sum_{\mathbf{k}} V(|\mathbf{k}|) |\tilde{n}(\mathbf{k})|^2 + \Phi_0, \tag{5.2}$$

where the sum is over all reciprocal lattice vector $\mathbf{k}$'s of the simulation box such that $0 < |\mathbf{k}| \leq K$, $\tilde{n}(\mathbf{k}) = \sum_{j=1}^{N} \exp(-i\mathbf{k} \cdot \mathbf{r}_j)$, and

$$\Phi_0 = [N(N-1) - N \sum_{\mathbf{k}} \tilde{v}(\mathbf{k})]/2v_F \tag{5.3}$$

is a constant independent of the particle positions $\mathbf{r}^N$. Thus, the first term on the right-hand side of Eq. (5.2) is the only configuration-dependent contribution to the potential energy

$$\Phi^*(\mathbf{r}^N) = \frac{1}{2v_F} \sum_{0<|\mathbf{k}|\leq K} V(\mathbf{k})|\tilde{n}(\mathbf{k})|^2. \tag{5.4}$$

Since $V(k) > 0$ and $v_F > 0$, Eq. (5.4) shows that $\Phi^*(\mathbf{r}^N) \geq 0$. Therefore, if configurations such that $\Phi^*(\mathbf{r}^N) = 0$ exist, then they are the classical ground states of this potential. These configurations are achieved by constraining $\tilde{n}(\mathbf{k})$ to zero for all $0 < |\mathbf{k}| < K$ and are said to be stealthy up to K. Since $\tilde{n}(\mathbf{k})$ is related to the structure factor $S(\mathbf{k})$ by $S(\mathbf{k}) = |\tilde{n}(\mathbf{k})|^2/N$ for every $\mathbf{k} \neq \mathbf{0}$, constraining $\tilde{n}(\mathbf{k})$ to zero is equivalent to constraining $S(\mathbf{k})$ to zero. Let M be half the number of $\mathbf{k}$ points in the summation of Eq. (5.2) [1]; the parameter

$$\chi = \frac{M}{d(N-1)} \tag{5.5}$$

determines the degree to which the ground states are constrained and therefore the degeneracy and disorder of the ground states [328]. For a fixed K, the parameter χ is inversely proportional to the density [27, 325, 352]. When $\chi \leq \chi^*_{max}$, where χ^*_{max} is a dimension-dependent constant, all the constraints are indeed satisfiable, thus $\Phi^*(\mathbf{r}^N)$ of the classical ground states is zero [325]. The χ values we study in this chapter are always less than χ^*_{max}.

[1] Since $|\tilde{n}(\mathbf{k})|^2 = |\tilde{n}(-\mathbf{k})|^2$, M is the number of independent constraints.

In this section we choose $N = 100$, $K = 1$, and $V(k) = 1$. The relatively small choice of N increases the precision of the ground states we find. We will see that high precision is important in extracting an analytical model from numerical results. The constant K and the magnitude of $V(k)$ simply set the length scale and the energy scale. Although the function form of $V(k)$ could theoretically affect the probability of sampling different parts of the ground-state manifold, it does not affect the manifold itself [325, 352]. As explained in Ref. [352], we use a rhombic simulation box with a 60° interior angle to alleviate finite-size effect.

The ground states reported in this section are produced by the following steps.

1. Start from a Poisson (i.e., ideal gas) initial configuration.
2. Minimize $\Phi^*(\mathbf{r}^N)$ [in Eq. (5.4)] using the low-storage BFGS algorithm [214, 183, 150].
3. Minimize $\Phi^*(\mathbf{r}^N)$ using the MINOP algorithm [69].
4. If $\Phi^*(\mathbf{r}^N) < 10^{-20}$, we successfully find a relatively high-precision ground state.
5. Otherwise, what we find is either an imprecise ground state or a local minimum of $\Phi^*(\mathbf{r}^N)$. Therefore, we discard this configuration.

As detailed in Ref. [352], the low-storage BFGS algorithm is the fastest in minimizing $\Phi^*(\mathbf{r}^N)$, while the MINOP algorithm finds the most precise ground states. Therefore, we minimize $\Phi^*(\mathbf{r}^N)$ using these two algorithms consecutively to maximize both efficiency and precision.

These steps are performed N_t times for a variety of simulation box side lengths (and therefore a variety of χ's), listed in Table 5.1 [2]. As detailed in Ref. [328], for a finite system, only certain values of χ are allowed. The χ values in Table 5.1 contain all possible choices in the range $0.5 < \chi < \chi^*_{max}$, which covers the previously reported

[2]The reader will notice that the success rate reported in Table 5.1 is dramatically nonuniform. This is another unusual feature of this class of phases that deserves further attention.

Table 5.1 The χ values, number of trials N_t, and number of successes N_s for each simulation box side length L.

L	χ	N_t	N_s
56	0.5303...	1000000	15615
57	0.5606...	199915	17127
58	0.5909...	200000	411
59	0.6060...	199965	8875
60	0.6363...	1000000	27788
62	0.6666...	1000000	76727
63	0.6818...	1000000	157501
64	0.7121...	200000	119563
65	0.7424...	1000000	165203
66	0.7575...	200000	80258
68	0.7878...	200000	2577
70	0.8787...	200000	0

stacked-slider phase regime in two dimensions, $0.57... \leq \chi < 0.77...$ [328, 27]. Except for $\chi = 0.8787\ldots$, where we could not precisely identify ground states, we plot the real-space configuration and reciprocal-space structure factor of at least 50 successful energy minimized results and visually inspect them. We divide them into different categories based on their appearances and then present representative configurations below.

5.2.2 Results

Representative numerically obtained ground-state configurations and their structure factors (in logarithmic scales) are presented in Figs. 5.1-5.3. For $0.5303\ldots \leq \chi \leq 0.6060\ldots$, the ground-state manifold appears to contain a variety of structures (see Fig. 5.1). Except for the first one, all real-space configurations in Fig. 5.1 appear to be Bravais lattices. However, their structure factors are not as simple as a collection of Bragg peaks among a zero-intensity background, suggesting that the real-space configurations are not perfect Bravais lattices.

At $\chi = 0.6363\ldots$ and $\chi = 0.6666\ldots$ a type of relatively-simple-looking configuration appears (see Fig. 5.2). The real-space configurations appear to be comprised

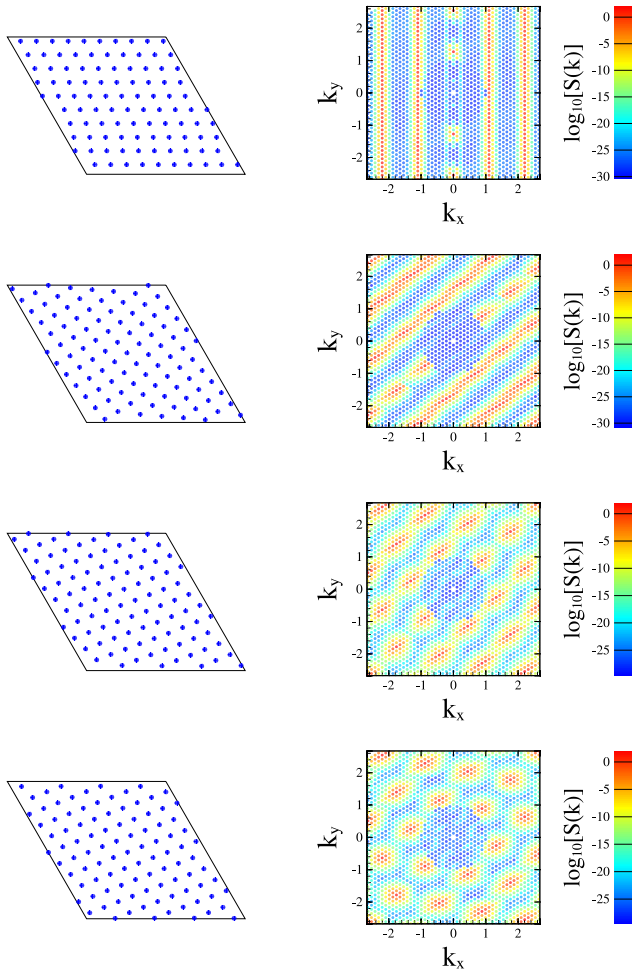

Figure 5.1 Four representative numerically obtained ground-state configurations at $\chi = 0.5606\ldots$ (left) and their corresponding structure factors (right), where colors indicate intensity values at reciprocal lattice points.

of straight lines of particles with wavelike displacements relative to each other. The structure factors, on the other hand, consist of straight lines of nonzero values in a background of virtually zero ($< 10^{-20}$) intensities.

For $\chi \geq 0.6818\ldots$, the results are similar to that in Fig. 5.2, but there exist so many constraints that the nonzero-value lines in the structure factor have to be interrupted. The interruptions grow in length as χ increases and eventually, at $\chi = 0.7878\ldots$, the only nonzero structure factors are the Bragg peaks and the real-space configuration becomes a Bravais lattice.

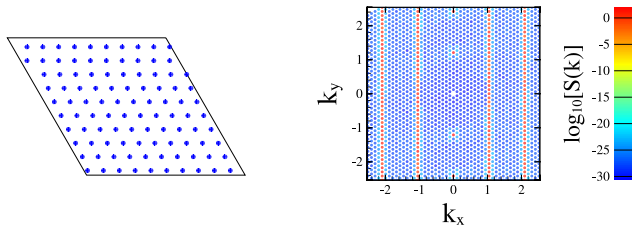

Figure 5.2 A numerically obtained ground-state configuration at $\chi = 0.6363\ldots$ (left) and the corresponding structure factor (right), where colors indicate intensity values at reciprocal lattice points.

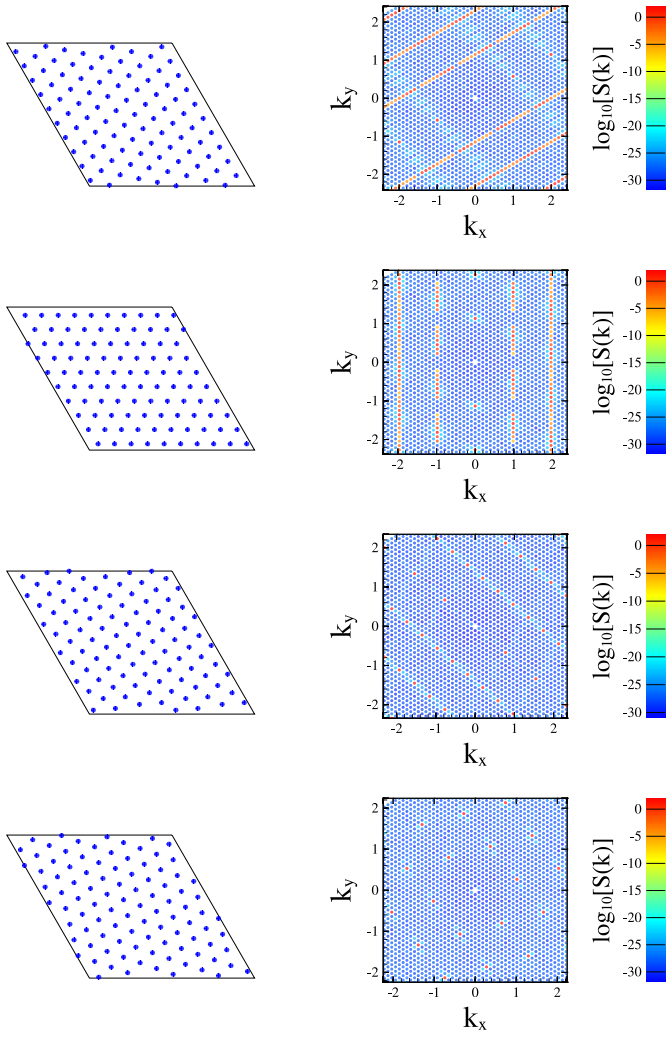

Figure 5.3 Shown on the left are four representative numerically obtained ground-state configurations at $\chi = 0.6818\ldots$ (first row), $\chi = 0.7121\ldots$ (second row), $\chi = 0.7424\ldots$ (third row), and $\chi = 0.7878\ldots$ (fourth row). On the right are their corresponding structure factors, where colors indicate intensity values at reciprocal lattice points.

5.3 Analytical Model of Two-Dimensional Stacked-Slider Phase

In this section we look closer at the simulation results that yield stacked-slider phases to see if an exact analytical construction can be extracted. We will see that understanding the configuration shown in Fig. 5.2 is the key to understanding other configurations. The real-space configuration in Fig. 5.2 seems to be made of straight horizontal lines that are displaced relative to each other. Are the displacements of different horizontal lines independent of each other or correlated in some way? To answer this question, we numerically constructed a configuration that is made of horizontal straight lines of particles, just like the one shown in Fig. 5.2, but with independent random displacements along each horizontal line. The structure factor of the new configuration has exactly the same support [the set of $\mathbf{k}$'s such that $S(\mathbf{k}) \neq 0$] as the one shown in Fig. 5.2. Thus, the new configuration is also a ground state at this χ value. Therefore, the displacements of each line do not need to be correlated in any way. This allows us to find a two-dimensional stacked-slider phase model, depicted in Fig. 5.4.

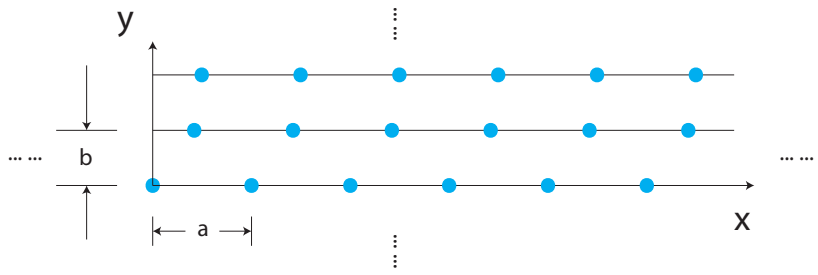

Figure 5.4 Schematic plot of the two-dimensional stacked-slider phase model. Each horizontal line of particles [indicated by large (blue) dots] form a one-dimensional integer lattice with lattice spacing a. Then multiple horizontal integer lattices are stacked vertically, with spacing b. Each horizontal line of particles can be translated freely to slide with respect to each other.

This analytical model allows the calculation of various properties of the two-dimensional stacked-slider phases. One can find the analytical pair correlation function and structure factor of this model, assuming that the displacement of each line is independent and uniformly distributed between 0 and a. The pair correlation function $g_2(\mathbf{r})$ is defined such that $\rho g_2(\mathbf{r})d\mathbf{r}$ is the conditional probability that a particle is found in the volume element $d\mathbf{r}$ about $\mathbf{r}$, given that there is a particle at the origin. For the two-dimensional stacked-slider phase, $g_2(\mathbf{r})$ can be found directly from the definition of this model:

$$g_2(x,y) = b\sum_{j\neq 0}\delta(y-bj) + ab\delta(y)\sum_{j\neq 0}\delta(x-aj), \tag{5.6}$$

where x and y are horizontal and vertical coordinates, both summations are over all nonzero integers j, and δ denotes the Dirac delta function. The structure factor $S(\mathbf{k})$ can be found by Fourier transforming $g_2(\mathbf{r}) - 1$:

$$S(\mathbf{k}) = 1 + \rho F[g_2(\mathbf{r}) - 1], \tag{5.7}$$

where $F[\cdots]$ denotes Fourier transform. Substituting (5.6) into (5.7), one gets:

$$\begin{aligned} S(\mathbf{k}) = {} & \frac{2\pi\delta(k_x)}{a}\left(\frac{2\pi}{b}\,\mathrm{III}_{2\pi/b}(k_y) - 1\right) \\ & + \frac{2\pi}{a}\,\mathrm{III}_{2\pi/a}(k_x) - \frac{4\pi^2}{ab}\delta(k_x)\delta(k_y), \end{aligned} \tag{5.8}$$

where k_x and k_y denote the horizontal and vertical components of $\mathbf{k}$, respectively, and $\mathrm{III}_T(t) = \sum_{j=-\infty}^{+\infty}\delta(t-jT)$ is the Dirac comb function. Both the pair correlation function (5.6) and the structure factor (5.8) are anisotropic, since swapping x and y in (5.6) and (5.8) gives different expressions.

A topological property this model can predict is the connectedness of the ground-state manifold, i.e., whether or not a ground state can be continuously deformed to

another ground state without crossing any energy barrier. Each stacked-slider configuration is obviously continuously connected to a rectangular lattice by the sliding motion of different lines. However, there are many permutations of the rectangular lattice. Are these permutations connected to each other through vertical and horizontal sliding motions? In the Appendix, we show that for a finite-size rectangular lattice consisting of N particles, all permutations are connected if and only if N is even.

Having found an analytical model of the ground states in this χ range, we move on to lower and higher χ ranges. The lower χ simulation results appear to be more complex. The first configuration in Fig. 5.1 appears to be similar to our existing analytical model, except that the nonzero-value regions in the structure factor are not strictly lines: The highest-intensity lines [$S(\mathbf{k}) \sim 10^0$] are surrounded by lower-intensity regions [$S(\mathbf{k}) \sim 10^{-10}$], which are surrounded by even lower-intensity regions [$S(\mathbf{k}) \sim 10^{-20}$]. The structure factor in the lower-intensity regions are very small, but are still much larger than the machine precision. (We use double-precision numbers, which have around 16 significant digits, to calculate $\tilde{n}(\mathbf{k})$. Therefore, the machine precision of $S(k) = |\tilde{n}(\mathbf{k})|^2/N$ should be on the order of $(10^{-16})^2/N = 10^{-34}$.) So a natural question arises: Are the lower-intensity regions real or are they an artifact of finite-precision simulations?

To answer this question, we chose a $\mathbf{k}$ point right next to the highest-intensity line and plotted the structure factor at this $\mathbf{k}$ point versus the potential energy during the energy minimization (see Fig. 5.5). As Φ^* goes to zero, the structure factor at this $\mathbf{k}$ point also goes to zero. Thus, we believe the lower-intensity regions are the result of numerical imprecision. If one could carry out an infinite-precision simulation and drive this configuration to a true ground state, the structure factors in the lower-intensity regions should go to zero and the configuration would become consistent with our analytical model.

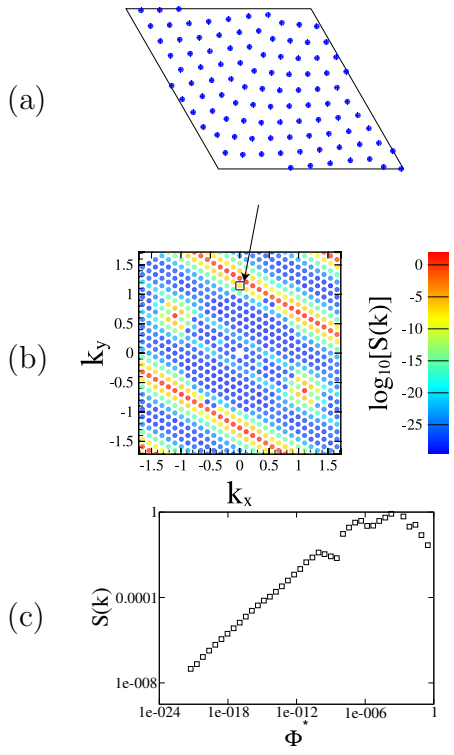

Figure 5.5 (a) A numerically obtained ground state at $\chi = 0.5606\ldots$. (b) The corresponding structure factor. A specific $\mathbf{k}$ point is indicated by a black square and an arrow. (c) The structure factor at this particular $\mathbf{k}$ point is plotted against total energy Φ^* during the optimization, showing $S(\mathbf{k}) \to 0$ as $\Phi^* \to 0$.

Having understood the first configuration in Fig. 5.1, let us move on to other configurations in that figure. The second and third configurations appear to be intermediate configurations between the first one and the fourth one. The fourth configuration looks like a Bravais lattice, except that the Bragg peaks are smeared out. Again, to find out whether this broadening of the Bragg peaks is real or artificial, we plotted the structure factor at a $\mathbf{k}$ point near a Bragg peak versus the potential energy in Fig. 5.6. We find again that the structure factor at this $\mathbf{k}$ point goes to zero as Φ^* goes to zero. Thus, the smearing out of the Bragg peaks is also due to numerical imprecision. If one could carry out an infinite-precision energy minimization on this configuration, one should get a Bravais lattice.

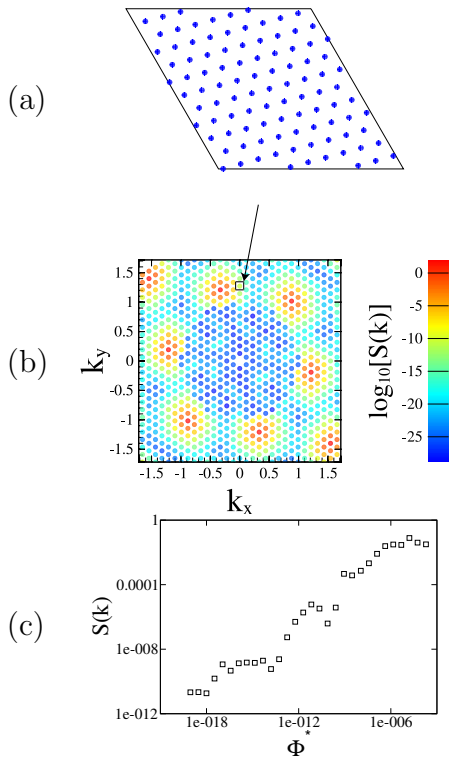

Figure 5.6 (a) A numerically obtained ground state at $\chi = 0.5606\ldots$. (b) The corresponding structure factor. A specific $\mathbf{k}$ point is indicated by a black square and an arrow. (c) The structure factor at this particular $\mathbf{k}$ point is plotted against total energy Φ^* during the optimization, showing $S(\mathbf{k}) \to 0$ as $\Phi^* \to 0$.

So far we have demonstrated that the numerically obtained ground states follow a simple model at $\chi = 0.6363\ldots$ and $\chi = 0.6666\ldots$. We have also demonstrated that while the numerically obtained ground states for $0.5303\ldots \leq \chi < 0.6363\ldots$ appear to be richer, they are actually exactly the same as either the model or a Bravais lattice if we could perform infinite-precision simulations. However, as we move to higher χ's, the ground states start to lose degrees of freedom. As shown in Fig. 5.3, at $\chi = 0.6818\ldots$, the high-intensity lines in the structure factor develop zero-intensity interruptions. In our stacked-slider phase model, if each line of particles could move independently, then the high-intensity lines in the structure factor would have no interruptions. Thus, these interruptions indicate constraints in the displacements of each line of particles. At $\chi = 0.7121\ldots$, the lines are interrupted even further,

indicating even more constraints in the displacements of each line. At $\chi = 0.7424\ldots$, the structure becomes a two-particle-basis crystal. Eventually, at $\chi = 0.7878\ldots$, the structure becomes a Bravais lattice.

Starting from $\chi = 0.6818\ldots$, the stacked-slider phase become more constrained as χ increases. To study how constrained this phase is at different χ values, we calculate the number of zero eigenvalues n_e of the Hessian matrix of the potential energy. This number is equal to the number of independent ways to deform the structure such that the energy scales more slowly than quadratic, which is an upper bound of the dimensionality of the ground-state configuration space n_c [i.e. the number of independent ways to deform the structure such that the $\Phi^*(\mathbf{r}^N)$ remains zero]. For $\chi < 0.6818\ldots$, our model predicts $n_c = 11$ (since there are two translational degrees of freedom, and nine independent ways to slide the ten lines of particles relative to each other) and our calculation also find $n_e = 11$. At $\chi = 0.6818\ldots$, $0.7121\ldots$, $0.7424\ldots$, and $0.7878\ldots$, our calculations find $n_e = 9$, 5, 3, and 2, respectively. This calculation suggests that as χ increases, n_c gradually decreases. Eventually, $n_c = 2$, indicating that there is no way to deform the structure other than trivial translations.

5.4 Generalized Stacked-Slider Phase Model

We now generalize the two-dimensional stacked-slider phase model to higher dimensions. To begin with, we present and prove the following theorem:

Stealthy Stacking Theorem. Let d_P and d_Q be positive integers. Let W be $(d_P + d_Q)$-dimensional Euclidean space. Let W_P be a d_P-dimensional subspace of W and W_Q be the d_Q-dimensional orthogonal complement space of W_P. Let P be a point pattern in W_P with density ρ_P. For each point $\mathbf{a} \in P$, let $Q(\mathbf{a})$ be a point pattern in W_Q with some density ρ_Q independent of $\mathbf{a}$. If P is stealthy up to certain reciprocal-space cutoff K_P and all $Q(\mathbf{a})$'s are stealthy up to certain reciprocal-space

cutoff K_Q in their subspace, then the following point pattern in W,

$$\{\mathbf{a}+\mathbf{b}|\mathbf{a}\in P, \mathbf{b}\in Q(\mathbf{a})\} \tag{5.9}$$

is a stealthy point pattern up to $K = min(K_P, K_Q)$.

Proof. The collective density variable of the point pattern in Eq. (5.9) is

$$\tilde{n}(\mathbf{k}) = \sum_{\mathbf{a}\in P}\sum_{\mathbf{b}\in Q(\mathbf{a})} \exp[-i\mathbf{k}\cdot(\mathbf{a}+\mathbf{b})]. \tag{5.10}$$

Since W_P and W_Q are two orthogonal complementary subspaces of W, we can divide vector $\mathbf{k}$ into two parts $\mathbf{k} = \mathbf{k}_P + \mathbf{k}_Q$, where $\mathbf{k}_P \in W_P$ and $\mathbf{k}_Q \in W_Q$. Therefore,

$$\begin{aligned}\tilde{n}(\mathbf{k}) &= \sum_{\mathbf{a}\in P}\sum_{\mathbf{b}\in Q(\mathbf{a})} \exp[-i(\mathbf{k}_P+\mathbf{k}_Q)\cdot(\mathbf{a}+\mathbf{b})] \\ &= \sum_{\mathbf{a}\in P}\exp(i\mathbf{k}_P\cdot\mathbf{a})\sum_{\mathbf{b}\in Q(\mathbf{a})}\exp(-i\mathbf{k}_Q\cdot\mathbf{b}).\end{aligned} \tag{5.11}$$

For any $\mathbf{k}$ such that $0 < |\mathbf{k}| \le K$, $|\mathbf{k}_Q| \le |\mathbf{k}| \le K \le K_Q$. If $\mathbf{k}_Q \neq \mathbf{0}$, then the stealthiness of point patterns $Q(\mathbf{a})$ gives

$$\sum_{\mathbf{b}\in Q(\mathbf{a})}\exp(-i\mathbf{k}_Q\cdot\mathbf{b}) = 0 \tag{5.12}$$

and therefore $\tilde{n}(\mathbf{k}) = 0$. On the other hand, if $\mathbf{k}_Q = \mathbf{0}$, then $\mathbf{k}_P = \mathbf{k}$ and Eq. (5.11) becomes

$$\tilde{n}(\mathbf{k}) = N_{Q(\mathbf{a})}\sum_{\mathbf{a}\in P}\exp(-i\mathbf{k}\cdot\mathbf{a}), \tag{5.13}$$

where $N_{Q(\mathbf{a})}$ is the number of particles in pattern $Q(\mathbf{a})$, which is independent of $\mathbf{a}$ because all the $Q(\mathbf{a})$'s have the same density. Since $0 < |\mathbf{k}| \le K \le K_P$, the

stealthiness of point pattern P gives

$$\tilde{n}(\mathbf{k}) = 0. \tag{5.14}$$

To summarize, for any $\mathbf{k}$ such that $0 < |\mathbf{k}| \leq K$, whether or not $\mathbf{k}_Q = \mathbf{0}$, $\tilde{n}(\mathbf{k})$ is always zero. Therefore, the point pattern (5.9) is stealthy up to K.

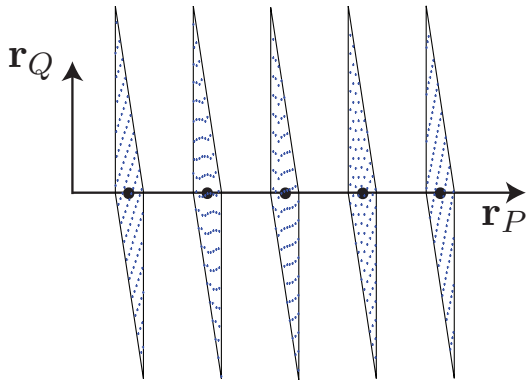

Figure 5.7 Schematic plot of the stacked-slider phase model. The large black dots form an integer lattice (point pattern P). By replacing each black dot with a two-dimensional stealthy point pattern (indicated by small blue dots) of the same density [point patterns $Q(\mathbf{a})$], the overall three-dimensional point pattern consisting of all the small blue dots is stealthy. The two vectors $\mathbf{r}_P$ and $\mathbf{r}_Q$ are in subspaces W_P and W_Q, respectively. Note that since some $Q(\mathbf{a})$'s are two-dimensional stacked-slider configurations, this configuration allows both interlayer and intralayer sliding motions, as detailed in Sec. 5.3.

The parameter χ of this point pattern can be calculated using Eq. (35) of Ref. [325]. Our calculation yields

$$\chi = \frac{v_1(d_P + d_Q; K)}{2(d_P + d_Q)(2\pi)^{d_P+d_Q}\rho_P\rho_Q}, \tag{5.15}$$

where $v_1(d; r)$ is the volume of a d-dimensional hypersphere of radius r. In the case $K_P = K_Q$, using Eq. (35) of Ref. [325], Eq. (5.15) can be simplified to:

$$\chi = \frac{2v_1(d_P + d_Q; 1)}{v_1(d_P; 1)v_1(d_Q; 1)} \frac{d_P d_Q}{d_P + d_Q} \chi_P \chi_Q. \tag{5.16}$$

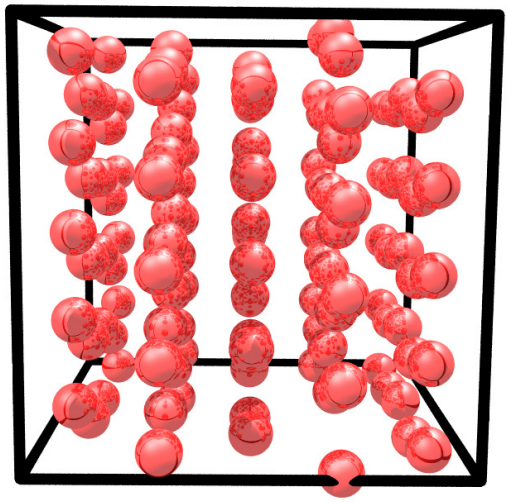

Figure 5.8 Three-dimensional stacked-slider configuration stealthy up to $\chi = 0.6981\ldots$. This configuration is obtained by sliding each vertical plane of particles relative to each other and then sliding each vertical line in each plane relative to each other starting from the simple cubic lattice.

The aforementioned theorem allows us to construct stacked-slider configurations in higher dimensions. To construct a stacked-slider configuration in $d \geq 2$, choose two lower dimensions d_P and d_Q such that $d_P + d_Q = d$. Choose a d_P-dimensional stealthy configuration P and replace each particle $\mathbf{a}$ in P with a d_Q-dimensional stealthy configuration $Q(\mathbf{a})$ and the resulting d-dimensional configuration is a stacked-slider one. The resulting configuration is often anisotropic, since d_P dimensions are treated separately from the remaining d_Q dimensions. See Fig. 5.7 for an illustration of a three-dimensional stacked-slider configuration with $d_P = 1$ and $d_Q = 2$.

Certain three-dimensional crystal structures can allow sliding deformations while remaining stealthy at relatively large (greater than 0.5) χ. As Fig. 5.8 shows, the simple cubic lattice allows the sliding motion of each two-dimensional square-lattice layer and the sliding motion of each line of particles inside every layer for χ up to $0.6981\ldots$. Barlow packings [276], including the face-centered-cubic packing and the hexagonal close packing, also allow the sliding motion of each triangular-lattice layer of particles for χ up to $0.7600\ldots$.

Equation (5.16) can be used to calculate the maximum χ values of the stacked-slider-phase, χ^{ss}_{max}, assuming unconstrained sliding motions, in each space dimension d. To do this one can try all possible combinations of positive integers d_P and d_Q such that $d_P + d_Q = d$, and let χ_P and χ_Q equal to χ^*_{max} in d_P and d_Q dimensions, respectively. Our calculations for $2 \leq d \leq 4$ are summarized in Table 5.2. There is no obvious trend in these low dimensions. However, as d increases, the factor $\frac{2v_1(d_P+d_Q;1)}{v_1(d_P;1)v_1(d_Q;1)}\frac{d_P d_Q}{d_P+d_Q}$ in Eq. (5.16) decreases for any d_P and d_Q. Thus, χ^{ss}_{max} should become arbitrarily small in sufficiently high dimensions.

Table 5.2 Comparison of the maximum χ value of stacked-slider-phases predicted by the generalized model χ^{ss}_{max} and the maximum χ value of Bravais lattices χ^*_{max} in two, three, and four dimensions.

d	χ^{ss}_{max}	χ^*_{max}	$\chi^{ss}_{max}/\chi^*_{max}$
2	$\pi/4$	$\pi/\sqrt{12}$	0.8660...
3	$\frac{4\pi}{9\sqrt{3}}$	$\frac{2\sqrt{2}\pi}{9}$	0.8712...
4	$\frac{\sqrt{2}\pi^2}{16}$	$\frac{\pi^2}{8}$	0.7071...

Similar to two-dimensional stacked-slider configurations, the higher-dimensional ones also have implicit constraints [i.e. $\mathbf{k}$ vectors such that $|\mathbf{k}| > K$ and $S(\mathbf{k}) = 0$]. As seen in Eq. (5.11), $S(\mathbf{k}) = |\tilde{n}(\mathbf{k})|^2/N = 0$ as long as $0 < |\mathbf{k}_Q| \leq K$. One can thus choose arbitrarily large $\mathbf{k}_P$ such that $|\mathbf{k}| = |\mathbf{k}_P + \mathbf{k}_Q| > K$.

5.5 Feasible Region of the Configuration Space

Although stacked-slider configurations are part of the ground-state manifold of stealthy potentials, we will show in this section that they are not entropically favored, as indicated in Ref. [325]. Entropically favored ground states are the configurations that most likely appear in the canonical ensemble in the zero-temperature limit [325]. In this limit, as a good approximation, the system can only visit part of the configuration space where $\Phi^*(\mathbf{r}^N)$ [in Eq. (5.4)] is less than ϵ, where $\epsilon > 0$ tends to zero as the temperature tends to zero. This part of the configuration space is

therefore called the feasible region. If the feasible region corresponding to one set of the ground states is much smaller than the entire feasible region in the configuration space, this set will almost never appear in the canonical ensemble, i.e., they are not entropically favored.

In the infinite-system-size limit, the feasible region of any stacked-slider configuration is much smaller than that of any crystal if both the stacked-slider configuration and the crystal are ground states. This is because as $N \to \infty$, the configurational dimension n_c [i.e., the number of independent ways to deform the structure such that the $\Phi^*(\mathbf{r}^N)$ remains zero] of stacked-slider phases scales more slowly than the number of particles N. For example, for a two-dimensional stacked-slider configuration in which each row of particles can slide independently, n_c scales as $\sqrt{N}$. As discussed in Sec. 5.3, the number of zero eigenvalues of the Hessian matrix of the potential energy n_e is equal to n_c. Since a nonzero eigenvalue of the Hessian matrix corresponds to a quadratic scaling in one direction, in the dN-dimensional configuration space, $\Phi^*(\mathbf{r}^N)$ has quadratic scaling in $dN - n_c$ directions. In these directions, as $\epsilon \to 0$, the width of the feasible region scales as $\sqrt{\epsilon}$. In the remaining n_c directions, the width of the feasible region is much larger, since these directions correspond to translations of different rows of particles, which keeps $\Phi^*(\mathbf{r}^N)$ zero. If we let the widths of the feasible region in these directions be L, then the total volume of the feasible region of the stacked-sliding phase is approximately

$$V_s \approx L^{n_c} \epsilon^{(dN-n_c)/2} \approx L^{\sqrt{N}} \epsilon^{(dN-\sqrt{N})/2}. \tag{5.17}$$

In the case of a crystalline structure, n_e scales as N when $N \to \infty$. This can be seen in Fig. 5.9, where we plot $f = n_e/dN$ versus N for triangular lattices at $\chi = 0.6$. This figure shows that f tends to some constant as N grows, which means n_e scales as N. Since a zero eigenvalue of the Hessian matrix of $\Phi^*(\mathbf{r}^N)$ implies a

slower-than-quadratic scaling in some direction, the width of the feasible region in these n_e directions scales larger than $\sqrt{\epsilon}$ as $\epsilon \to 0$. Let the widths of the feasible region in these n_e directions be ϵ^x, where $0 < x < 1/2$ is some exponent. The width of the feasible region in the remaining $dN - n_e$ directions scales as $\sqrt{\epsilon}$. The total volume of the feasible region of a crystal is approximately

$$V_c \approx \epsilon^{(dN-n_e)/2}\epsilon^{n_e x} \approx \epsilon^{dN(1-f)/2}\epsilon^{dNfx}. \tag{5.18}$$

The ratio of V_s and V_c is approximately

$$\frac{V_s}{V_c} \approx L^{\sqrt{N}}\epsilon^{[dNf(1-2x)-\sqrt{N}]/2}. \tag{5.19}$$

Since $x < 1/2$, as $N \to \infty$ and $\epsilon \to 0$, $\frac{V_s}{V_c} \to 0$. Therefore, the feasible region of the stacked-slider phase is much smaller than that of the crystal. Since there are always crystalline structures competing with the stacked-slider phase, the latter is never entropically favored.

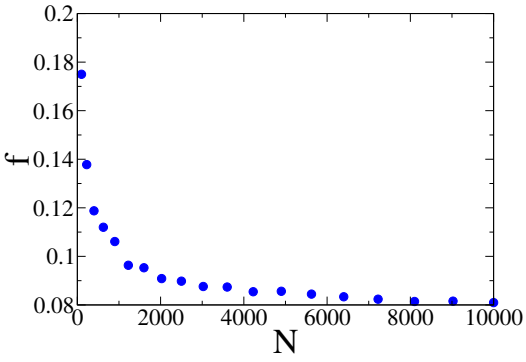

Figure 5.9 Fraction of zero eigenvalues of the Hessian matrix of the potential energy $f = \dfrac{n_e}{dN}$ for triangular lattices of various numbers of particles N at $\chi = 0.6$.

5.6 Relative Stability of Stacked-Slider Phases

We have shown that the feasible region of stacked-slider phases is always smaller than that of crystal phases and thus concluded that stacked-slider phases are never equilibrium phases at $T = 0$. This conclusion is confirmed by low-temperature molecular dynamics simulations reported in Ref. [352], which found disordered structures for $\chi < 1/2$ and crystalline structures for $\chi > 1/2$. However, this simple conclusion cannot explain or predict energy minimization results from high-temperature initial configurations that were used previously [328], where a transition from disordered phases to metastable stacked-slider phases was observed as χ increases, characterized by the change of the support of $S(\mathbf{k})$. In two dimensions, Ref. [328] reported that this transition is at $\chi = 0.57\ldots$, but high-fidelity simulations, reported in Sec. 5.2, produced stacked-slider configurations at $\chi = 0.5305\ldots$, suggesting that the transition is earlier than $0.5305\ldots$. Another observation on the disordered region supports our result: Section V of Ref. [27] reported that the fraction of normal modes with vanishing frequency f in disordered phases is exactly $1 - 2\chi$ for $\chi < 1/2$. However, this exact relation cannot be true for the $\chi > 1/2$ region, since f is non-negative. This suggests that there exists a sharp transition at $\chi = 1/2$, which is likely the phase transition to the stacked-slider phase. Although Ref. [27] only reported the relation $f = 1 - 2\chi$ in two dimensions, it explained this relation by simple counting arguments involving the number of constraints versus the number of degrees of freedom and hence this relation should apply in any dimension. Therefore, for any d, as long as stacked-slider phases exist for some χ above $1/2$, there should be a *nonequilibrium* phase transition from disordered phases to stacked-slider phases at the threshold $\chi = 1/2$.

It is noteworthy that one dimension is an exception of the above discussion. Previously, the existence of implicit constraints [$\mathbf{k}$'s such that $|\mathbf{k}| > K$ and $S(\mathbf{k}) = 0$] was often used to distinguish stacked-slider phases from disordered phases [328, 27]. Therefore, one-dimensional stealthy ground states in the range $1/3 < \chi < 1/2$, proven

Table 5.3 Comparison of the properties of some common states of matter. Here crystals and quasicrystals signify perfect crystals and perfect quasicrystals, respectively, without any defects (e.g., phonons and phasons). The checks and crosses indicate whether or not different phases have the attributes listed in the first column.

Property	Crystals [262]	Quasicrystals [269, 179, 180, 34, 76]	Stacked-slider phases	Disordered ground states of stealthy potentials [328, 329, 26, 27, 325]	Liquid crystals [47]	Liquids [289]
periodicity	✓	✗	✗	✗	✗	✗
positive shear modulus	✓	✓	✗	✗	✗	✗
hyperuniformity	✓	✓	✓	✓	✗	✗
anisotropy	✓	✓	✓	✗	✓	✗
long-range orientational order	✓	✓	✓	✗	✓	✗

to have implicit constraints [83], were considered to be stacked-slider phases [27]. However, this study suggests that one-dimensional stealthy ground states in this range are not a typical stacked-slider phase. First, our model only predicts stacked-slider phases if the space dimension d is a sum of two positive integers $d = d_P + d_Q$. This requires that $d \geq 2$. Second, the χ range of the one-dimensional stealthy ground states with implicit constraints is also very different from that of the higher-dimensional stacked-slider phases. We also found that one-dimensional stealthy ground states in this χ range satisfy the relation $f = 1 - 2\chi$ and can be obtained from energy minimizations starting from random initial configurations with 100% success rate; both are characteristics of disordered phases [27].

5.7 Conclusions and Discussion

In this chapter we studied using numerical and theoretical techniques stacked-slider phases, which are metastable states that are part of the ground-state manifold of stealthy potentials at densities in which crystal ground states are favored entropically in the canonical ensemble in the zero-temperature limit [325, 352]. The numerical results suggested analytical models of this phase in two, three and higher dimensions. Utilizing this model, we estimated the size of the feasible region of the stacked-slider phase, finding it to be smaller than that of crystal structures in the infinite-system-size limit, which is consistent with our recent previous work [325, 352]. In two dimensions, we also determined exact expressions for the pair correlation function and structure factor of the analytical model of stacked-slider phases, and analyzed the connectedness of the ground-state manifold of stealthy potentials in this density regime.

Our analytical constructions demonstrate that stacked-slider phases are nonperiodic, statistically anisotropic structures that possess long-range orientational order but have zero shear modulus. Since stacked-slider phases are part of the ground-state manifold of stealthy potentials, they are also hyperuniform. Therefore, stacked-slider phases are distinguishable states of matter that are uniquely different from some common states of matter listed in Table 5.3. Note that distinctions between the attributes indicated in the table may be subtly different. For example, crystals, quasicrystals, and stacked-slider phases all have long-range orientational order, but with different symmetries. While crystals can only have twofold, threefold, fourfold, or sixfold rotational symmetries, quasicrystals have prohibited crystallographic rotational symmetries. Stacked-slider phases generally do not have any rotational symmetry, but the fact that they can be constructed by stacking lower-dimensional stealthy configurations in a higher-dimensional space makes the stacking directions different from the sliding directions, giving them their unique orientational order.

Our understanding of stacked-slider phases is only in its infancy with many open questions. For example, what is the nature of the associated excited states? Can stacked-slider phases emerge from particles interacting with other potentials not necessarily as ground states? Can such phases be entropically favored in some ensemble and with what other phases would it coexist? This is just a partial list of possible of future avenues of research in our understanding of this unusual phase of matter.

5.8 Appendix: Connectedness of Permutations of 2D Stacked-Slider Phase

As discussed in Sec. 5.3, each two-dimensional stacked-slider configuration is connected to a permutation of the rectangular lattice. Therefore, a natural question is whether or not these permutations of the rectangular lattice are also connected through sliding motions. If all permutations of the rectangular lattice are connected, then the entire stacked-slider phase ground-state manifold is connected. We will show that, for a rectangular lattice consisting of A rows and B columns of particles, if each row and each column can slide individually, then all permutations of the rectangular lattice are connected if and only if AB is even. We will number all the particles from 1 to AB. Each permutation will be represented by an $A \times B$ matrix. Three different sliding motions will be frequently used in this section. They are as follows:

- Move the top row of particles to the right by one particle spacing, denoted by $\overset{\rightarrow}{\Rightarrow}$;
- move the leftmost column of particles upward by one particle spacing, denoted by $\overset{\uparrow}{\Rightarrow}$;
- and move the leftmost column of particles downward by one particle spacing, denoted by $\overset{\downarrow}{\Rightarrow}$.

As an example of this notation, for $A = B = 2$, permutations $\begin{pmatrix} 1 & 2 \\ 3 & 4 \end{pmatrix}$ and $\begin{pmatrix} 2 & 1 \\ 3 & 4 \end{pmatrix}$ are connected because

$$\begin{pmatrix} 1 & 2 \\ 3 & 4 \end{pmatrix} \overset{\rightrightarrows}{\Rightarrow} \begin{pmatrix} 2 & 1 \\ 3 & 4 \end{pmatrix}. \tag{5.20}$$

Similarly, permutations $\begin{pmatrix} 1 & 2 \\ 3 & 4 \end{pmatrix}$ and $\begin{pmatrix} 3 & 2 \\ 1 & 4 \end{pmatrix}$ are connected because

$$\begin{pmatrix} 1 & 2 \\ 3 & 4 \end{pmatrix} \overset{\downarrow}{\Rightarrow} \begin{pmatrix} 3 & 2 \\ 1 & 4 \end{pmatrix}. \tag{5.21}$$

So far we have demonstrated that it is possible to swap the two adjacent particles in the first row [by Eq. (5.20)] or the two adjacent particles in the first column [by Eq. (5.21)] for $A = B = 2$. Since the system has translational symmetry, one can swap any two adjacent particles. The swapping of any two nonadjacent particles can be done by a series of adjacent-particle swapping. For example, to swap nonadjacent particles 1 and 4 in $\begin{pmatrix} 1 & 2 \\ 3 & 4 \end{pmatrix}$, one can swap particles 1 and 2, then swap particles 1 and 4, and then swap particles 2 and 4. Finally, since we can swap any two particles, we can connect one permutation to any other permutation by swapping each particle with the particle in its new place. Therefore, all permutations of 2×2 rectangular lattices are connected by row-sliding and column-sliding movements.

Next, we show that one can swap two adjacent particles for $A = 3$ and $B = 4$. To swap the first two particles in the first row, one can perform the following sliding

operations:

$$\begin{pmatrix} 1 & 2 & 3 & 4 \\ 5 & 6 & 7 & 8 \\ 9 & 10 & 11 & 12 \end{pmatrix} \overset{\rightarrow}{\Rightarrow} \begin{pmatrix} 4 & 1 & 2 & 3 \\ 5 & 6 & 7 & 8 \\ 9 & 10 & 11 & 12 \end{pmatrix} \overset{\uparrow}{\Rightarrow} \begin{pmatrix} 5 & 1 & 2 & 3 \\ 9 & 6 & 7 & 8 \\ 4 & 10 & 11 & 12 \end{pmatrix}$$
$$\overset{\rightarrow}{\Rightarrow} \begin{pmatrix} 3 & 5 & 1 & 2 \\ 9 & 6 & 7 & 8 \\ 4 & 10 & 11 & 12 \end{pmatrix} \overset{\downarrow}{\Rightarrow} \begin{pmatrix} 4 & 5 & 1 & 2 \\ 3 & 6 & 7 & 8 \\ 9 & 10 & 11 & 12 \end{pmatrix} \overset{\rightarrow}{\Rightarrow} \begin{pmatrix} 2 & 4 & 5 & 1 \\ 3 & 6 & 7 & 8 \\ 9 & 10 & 11 & 12 \end{pmatrix}$$
$$\overset{\uparrow}{\Rightarrow} \begin{pmatrix} 3 & 4 & 5 & 1 \\ 9 & 6 & 7 & 8 \\ 2 & 10 & 11 & 12 \end{pmatrix} \overset{\rightarrow}{\Rightarrow} \begin{pmatrix} 1 & 3 & 4 & 5 \\ 9 & 6 & 7 & 8 \\ 2 & 10 & 11 & 12 \end{pmatrix} \overset{\rightarrow}{\Rightarrow} \begin{pmatrix} 5 & 1 & 3 & 4 \\ 9 & 6 & 7 & 8 \\ 2 & 10 & 11 & 12 \end{pmatrix}$$
$$\overset{\downarrow}{\Rightarrow} \begin{pmatrix} 2 & 1 & 3 & 4 \\ 5 & 6 & 7 & 8 \\ 9 & 10 & 11 & 12 \end{pmatrix}. \quad (5.22)$$

To swap the first two particles in the first column, one can perform the following sliding operations starting from the third-to-last configuration in Eq. (5.22):

$$\begin{pmatrix} 1 & 3 & 4 & 5 \\ 9 & 6 & 7 & 8 \\ 2 & 10 & 11 & 12 \end{pmatrix} \overset{\downarrow}{\Rightarrow} \begin{pmatrix} 2 & 3 & 4 & 5 \\ 1 & 6 & 7 & 8 \\ 9 & 10 & 11 & 12 \end{pmatrix} \overset{\rightarrow}{\Rightarrow} \begin{pmatrix} 5 & 2 & 3 & 4 \\ 1 & 6 & 7 & 8 \\ 9 & 10 & 11 & 12 \end{pmatrix}. \quad (5.23)$$

Equations (5.22) and (5.23) shows the steps to swap the first two particles in the first row, or the first two particles in the first column, for $A = 3$ and $B = 4$. This can be generalized to any $A > 3$ and any even $B > 4$. The generalization to $A > 3$ is more obvious because the same steps can be directly applied to any A and achieve the same goal. The generalization to larger even B is less obvious. For this case, one needs to repeat the first four operations in Eq. (5.22) $(B/2 - 1)$ times and then

perform the rest of the steps in Eq. (5.22) or (5.23). Since it is possible to swap any two adjacent particles for any A and any even B , from the same argument as the $A = B = 2$ case, all permutations of particles for any A and any even B are also connected. Similarly, all permutations of particles for any even A and any B are also connected because a 90° rotation turns it to the even B case. Therefore, all permutations are connected as long as AB is even.

When AB is odd, not all permutations are connected. This is because none of the sliding operations change the parity of the permutation. Thus, two permutations with different parity cannot be connected with any combinations of sliding operations.

Chapter 6

Transport, Geometrical and Topological Properties of Stealthy Disordered Hyperuniform Two-Phase Systems

6.1 Introduction

A hyperuniform many-particle system is one in which the structure factor approaches zero in the infinite-wavelength limit.[317] In such systems, density fluctuations (measured by the variance of number of particles inside a spherical window) are anomalously suppressed at very large lengths scales, a "hidden" order that imposes strong global structural constraints.[317, 307] All structurally perfect crystals and quasicrystals are hyperuniform,[317, 349] but typical disordered many-particle systems, including gases, liquids, and glasses, are not. Disordered hyperuniform many-particle systems are exotic states of amorphous matter that have attracted considerable recent attention.[317, 349, 74, 347, 149, 18, 173, 77, 177, 136, 142, 66, 68, 341, 211, 95,

325, 328, 352, 353, 28, 216, 307, 343] Materials that are simultaneously disordered and hyperuniform can be regarded to be exotic states of matter that lie between a crystal and a liquid; they behave more like crystals in the manner in which they suppress large-scale density fluctuations, and yet they also resemble typical statistically isotropic liquids and glasses with no Bragg peaks.[325]

An important class of disordered hyperuniform many-particle systems is comprised of the classical ground states of "stealthy potentials,"[328, 325, 352, 353] which are bounded, long-range, pairwise additive potentials designed in Fourier space. These classical ground states are of particular fundamental interest because they can be degenerate and noncrystalline. A nonnegative parameter inversely proportional to the number density, χ, controls the degree of order of such ground states. For $\chi < 0.5$, the ground states are overwhelmingly highly degenerate and disordered. As χ increases above 0.5, long-range translational and rotational order begins to emerge and eventually the system crystallizes. We have previously studied these disordered ground states, and computed their pair correlation functions,[328, 329, 26, 352, 325] structure factors,[328, 329, 26, 352, 325] Voronoi cell volume distribution,[328, 352] and particle-exclusion probabilities.[325]

Some initial studies have demonstrated that stealthy hyperuniform systems are endowed with novel thermodynamic and physical properties. For example, their low-temperature excited states are characterized by negative thermal expansion behavior.[28] It has also been shown that dielectric networks derived from stealthy disordered hyperuniform point configurations possess complete photonic band gaps comparable in size to those of a photonic crystal, while at the same time maintain statistical isotropy, enabling waveguide geometries not possible with photonic crystals as well as high-density disordered transparent materials.[95, 94, 189, 178] However, the determination of physical/chemical properties of stealthy disordered hyperuniform materials is generally an unexplored area of research.

In this chapter, we investigate steady-state and time-dependent diffusion properties of certain decorations of stealthy disordered hyperuniform ground-state point configurations in two and three dimensions. In particular, we derive two-phase heterogeneous media from point configurations by decorating the point configurations with spheres (circles); specifically, all points are circumscribed by spheres of radius a that generally may overlap with one another. By varying the radius, the fraction of space occupied by the spheres will vary. We study the effective transport properties of these disordered two-phase systems, including the effective diffusion coefficient,[305] and static and time-dependent characteristics of diffusion-controlled reactions at the interfaces between the two continuous phases, as well as the trapping rate (or its inverse, the mean survival time) as well as the principal (largest) relaxation time.[245, 308] Quantifying the effective diffusion coefficient is of importance not only because it has direct applications (e.g., diffusion of fuel and oxygen in a fuel cell [351], diffusion tensor magnetic resonance imaging, [266, 327] regulation and metabolism of normal organs, [59, 106] and drug release from porous matrices [175]), but also because its determination translates immediately into equivalent results for the effective thermal and electric conductivity, the effective dielectric constant, and the effective magnetic permeability for reasons of mathematical analogy,[305] and is therefore related to a host of applications. Diffusion-controlled reactions arise in widely different processes, such as heterogeneous catalysis,[22] gas sensor operation,[260] cell metabolism,[252] crystal growth,[336] and nuclear magnetic resonance (NMR).[24, 207, 284]

These transport properties are related to several statistical geometrical and topological characteristics, which we therefore also study. These include the pore-size functions (the distribution of the distance from a randomly chosen location in the void phase to the closest phase boundary),[303] the quantizer error (a moment of the pore-size function, which is related to the principal relaxation time),[308, 303] the order metric τ (a measure of the translational order of point configurations),[325] and

the percolation threshold or the critical radius (the radius of the spheres at which a specific phase becomes connected) of each phase.[250, 184, 234, 235]

We compare the aforementioned physical and geometrical properties of our two-phase system derived from decorated stealthy ground states, as a function of the tuning parameter χ, with those of two other two-phase media: (1) equilibrium disordered (fluid) hard-sphere systems and (2) decorated Poisson point processes (ideal-gas configurations). The former has short-range order that is tunable by its volume fraction but no long-range order. The latter has neither short-range order nor long-range order. Through comparison, we find that some of these quantities are dramatically affected by the degree of long-range order, while other quantities are much more sensitive to the degree of short-range order. Because many of these quantities depend on the density, we re-scale all systems to unit number density to ensure a fair comparison.

Among our major findings, we show that these transport, geometrical and topological properties of our two-phase media are generally distinctly different from those of equilibrium hard-sphere systems and spatially uncorrelated overlapping spheres. At high χ values, the stealthy disordered two-phase media can attain nearly maximal effective diffusion coefficient, while also maintaining isotropy. This novel property could have practical implications, e.g., optimal and isotropic drug release from designed nanoparticles. Stealthy ground states tend to ideal gases configurationally in the $\chi \to 0$ limit. [325] Nevertheless, we find that even in the low-χ regime, our two-phase media have much lower principal relaxation time than that of equilibrium hard-sphere systems of similar degrees of order, indicating that the formation of large holes in the stealthy systems is strongly suppressed. Lastly, we also find that the aforementioned geometrical and topological quantities are strongly correlated with each other.

The rest of the chapter is organized as follows: In Sec. 6.2, we give precise definitions of the stealthy potential and the aforementioned transport, geometrical and

topological quantities. In Sec. 6.3, we present our numerical method to calculate them. We present our results in Sec. 6.4 and conclusions in Sec. 6.5.

6.2 Mathematical Definitions and Background

6.2.1 Preliminaries

This chapter studies properties of point-particle systems as well as two-phase heterogeneous media derived from certain decorations of these point configurations. A point-particle system consists of N point particles with a certain probability density function $P(\mathbf{r}^N)$, where $\mathbf{r}^N \equiv \mathbf{r}_1, \mathbf{r}_2, ..., \mathbf{r}_N$ is the particle positions, in a simulation box of volume v_F under periodic boundary conditions in d-dimensional Euclidean space $\mathbb{R}^d$, where d is 2 or 3. The number density is defined as $\rho = N/v_F$. The "Poisson point process" (also called "ideal gas") is produced by the probability density function $P(\mathbf{r}^N) = v_F^{-N}$ that does not depend on particle positions $\mathbf{r}^N$. The equilibrium hard-sphere point process of radius a is another point process with $P(\mathbf{r}^N)$ equal to a positive constant if the distance between every pair of points is larger than $2a$ and zero otherwise.

A realization of a two-phase medium can be mathematically described as a partition of a domain of space $\mathscr{V} \in \mathbb{R}^d$ with volume V into two separate regions, $\mathscr{V}_1$ and $\mathscr{V}_2$. It is characterized by an indicator function, $\mathcal{I}(\mathbf{x})$, where $\mathbf{x}$ is any position in the two-phase medium. The indicator function $\mathcal{I}(\mathbf{x})$ is one if $\mathbf{x} \in \mathscr{V}_1$ and zero if $\mathbf{x} \in \mathscr{V}_2$. The volume fraction of phase 1 is given by $\phi_1 =< \mathcal{I}(\mathbf{x}) >$, where $< \cdots >$ denotes an ensemble average. That of the other phase is given by $\phi_2 = 1 - \phi_1$. Let $\partial\mathscr{V}$ be the interface between $\mathscr{V}_1$ and $\mathscr{V}_2$, the specific surface, i.e., the total area of $\partial\mathscr{V}$ divided by V, is given by:

$$s =< |\nabla \mathcal{I}(\mathbf{x})| > . \tag{6.1}$$

The two-phase media that we consider here are derived from point configurations by decorating the point configurations with spheres (circles); specifically, each point is circumscribed by a sphere of radius a that generally may overlap with one another. Therefore, it is composed of a void region (phase 1) and a particle region (phase 2). When such a mapping is applied to a Poisson point process, the decorated system is also called "fully penetrable spheres" [235] or "spatially uncorrelated spheres." [184]

6.2.2 Stealthy potentials and their entropically favored ground states

Consider point processes that are obtained from the canonical ensemble probability distribution function defined by

$$P(\mathbf{r}^N) = \exp[-\beta\Phi(\mathbf{r}^N)]/Z, \tag{6.2}$$

where $\Phi(\mathbf{r}^N)$ is an interaction potential, β is the inverse temperature, and $Z = \int \exp[-\beta\Phi(\mathbf{r}^N)]d\mathbf{r}^N$ is the partition function. Of particular interest in this chapter is the "stealthy" interaction potential:

$$\begin{aligned}\Phi(\mathbf{r}^N) &= \frac{1}{2v_F}\sum_{0<\mathbf{k}<K}|\tilde{n}(\mathbf{k})|^2 + \Phi_0 \\ &= \sum_{i<j}\frac{1}{v_F}\sum_{0<\mathbf{k}<K}\exp(i\mathbf{k}\cdot\mathbf{r}_{ij}),\end{aligned} \tag{6.3}$$

where the sum is over all reciprocal lattice vector $\mathbf{k}$'s of the simulation box such that $0 < |\mathbf{k}| \leq K$, $\tilde{n}(\mathbf{k}) = \sum_{j=1}^{N}\exp(-i\mathbf{k}\cdot\mathbf{r}_j)$,

$$\Phi_0 = [N(N-1) - \sum_{0<\mathbf{k}<K} N]/2v_F \tag{6.4}$$

is a constant independent of the particle positions $\mathbf{r}^N$, and the second equal sign in Eq. (6.3) can be proved by Parseval's theorem. Such potential is interesting not only because it is a pairwise additive potential [as the right side of Eq. (6.3) shows], but also because it allows one to directly tune the structure factor

$$S(\mathbf{k}) = |\tilde{n}(\mathbf{k})|^2/N. \tag{6.5}$$

The ground state (i.e., $\beta \to +\infty$ or zero-temperature state) of this potential is obtained by constraining $S(\mathbf{k}) = 0$ for all $0 < |\mathbf{k}| \leq K$.[328, 325]

Let M be half the number of $\mathbf{k}$ points in the summation of Eq. (6.3) [1]; the parameter

$$\chi = \frac{M}{d(N-1)} \tag{6.6}$$

determines the degree to which the ground states are constrained and therefore the degeneracy and disorder of the ground states.[328] For $\chi < 0.5$, the ground states are typically disordered and uncountably infinitely degenerate.[325, 352] Therefore, there are multiple ways to assign different weights (i.e., probabilities) to different sets of ground states. One way of particular interest is the zero-temperature ($\beta \to +\infty$) limit of Eq. (6.2). Ground states drawn from such distribution are called "entropically favored ground states".[325, 352] It is interesting to note that in the $\chi \to 0$ and $a \to 0$ limit, both entropically favored ground states of stealthy potentials and equilibrium hard-sphere point processes tend to Poisson point process geometrically. In the rest of the chapter this fact will be frequently used to test our simulation results since many properties of the Poisson point process have been studied previously.

[1] Since $|\tilde{n}(\mathbf{k})|^2 = |\tilde{n}(-\mathbf{k})|^2$, M is the number of independent constraints.

6.2.3 Transport properties

This chapter studies the following steady-state and time-dependent diffusion properties in phase 1 (the void phase) of decorated entropically favored ground states of stealthy potentials, and compare them with that of decorated Poisson point process and equilibrium disordered (fluid) hard-sphere system at unit number density.

Effective diffusion coefficient

Consider the steady-state diffusion problem of some species with concentration field $c(\mathbf{x})$ in a two-phase medium in which phase 1 is the space in which diffusion occurs and phase 2 are "obstacles" that the diffusing species cannot enter. In phase 1, the flux of the species, $\mathbf{J}(\mathbf{x})$, is predicted by Fick's first law:

$$\mathbf{J}(\mathbf{x}) = D\nabla c(\mathbf{x}),\ \mathbf{x} \in \mathscr{V}_1 \tag{6.7}$$

where D is a diffusion coefficient which we set to unity for simplicity. However, Eq. (6.7) is valid only in phase 1 and has to be paired with the following Neumann boundary condition:

$$\mathbf{n} \cdot \mathbf{J} = 0,\ \text{on}\ \partial\mathscr{V}, \tag{6.8}$$

where $\mathbf{n}$ is the normal vector of the surface. We see that the inclusion of such obstacles adds a complicated boundary condition and makes the overall diffusion problem difficult. Nevertheless, on a length scale much larger than the characteristic length of the obstacles, the system can be homogenized [305] and characterized by an "effective" diffusion coefficient, D_e, defined by the average Fick's first law:

$$< \mathbf{J}(\mathbf{x}) >= D_e < \nabla c(\mathbf{x}) > ,\ \text{for any}\ \mathbf{x} \tag{6.9}$$

where angular brackets denote ensemble averages.

The effective diffusion coefficient of an isotropic two-phase medium must satisfy the Hashin-Shtrikman (HS) upper bound.[129] For our case where phase 1 has unit diffusion coefficient and phase 2 cannot be entered, this bound in d dimensions is given by:

$$D_e \leq \frac{d-1}{d-1+\phi_2}. \tag{6.10}$$

This bound is optimal because it is realizable by certain model microstructures, including the "coated-sphere model" described in Ref. [128], and is therefore the best possible bound for isotropic systems given volume-fraction information only.

Diffusion-controlled reactions

Consider the problem of diffusion and reaction among absorbing "traps" in the random medium. Let phase 1 be the region in which diffusion occurs and phase 2 be the trap region, the diffusion process in phase 1 is governed by the same Fick's first law but with time dependency:

$$\mathbf{J}(\mathbf{x},t) = D\nabla c(\mathbf{x},t), \text{ in } \mathscr{V}_1. \tag{6.11}$$

This equation, combined with the conservation of the diffusing species inside phase 1, $\nabla \cdot \mathbf{J} = \frac{\partial c}{\partial t}$, yields Fick's second law:

$$\frac{\partial c(\mathbf{x},t)}{\partial t} = D \triangle c(\mathbf{x},t), \text{ in } \mathscr{V}_1. \tag{6.12}$$

If phase 2 are absorbing "traps" (rather than impenetrable obstacles as in the aforementioned effective diffusion problem), the boundary condition has to be changed. In the diffusion-controlled limit, i.e., when the reaction rate at the interface is infinite, we have the following boundary condition:[308]

$$c(\mathbf{x},t) = 0, \text{ on } \partial\mathscr{V}. \tag{6.13}$$

If we also set the initial concentration to be uniform outside of traps:

$$c(\mathbf{x}, 0) = c_0, \text{ in } \mathscr{V}_1, \tag{6.14}$$

then we have the survival problem. The "survival probability," $p(t)$ is equal to the fraction of reactant not yet absorbed at time t:[308, 305]

$$p(t) = \frac{\int_{\mathbb{R}^d} c(\mathbf{x}, t) d\mathbf{x}}{\int_{\mathbb{R}^d} c(\mathbf{x}, 0) d\mathbf{x}}. \tag{6.15}$$

The mean survival time of the reactant is the zeroth moment of $p(t)$:[2]

$$T_{mean} = \int_0^\infty p(t) dt. \tag{6.16}$$

The survival probability can be decomposed as a sum of exponential functions:

$$p(t) = \sum_{n=1}^{\infty} I_n \exp(-t/T_n), \tag{6.17}$$

where I_n are coefficients and T_n are relaxation times. The largest relaxation time is called "principal relaxation time" and by convention denoted T_1. These quantities can be measured directly by NMR experiments since in NMR experiment of fluid-saturated porous media, proton magnetization decays mainly on the phase boundary.[284, 24, 207]

It is worth noting that although the above problems involve differential equations, D_e, $p(t)$, and T_{mean} can actually be calculated much more efficiently by simulating Brownian motions using the so-called "first-passage time" technique. (See the Sec. 6.3 for details.) The effective diffusion coefficient can be found from the ratio of the mean square displacement of such Brownian particles and the time spent. The survival

[2]Note that the commonly used notation for the mean survival time is τ [308, 305]. Here, we use T_{mean} to avoid confusion with the order metric τ.

probability $p(t)$ is equal to the probability that a Brownian particle have never reached any trap at time t. The mean survival time, T_{mean}, can be calculated by integrating $p(t)$ but can also be calculated, more easily, by finding the average time needed for a particle to reach a trap the first time. It is also worth noting that while the effective diffusion coefficient is identically zero as long as the void phase is not percolating, T_{mean} and T_1 are both positive until the spheres cover the entire space.[305]

6.2.4 Geometrical and topological properties

We also studies the following geometrical and topological properties that are intimately related to the aforementioned diffusion characteristics.

Hyperuniformity and stealthiness in many-particle systems and two-phase media

As we have explained earlier, a hyperuniform many-particle system is one in which the structure factor, Eq. (6.5), approaches zero in the $\mathbf{k} \to \mathbf{0}$ limit. The name "hyperuniform" refers to an anomalous suppression of density fluctuations: Consider random placements of a spherical observation window of radius R in a d-dimensional many-particle system. The number of points contained in such window, $N(R)$, is a random variable. For a uniform but not hyperuniform many-particle system (e.g., ideal gas without a gravity field), $\sigma_N^2(R)$ for large R scales as R^d. For a hyperuniform system, $\sigma_N^2(R)$ for large R grows more slowly than R^d. It has been proved that the above-mentioned two conditions of hyperuniformity, $\lim_{\mathbf{k}\to\mathbf{0}} S(\mathbf{k}) = 0$ and $\sigma_N^2(R)$ for large R grows more slowly than R^d, are mathematically equivalent.[317]

A similar definition exists for two-phase media.[307] One can compute the volume fraction of either phase inside a spherical observation window of radius R and find its variance. For large R, this variance scales as R^{-d} for typical (non-hyperuniform) random two-phase media and decreases faster than R^{-d} for hyperuniform two-phase

media. An equivalent condition for hyperuniformity is that $\lim_{\mathbf{k}\to\mathbf{0}} \tilde{\chi}_V(\mathbf{k}) = 0$, where

$$\chi_V(\mathbf{k}) = \frac{1}{v_F}|\mathcal{J}(\mathbf{k})|^2 \tag{6.18}$$

is called the "spectral density" and $\mathcal{J}(\mathbf{k})$ is the Fourier transform of $\mathcal{I}(\mathbf{x}) - \phi_1$.[300]

Stealthy hyperuniform many-particle systems or two-phase media are subsets of hyperuniform many-particle systems or two-phase media in which $S(\mathbf{k})$ or $\chi_V(\mathbf{k})$ is zero for a range of $\mathbf{k}$ vectors around the origin, i.e.,

$$S(\mathbf{k}) = 0 \text{ or } \chi_V(\mathbf{k}) = 0 \text{ for } 0 \leq |\mathbf{k}| \leq K, \tag{6.19}$$

where K is some positive number. For the many-particle systems mentioned in this chapter, the ground state of "stealthy" potentials are stealthy and hyperuniform while equilibrium hard-sphere systems and Poisson point process are neither stealthy nor hyperuniform.

Packing and packing fraction

When we decorate a point-particle configuration by replacing points with spheres of radius a, the whole collection of spheres is considered a "sphere packing" if each pair of point particles is separated by a distance of at least $2a$ (i.e., if the spheres do not overlap). The fraction of space occupied by the union of spheres, ϕ_2, is called the packing fraction ϕ_p. Of particular interest in this chapter is the maximum packing radius a_p^{max}, which is half the minimum separation distance between two particles, and maximum packing fraction ϕ_p^{max}, which is the volume fraction of phase 2 when $a = a_p^{max}$.

Why should we study the maximum packing fraction? One important reason is that when we decorate a point configuration and map it into a two-phase medium, if spheres do not overlap, then the spectral density $\tilde{\chi}_V(\mathbf{k})$ of the two-phase medium is

proportional to the structure factor $S(\mathbf{k})$ of the underlying point configuration:[306]

$$\tilde{\chi}_V(\mathbf{k}) = \frac{\phi_2}{v_1(a)} \left(\frac{2\pi a}{|\mathbf{k}|} \right)^d J_{d/2}^2(|\mathbf{k}|a) S(\mathbf{k}) \ (a \leq a_p^{max}), \tag{6.20}$$

where $v_1(a)$ is the volume of a d-dimensional sphere of radius a and $J_{d/2}(x)$ is the Bessel function of order $d/2$. Therefore, a decorated stealthy point configuration is a stealthy two-phase medium if $\phi_2 < \phi_p^{max}$. When $\phi_2 > \phi_p^{max}$, however, Eq. (6.20) no longer holds and we will see in Sec. 6.4.1 that decorated systems are generally no longer stealthy or hyperuniform.

Nearest-neighbor and pore-size functions

Given a point-particle system, the void-exclusion probability $E_V(r)$ is the probability that a spherical cavity of radius r, centered at a random location, is empty of particles. A related quantity is $H_V(r) = -[\partial E_V(r)]/(\partial r)$, the probability density function of the distance to the nearest particle from a randomly chosen location. A different interpretation of E_V is that if each point particle is replaced with a sphere of radius a, then $E_V(a)$ is the volume fraction of the space outside of the spheres, i.e.,

$$E_V(a) = \phi_1 = 1 - \phi_2. \tag{6.21}$$

Since H_V is the negative derivative of E_V, $H_V(a)$ is the specific surface s.[305]

Another quantity related to $E_V(r)$ is the scaled dimensionless quantizer error $\mathcal{G}$. For a point configuration with positions $\mathbf{r}_1, \mathbf{r}_2, \ldots$, a quantizer is a device that takes as an input a position $\mathbf{x}$ in $\mathbb{R}^d$ and outputs the nearest point $\mathbf{r}_i$ of the configuration to $\mathbf{x}$. Assuming $\mathbf{x}$ is uniformly distributed, one can define a mean square error, which can be obtained from $E_V(r)$ via the relation:[303]

$$\mathcal{G} = \frac{2\rho^{\frac{2}{d}}}{d} \int_0^\infty r E_V(r) dr. \tag{6.22}$$

Finally, two more related quantities can be defined for two-phase media. The pore-size cumulative distribution function, $F(\delta)$, is defined as the fraction of pore space (i.e., space covered by phase 1) which has a pore radius larger than δ. The function $F(\delta)$ of our decorated system is trivially related to $E_V(r)$ of the underlying point-particle system:

$$F(\delta) = \frac{E_V(\delta + a)}{E_V(a)}. \tag{6.23}$$

Moreover, the associated pore-size probability density function is given by $P(\delta) = -[\partial F(\delta)]/(\partial\delta)$. This pore-size function at the origin is related to the specific surface, s, by

$$P(\delta = 0) = \frac{s}{\phi_1}. \tag{6.24}$$

It is interesting to note that the moments of $F(\delta)$ are related to the mean survival time and principle relaxation time via the following rigorous lower bounds [308]:

$$T_{mean} \geq \frac{1}{D}\left(\int_0^\infty F(\delta)d\delta\right)^2, \tag{6.25}$$

and

$$T_1 \geq \frac{2}{D}\int_0^\infty \delta F(\delta)d\delta. \tag{6.26}$$

We see that $\mathcal{G}$ is proportional to the first moment of $F(\delta)$ in the $a \to 0$ limit and is therefore related to the principal relaxation time.

Order metric τ

We will be studying the above properties for systems of varying degrees of order. Therefore, it is desirable to have a way to quantify such order. Moreover, since the underlying point-configurations we study include both stealthy ground states, which have long-range order, and equilibrium liquid hard-sphere systems, which have short-range order, we desire an order metric that reflects short-range order and long-range

order equally well. A suitable choice is the order metric τ, introduced in Ref. [325] and defined as:

$$\tau = \frac{1}{D^d}\int_0^\infty [g_2(r)-1]^2 d\mathbf{r} = \frac{1}{(2\pi)^d D^d}\int_0^\infty [S(k)-1]^2 d\mathbf{k}, \tag{6.27}$$

where D is some characteristic length scale, $g_2(r)$ is the pair correlation function,[46] $S(k)$ is the angular average of $S(\mathbf{k})$, and the second equal sign can be proved by Parseval's theorem. In this chapter, we simply let $D = 1$ because we always rescale the configuration to make the number density unity.

Percolation threshold and critical radius

Since the effective diffusion coefficient is trivially zero when the void phase is topologically disconnected, it is important to quantify when the phases are connected. To do this, we will be considering the percolation properties of the systems. As we specified earlier, we map point configurations into two-phase media by replacing each point with a sphere of radius a. For phase 2, the critical or percolation radius, a_{2c}, is the minimum a such that a connected part of phase 2 becomes infinite in size. The percolation volume fraction, ϕ_{2c}, is the fraction of space occupied by the union of spheres of radius a_{2c}.

We can define similar percolation characteristics of the void phase.[248, 231] The percolation radius of the void phase, a_{1c}, is defined as the maximum a such that there is still an infinite-sized connected part of phase 1. The percolation volume fraction, ϕ_{1c}, is the volume fraction of phase 1 at radius a_{1c}. In two dimensions, it is very rare to have both phases percolating simultaneously (see Ref. [271] for such a rare example). In our case, $a_{1c} = a_{2c}$ and $\phi_{1c} = 1 - \phi_{2c}$. In three dimensions, however, both phases can simultaneously percolate, i.e., the two-phase system is bicontinuous.

Indeed, this is the case for our 3D systems and hence we must compute a_{1c} and a_{2c} separately.

6.3 Simulation Details

6.3.1 Generating entropically favored stealthy ground states

We generate entropically favored ground states of stealthy potentials using the same protocol as our previous work.[352] This protocol involves performing molecular dynamics (MD) simulations at a very low temperature ($\beta = 5\times10^5$ in 2D and $\beta = 1\times10^6$ in 3D in dimensionless units), taking snapshots periodically, and performing a local energy minimization starting from each snapshot. Because the MD temperature is sufficiently low, the snapshots before energy minimization are already very close to ground states. Therefore, the ground states produced by the subsequent energy minimization closely follow the canonical distribution in the zero-temperature limit. We generate 20,000 configurations per χ value, same as Ref. [352]. The only two differences between this work and our previous work [352] are (1) system sizes are different (see Appendix A for our choice of system sizes and the justification), and (2) each configuration is rescaled to unit number density (in order to ensure a fair comparison).

6.3.2 Generating equilibrium disordered hard-sphere systems

We also generate equilibrium disordered hard-sphere systems via standard Monte-Carlo techniques in order to compare their statistics with entropically favored stealthy ground states' statistics. Depending on the packing fraction ϕ, an equilibrium hard-sphere system can be disordered (liquid-like) or crystalline. Disordered equilibrium hard-sphere system exists for $0 < \phi < 0.69$ in 2D and $0 < \phi < 0.49$ in 3D.[305]

Therefore, the packing fraction we used include $\phi = 0.05$, 0.1, 0.15, 0.2, 0.25, 0.3, 0.35, 0.4, 0.45, 0.5, 0.55, 0.6, 0.65, and 0.68 in 2D and $\phi = 0.05$, 0.1, 0.15, 0.2, 0.25, 0.3, 0.35, 0.4, 0.45, and 0.48 in 3D. For each ϕ in each dimension, we generate equilibrium hard-sphere systems with $N = 100$, 300, and 500 particles. In each case, the system was first equilibrated with $3 \times 10^6 N$ trial moves. After that, we sample a configuration every $300N$ trial moves until we obtain 20,000 configurations. Similar to the stealthy ground states, we keep the number density $\rho = 1$. Therefore, we adjust sphere radius to attain a desired packing fraction.

6.3.3 Calculating survival probability, mean survival time, and principal relaxation time

Because the method we used to calculate the effective diffusion coefficient is an extension of the method to calculate survival probability and mean survival time, we will explain the latter method first. The survival probability $p(t)$ and mean survival time T_{mean} can be calculated by simulating particles undergoing Brownian motions.

The Brownian motion can be simulated very efficiently using the first-passage-time technique.[312] The key idea of this technique is that for a Brownian particle at a particular location, let $\mathscr{R}$ be the distance between it and the closest phase boundary. Construct a sphere centered at the particle with radius $\mathscr{R}$ (which is called a first-passage-time sphere). Let $t_{\mathscr{R}}$ be the time needed for the particle to reach the surface of such sphere for the first time, the distribution of $t_{\mathscr{R}}$ can be calculated analytically. In 3D, the cumulative distribution function (CDF) of $t_{\mathscr{R}}$ is[312]

$$F(t_{\mathscr{R}}) = 1 + 2\sum_{m=1}^{\infty}(-1)^m \exp\left(-\frac{Dm^2\pi^2 t_{\mathscr{R}}}{\mathscr{R}^2}\right). \tag{6.28}$$

In 2D, Ref. [312] did not provide the distribution of t_R. Here we find the following explicit 2D expression for t_R:

$$F(t_{\mathscr{R}}) = 1 - 2\sum_{m=1}^{\infty} \frac{\exp(-Dw_m^2 t_{\mathscr{R}}/\mathscr{R}^2)}{w_m J_1(w_m)}, \tag{6.29}$$

where $J_n(x)$ is the Bessel function of order n, and w_n is the nth root of $J_0(x)$. The mean of $t_{\mathscr{R}}$, in any dimension, is simply $\mathscr{R}^2/2dD$.

Therefore, the Brownian motion inside the first-passage-time sphere does not need to be simulated in detail. One simply moves the particle to a random location on the surface of such sphere, and increase the time by a certain amount, as detailed below. When calculating the mean survival time T_{mean}, the time increment can simply be $\mathscr{R}^2/2dD$, the mean of $t_{\mathscr{R}}$. When calculating $p(t)$, however, the time increment has to be a random number drawn from the distributions given in Eq. (6.28) or (6.29). The process of finding $\mathscr{R}$, moving the particle, and increasing the time is repeated until the Brownian particle gets very close ($10^{-5}a$) to a trap, at which time the Brownian particle is deemed trapped. In our implementation, Eqs. (6.28)-(6.29) are pre-computed and tabulated to accelerate the simulation. For each configuration, we simulate 10 Brownian trajectories to calculate T_{mean} and 1000 trajectories to calculate $p(t)$. When calculating $p(t)$, each trajectory is additionally sampled 100 times, with different random time increments drawn from distributions (6.28)-(6.29).

After calculating $p(t)$, we calculate the principal relaxation time T_1 by fitting $p(t)$ in the range $10^{-5} < p(t) < 10^{-3}$ to the asymptotic equation

$$\ln[p(t)] \approx c + t/T_1, \tag{6.30}$$

where c and T_1 are fitting parameters.

6.3.4 Calculating effective diffusion coefficient

The effective diffusion coefficient D_e can also be calculated using first-passage-time techniques. [159, 161, 313] In this case, however, the Brownian particle cannot be deemed trapped when it is sufficiently close to the phase boundary because phase 2 is now non-absorbing obstacles rather than absorbing traps. Instead, we construct a first-passage-time sphere of radius $\mathscr{R} = 10^{-2}$, find a random place on the surface of the first-passage-time sphere that is outside of the obstacle phase, and move the Brownian particle to that random place. Although this first-passage-time sphere contains two phases, the mean time taken for the Brownian particle to reach such surface could still be computed analytically and was given in Ref. [161]:

$$t_{\mathscr{R}} = \frac{\mathscr{R}^2(1 + v_2/v_1)}{2d}, \tag{6.31}$$

where v_2/v_1 is the volume of the obstacle phase divided by the volume of the conducting phase inside the first-passage-time sphere and can be found analytically.

The process of constructing a first-passage-time sphere and moving the point particle is repeated to form a Brownian trajectory. In the infinite-time limit, the effective diffusion coefficient is given by:[161]

$$D_e = \lim_{t\to\infty} \frac{< |\mathbf{R}(t)|^2 >}{2dt}, \tag{6.32}$$

where $< |\mathbf{R}(t)|^2 >$ is the mean-squared displacement of a Brownian particle at time t. In practice, in a finite-time simulation, one should only consider the time regime in which the mean square displacement is strongly linear in time, since for sufficiently early times the mean square displacement is either ballistic or grows faster than linear in time.[313] We find D_e by fitting $< |\mathbf{R}(t)|^2 >$ versus t and extracting the slope of the line after some sufficiently large dimensionless time. We define the unit of time

to be

$$t^* = \frac{1}{\rho^{2/d} D}, \tag{6.33}$$

and set both ρ and D to be unity. The point in time in which $< |\mathbf{R}(t)|^2 >$ first becomes a strongly linear function occurs when the Brownian particle sufficiently samples the two-phase system such that it can be viewed effectively as Brownian motion in a homogeneous medium. For the microstructures that we considered here, we find that the linear regime occurs in the dimensionless time interval $40 < t < 100$, i.e., we determine D_e from the linear relationship

$$< |\mathbf{R}(t)|^2 >= (2dD_e)t + c, \ 40 < t < 100. \tag{6.34}$$

To get a sense of the possible behaviors of the mean square displacements as a function of time, we show examples in Fig. 6.1 at several values of a for a three-dimensional system at $\chi = 0.1333\cdots$ and indicate the linear fit in each case. This fitting procedure works especially well near percolation, which is the most difficult regime to simulate. For this particular system, the void phase stops percolating at obstacle radius $a_{1c} = 0.80$. Figure 6.1 shows that for $a = 0.7 < a_{1c}$, $< |\mathbf{R}(t)|^2 >$ is linear with t. For $a = 0.8 = a_{1c}$, only a fraction of configurations still have a percolating void phase, and our fitting procedure was able to distinguish the initial uprise in $< |\mathbf{R}(t)|^2 >$ (contributions mainly from Brownian particles moving inside a "cage", i.e., a disconnected part of the void phase) from the steady increase in $< |\mathbf{R}(t)|^2 >$ (contributions from Brownian particles that are in a percolating part of the void phase). For $a = 0.9 > a_{1c}$, all Brownian particles are caged, and the fit has a virtually zero slope (and therefore produces a virtually zero D_e).

We simulate 1 Brownian trajectory per configuration to calculate D_e. In Fig. 6.2, we compare the computed D_e with the distribution of the void-phase percolation threshold and find that D_e becomes zero right after all configurations stop percolat-

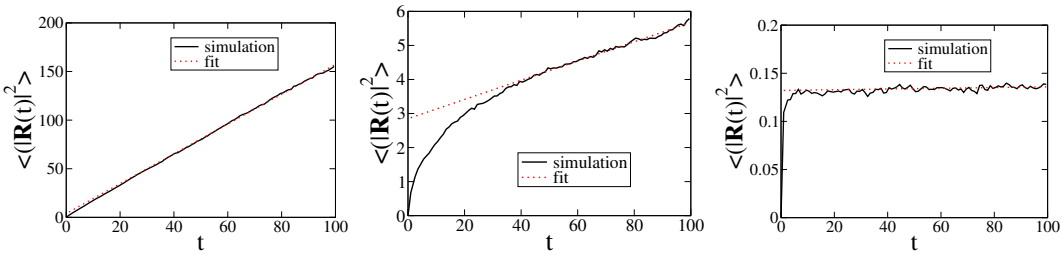

Figure 6.1 The mean square displacement of Brownian particles, averaged over 20,000 configurations, $< |\mathbf{R}(t)|^2 >$, versus time, t, for a three-dimensional system at $\chi = 0.1333\cdots$ with obstacle radii $a = 0.7$ (left), 0.8 (middle), and 0.9 (right). For this particular system, the percolation threshold of the void phase is $a_{1c} = 0.80$, and hence D_e must vanish for larger values of a.

ing. The fact that our measured D_e diminishes to zero at the percolation threshold indicates that our choice of the fitting range in Eq. (6.34) is appropriate.

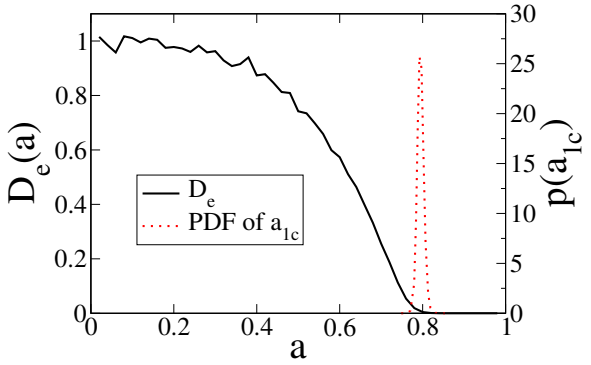

Figure 6.2 Comparing the calculated effective diffusion coefficient, D_e, with the probability density function (PDF) of the void-phase percolation threshold, $p(a_{1c})$, for three dimensions, $\chi = 0.1333$. The calculated D_e becomes zero when the void phase stops percolating.

6.3.5 Calculating percolation thresholds

Generally speaking, the precise calculation of the percolation threshold of disordered systems require very large system sizes. For example, to accurately determine the percolation threshold of 3D fully penetrable spheres, Ref. [184] employed systems of up to $N = 7 \times 10^8$ particles. The whole system is divided into smaller cubes and the content particles in each cube is generated only when such cube is being probed.

Unfortunately, our protocol of low-temperature MD and a subsequent energy minimization does not allow us to save time by only generating required parts of the configuration. Moreover, in order to accurately follow the canonical-ensemble distribution at zero-temperature limit, the MD temperature has to be so low such that many (7.5×10^7) time steps are required to produce a sufficiently long trajectory. The requirement of a very large number of time steps forces us to further sacrifice system size. As a result, our system is limited to several hundred particles. Therefore, accurate determination of the percolation threshold is extremely challenging. Thus we experimented with two advanced algorithms to minimize finite-size effect in order to obtain relatively accurate results. We will first explain how to use these two methods to determine the percolation threshold for the particle phase, and then describe the generalizations to the void phase.

One of them, which we call "P_1 maximum method," is described in Ref. [213]. Starting from a random particle in a configuration, one randomly chooses two of its periodic images in two different directions. The quantity P_1 (denoted as $R_\infty^{(1)}$ in Ref. [213]) is defined as the probability that this particle is connected to one of the chosen periodic images but not the other. At the percolation threshold, P_1 attains its maximum. Therefore, one can numerically find P_1 as a function of sphere radius a and find its maximum in order to find the percolation threshold. In our implementation, we calculate $P_1(a)$ for various a's starting from $a = 0$, with increment $\delta a = 0.001$, until $P_1(a)$ develops a peak and then returns to zero. We then select all data points such that $P_1(a) > 0.9 \cdot P_1^{max}$, where P_1^{max} is the maximum of $P_1(a)$, and perform a quadratic fit of the selected data points. The maximum of the fitted function gives the percolation radius a_{2c}.

Ref. [213] measures the percolation radii a_{2c} using several different system sizes and then extrapolates to the infinite-system-size limit. However, when we perform the same fitting procedure using different system sizes, we did not find a clear trend:

In each dimension, for some χ values larger systems produces larger a_{2c} while for other χ values larger systems produces smaller a_{2c}. Moreover, the extrapolated a_{2c}, as a function of χ, is not as smooth as the un-extrapolated one. We therefore conclude that random noise is probably more important than finite-size effect in this case and extrapolation is not proper. Thus, we will simply use a_{2c} of our largest system as an estimate of the infinite-system-size a_{2c}.

After finding the percolation radius a_{2c}, we determine the percolation volume fraction ϕ_{2c}. One could have simply read this quantity from a plot of the quantity $E_V(r)$, since $\phi_{2c} = 1 - E_V(a_{2c})$. However, we decide to use a somewhat more accurate method: we divide the whole simulation box into 12000×12000 pixels (in 2D) or 1200×1200×1200 voxels (in 3D) and find out if the center of each pixel or voxel is inside any sphere of radius a_c. We then count the number of pixels or voxels that are centered inside spheres to find out the volume fraction. From our experience, this procedure gives us a four-significant-figures precision in ϕ_c.

The other method we employed, which we call "M_2 intersection method," is introduced in Ref. [360]. At a given radius a, define s_{max} to be the size of the largest cluster, M_2 (denoted as R_2 in Ref. [360]) is defined as:

$$M_2 = \frac{\langle s_{max}^2 \rangle - \langle s_{max} \rangle^2}{\langle s_{max} \rangle^2}, \tag{6.35}$$

where $\langle \cdots \rangle$ denotes an ensemble average. As Ref. [360] shows, at the percolation threshold, M_2 is the same for different system sizes. Therefore, one can compute M_2 as a function of a, and find the intersection of $M_2(a)$ for different system sizes to find a_{2c}. Following Ref. [360], we use three different N's for each χ value, and perform an extrapolation to find a_{2c} in the infinite-N limit. After that, we use the same procedure discussed in the previous paragraph to calculate ϕ_{2c} from a_{2c}.

We have used both methods to calculate the percolation volume fraction ϕ_{2c} of decorated stealthy ground states at various χ's in 2D and 3D. They are presented in Fig. 6.3. Figure 6.3 also presents ϕ_{2c} for decorated Poisson point processes obtained from Refs. [184] and [234], which are $\phi_{2c} = 0.676339$ in 2D and $\phi_{2c} = 0.289573$ in 3D. These results can be used as benchmarks since Poisson point processes are geometrically equivalent to entropically favored stealthy ground states at $\chi = 0$. We see that in 2D, while both methods give results that approaches the Poisson value very well in the $\chi \to 0$ limit, the P_1 maximum method produces much smoother results. In 3D, however, although both methods produce relatively smooth results, only results from the M_2 intersection method approaches the Poisson value very well in the $\chi \to 0$ limit. Therefore, we decide to choose the P_1 maximum method in 2D and the M_2 intersection method in 3D for the rest of the chapter. It is interesting to note that to our knowledge, the P_1 maximum method has been demonstrated to work well in 2D [213] but not in 3D, while the M_2 intersection method has been demonstrated to work well in 3D [360] but not in 2D. It is possible that these two methods are just more suited to their respective dimensions.

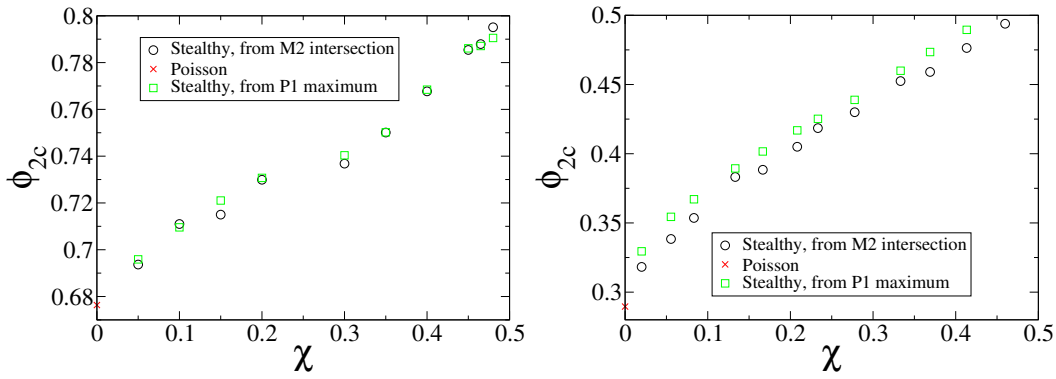

Figure 6.3 Particle-phase percolation volume fraction ϕ_{2c} of entropically favored stealthy ground states at different χ's in 2D (left) and 3D (right).

Besides the percolation threshold of the spheres, we also study the percolation threshold of the void phase. In two dimensions, the percolation radius of the void

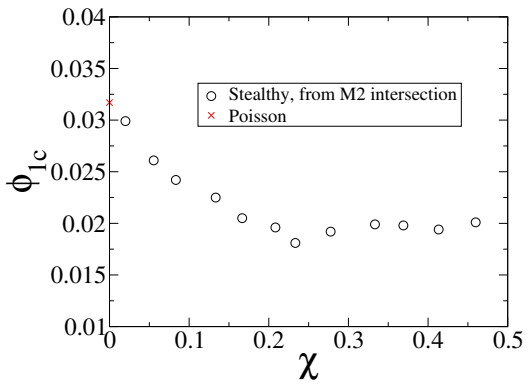

Figure 6.4 Void-phase percolation volume fraction ϕ_{1c} of entropically favored stealthy ground states at different χ's in 3D.

phase, a_{1c}, is equal to the percolation radius of the spheres, a_{2c}. In three dimensions, however, a_{1c} has to be calculated separately. We compute a_{1c} in three dimensions by performing a Voronoi tessellation of each configuration, and then computing M_2 of the Voronoi vertices. As in the particle-phase case, the intersection of $M_2(a)$ at different system sizes gives a_{1c}. Similar to the particle-phase case, a_{1c} can then be converted to ϕ_{1c} by digitization, the result of which is presented in Fig. 6.4. Similar to the particle-phase case, we compare ϕ_{1c} for our systems with that for the decorated Poisson point processes obtained from Ref. [231], $\phi_{1c} = 0.0317$. Combining the ϕ_{2c} and ϕ_{1c} results, we see that as χ increases from 0 to 0.46, the ϕ_2 range for bicontinuity moves upwards, from $0.290 < \phi_2 < 0.997$ to $0.494 < \phi_2 < 0.998$, respectively.

6.3.6 Calculating $E_V(r)$, $\mathcal{G}$, and τ

The quantities $E_V(r)$ and $\mathcal{G}$ are calculated by first computing $H_V(r)$. For each configuration of N point particles, $100N$ random locations in 2D or $10N$ random locations in 3D are generated in the simulation box. For each location, the distance from it to its nearest particle is found. These distances are then binned to yield $H_V(r)$. We then integrate $H_V(r)$ using trapezoidal rule to find $E_V(r)$. The quantizer error $\mathcal{G}$ is obtained by another integration of $rE_V(r)$, using trapezoidal rule, as Eq. (6.22)

shows. The numerically obtained $H_V(r)$ always have compact support, and thus the above-mentioned integrations does not need to be truncated.

The order metric τ can be computed from either $g_2(r)$ or $S(k)$, as Eq. (6.27) shows. We have tried both approaches. The real-space integration in Eq. (6.27) is truncated at half the simulation box side length and the reciprocal space integration in Eq. (6.27) is truncated at $6K$, where K is the cutoff of the stealthy potential (as detailed in Sec. 6.2.2).

6.4 Results

We present visualizations of our two-phase systems derived from decorated stealthy ground states in Figs. 6.5 - 6.7. In three dimensions, we present separate figures for the particle phase and the void phase for clarity. In the rest of the section, we present the above-mentioned properties of our two-phase systems, and compare them with decorated Poisson point process and hard-sphere point process.

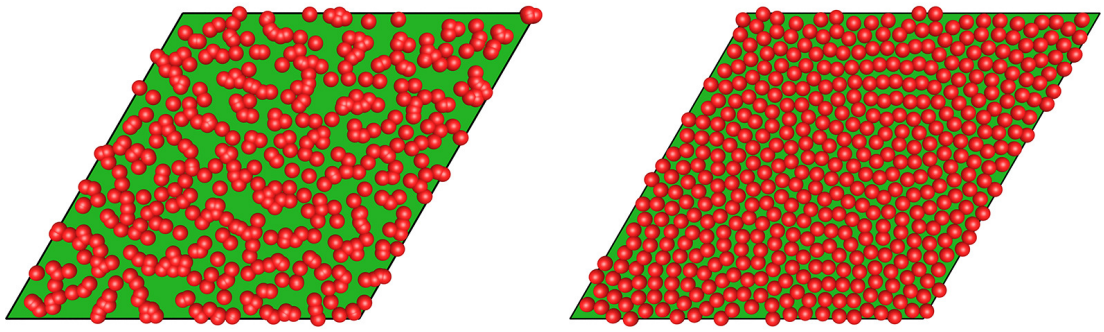

Figure 6.5 Decorated stealthy ground states in two dimensions at $\chi = 0.05$ (left) and $\chi = 0.48$ (right), at $a = 0.5$. The void phase is marked green.

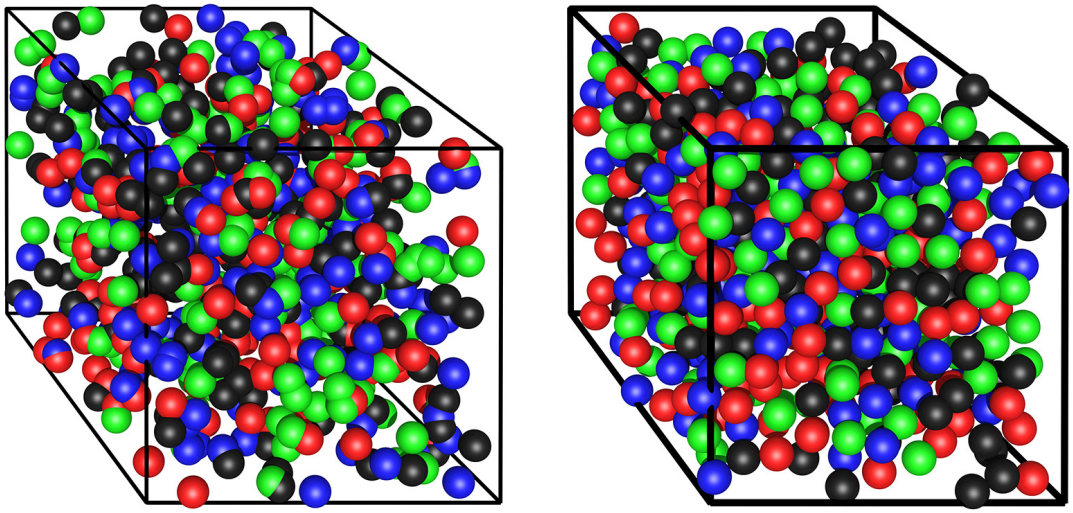

Figure 6.6 Decorated stealthy ground states in three dimensions at $\chi = 0.02$ (left) and $\chi = 0.4598...$ (right), at $a = 0.5$. Each sphere is randomly assigned to one of four colors in order to improve visual clarity.

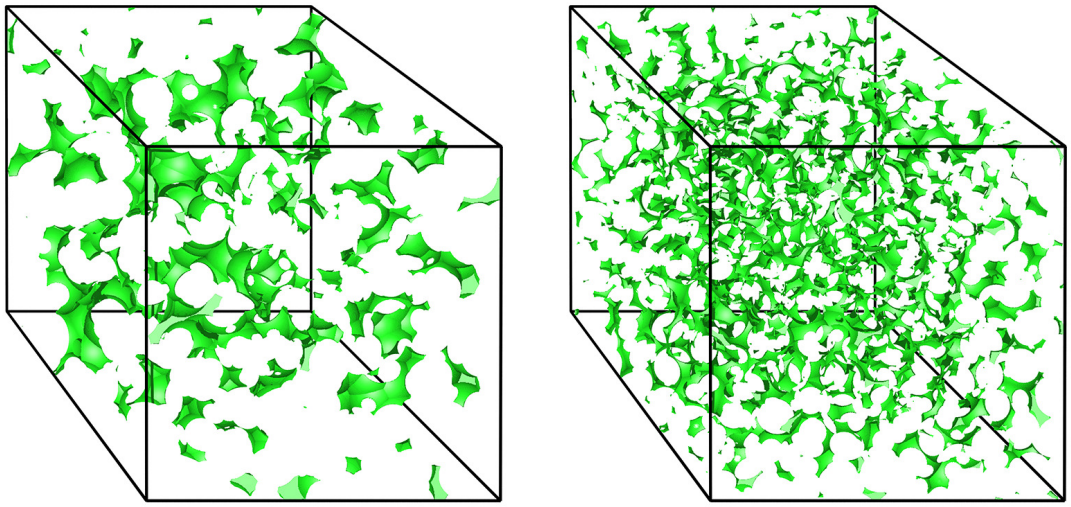

Figure 6.7 Void phase in decorated stealthy ground states in three dimensions at $\chi = 0.02$ (left) and $\chi = 0.4598...$ (right), at the void-phase percolation threshold $a_{1c} = 0.8970$ (left) or 0.6992 (right).

6.4.1 Packing fraction and stealthiness

We present the maximum packing fraction of decorated stealthy ground states, ϕ_p^{max}, in Fig. 6.8. In each dimension, as χ increases, ϕ_p^{max} remains to be zero for χ up to about 0.3 and then start to increase. This indicates that for $\chi \leq 0.3$, particles in entropically favored stealthy ground states can become arbitrarily close to each other. As χ becomes higher, particles develop an effective hard core that are impenetrable. The development of such hard core was also observed in Ref. [328].

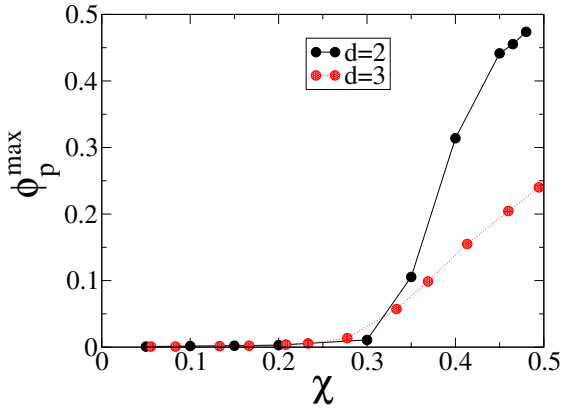

Figure 6.8 Maximum packing fraction ϕ_p^{max}, averaged over all configurations, of decorated stealthy ground states in two and three dimensions as a function of χ.

When we decorate a stealthy ground state and map it into a two-phase medium, if $\phi_2 \leq \phi_p^{max}$, then Eq. (6.20) ensures that the resulting two-phase medium is also stealthy. However, if $\phi_2 > \phi_p^{max}$, will the resulting two-phase medium also be stealthy or hyperuniform? To answer this question, we decorated a two-dimensional stealthy ground state of $N = 111$ particles at $\chi = 0.45$ with several different sphere radii a, digitized the resulting two-phase medium into 10000×10000 pixels, and calculated the spectral density $\tilde{\chi}_V(k)$ using Eq. (6.18). The result is presented in Fig. 6.9. For this particular system, the maximum packing radius is $a_p^{max} = 0.407$. We see that for $a < a_p^{max}$, $\tilde{\chi}_V(k)$ is zero for $k < 4.7$. For $a > a_p^{max}$, however, $\tilde{\chi}_V(k)$ is positive

and does not tend to zero as $k \to 0$. Therefore, a decorated stealthy ground state is generally neither stealthy nor hyperuniform if $\phi_2 > \phi_p^{max}$.

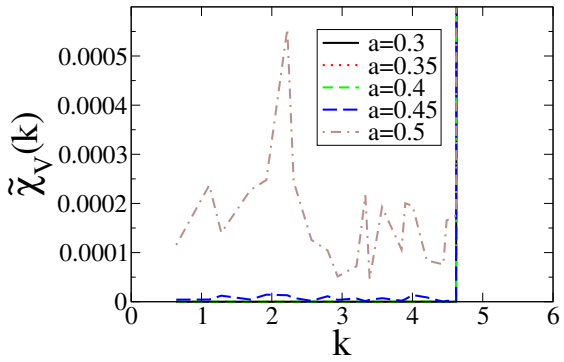

Figure 6.9 Spectral density $\tilde{\chi}_V(k)$ of a two-phase medium obtained from decorating a two-dimensional stealthy ground state with $N = 111$ particles at $\chi = 0.45$ with several different sphere radii a.

6.4.2 Effective diffusion coefficient

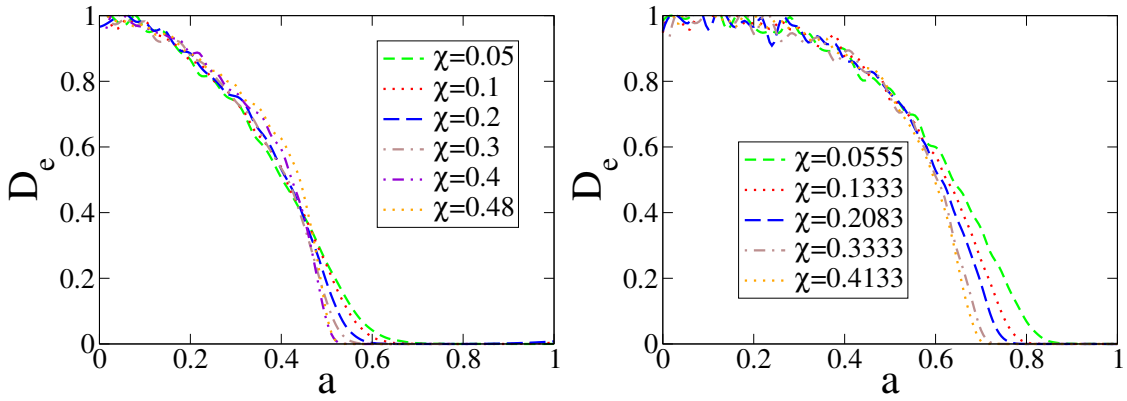

Figure 6.10 The effective diffusion coefficient, D_e, for our two-phase systems derived from decorated stealthy ground states in two (left) and three (right) dimensions as a function of sphere radius a. The number density ρ is fixed to be unity.

We present the calculated effective diffusion coefficient for our two-phase systems derived from decorated stealthy ground states in Fig. 6.10. It is interesting to note that in two dimensions, the curves of $D_e(a)$ cross over each other for different values of χ: while for smaller a higher χ produces a higher D_e, for larger a higher χ produces

a smaller D_e. An explanation for such phenomenon will be presented in the next paragraph.

It is also useful to plot D_e versus the particle-phase volume fraction, ϕ_2, by mapping a to ϕ_2 using Eq. (6.21). We present such plots in Fig. 6.11. These plots show that higher χ values (more ordered arrangements of the obstacle phase) always produce higher D_e at the same volume fraction, which is consistent with our intuition: a more ordered arrangement of the obstacles leaves more space between them, and produces a higher D_e. So why did we see the opposite relationship between χ and D_e in Fig. 6.10, except for smaller a in 2D? It turns out that a lower χ induces more overlap between the spherical obstacles and thus results in a lower ϕ_2. This in turn produces a higher D_e.

With D_e plotted versus ϕ_2, it is interesting to compare our result with the HS upper bound given in Eq. (6.10). We make such comparison in Fig. 6.11. Our result is consistent with the upper bound for any χ and ϕ_2 except for small fluctuations, but the bound is sharp only for smaller ϕ_2.

If it is desired to find structures that maximizes D_e, then any one of the degenerate structures that achieves the HS bound is optimal. We see that our two-phase systems derived from decorated stealthy ground states at very high χ's are very close to being optimal for ϕ_2 up to 0.4-0.5. In two dimensions, this ϕ_2 range coincides with ϕ_p^{max} at high χ's. Since decorated stealthy ground states loses stealthiness as ϕ_2 increases beyond ϕ_p^{max}, our results suggest that a loss of stealthiness causes D_e to stop being optimal. In three dimensions, however, D_e is less sensitive to structures. Thus, although decorated stealthy ground states (at high χ's) stops being a packing at around $\phi_2 = 0.2$, D_e does not deviate from the optimal value until about $\phi_2 = 0.5$. Our observation that D_e is less sensitive to structures in 3D than in 2D is consistent with the trends indicated in Ref. [299], which found that in the infinite-d limit, D_e is

given exactly by the arithmetic average of the diffusion coefficients of the two phases (weighted by their volume fraction), independent of the structure.

In Fig. 6.11 we also present D_e of decorated lattice structures (i.e., periodic arrays of spherical inclusions). Since these lattice structures are stealthy with even higher χ values, unsurprisingly, their D_e sticks with the HS upper bound for an even larger ϕ_2 range.

Lastly, we would like to mention a difference between the support of D_e as a function of ϕ_2 in 2D versus 3D. While D_e for for our two-phase systems in 2D diminishes to zero at $\phi_2 \approx 0.8$, in 3D D_e does not vanish until $\phi_2 \approx 0.97$. This difference emerges from the difference in the topological (connectedness) characteristics of the void phase between these dimensions.

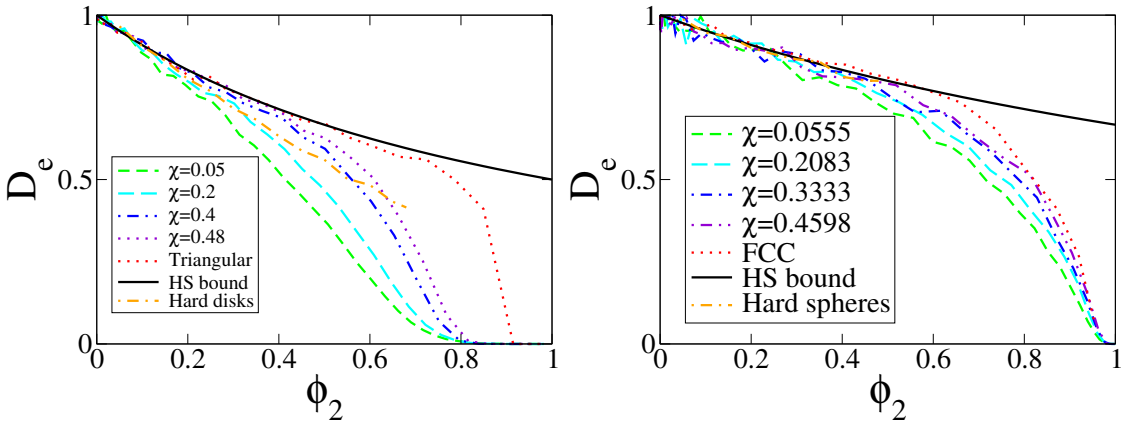

Figure 6.11 The effective diffusion coefficient, D_e, for our two-phase systems derived from decorated stealthy ground states in two (left) and three (right) dimensions as a function of particle-phase volume fraction ϕ_2. The number density ρ is fixed to be unity. The optimal Hashin-Shtrikman (HS) upper bound, D_e for triangular lattice and face-centered cubic (FCC) lattice, and D_e for equilibrium hard disks and spheres are also plotted.

6.4.3 Survival probability and mean survival time

We have computed the mean survival time, T_{mean}, of a diffusing reactant with unit diffusion coefficient, in our two-phase systems derived from decorated stealthy ground states. These results are summarized in Fig. 6.12. For comparison, the same quantity

for equilibrium disordered hard-sphere systems are also included. Clearly, increasing order (increasing χ for stealthy ground states or increasing ϕ_2 for hard spheres) suppresses T_{mean}. However, there is a crossover between the curves for stealthy ground states and that for equilibrium disordered hard spheres. This crossover is expected because as ϕ_2 increases, an equilibrium hard-sphere system becomes more ordered, and therefore comparable to a stealthy two-phase medium with a higher χ. In Fig. 6.13, we plot T_{mean} versus χ for $\phi_2 = 0.2$ and 0.5. We see that in 2D, T_{mean} is somewhat more sensitive to χ than in 3D.

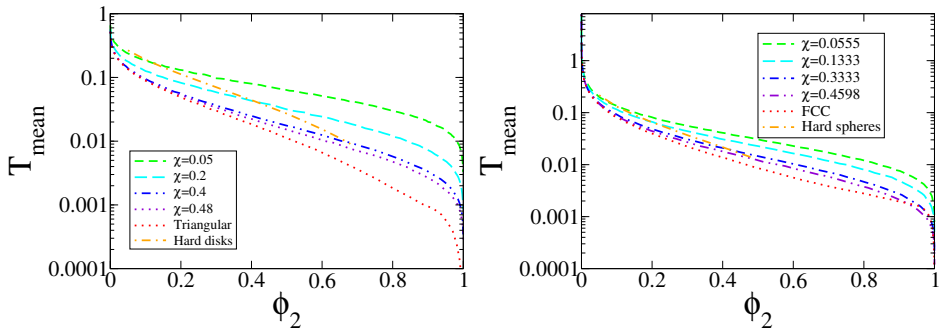

Figure 6.12 The mean survival time, T_{mean}, as a function of particle-phase volume fraction ϕ_2, for our two-phase systems derived from decorated stealthy ground states in 2D (left) and 3D (right). The same quantity for equilibrium disordered hard-sphere system is also included for comparison. The number density ρ is fixed to be unity.

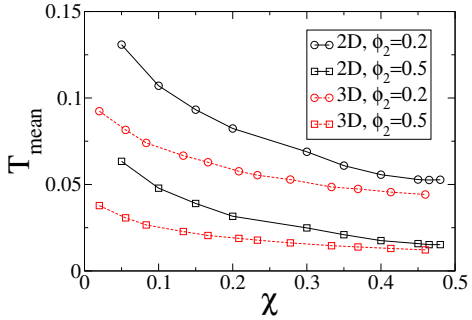

Figure 6.13 The mean survival time T_{mean} for our two-phase systems derived from decorated stealthy ground states in two and three dimensions at phase 2 volume fraction $\phi_2 = 0.2$ and 0.5. The number density ρ is fixed to be unity.

In Fig. 6.14 we present the survival probability, $p(t)$, at $\phi_1 = 0.5$, for our two-phase systems derived from decorated stealthy ground states and equilibrium disordered hard spheres. The same crossover phenomenon also appears here, suggesting that the long-range order possessed by stealthy ground states suppresses $p(t)$ at large t more efficiently, while the short-range order possessed by equilibrium disordered hard spheres suppresses $p(t)$ at small t more efficiently.

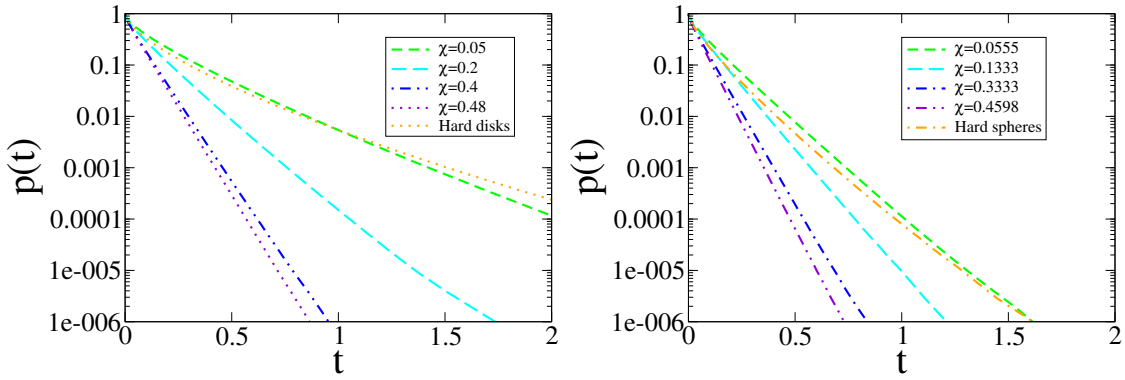

Figure 6.14 The survival probability $p(t)$ for our two-phase systems derived from decorated stealthy ground states in 2D (left) and 3D (right) at phase 2 volume fraction $\phi_2 = 0.2$. The same quantity for equilibrium disordered hard-sphere system is also included for comparison. The number density ρ is fixed to be unity.

In Fig. 6.15 we present the principal relaxation time T_1 for our two-phase systems derived from decorated stealthy ground states. It turns out that T_1 is much more sensitive to χ in 2D than in 3D. More interestingly, one can compare T_1 of stealthy ground states and equilibrium disordered hard disks at the same order metric τ. We present such comparison in Fig. 6.16. In two dimensions, one can see that at $\phi_2 = 0.2$, T_1 of equilibrium disordered hard disks is much higher than that of our two-phase systems derived from decorated stealthy ground states with similar τ's. As we explained earlier, T_1 is related to the pore-size distribution. Therefore, our results suggest that hyperuniformity suppresses the formation of large holes, even in the very disordered regime. As ϕ_2 increases to 0.5, however, the difference between the two systems diminishes. Our finite-sized simulation results suggest that at this value of

ϕ_2, even equilibrium hard-sphere systems suppress the formation of large holes very well. [3]

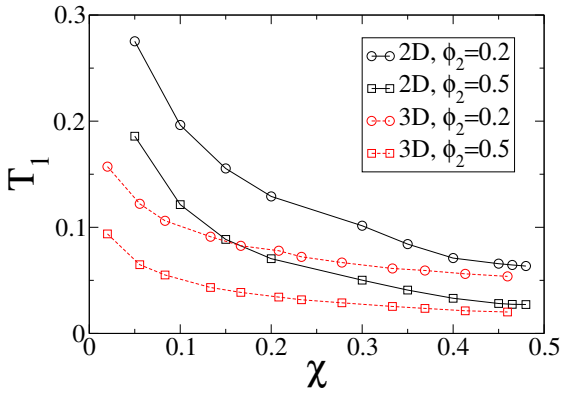

Figure 6.15 Principal relaxation time T_1 for our two-phase systems derived from decorated stealthy ground states in two and three dimensions at phase 2 volume fraction $\phi_2 = 0.2$ and 0.5. The number density ρ is fixed to be unity.

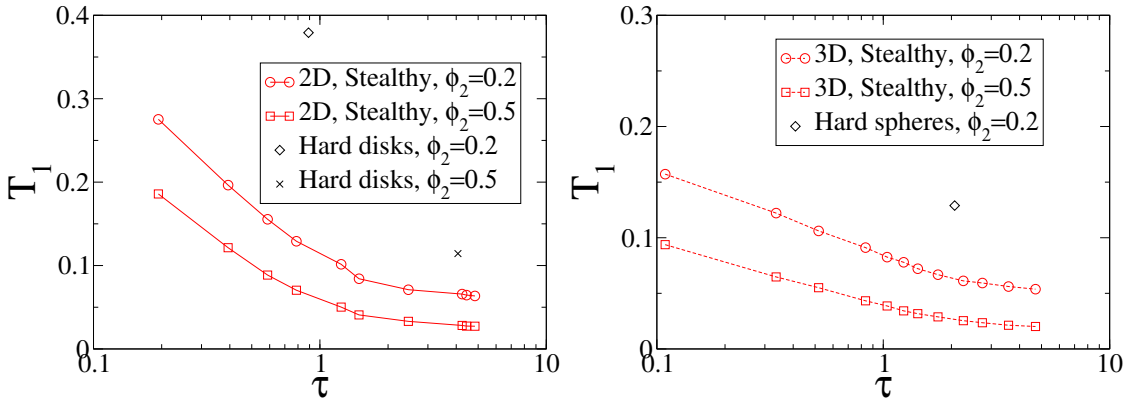

Figure 6.16 Principal relaxation time T_1 for our two-phase systems derived from decorated stealthy ground states and equilibrium disordered hard spheres in 2D (left) and 3D (right) at volume fraction $\phi_2 = 0.2$ and 0.5. The number density ρ is fixed to be unity.

[3] We should clarify that in the infinite-system-size limit, T_1 of equilibrium disordered hard-sphere systems is actually infinite because of a non-zero probability of forming arbitrarily large holes (i.e., $P(\delta)$ is non-zero for arbitrarily large δ). [308] For finite-sized systems, however, T_1 is finite. For decorated stealthy ground states, it is unclear whether or not T_1 would be infinite in the infinite-system-size limit.

6.4.4 Geometrical and topological properties

The percolation volume fraction for both phases in 2D and 3D was already presented in Fig. 6.3 and 6.4. The void-exclusion probability $E_V(r)$, quantizer error $\mathcal{G}$, and order metric τ are presented in Figs. 6.17-6.19. We see that in each dimension, as χ increases, ϕ_c increases, $E_V(r)$ at any r decreases, $\mathcal{G}$ decreases, and τ increases.

The order metric τ can be computed from either $g_2(r)$ or $S(k)$, as shown in Fig. 6.19. In 2D, the results from these two approaches have good consistency. However, in 3D, τ computed from $g_2(r)$ is often slightly lower than τ computed from $S(k)$. We discovered that this is because $g_2(r)$ is still oscillating around 1 at half the simulation box side length, where the integration in Eq. (6.27) has to be cut off. Therefore, such a cutoff should make τ computed from $g_2(r)$ too low. We thus use τ computed from $S(k)$ in the rest of the chapter. It is seen that τ is very sensitive at detecting the rise in short-range and long-range order as χ increases.

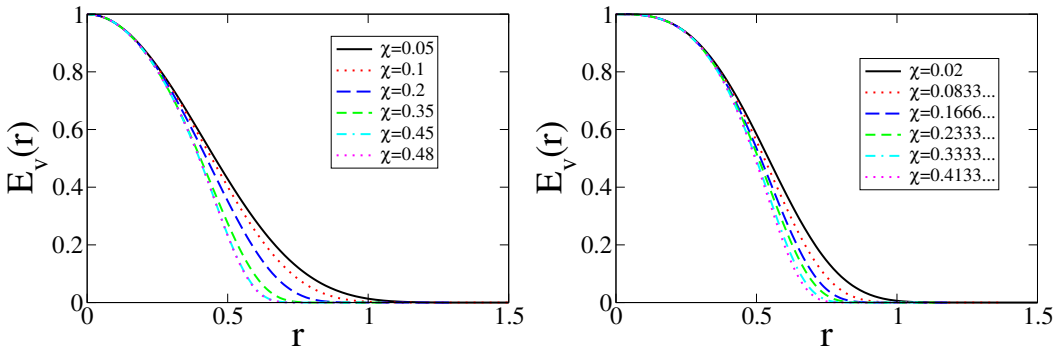

Figure 6.17 Void-exclusion probability $E_V(r)$ of entropically favored stealthy ground states in two (left) and three (right) dimensions at unit number density.

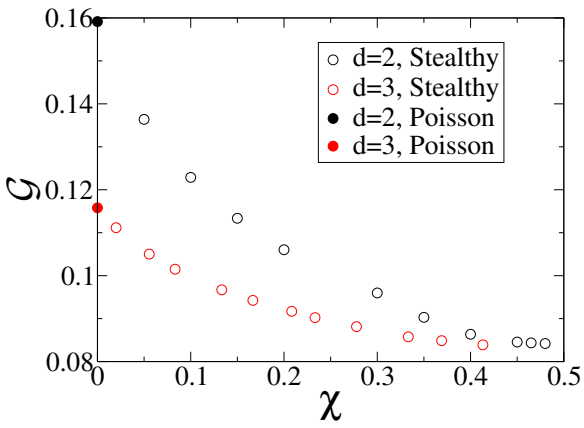

Figure 6.18 Quantizer error $\mathcal{G}$ of entropically favored stealthy ground states in two and three dimensions at unit number density.

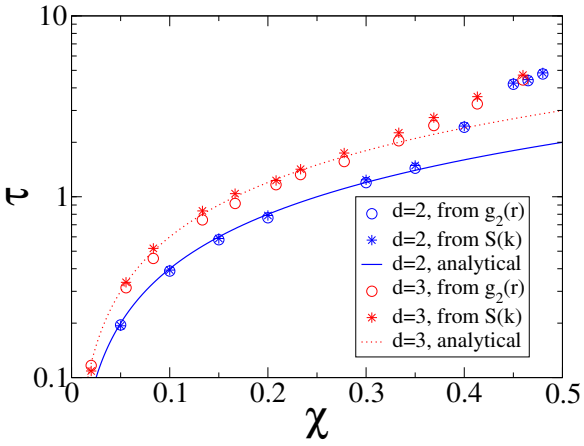

Figure 6.19 Order metric τ of entropically favored stealthy ground states in two and three dimensions at unit number density, calculated from pair correlation function $g_2(r)$ and structure factor $S(k)$. We also include an analytical approximation for τ, given in Ref. 18, which is $\tau = 2d\chi$.

6.4.5 Correlations between geometrical properties, and comparison with equilibrium disordered hard-sphere systems

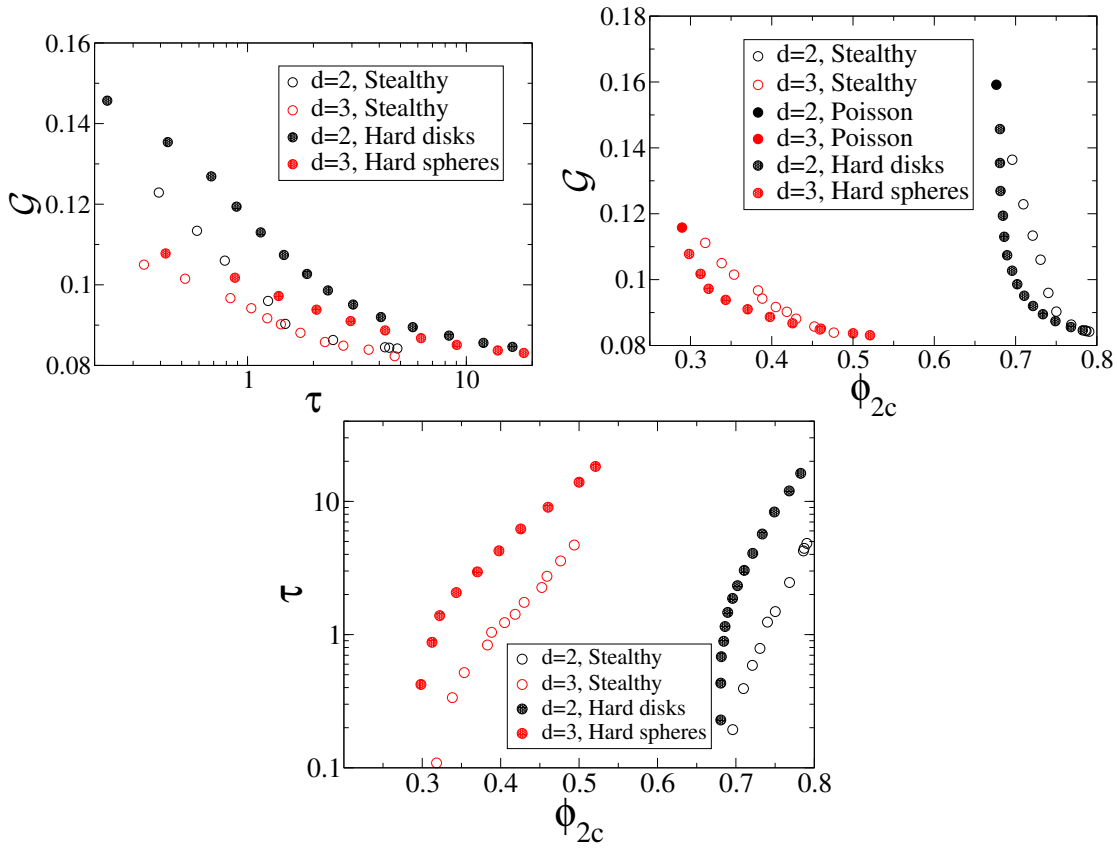

Figure 6.20 Correlations between quantizer error $\mathcal{G}$, order metric τ, and percolation volume fraction ϕ_c at unit number density.

In Fig. 6.20, we explore the correlation between $\mathcal{G}$, τ, and ϕ_c, and compare that for entropically favored stealthy ground states with that for equilibrium disordered hard-sphere systems. It is interesting to note that these two systems behave very differently. At the same τ, stealthy systems give lower values of $\mathcal{G}$, indicating $\mathcal{G}$ is more sensitive to long-range order than to short-range order. At the same τ or $\mathcal{G}$, stealthy systems give higher values of ϕ_{2c}, indicating that ϕ_{2c} is even more sensitive to long-range order than to short-range order.

6.5 Conclusions and Discussion

In this work, we decorated stealthy disordered hyperuniform point configurations of different degrees of order with spheres of various radii, and computed several transport and structural properties of these decorated systems. The transport properties that we studied include effective diffusion coefficient D_e, mean survival time T_{mean}, survival probability $p(t)$, and principal relaxation time T_1. The structural properties examined include hyperuniformity and stealthiness, maximum packing fraction ϕ_p^{max}, the void-exclusion probability E_V, the order metric τ, and the percolation thresholds ϕ_{1c} and ϕ_{2c}. We showed that the order metric τ is an exquisite detector of both short- and long-range translational order. While all geometrical and topological quantities are strongly correlated (positive correlation between ϕ_{2c} and τ, and negative correlation between $\mathcal{G}$ and the former two quantities), the relation between the physical quantities are more complex: While D_e increases as χ increases or as ϕ_2 decreases, T_{mean} and T_1 increases as χ decreases or as ϕ_2 decreases. Therefore, there is no simple relationship between D_e and T_{mean} or T_1. Another reason why there is no such relationship is because if phase 1 ceases to percolate, then D_e becomes zero but T_{mean} and T_1 are still positive [305].

Besides finding correlations between geometrical and topological properties, we find that in the highly disordered ($\chi \ll 1$) regime, T_1 of our two-phase systems derived from decorated stealthy ground states is much lower than that of equilibrium hard-sphere system. Together with the void-exclusion probability, low T_1 suggests that the formation of large holes is strongly suppressed, even though the configuration appears completely disordered.

In the higher order ($\chi \approx 0.5$) regime, D_e of our disordered isotropic two-phase systems derived from decorated stealthy ground states is very close to the Hashin-Shtrikman upper bound for $0 \leq \phi_2 < \phi_p^{max}$, where ϕ_p^{max} is the maximum packing fraction. Since such decorated systems maintain stealthiness if and only if $\phi_2 < \phi_p^{max}$,

our results suggest a connection between stealthiness and the ability to have a nearly optimal (maximal) D_e. The fact that stealthy disordered two-phase media have nearly optimal D_e could have practical implications, e.g., optimal and isotropic drug release from designed nanoparticles. Although nearly optimal D_e can also be achieved by lattice structures (i.e., periodic arrays of inclusions), the latter are always anisotropic. Thus, if one desires isotropic two-phase media with highest possible D_e at a specific volume fraction, disordered stealthy two-phase media could be the best choice.

Disordered stealthy ground states are uncountably infinitely degenerate.[352] The maximum packing fraction ϕ_p^{max} varies among configurations. In the future, it would be interesting to design algorithms that sample stealthy ground states with a bias toward configurations with higher ϕ_p^{max} values. With such an algorithm, one would be able to design isotropic two-phase media with nearly optimal D_e with very high ϕ_2.

Lastly, we would like to mention that although here we only study the diffusion problem of point Brownian particles, the diffusion problem of finite-sized Brownian particles has also been of interest.[15] It is noteworthy that our results can be trivially extended to the latter case. The diffusion of Brownian particles of radius b among obstacles of radius a is equivalent to the diffusion of point Brownian particles among obstacles of radius $a+b$. This mapping was previously exploited to quantify diffusion of finite-sized spheres in various models of porous media.[160]

Interestingly, one can relate the transport properties computed here (D_e, T_{mean}, and T_1) to different physical properties of the same systems via cross-property relations, including those that relate them to the elastic moduli, [108, 109] as well as fluid permeability. [20, 297] In future work, we will carry out such analyses.

6.6 Appendix A: System Sizes

As discussed in Sec. 6.3.1, it is nontrivial to choose the system size N and parameter χ, especially because one of our protocol to calculate the percolation threshold requires three different N's for each χ. We enumerated all possible choices of N's and χ's for $N < 1000$ and picked up some χ values that allow at least three different choices of N's. Our choice of N and χ in 2D and 3D are listed in Tables 6.1 and 6.2. It is desirable to consider values of χ higher than 0.4133... in 3D, but our enumeration did not find such a χ value that satisfies the above condition. Therefore, we chose three more N's that allow χ to be very close to 0.4598 but makes χ differ in the fifth decimal place. See the caption for Table 6.2 for details. Except for the percolation threshold calculation, we only use the largest N for each χ and d.

Table 6.1 Our choice of parameter χ's, and the corresponding three different numbers of particles, N_1, N_2, and N_3 in 2D.

χ	N_1	N_2	N_3
0.05	151	451	751
0.1	106	301	496
0.15	101	311	501
0.2	106	301	511
0.3	101	301	511
0.35	121	301	481
0.4	106	271	511
0.45	111	311	471
0.465	101	301	501
0.48	126	326	476

Table 6.2 Our choice of parameter χ's, and the corresponding three different numbers of particles, N_1, N_2, and N_3 in 3D. The "*" mark indicates that χ values differ starting from fifth decimal place between the three choices of N.

χ	N_1	N_2	N_3
0.02	151	351	651
0.0555...	127	259	421
0.0833...	109	281	497
0.1333...	176	311	476
0.1666...	135	321	459
0.2083...	113	257	425
0.2333...	101	161	431
0.2777...	121	319	475
0.3333...	101	302	480
0.3690...	113	309	477
0.4133...	101	276	426
0.4598...*	167	383	520

6.7 Appendix B: Properties of Stealthy Point Configurations and Decorated Systems

In this section we tabulate all of the physical and geometrical properties of stealthy point configurations and decorated systems that we study in this chapter (Tables III and IV).

Table 6.3 Principal relaxation time T_1 at $\phi = 0.2$ and $\phi = 0.5$, order metric τ, quantizer error $\mathcal{G}$, void-phase and particle-phase percolation volume fraction ϕ_{1c} and ϕ_{2c}, and void-phase and particle-phase percolation radius a_{1c} and a_{2c} for different parameter χ's in 2D.

χ	T_1 ($\phi = 0.2$)	T_1, ($\phi = 0.5$)	τ	$\mathcal{G}$	$\phi_{1c} = 1 - \phi_{2c}$	$a_{1c} = a_{2c}$
0.05	0.2753	0.1858	0.193	0.1364	0.3041	0.5840
0.1	0.1964	0.1214	0.393	0.1229	0.2904	0.5692
0.15	0.1554	0.0886	0.588	0.1134	0.2790	0.5564
0.2	0.1291	0.0704	0.787	0.106	0.2693	0.5448
0.3	0.1015	0.0502	1.241	0.096	0.2597	0.5238
0.35	0.0842	0.0408	1.488	0.0903	0.2498	0.5117
0.4	0.0710	0.0331	2.459	0.0863	0.2316	0.5071
0.45	0.0657	0.0282	4.248	0.0845	0.2139	0.5083
0.465	0.0645	0.0274	4.443	0.0844	0.2129	0.5082
0.48	0.0635	0.0272	4.839	0.0842	0.2095	0.5090

Table 6.4 Same as above, except for 3D.

χ	T_1 ($\phi = 0.2$)	T_1 ($\phi = 0.5$)	τ	$\mathcal{G}$	ϕ_{2c}	ϕ_{1c}	a_{2c}	a_{1c}
0.02	0.1572	0.0938	0.107	0.1111	0.3182	0.0299	0.4483	0.8970
0.0555	0.1221	0.0647	0.336	0.1050	0.3384	0.0261	0.4536	0.8572
0.0833	0.1061	0.0551	0.518	0.1015	0.3536	0.0242	0.4583	0.8351
0.1333	0.0911	0.0433	0.835	0.0967	0.3832	0.0225	0.4672	0.8019
0.1666	0.0826	0.0387	1.040	0.0942	0.3884	0.0205	0.4664	0.7878
0.2083	0.0779	0.0342	1.231	0.0917	0.405	0.0196	0.4702	0.7700
0.2333	0.0722	0.0317	1.420	0.0902	0.4185	0.0181	0.4739	0.7623
0.2777	0.0668	0.0289	1.745	0.0881	0.4300	0.0192	0.4753	0.7446
0.3333	0.0612	0.0254	2.258	0.0858	0.4525	0.0199	0.4804	0.7253
0.369	0.0593	0.0236	2.740	0.0849	0.4591	0.0198	0.4814	0.7166
0.4133	0.0561	0.0213	3.575	0.0839	0.4764	0.0194	0.4864	0.7082
0.4598	0.0537	0.0202	4.704	0.0823	0.4939	0.0201	0.4917	0.6992

Chapter 7

Can Exotic Disordered "Stealthy" Particle Configurations Tolerate Arbitrarily Large Holes?

7.1 Introduction

Statistical-mechanical studies of disordered many-particle systems often focus on quantifying various statistics of particle locations. This includes n-body correlation functions,[345, 220, 46, 91] the structure factor,[345, 46, 220] nearest-neighbor probability distributions,[314, 298] and various statistics of the corresponding Voronoi cells.[279, 258, 133, 277, 264, 187] However, rather than considering the particles themselves, it has been suggested that the space outside of the particles (void space) may be even more fundamental and contain greater statistical-geometrical information.[301, 303] A major focus of this chapter is the study of a particular property of the void space between point particles in disordered "stealthy" systems,[328, 26, 325, 352, 353] which are disordered many-particle configurations that anomalously suppress large-scale density fluctuations, endowing them with unique physical properties. [28, 95, 94,

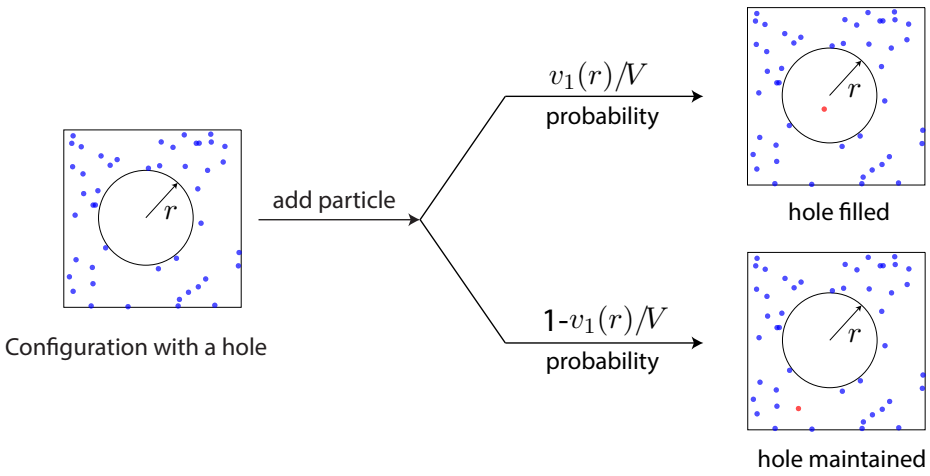

Figure 7.1 In a Poisson point configuration (ideal gas), particle locations are random and uncorrelated. If there is a hole of volume $v_1(r)$ in a configuration of volume V, then when one adds another particle (marked red), the probability that this hole remains empty is $1 - v_1(r)/V$. Thus, if there is a total of N particles, the overall probability that such a sphere remains empty is $[1 - v_1(r)/V]^N \approx \exp[-(N/V)v_1(r)] = \exp[-\rho v_1(r)]$, implying that holes can be arbitrarily large. For correlated homogeneous point configurations (*e.g.,* liquids), the probability of finding a very large hole of radius r will generally decrease relative to the Poisson case. For some correlated point configurations (*e.g.,* crystals and special disordered systems), the probability of finding an arbitrarily large hole is exactly zero.

189, 178, 355] The specific question that we investigate is whether disordered stealthy systems can contain arbitrarily large holes. Here we define a "hole" as a spherical region of a certain radius that is empty of particle centers. It is noteworthy that this hole statistic plays a central role in the "quantizer" and "covering" problems that arise in discrete geometry.[61, 303] It is also noteworthy that the question of the formation of very large holes is of fundamental importance in understanding thermodynamic phase separations into dense liquid phases and "hollow" phases.[35, 162]

Given a general many-particle system in d-dimensional Euclidean space $\mathbb{R}^d$, can one find arbitrarily large holes? For disordered systems, the answer to this question is often "yes." Consider the void-exclusion probability function, $E_V(r)$, which gives the probability of finding a randomly located spherical cavity of radius r empty of particles.[301] If $E_V(r)$ is non-zero for an arbitrarily large r, then one can find ar-

bitrarily large holes in the infinite system, even if these are very rare events. For example, as explained in Fig. 7.1, the void-exclusion probability for a Poisson point process (*i.e.*, an ideal gas) at number density ρ is given by [301]

$$E_V(r) = \exp[-\rho v_1(r)], \tag{7.1}$$

where $v_1(r) = \pi^{d/2} r^d / \Gamma(1 + d/2)$ is the volume of a d-dimensional sphere of radius r,[303] and $\Gamma(x)$ is the gamma function. Although E_V decays exponentially as $v_1(r)$ increases, it is always positive for any finite r. Thus, no matter how large a hole is desired, the rare event of forming such a hole can always be observed in the infinite system. Similarly, $E_V(r)$ is found to be positive for arbitrarily large r's for equilibrium hard-sphere fluid systems across dimensions.[314] Therefore, they also allow arbitrarily large holes. It is noteworthy that $E_V(r)$ can be expanded as a series involving n-body correlation functions.[314] Therefore, $E_V(r)$ requires many-body correlation information to quantify the probability of hole formation.

Even for many-particle systems in which $E_V(r)$ is not exactly known in the large-r limit, there are often strong arguments indicating that holes of arbitrary sizes can occur. For equilibrium systems of particles interacting with some potentials (*e.g.*, Lennard-Jones potential) at some positive temperature T, the free energy cost of creating a hole, ΔF, often scales as the hole volume and/or hole surface area, and is therefore finite. Thus, the probability of finding a large hole [roughly $\exp(-\Delta F/T)$] is also nonzero. Moreover, hard-sphere systems in a glassy or crystalline state away from jamming points possess collective motions that can produce arbitrarily large holes in the infinite-system limit.[17]

Besides the aforementioned many-particle systems with unbounded hole sizes, we also know of several systems in which the hole radii are bounded from above. A simple class of systems whose hole probability must have compact support are perfect

crystalline (periodic) many-particle systems. Spheres large enough to encompass entire unit cells always contain particles. Thus, holes of arbitrarily-large radii cannot exist. A simple disordered class is saturated random sequential addition (RSA) sphere packings across dimensions. RSA is a time-dependent packing process, in which congruent hard spheres are randomly and sequentially placed into a system without overlap. In the infinite-time limit, the system becomes saturated, *i.e.,* spheres can no longer be added to the packing, and hence holes must be finite in size. By contrast, RSA packings below the saturation density were found to have positive $E_V(r)$ for arbitrarily large r,[251] and therefore allow for the presence of very large holes.

So far we have seen that although all perfect crystalline many-particle systems prohibit arbitrarily large holes, many disordered many-particle systems allow them. A promising class of amorphous structures that may not tolerate arbitrarily large holes is disordered hyperuniform systems. Such systems have received considerable attention because they anomalously suppress density fluctuations.[28, 95, 94, 189, 178, 355] Specifically, if one places a spherical window of radius R into a d-dimensional many-particle system and counts the number of particles in the window, then the number variance, $\sigma^2(R)$, scales as R^d for large R in typical disordered systems. Any system in which $\sigma^2(R)$ grows slower than R^d is said to be hyperuniform.[317] Equivalently, a hyperuniform many-particle system is one which the structure factor $S(\mathbf{k})$ tends to zero as the wavenumber $|\mathbf{k}|$ tends to zero,[317] *i.e.,*

$$\lim_{|\mathbf{k}|\to 0} S(\mathbf{k}) = 0. \tag{7.2}$$

Disordered hyperuniform systems are a good starting point to search for more examples of disordered systems with bounded hole sizes because the formation of large holes might be inconsistent with hyperuniformity, which suppresses large-scale density fluctuations.

However, we know that not all disordered hyperuniform systems prohibit arbitrarily large holes. For example, in a hyperuniform fermionic-point process in d spatial dimensions, $E_V(r)$ scales as $\exp(-cr^{d+1})$ (where c is a constant) for large r.[315] Also, the hyperuniform two-dimensional one-component plasma possesses an $E_V(r)$ that scales as $\exp(-cr^4)$ for large r.[138, 107] Both of these systems thus allow arbitrarily large holes. Therefore, hyperuniformity alone is not a sufficient condition to guarantee boundedness of the hole size. Nevertheless, different hyperuniform systems have different levels of suppression for large-scale density fluctuations. While any system in which $\lim_{|\mathbf{k}|\to 0} S(\mathbf{k}) = 0$ is considered hyperuniform, the "stealthy" variants of hyperuniform systems have $S(\mathbf{k}) = 0$ in the entire interval $|\mathbf{k}| \in (0, K]$ for a certain value of K. Stealthy hyperuniform systems are known to possess many unique thermodynamic and nonequilibrium physical properties, including negative thermal expansion behavior,[28] complete isotropic photonic band gaps comparable in size to those of a photonic crystal,[95, 94, 189] transparency even at high densities,[178] and nearly optimal transport properties.[355] The behavior of $S(\mathbf{k})$ near $\mathbf{k} = \mathbf{0}$ in stealthy systems is identical to that in perfect crystals. Since perfect crystals prohibit large holes, could stealthy hyperuniform systems also prohibit large holes?

In this chapter, we present strong numerical evidence that disordered stealthy systems indeed prohibit arbitrarily large holes. It is nontrivial to study the existence of large holes not only because formation of large holes is extremely rare, but also because numerical simulations are limited to finite-sized systems and one wants to infer the infinite-volume-limit behaviors. With periodic boundary conditions, such systems are always perfect crystals, even if the repeating units may be very large. As we have mentioned, perfect crystals always have bounded hole sizes. We developed two numerical techniques to overcome these issues to distinguish whether a system can tolerate arbitrarily large holes or not that can be applied to infer the maximum hole size in general disordered systems (whether they are stealthy or not) in the

infinite-volume limit. Specifically, we first attempt to determine the maximum size of the holes that naturally emerges in stealthy hyperuniform systems across the first three space dimensions by studying the tail behavior of $E_V(r)$. We find that the tail of $E_V(r)$ for stealthy systems is qualitatively similar to that for crystals and saturated RSA sphere packings, which have finite holes, and is qualitatively different from that for Poisson point processes with unbounded hole sizes. We then determine the maximum hole size that any stealthy system can possess across the first three space dimensions. To do this, we generate large stealthy systems with largest possible holes by imposing repulsion fields with sizes equal to the desired hole sizes in stealthy systems. We discover that this method can only create holes of certain finite sizes without breaking stealthiness. In stealthy configurations with largest possible holes, particles concentrate in concentric shells around the hole. Analytical studies on this pattern allows us to derive a conjectured upper bound of the hole radius for all stealthy systems. Our results suggest that there exists an upper bound on the sizes of solute particles that a stealthy solvent can dissolve, since particles with exclusion radii above this upper bound would create intolerably large holes.

The rest of the chapter is organized as follows: Section 7.2 defines stealthy point patterns and two associated parameters, χ and K. Section 7.3 studies maximum hole sizes and the tail behavior of $E_V(r)$ in such systems. Section 7.4 defines the repulsion field we used to create holes, study the pattern of stealthy systems with such holes, and conjecture an upper bound for the hole radius, in one to three dimensions. Section 7.5 provides concluding remarks and discussions.

7.2 Mathematical Definitions

For a single-component system with N particles, located at $\mathbf{r}^N = \mathbf{r}_1, \mathbf{r}_2, \cdots, \mathbf{r}_N$, in a simulation box of volume V with periodic boundary conditions in a d-dimensional

Euclidean space $\mathbb{R}^d$, the static structure factor is defined as $S(\mathbf{k}) = |\sum_{j=1}^{N} \exp(-i\mathbf{k} \cdot \mathbf{r}_j)|^2/N$, where i is the imaginary unit and $\mathbf{k}$ is a d-dimensional wavevector (which must be integer multiples of the reciprocal lattice vectors of the simulation box).[46, 45]

As we have explained earlier, a hyperuniform system is defined as one in which the number variance $\sigma^2(R)$ grows more slowly than R^d for large window radius R, or a system in which $\lim_{|\mathbf{k}|\to 0} S(\mathbf{k}) = 0$. Stealthiness is a stronger condition than hyperuniformity. For some positive K, we call a system "stealthy up to K" if

$$S(\mathbf{k}) = 0 \text{ for all } 0 < |\mathbf{k}| < K. \tag{7.3}$$

For particles interacting with a pair potential $v(\mathbf{r})$, the total potential energy is given by

$$\begin{aligned} \Phi(\mathbf{r}^N) &= \sum_{i<j} v(\mathbf{r}_{ij}) \\ &= \frac{N}{2V} \sum_{\mathbf{k}} \tilde{v}(\mathbf{k}) S(\mathbf{k}) + \Phi_0 \end{aligned} \tag{7.4}$$

where $\tilde{v}(\mathbf{k})$ is the Fourier transform of $v(\mathbf{r})$, and we set the structure-independent constant Φ_0 in the second line of Eq. (7.4) (defined in Ref. [353]) to be zero in this chapter.

Our focus in the current chapter is on stealthy potentials that take the following form:

$$\tilde{v}(\mathbf{k}) = \begin{cases} V(|\mathbf{k}|), & \text{if } 0 < |\mathbf{k}| \leq K, \\ 0, & \text{otherwise,} \end{cases} \tag{7.5}$$

where $V(|\mathbf{k}|)$ is an arbitrary positive function. For present purposes, we choose $V(|\mathbf{k}|) = 1$ for simplicity. However, one could alternatively consider other functional forms of $V(|\mathbf{k}|)$, all of which have the same ground-state manifold.[325] (In

Sec. 5, we provide examples of physical many-particle systems whose interactions approximate stealthy potentials.) In any case, because $\tilde{v}(\mathbf{k})$ has compact support, the corresponding direct-space potential $v(\mathbf{r})$ is a bounded (soft), oscillating long-ranged function.[325] Because $S(\mathbf{k})$ is by definition always non-negative, a configuration is a ground state of this potential if it is stealthy up to K, *i.e.*, if $S(\mathbf{k})$ is constrained to zero for all $0 < |\mathbf{k}| < K$.

Only half of these constraints are independent. This is because by definition, $S(\mathbf{k}) = S(-\mathbf{k})$. Let the number of independent constraints be M, so the parameter

$$\chi = \frac{M}{d(N-1)} \tag{7.6}$$

quantifies the fraction of degrees of freedom that is constrained. Because χ is proportional to M, it is also proportional to $v_1(K)$, the volume of a d-dimensional sphere of radius K. Indeed, we have previously found [325]

$$\rho\chi = \frac{v_1(K)}{2d(2\pi)^d}. \tag{7.7}$$

It was found that for $\chi < 0.5$, the ground states of stealthy potentials are uncountably infinitely degenerate, and possess no long-range order.[352] As χ increases beyond 0.5, the ground states are still uncountably infinitely degenerate, but develop long-range translational and orientational order.[353] As χ increases further, these ground states eventually undergo phase transitions into the integer lattice, the triangular lattice, and the BCC lattice in one, two, and three dimensions, respectively.[325] In this chapter, we want to study hole sizes of disordered stealthy systems, and will therefore focus on the $\chi < 0.5$ range. Because ground states of the stealthy potentials are uncountably infinitely degenerate, one can have different ways to sample the ground states, which assign different weights to different parts of the ground state manifold. We have previously focused on the zero-temperature limit of the canonical

ensemble (*i.e.*, define the probability measure $P(\mathbf{r}^N) \propto \exp[-\Phi_s(K;\mathbf{r}^N)/k_BT]$, where k_B is the Boltzmann constant and T is the temperature, and then take the $T \to 0$ limit). However, in this chapter, we will also assign different weights to bias toward configurations with large holes.

7.3 Hole Probability and Maximum Hole Size in Unbiased Stealthy Systems

If an upper bound on the hole sizes exists, how should it depend on K and χ? The K dependence can be easily ascertained from a scaling argument: If there exists a configuration with hole size R that is stealthy up to K, then by rescaling the real-space configuration by a factor α, one can create another configuration with hole size $R\alpha$, stealthy up to K/α. Therefore, the maximum hole radius, R_c, must be inversely proportional to K. Therefore, we henceforth study the dimensionless hole size, R_cK, rather than R_c itself.

A different argument can shed light on the dependence of the hole size on χ. A superposition of multiple configurations, each stealthy up to a certain K, is also stealthy up to the same K.[325] Therefore, if there exist n configurations, each with a hole of radius R that is stealthy up to K, then one could superpose them with hole centers aligned to create another configuration with the same hole radius R and K. However, since the number of particles increases by a factor of n, χ decreases by a factor of n. Therefore, if there exists a configuration of a certain hole size and K at some χ value, then there exists a configuration of the same hole size and K at arbitrarily small χ values. In other words, R_cK as a function of χ must achieve the global maximum in the $\chi \to 0^+$ limit.

With these preliminary analytical results in mind, let us examine the numerical results from unbiased ground states of stealthy potentials (*i.e.*, $T = 0$ limit of the

canonical ensemble). We have previously generated such ground states in two and three dimensions for various χ values by performing low-temperature ($k_BT = 2\times10^{-6}$ in 2D and $k_BT = 10^{-6}$ in 3D) molecular dynamics simulations, periodically taking snapshots, and then minimizing the energy starting from each snapshot; see Ref. [355] for more details. For each χ, we generated 20,000 configurations. The number of particles, N, is always between 421 and 751 and is detailed in Ref. [355]. For each configuration, we rescaled it to unity K and performed a Voronoi tessellation and found out the largest distance between each Voronoi vertex and its neighbor particles. This distance is the maximum hole size for any particular configuration. We then determined the maximum hole size among all 20,000 configurations and plotted them as a function of χ in Fig. 7.2. For a comparison, we also present the same quantity for Poisson point processes at the same conditions, derived in the Appendix. As Eq. (7.7) shows, with K fixed to unity, ρ is inversely proportional to χ. Thus, it is not surprising that R_c for Poisson processes increases as χ increases. In unbiased stealthy ground states, however, R_c weakly increases with increasing χ and saturates at some constant value, suggesting that R_c is bounded for stealthy ground states with fixed K. The critical radius R_c decreases slightly as χ tends to zero because unbiased stealthy ground states become less ordered. Therefore, although large hole formation is still possible, its probability decreases. When this probability is too low, it becomes computationally more difficult to find such a large hole with only 20,000 configurations.

Examining the large-r tail behavior of $E_V(r)$ suggests strongly that R_c is finite in stealthy systems. As we have explained in Sec. I, if the hole size is bounded, $E_V(r)$ for some value of r must be identically zero, instead of being exponentially small. In Fig. 7.3, we closely examine the tails of $E_V(r)$ of stealthy systems in the first three space dimensions in a semi-log scale. As we showed earlier, numerically found R_c suffer from greater sampling errors if χ is too small. Thus, to study the

tail behavior of $E_V(r)$, we choose sufficiently large χ values (0.45-0.46) in Fig. 7.3. Nevertheless, we will show in the next section that smaller χ values do not result in any qualitative difference. For purposes of comparison, we compare our results for stealthy systems to $E_V(r)$ for systems in which we know that the holes must be finite in size, namely, lattices in which $E_V(r)$ is given exactly[303] and saturated RSA sphere packings; and contrast our results to Poisson point processes, in which hole sizes are unbounded. As Fig. 7.3 shows, the tail behavior of stealthy systems resembles that of crystalline structures and saturated RSA packings. For each of these systems, the logarithm of $E_V(r)$ must decay to its bounded cut-off value of R_c with an infinite slope at which $E_V(R_c) = 0$, which may be regarded to be singularity. However, these figures necessarily present $E_V(r)$ above certain positive lower limits and hence only nearly-infinite slopes are apparent. By contrast, Poisson point processes and equilibrium hard-sphere fluids (not shown in the figure), which have unbounded R_c's, possess $\log[E_V(r)]$'s that comparatively have very small slopes on the scale of the figures, without any singularity. Note that although $E_V(r)$ of RSA packings have been studied before,[251, 356] this is the first study that focuses on its tail behavior.

It is noteworthy that the three lattice structures we chose (integer, triangular, and BCC lattice) are the optimal solutions of the covering and quantizer problems [61] in their respective dimensions. In a specific dimension and density, the covering problem asks for the configuration with the smallest cutoff in $E_V(r)$ (*i.e.,* the smallest R_c), while the quantizer problem asks for the configuration that minimizes the so-called "quantizer error," defined as[303]

$$\mathcal{G} = \frac{2}{d}\int_0^\infty r E_V(r) dr. \tag{7.8}$$

As Fig. 7.3 shows, in two and three dimensions, $E_V(r)$ of stealthy systems at $\chi = 0.45 - 0.46$ is quite close to $E_V(r)$ of the triangular and BCC lattices. Therefore,

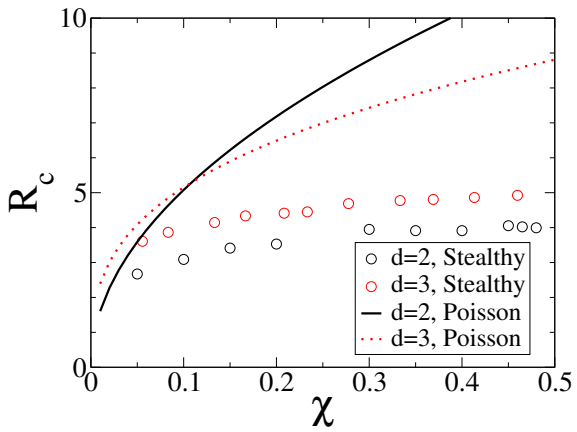

Figure 7.2 Maximally observed R_c in 20,000 entropically favored stealthy ground states, rescaled to unity K. The number of particles per configuration, N, depends on χ and space dimensions but is always between 421 and 751 and is given in Ref. [355]. The same quantity for Poisson point processes (ideal gas) at the same density is also plotted for comparison.

stealthy ground states at high χ values should provide nearly optimal solutions to these two problems.

7.4 Stealthy Configurations with Largest Possible Holes

In the previous section we studied the largest holes naturally occurring in unbiased disordered ground states of stealthy potentials. In this section, we study the maximum hole sizes consistent with stealthiness. To do so, we impose a radial exclusion field at the center of the simulation box to bias the configuration toward ones with largest holes. We combine the stealthy potential with such an exclusion field, and try to find the ground state of the system. We then study the patterns of the resulting ground states.

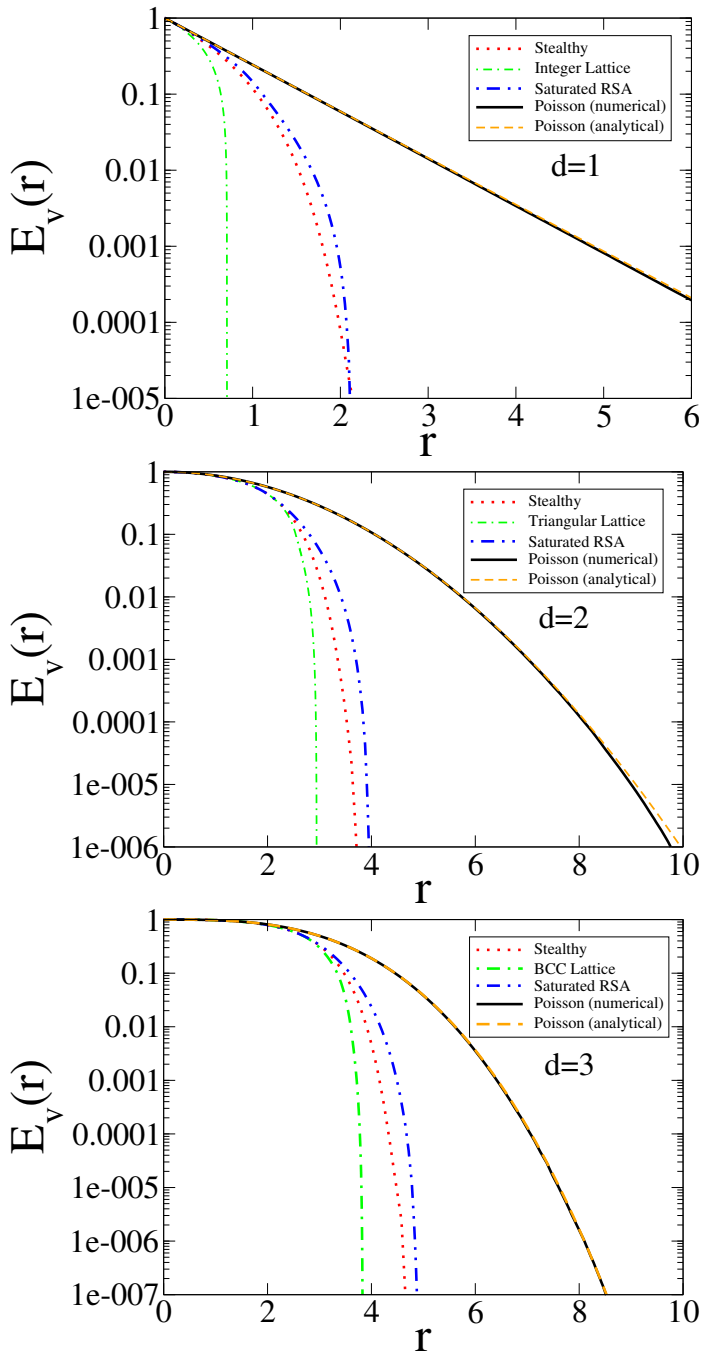

Figure 7.3 Numerically computed $E_V(r)$ for (top) a stealthy system at $\chi = 0.45$ in 1D, (middle) a stealthy system at $\chi = 0.45$ in 2D, and (bottom) a stealthy system at $\chi = 0.46$ in 3D. For comparison, we also present $E_V(r)$ of perfect crystals (integer, triangular, and BCC lattices[303]), saturated RSA packings, and Poisson point processes at the same number density across the first three space dimension. For Poisson point processes, we present both numerically found $E_V(r)$ and exact analytical predictions for $E_V(r)$. The excellent agreement between these numerical and exact results is a testament to the numerical precision of our calculations.

7.4.1 Simulation details

To bias toward configurations with large holes, we let the total potential energy be a sum of the stealthy potential contribution and the exclusion field contribution:

$$\Phi(\mathbf{r}^N) = \Phi_s(K;\mathbf{r}^N) + \Phi_{ex}(R_f;\mathbf{r}^N), \tag{7.9}$$

where $\Phi_s(K;\mathbf{r}^N)$ is the stealthy potential given in Eq. (7.5), and $\Phi_{ex}(R_f;\mathbf{r}^N)$ is the exclusion-field contribution, given by

$$\Phi_{ex}(R_f;\mathbf{r}^N) = \sum_i F(R_f;r_{ic}), \tag{7.10}$$

where r_{ic} is the radial distance from particle i to the center of the simulation box,

$$F(R_f;r_{ic}) = \begin{cases} (R_f/r_{ic}-1), & \text{if } r_{ic} < R_f, \\ 0, & \text{otherwise,} \end{cases} \tag{7.11}$$

and R_f is the radius of the exclusion field. By varying R_f, we can probe the largest possible hole size in a particular system. Before R_f reaches R_c (the upper bound of the hole radius), Φ_{ex} can be zero. However, once R_f surpasses R_c for a particular system, Φ_{ex} must be positive.

If we can find a configuration for which $\Phi(\mathbf{r}^N) = 0$, then both $\Phi_s(K;\mathbf{r}^N)$ and $\Phi_{ex}(R_f;\mathbf{r}^N)$ must be zero, and therefore this configuration is stealthy up to K while simultaneously having a hole radius R_f. To test if there are such configurations, we perform energy minimizations using the L-BFGS algorithm,[214, 183, 150] starting from many random initial configurations, and finding if the ending $\Phi(\mathbf{r}^N)$ in any configuration dropped below a strong tolerance of 10^{-10}. We consider a certain number, R_c, to be the numerically found maximum hole size if a zero-energy configuration is found within N_{trial} energy minimization trials for $R_f = R_c$, but not found for

$R_f = R_c + \delta_R$. Here we choose $N_{trial} = 100$ and $\delta_R = 0.01$. For a two-dimensional system at $\chi = 0.10$, and $N = 400$, with this choice of N_{trial} and δ_R we find $R_cK = 4.58$; while using $N_{trial} = 1000$ and $\delta_R = 0.0001$, we find $R_cK = 4.5903$. Therefore, our choice of N_{trial} and δ_R produces R_cK values with approximately 10^{-2} precision. As explained in our previous work,[352] to minimize boundary effects for the stealthy potential, we use a rhombic simulation box with a 60° interior angle in 2D and a simulation box in the shape of a fundamental cell of a body-centered cubic lattice in 3D with periodic boundary conditions.

As a test for this methodology, we combined the exclusion field [Eq. (7.10)] with following pair potential

$$\Phi_h(\mathbf{r}^N) = \sum_{i<j} v(r_{ij}), \tag{7.12}$$

where

$$v(r_{ij}) = \begin{cases} (1 - r_{ij})^2, & \text{if if } r_{ij} < 1 \\ 0, & \text{otherwise,} \end{cases} \tag{7.13}$$

and performed energy minimizations in two dimensions. For this potential to be zero, any pair of particles cannot be closer than distance 1. Therefore, the ground state of this potential corresponds to an equilibrium hard disk system of diameter 1. As we have mentioned in Sec. I, any such system in the infinite-volume limit must possess an unbounded hole size. Nevertheless, the formation of very large holes is still very rare and may be difficult to observe if one simply samples unbiased configurations. We performed our simulation on an $N = 400$ system with volume fraction $\eta = 0.5$. As shown in Fig. 7.4, the energy minimization algorithm is capable of creating a hole of of radius $R = 9.2$, although the probability of finding such a hole in an unbiased system is extremely small. According to Eq. (4.21) of Ref. [314], $E_V(9.2) = 4 \times 10^{-279}$. This demonstrates that if the hole size is unbounded in the infinite-system-size limit for some system, this numerical protocol can indeed create very large holes in a finite-

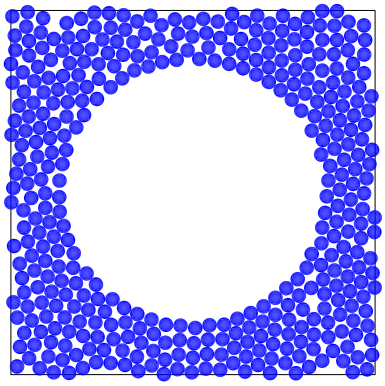

Figure 7.4 A configuration obtained by energy minimization using the potential in Eq. (7.12) and an external field of radius $R_f = 9.2$. The simulation box contains $N = 400$ particles and has side length $L = 25$.

size simulation. Figure 7.4 also shows that in creating such a large hole, the particles are pushed to each other as closely as possible (*i.e.,* up to interparticle contacts). Therefore, even larger holes should be possible if we simulated larger systems at the same volume fraction.

7.4.2 One-dimensional study

We first examine R_cK values found by the above-mentioned algorithm in 1D, since this is computationally the easiest dimension to study and will shed light on corresponding results in higher dimensions. Our result for several different χ's and system sizes are summarized in Fig. 7.5. It appears that R_cK as a function of χ is chaotic and displays no systematic trend. Nevertheless, Fig. 7.5 does show that R_cK is always close to π but never exceeds it. As we will see later, π is the upper bound of R_cK in 1D.

Examining stealthy configurations with hole sizes $R_f \approx \pi/K$ reveals a more interesting behavior. Such a configuration is shown in Fig. 7.6. At exclusion-field size

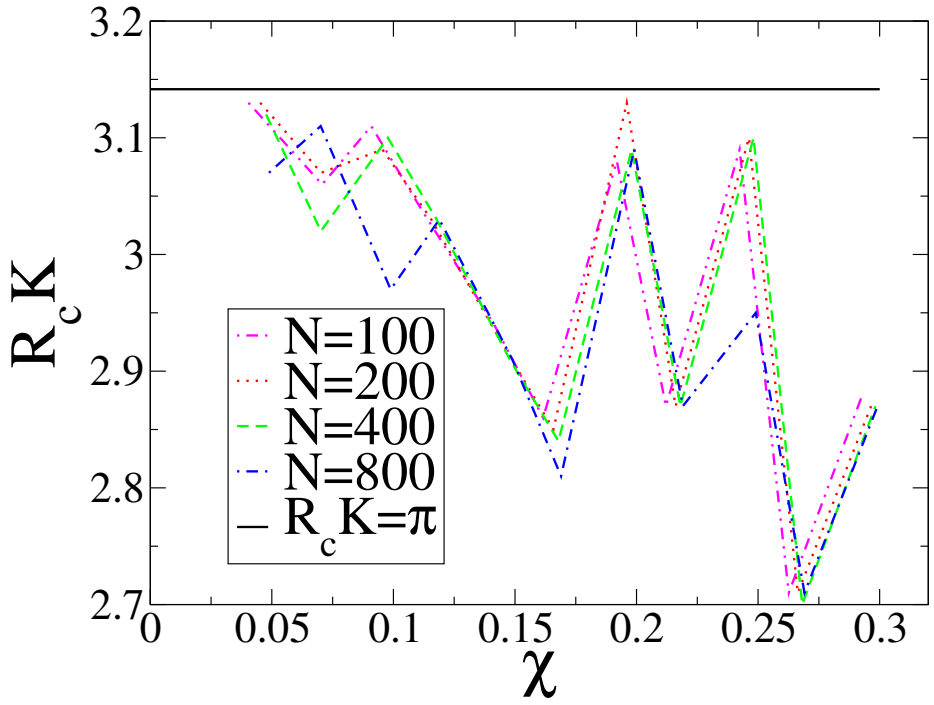

Figure 7.5 Numerically found maximum R_cK, as a function of χ, in 1D biased stealthy configurations for various system sizes.

$R_f = 3.1/K$, 100 particles self-assemble into 10 clusters, each containing 10 particles. These clusters then form a one-dimensional integer lattice.

As we have explained in Sec. 7.3, a superposition of multiple integer lattices, with hole centers aligned, have the same R_cK as a single integer lattice. It is straightforward to calculate R_cK of an integer lattice: If the distance between neighboring lattice sites is L, then the maximum hole radius is $L/2$, and the stealthy range K is equal to the location of the first Bragg peak, $2\pi/L$. Therefore, R_cK of any integer lattice is simply π. To summarize, the numerically found hole radius is never above π/K; and superposed integer lattices can indeed achieve hole radius π/K. Therefore, we expect that π/K is an upper bound of the hole size for stealthy 1D structure at any χ.

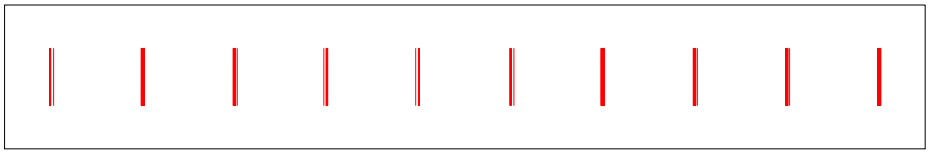

Figure 7.6 A 1D biased stealthy configuration of $N = 100$ particles obtained by energy minimization using the stealthy potential of $K = 1$ and an external field of radius $R_f = 3.1$ at $\chi = 0.1$. The particles self-assemble into 10 clusters. Although particles in the same cluster may not be distinguishable from each other here, we have examined the configuration and find that each cluster contains exactly 10 particles.

7.4.3 Two- and three-dimensional studies

We now move on to study maximum hole sizes in two and three dimensions. As we will see, these higher dimensions are computationally more challenging than 1D because the structures that maximize the hole size is not periodic. The R_cK values found by the algorithm mentioned in Sec. 7.4.1 is presented in Fig. 7.7. Similar to the 1D case, the dependence of R_cK on χ or N is weak and non-systematic. However, 2D configurations, one of which is shown in Fig. 7.8, exhibit a more complicated pattern with sixfold rotational symmetry, in which particles concentrate in a lower-dimensional manifold. Although this pattern is non-crystalline, it is still much more ordered than unbiased stealthy ground states at this χ value.[352] Note that the configuration shown in Fig. 7.8 and related ones are stealthy and hyperuniform, even though they are not homogeneous. Since stealthiness is defined as $S(\mathbf{k}) = 0$ for all $|\mathbf{k}| < K$, this implies no single scattering and an associated anomalous suppression of density fluctuations for wavelengths above $2\pi/K$. In this configuration, $2\pi/K$ is the distance between two consecutive rings. For any wavelength larger than $2\pi/K$, the higher densities concentrated in the rings will cancel out the lower densities between the rings, which suppresses the overall density fluctuations. Such cancellation no longer occurs for wavelengths below $2\pi/K$, but the resulting density fluctuations are compatible with stealthiness.

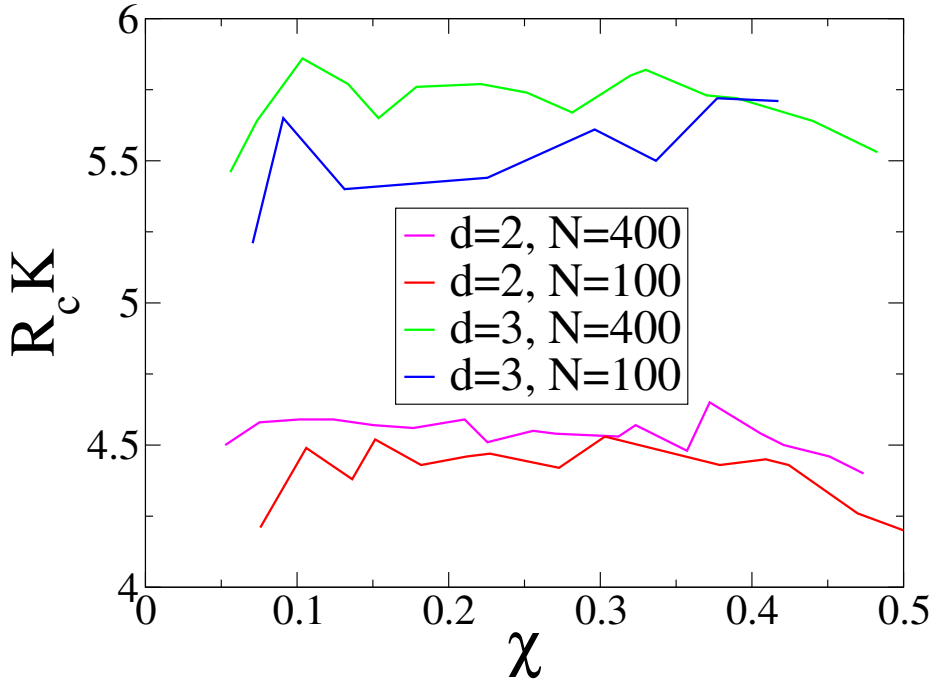

Figure 7.7 Numerically obtained maximum R_cK, as a function of χ, in 2D and 3D biased stealthy configurations.

To better reveal the intricacies of these patterns, we computed the one-body correlation function, $g_1(\mathbf{r})$, of a 2D system of $\chi = 0.1$ and $N = 400$, shown in Fig. 7.9A. The plot shows high-intensity concentric shells around the exclusion field (located at the center of the simulation box) and honeycomb network structures away from the exclusion field. Figure 7.9B also shows $g_1(\mathbf{r})$ of a larger 2D system, which exhibits the same pattern. Figure 7.9C shows $g_1(\mathbf{r})$ of a 3D system, which again has concentric shells around the exclusion field, but the structure away from the center is not obvious.

By pushing R_cK to its numerical limit, we obtain periodic structures in 1D but non-periodic structures in 2D and 3D. Is it possible that this transition from periodic structures to non-periodic structures arises from increased numerical difficulties in higher dimensions? To eliminate this possibility, we analytically calculated R_cK values for various 2D and 3D periodic structures for comparisons. In 2D, crystal structures achieve $R_cK = 4.44$ but the system shown in Fig. 7.9 achieved $R_cK =$

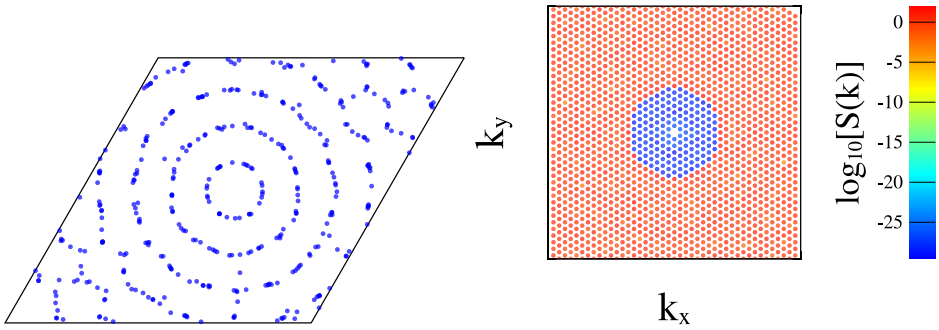

Figure 7.8 (left) A 2D biased stealthy configuration of $N = 400$ particles obtained by energy minimization using the stealthy potential of $K = 1$ and an external field of radius $R_f = 4.58$ at $\chi = 0.1$. (right) Its corresponding structure factor $S(\mathbf{k})$, which is less than 10^{-25} in the $0 < |\mathbf{k}| \leq K$ range, verifying the stealthiness with high precision. Notice that it also reveals underlying sixfold rotational symmetry of the structure.

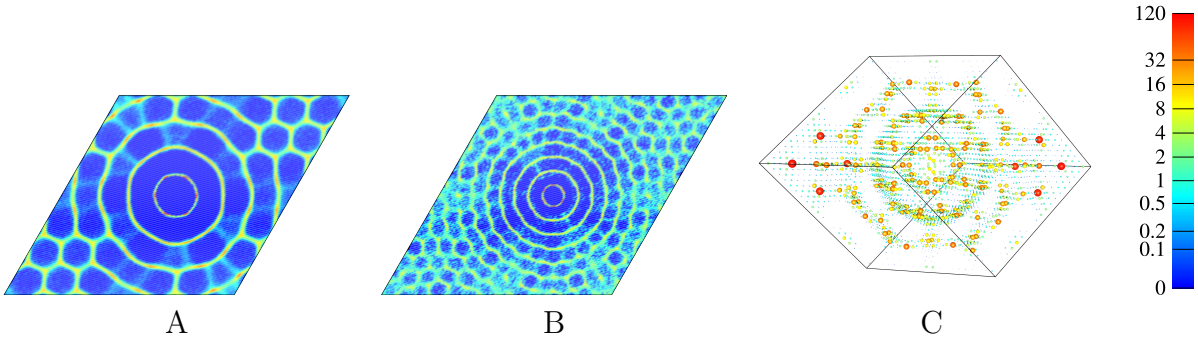

Figure 7.9 Numerically obtained $g_1(\mathbf{r})$ for (A) $d = 2$, $N = 400$, $R_cK = 4.58$, averaged over 3449 biased stealthy configurations that also exhibit sixfold rotational symmetry; (B) $d = 2$, $N = 1600$, $R_cK = 4.60$, averaged over 72 configurations; and (C) $d = 3$, $N = 400$, $R_cK = 5.85$, averaged over 5174 configurations. The χ value is always 0.10. In 3D, $g_1(\mathbf{r})$ is represented by color-coded spheres with volumes proportional to $g_1(\mathbf{r})$ at the spheres' location. Notice that there is a tendency for particles to concentrate in a lower-dimensional manifold.

4.6; while in 3D crystal structures achieve $R_cK = 5.44$ but the system shown in Fig. 7.9 achieved $R_cK = 5.85$. Therefore, these non-periodic structures indeed have the largest known value of R_cK.

Table 7.1 Maximum dimensionless hole size, R_cK, for various 2D crystalline structures.

Crystal	R_cK
Square lattice	4.44
Honeycomb crystal	4.19
Triangular lattice	4.19
Kagome crystal	3.63

Table 7.2 Maximum dimensionless hole size, R_cK, for various 3D crystalline structures.

Crystal	R_cK
Face-centered cubic	5.44
Simple cubic	5.44
Hexagonal close packed	5.13
Mean centered-cuboidal lattice [60]	5.03
Body-centered cubic	4.97
Simple Hexagonal	4.80
Diamond	4.71
Pyrochlore crystal [238]	4.51

It would be useful to analytically model these $g_1(\mathbf{r})$ functions to find the maximum dimensionless hole size in the infinite-system-size limit. We will focus on the rings before considering the honeycomb-like structure away from the hole center. Comparing Fig. 7.9A with Fig. 7.9B, we see that increasing N increases the number of rings. Therefore, we expect infinitely many rings in the infinite-system-size limit.

It is instructive to model an isotropic collection of concentric shells, for which we can write

$$g_1(\mathbf{r}) = \sum_{j=1}^{\infty} c_j \delta(|\mathbf{r}| - r_j), \tag{7.14}$$

where c_j is the intensity of the shells, δ is the Dirac delta function, and r_j is the location of the shells. To determine c_j and r_j, we computed the angular average of $g_1(\mathbf{r})$ shown in Fig. 7.9B, and identified five peaks from it. As Fig. 7.10 shows, r_j

appears linear with j, for which linear regression produces $r_j = 0.0612j - 0.01478$. By rescaling the configuration, we can eliminate one fitting parameter and get $r_j = j - b$, where $b = 0.242$.

To find c_j, we have computed the fraction of particles located on each ring, p_j. We find again p_j is linear with j, with linear regression result $p_j = 0.0275(j - 0.242) \propto r_j$. Because p_j is proportional to r_j, and is therefore proportional to the circumference of the rings, each ring has the same intensity. Neglecting a constant factor, we can then set $c_j = 1$.

To summarize, numerical results suggest that in the infinite-system-size limit,

$$g_1(\mathbf{r}) \propto \sum_{j=1}^{\infty} \delta(|\mathbf{r}| - j + b), \tag{7.15}$$

where constant b is numerically measured as 0.242 in 2D. Note that this equation also applies to the 1D numerical result (an integer lattice of particle clusters) if we let $b = 1/2$. The hole radius of this system is simply $R_c = 1 - b$, the radius of the first ring. After determining R_c, we should then ascertain K. Since $S(\mathbf{k})$ is zero for all $\mathbf{k}$ such that $0 < |\mathbf{k}| < K$, the collective coordinates $\tilde{\rho}(\mathbf{k}) = \sum_{j=1}^{N} \exp(-i\mathbf{k} \cdot \mathbf{r}_j)$ should also be zero. Thus, the Fourier transform of $g_1(\mathbf{r})$, which we denote by $\tilde{g}_1(\mathbf{k})$, should also be zero in this range. Fourier transforming Eq. (7.15) gives

$$\tilde{g}_1(\mathbf{k}) = \int_{\mathbf{r}} \exp(i\mathbf{k} \cdot \mathbf{r}) g_1(\mathbf{r}) \propto \sum_{j=1}^{\infty} \frac{(j-b)^{d/2}}{k^{d/2-1}} J_{d/2-1}[k(j-b)], \tag{7.16}$$

where $k \equiv |\mathbf{k}|$ is the wavenumber and J_ν is the Bessel function of order ν. In Eq. (7.16), letting $d = 1$, 2, and 3 respectively yields

$$\tilde{g}_1(k) \propto \sum_{j=1}^{\infty} \cos[k(j-b)] \qquad (d = 1), \tag{7.17}$$

$$\tilde{g}_1(k) \propto \sum_{j=1}^{\infty} (j-b) J_0[k(j-b)] \qquad (d=2), \tag{7.18}$$

and

$$\tilde{g}_1(k) \propto \sum_{j=1}^{\infty} (j-b) \cos[k(j-b) - \pi/2] \qquad (d=3). \tag{7.19}$$

For large x, $J_0(x)$ is asymptotically $x^{-1/2}\cos(x - \pi/4)$. Substituting this into Eq. (7.18) gives

$$\tilde{g}_1(k) \propto \sum_{j=1}^{\infty} \sqrt{\frac{j-b}{k}} \cos\left[k(j-b) - \frac{\pi}{4}\right] \qquad (d=2). \tag{7.20}$$

We have already seen in the previous section that, the solution to maximizing $R_c K = (1-b)K$ in 1D is $b = 1/2$ and $K = 2\pi$. Comparing Eq. (7.20) with Eq. (7.17), in light of the numerical result $b \approx 0.242$ $(d = 2)$, suggests that $b = 1/4$ in 2D. Somehow the $\pi/4$ phase factor in Eq. (7.20) changes b to $1/4$. If K is still 2π, then in 2D we have $R_c K = (1-b)K = 3\pi/2 \approx 4.71$, which is slightly above the numerically observed maximum dimensionless hole size $R_c K = 4.65$. Similarly, in 3D, the $\pi/2$ phase factor in Eq. (7.19) probably changes b to 0. If so, the maximum dimensionless hole size in 3D would be $R_c K = 2\pi$. The difference between 2π and the numerically observed maximum $R_c K = 5.86$ is nontrivial, but this can be explained by the increased numerical difficulty in 3D; for example, fewer concentric shells can be formed with the same number of particles in higher dimensions.

7.5 Conclusions

In this chapter, we have investigated the possibility of creating large holes in stealthy hyperuniform many-particle systems using numerical and analytical techniques. We demonstrated that hole sizes in such systems are bounded, first by examining the tail of $E_V(r)$ in unbiased ground states of stealthy potentials, and then by imposing radial

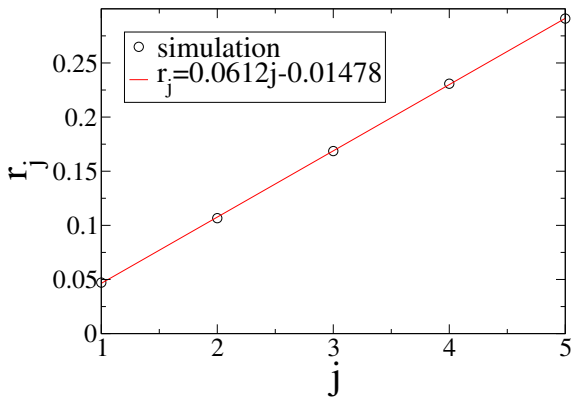

Figure 7.10 The peak locations of $g_1(r)$ for a 2D biased stealthy system of $N = 1600$ particles, at $\chi = 0.10$, with an exclusion hole of dimensionless radius $R_c K = 4.60$ at the origin, averaged over 72 configurations.

exclusion fields to bias stealthy configurations toward ones with the largest possible holes. These results suggest that holes larger than a certain upper bound cannot exist in such systems. We then found that $R_c K$ is bounded from above by π, $3\pi/2$, and 2π in one, two, and three dimensions. A conjectured formula for the upper bound on the dimensionless hole size in d dimensions is $(d+1)\pi/2$. An outstanding problem is a rigorous proof that stealthy infinite systems cannot tolerate holes of arbitrarily large sizes.

Our methods should be applicable to study the existence of arbitrarily large holes in other disordered many-particle systems. This is useful because maximum hole sizes and hole probabilities are related to several other important quantities, including the principal relaxation time T_1 associated with diffusion-controlled reactions among traps. Specifically, consider a reactive chemical species that can diffuse in the void space between particles, and can be absorbed when it is within a certain distance to any particle. The fraction of such species, released at time $t = 0$, that is not absorbed at time t (in other words, the survival probability of the molecules of such species),

can be expanded as a series of exponential functions [308]

$$p(t) = \sum_{n=1}^{\infty} I_n \exp(-t/T_n), \tag{7.21}$$

where I_n are coefficients and T_n are relaxation times. The largest relaxation time T_1 is called the "principal relaxation time." The relaxation times can be measured directly by NMR experiments, in which proton magnetization decays at the phase boundary.[284, 24, 207] It has been demonstrated that T_1 is determined by the largest holes in the configurations, and is therefore divergent if arbitrarily large holes can occur.[308] Indeed, for a reactive species in equilibrium hard-sphere systems, the large-t behavior of its survival probability is actually $p(t) \sim \exp[-t^{3/5}]$ in three dimensions.[308] It is noteworthy that stealthy trap model systems that prohibit arbitrarily large holes would have finite T_1 values.

The stealthy potential employed in this chapter is equivalent to a direct-space pairwise additive potential $v(r)$ whose shape can be tuned by changing the form of the compactly-supported non-negative function $\tilde{v}(\mathbf{k})$ in Eq. (7.4).[328, 352] This chapter and Refs. [328], [353] and [286] used a step-function $\tilde{v}(\mathbf{k})$, corresponding to a real-space pair potential that is a function that oscillates about zero and weakly decaying, similar to Friedel oscillations of the electron density in a variety of systems, including molten metals as well as graphene.[14, 21] However, one could also choose $\tilde{v}(\mathbf{k})$ to be the so-called "overlap" function (proportional to the intersection volume of two d-dimensional spheres of diameter K at distance k), in which the corresponding direct-space pair potential $v(r)$ is a positive decaying function with multiple minima,[28, 325] similar to effective pair interactions that arise in multilayered ionic microgels.[126]

It is interesting to note that if one could realize a solvent that is strictly stealthy, then its maximum hole size is related to the largest solute particles that it can dissolve. In a solvent with a finite value of R_c, particles with exclusion radius larger than

R_c would create intolerably large holes, and would therefore not dissolve. Solute particles smaller than R_c would dissolve in such a solvent, but the effective interactions between them deserve future research. Would particles larger than $R_c/2$ refuse to touch each other in order to avoid combining the holes they create? Also, if the solute particles are only slightly smaller than R_c, solvent particles should be concentrated in concentric-shell regions around the solute particles. Could the interference between these concentric shells induce very complicated effective interactions?

7.6 Appendix: Expected R_c for a Finite Number of Finite-Sized Poisson Configurations

Although there is no theoretical limit on the hole radii in Poisson configurations (ideal gas), one still expects to find a finite R_c if one only studies a finite number of finite sized configurations. If one studies a total of N_c configurations of N particles, one expects to see roughly N_cN uncorrelated holes. Of these N_cN holes, one expects to find the largest hole once. Therefore

$$E_V(R_c) = \exp[-\rho v_1(R_c)] = \frac{1}{N_cN}. \tag{7.22}$$

This equation predicts the largest hole size, R_c, as a function of ρ, N_c, and N. To find R_c presented in Fig. 7.2, notice that for stealthy systems of a given χ and K, ρ is given in Eq. (7.7). Substituting Eq. (7.7) into Eq. (7.22) yields

$$\frac{v_1(R_c)v_1(K)}{2d\chi(2\pi)^d} = \ln(N_cN). \tag{7.23}$$

Here we use $K = 1$, $N_c = 20000$, and $N = 500$ to be consistent with stealthy results.

Chapter 8

Rational Design of Stealthy Hyperuniform Patterns with Tunable Order

8.1 Introduction

In the field of statistical physics, the concepts of order and disorder are used to indicate either the presence or absence of some underlying symmetry or distance-dependent correlation in a many-particle system. In this regard, our physical intuition tells us that crystalline arrangements of matter (*e.g.*, Bravais lattices) are "more ordered" than non-lattice structures and quasicrystals, which in turn appear to be more regular in some sense than disordered systems such as liquids. Moreover, centuries of both experimental and theoretical findings have unequivocally demonstrated that such structural order is a visual manifestation of the underlying correlations that exist in a given many-particle system. As such, complex and necessarily distance-dependent many-particle interactions play a more crucial role in the description of more ordered (and therefore strongly correlated) condensed-phase systems such as solids and liquids

than in more disordered (and therefore weakly correlated) sparse systems such as low-density gases.

Despite the existence of a deterministic correspondence between these underlying correlations and the structure of matter, the identification of a simple metric which unambiguously quantifies the degree of order (or equivalently speaking, the degree of disorder or "randomness") in many-particle systems still remains an outstanding problem in statistical physics. In this work, we directly address this challenge and demonstrate that a potential avenue forward lies in the construction of order metrics that are not constrained by our *perception of order*, since this immensely non-trivial and highly redundant information handling process cannot reliably provide a *de facto* standard for quantifying order [19]. In this regard, human perception is an inherently limited and fallible process when faced with such a task, as we tend to identify patterns even when they do not necessarily exist on one hand (*i.e.*, the Gestalt laws of organization [114]), while mistaking certain intrinsic and complex patterns (*vide infra*) for randomness on the other. Instead, we will introduce and discuss an order metric herein that provides an *unbiased* estimate of order by *equally* accounting for the underlying correlations that exist across all relevant length scales in a given digitized two-phase (two-spin state) system of interest.

To motivate our overall objective, consider the patterns depicted in Fig. 8.1, which contain varying degrees of structural order ranging from a random (Poisson) configuration with no discernible short-, intermediate-, or long-range order to a strongly correlated crystalline configuration displaying order across all length scales. In such cases, it is not unreasonable to require that a useful order metric be unambiguously consistent with our intuitive sense of order. In between such extremal cases, however, our ability to discriminate among the subtle textural differences that exist in certain multi-particle configurations becomes increasingly less accurate and reliable. A particularly striking and quite pertinent example of such textural differences is *hid-*

den long-range order—the defining characteristic of stealthy hyperuniform disordered patterns [328, 325] that we will leverage to gain new insight into the construction of order metrics in this work.

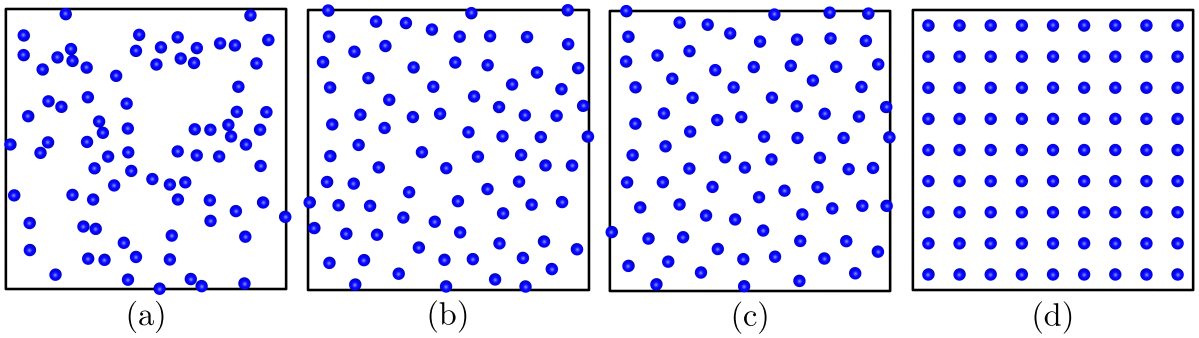

Figure 8.1 Graphical depiction of many-particle configurations (patterns) that contain varying degrees of structural order. (a) Disordered and random (Poisson) configuration with no discernible short-, intermediate-, or long-range order. (b) Configuration generated *via* random sequential addition (RSA) with short- and intermediate-range order [356]. (c) Inclusion of very small collective displacements of the particles in (b) to form a hyperuniform configuration [328], a statistically isotropic configuration that contains *hidden long-range order* yet displays no Bragg peaks. In comparing these two patterns by eye, it can be very difficult to detect the presence of such long-range order in the hyperuniform configuration. (d) Crystalline configuration displaying order across all length scales (and characterized by Bragg peaks).

Hyperuniform patterns (*e.g.*, atoms in a material, trees in a forest, stars in a galaxy, etc.) are exotic amorphous states of matter poised between perfect crystals and liquids in that they exhibit suppressed large-scale density fluctuations (like perfect crystals) while simultaneously presenting as statistically isotropic with no Bragg peaks (like liquids) [317, 349, 325, 306]. In this sense, hyperuniform systems are characterized by *hidden order that is not apparent on large length scales* [325] and are therefore endowed with several novel thermodynamic and physical properties. To date, these extraordinary states of matter can be found in maximally random jammed particle packings [74, 347, 149, 50], jammed athermal granular media [33], jammed thermal colloidal packings [173, 77], dynamical states of cold atoms [177], transitions in non-equilibrium systems [136, 142], quantum systems [88, 90, 315],

surface-enhanced Raman spectroscopy [66], terahertz quantum cascade lasers [68], wave dynamics in disordered potentials based on supersymmetry [346], avian photoreceptor patterns [145], as well as certain Coulombic systems [315]. Disordered hyperuniform patterns of the so-called *stealthy* variety have the additional (and unusual) property of being transparent to radiation across a select range of wavelengths. These systems are also quite remarkable in that particles interacting with certain long-range pairwise potentials can counterintuitively freeze into such disordered states at a temperature of absolute zero [328, 26, 325]. By mapping such stealthy hyperuniform configurations of particles onto network solids, what was previously thought to be impossible became possible: the rational design of disordered cellular solids that have complete isotropic photonic band gaps comparable in size to photonic crystals [95], thereby providing novel and unexplored ways to manipulate light [94, 189, 123, 178].

By providing such a complex landscape of textural differences, stealthy hyperuniform disordered patterns are the ideal candidates for discriminating order in the structure of matter and thus form the cornerstone of the order metric examined herein. Although there is no perfect order metric [321], the mere existence of disordered patterns that contain order hidden from human perception (or at least extremely difficult to discern by visual inspection) makes it quite desirable to formulate an order metric that is able to quantify the degree of order in a given pattern across all relevant length scales. Here we introduce a binary-system version of such a scalar order metric, denoted as τ, to rank digitized two-phase patterns by providing an unbiased estimate of the order contained within a given discretized pattern by equally accounting for contributions across short-, intermediate-, and long-range distances. In this regard, we note that such an order metric has been motivated by several of our earlier works and can be seen as either a discrete analog of an order metric utilized to study translational order in continuous point patterns [325] or as a reciprocal-space analog of the

real-space descriptors successfully employed in the inverse reconstruction of two-phase media textures [147].

We will focus our discussion on two-phase heterogeneous media (*e.g.*, composites, porous materials, polymer blends, biological media, suspensions, gels, etc.), as they represent a very general class of materials, yet we know very little about their existence as stealthy hyperuniform states from a fundamental theoretical perspective. As such, our ability to systematically generate stealthy hyperuniform disordered two-phase heterogeneous media *with a tunable degree of order* is currently lacking. This work also directly addresses this issue by bringing together aspects of pattern recognition, quantification of order in digitized two-phase media, and the theory of heterogeneous media [301] in the design of a series of algorithms that allow for the systematic identification and generation of digitized stealthy hyperuniform patterns. Hence, this work provides the first systematic means to design two-phase digitized stealthy hyperuniform patterns with a *tunable or prescribed degree of order*, which is an extremely timely advance as these exotic states of matter are endowed with a number of novel thermodynamic and physical properties that are only starting to be explored in the fields of materials science and engineering [26, 95, 189, 178]. Our focus on digitized representations of two-phase heterogeneous media is also motivated by the fact that digital images are necessarily pixelized (or voxelized) and modern three-dimensional (3D) printing technologies use digitized data as input, thus providing several immediate and practical applications of the work described herein.

After providing some necessary mathematical definitions and preliminaries, we will first demonstrate that τ, which is designed to discriminate among the subtle textural differences provided by stealthy hyperuniform patterns, is still consistent with the manner in which the human eye perceives order/disorder in clear-cut cases such as highly-ordered crystalline configurations as well as fully uncorrelated (Poisson) patterns. We do so by evaluating τ for a digitized representation of the *Mona Lisa*, which

is arguably one of the most easily recognizable and well-known images in existence to date, and then compare our findings with the most ordered and most disordered configurations of the same resolution. By evaluating τ on *all* stealthy hyperuniform patters discretized on several finite-sized lattices (obtained *via* an exhaustive enumeration algorithm), we demonstrate that τ is not only unambiguously consistent with our intuitive notion of order, but can also discriminate subtle textural differences (*e.g.*, hidden order) that exist in discrete stealthy hyperuniform patterns which are not easily discernible by visual inspection. We then showcase a series of algorithms that allow for the systematic identification and generation of digitized stealthy hyperuniform patterns with tunable or prescribed degrees of order before ending with some conclusions regarding the future outlook of the field.

8.2 Results

8.2.1 Mathematical definitions and preliminaries

In this chapter, we focus on two-dimensional (2D) patterns discretized by (square) pixels on a square ($\mathbf{Z}^2$) lattice (subject to periodic boundary conditions along the x- and y-axes). Such patterns can be represented mathematically by $\sigma(m,n)$, a function which takes two integers as input (m and n, the indices specifying the pixel location in the lattice) and yields a binary output (0 or 1) [73, 190, 51], which can be used to denote up/down spins (*i.e.*, the two-state Ising model [140, 39] for ferromagnetism in statistical mechanics), occupancy/vacancy (*i.e.*, the lattice gas model), or phase A/B in the case of digitized two-phase media. If L_1 and L_2 are the side lengths (in pixels) for a given pattern, then m and n are limited to $1 \leq m \leq L_1$ and $1 \leq n \leq L_2$, respectively. The total number of pixels (or sites) will be denoted as $N_s = L_1 \times L_2$, while N will represent the number of up spins or occupied sites (or the phase assigned a value of 1 in $\sigma(m,n)$ for the case of two-phase media) and is given by

$N = \sum_{m=1}^{L_1} \sum_{n=1}^{L_2} \sigma(m,n)$. Finally, we will let $f = N/N_s$ be the fraction of up spins, lattice occupancy, or fraction of a given phase in two-phase media.

The static structure factor, which describes how a material scatters incident radiation, plays a central role in the order metric defined in this work (*vide infra*) and is given by

$$S(\mathbf{k}) = \frac{1}{N} \left| \widetilde{\rho}(\mathbf{k}) \right|^2, \tag{8.1}$$

in which we utilized the following discrete form of the collective density variable [328]:

$$\widetilde{\rho}(\mathbf{k}) = \sum_{\text{sites}} \sigma(\mathbf{r}) e^{i\mathbf{k}\cdot\mathbf{r}} = \sum_{m=1}^{L_1} \sum_{n=1}^{L_2} \sigma(m,n) e^{i(k_x m + k_y n)}, \tag{8.2}$$

with k_x and k_y representing the x- and y-components of the wavevector $\mathbf{k}$. A digitized pattern will be referred to as "stealthy up to some exclusion radius K" if $S(\mathbf{k}) = 0$ for all $0 < |\mathbf{k}| \leq K$. When combined with the definition of $S(\mathbf{k})$ in equation (8.1), this has two important implications that will be used throughout this work. First, if a pattern $\sigma_1(m,n)$ is stealthy up to some K, then the inverse of this pattern, $\sigma_2(m,n) \equiv 1 - \sigma_1(m,n)$, is also stealthy up to the same K. This results from the fact that $\widetilde{\rho}_1(\mathbf{k})$ has to vanish for all $0 < |\mathbf{k}| < K$ when $\sigma_1(m,n)$ is stealthy up to K. In this case, $\widetilde{\rho}_2(m,n)$ also vanishes for all $0 < |\mathbf{k}| \leq K$, from which it follows that $S(\mathbf{k}) = \frac{1}{N} \left| \widetilde{\rho}_2(\mathbf{k}) \right|^2 = 0$ in this range of $\mathbf{k}$ making $\sigma_2(m,n)$ stealthy up to K as well. Second, if two patterns $\sigma_1(m,n)$ and $\sigma_2(m,n)$ are both stealthy up to some K and $0 \leq \sigma_1(m,n) + \sigma_2(m,n) \leq 1$ holds for every m and n, then the superposition of these two patterns, $\sigma_3(m,n) = \sigma_1(m,n) + \sigma_2(m,n)$, is also stealthy up to K. This results from the fact that the collective density variables for these two individual patterns are both zero. Since $\widetilde{\rho}_3(\mathbf{k}) = \widetilde{\rho}_1(\mathbf{k}) + \widetilde{\rho}_2(\mathbf{k}) = 0$, $S(\mathbf{k}) = 0$ for $\sigma_3(m,n)$, which makes this pattern also stealthy up to K. We denote such a pattern as "multi-stealthy" since this configuration is comprised of multiple stealthy configurations and note in

passing that such a configuration (by definition) is also endowed with the property of being "multi-hyperuniform".

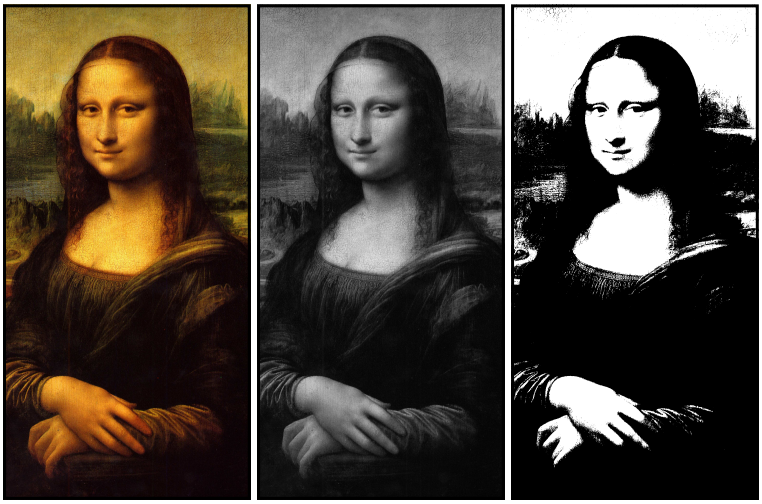

Figure 8.2 Graphical depiction of the famous portrait of the *Mona Lisa* by Leonardo da Vinci (*circa* 1503-1506) in RGB (the additive red–green–blue model), grayscale, and black & white formats, each discretized on a square lattice with a resolution of 2048×4096 pixels (with the white pixels in the black & white image having an occupancy of 31.7%). The RGB figure was converted to grayscale using the formula $Y = 0.2989 \cdot R + 0.5870 \cdot G + 0.1140 \cdot B$, and then to black & white using Otsu's method, which chooses the threshold value to minimize the intraclass variance of the thresholded black and white pixels [221]. The ratio of the order metric associated with the black & white (or binary) image of the *Mona Lisa*, $\tau[\mathscr{C}]$, to the order metric of an ensemble of Poisson configurations, $\tau[\mathscr{P}]$, was computed as $\tau[\mathscr{C}]/\tau[\mathscr{P}] \approx 10^5$, which quantitatively demonstrates that the *Mona Lisa* is significantly *more ordered* than a collection of random spatially uncorrelated configurations containing the same number of particles. With respect to the order metric corresponding to the most ordered (crystalline) configurations ($\tau[\mathscr{O}]$) that can be discretized on the same lattice, $\tau[\mathscr{C}]/\tau[\mathscr{O}] \approx 10^{-1}$, a finding which quantitatively delineates the degree of order in the *Mona Lisa* on a relative scale that spans six orders of magnitude (in τ) and again agrees with the general consensus that there is a high relative degree of order contained in this famous portrait.

8.2.2 Quantifying the degree of order in discrete patterns: The τ metric

Although no perfect order metric necessarily exists [321], many order metrics have been devised to quantify the degree of order/disorder of complex systems at various

length scales, including those that account for bond orientations [280, 249] and translational order [153, 326]. For some of these metrics, the degree of order is referenced to a particular perfect crystalline structure and in other instances a reference state is not assumed. Invariably, all previously employed order metrics incorporate only *spatially local* information in practice.

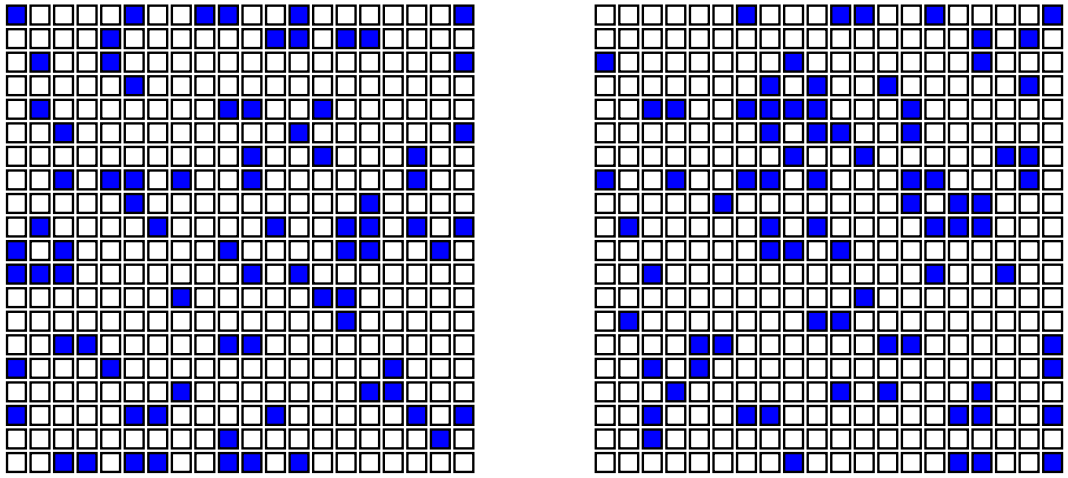

Figure 8.3 Graphical depiction of two patterns discretized on a periodic $L \times L$ square lattice (with $L = 20$) comprised of $N = 80$ particles ($f = 0.2$) which are represented by blue squares. While the disordered pattern ($\mathscr{C}$) on the *left* is hyperuniform and stealthy for an exclusion radius of $K = 1$ (in units of $2\pi/L$), the disordered pattern ($\mathscr{P}$) on the *right* is simply a Poisson (random) pattern that is neither stealthy nor hyperuniform. This figure demonstrates that while stealthy hyperuniform patterns look very similar at short-range, they contain *hidden long-range order* (*i.e.*, suppression of large-scale number density fluctuations) that is not easily detectable by eye. Since $\tau[\mathscr{C}]/\tau[\mathscr{P}] = 3/2$, the τ order metric quantitatively illustrates the fact that this disordered stealthy hyperuniform configuration—purely through the presence of hidden long-range order—is indeed significantly more ordered than the random Poisson pattern.

To allow for a quantitative measure of the degree of order contained within a given discrete pattern *across all relevant length scales* with respect to the uncorrelated system, we introduce the τ metric, defined as:

$$\tau[\mathscr{C}] \equiv \sum_{\mathbf{k}\neq\mathbf{0}} \left[S_{\mathscr{C}}(\mathbf{k}) - S_{\mathscr{P}}(\mathbf{k})\right]^2 = \sum_{\mathbf{k}\neq\mathbf{0}} \left[S_{\mathscr{C}}(\mathbf{k}) - 1 + f\right]^2 , \tag{8.3}$$

in which both summations are over all $\mathbf{k}$-vectors associated with the natural period of the simulation box (excluding the origin ($\mathbf{k} \neq \mathbf{0}$)) and $S_{\mathscr{C}}(\mathbf{k})$ and $S_{\mathscr{P}}(\mathbf{k}) = 1 - f$ are the structure factors, *i.e.*, the Fourier transforms of the corresponding real-space two-point correlation functions [146], for a configuration of interest ($\mathscr{C}$) and an *ensemble* of Poisson patterns ($\mathscr{P}$), respectively. In this regard, the definition of τ in equation (8.3) can be seen as a discrete extension of the order metric employed in our earlier study of translational order for point patterns in continuous spaces [325], in which $S_{\mathscr{P}}(\mathbf{k})$ is unity (as expected for continuous Poisson point patterns). Similar to the continuous case, this order metric will register large values due to the occurrence of sharp peaks in lattice patterns, which are of finite height in any finite system but become infinite (Dirac delta functions) in the infinite-system-size limit. Furthermore, this definition of also implies that τ is invariant with respect to trivial symmetry operations, including translations, rotations, and reflections. It is also important to stress here that τ will also register very large values in the vicinity of critical points (*e.g.*, Ising-like critical points [98, 97]), due to the fact that $S(\mathbf{k})$ diverges as $\mathbf{k} \to \mathbf{0}$ in the infinite-system-size limit. Hence, while one should exercise caution in interpreting such an order metric in the vicinity of a critical point, τ might also be fruitfully employed to detect whether a disordered system is in fact approaching a critical point. This is a potentially interesting research avenue to explore in the future as all of the examples considered herein are located far away from any critical points.

By defining τ with respect to an ensemble of spatially uncorrelated Poisson point processes, *i.e.*, a collection of random and disordered arrangements of particles that is characterized by $S_{\mathscr{P}}(\mathbf{k}) = 1 - f \; \forall \; \mathbf{k} \neq \mathbf{0}$, τ can also be seen as a reciprocal-space analog of the real-space descriptors successfully employed in the inverse reconstruction [147] of two-phase media textures. Such textures are of importance across a wide variety of fields, ranging from the *microscopic* length scales encountered in materials science (*e.g.*, the microstructure of sandstones, metal–ceramic composites, and

concrete) and systems biology (*e.g.*, the structure of plant and animal tissues, cell aggregates, and medical imaging) to the *macroscopic* length scales found in ecology (*e.g.*, distributions of trees in forests) and cosmology (*e.g.*, galaxy distributions and stellar constellations).

As seen in equation (8.3), τ accumulates the deviation of $S_{\mathscr{C}}(\mathbf{k})$ from unity for all $\mathbf{k} \neq \mathbf{0}$ (in a single period as defined by the $\mathbf{k}$–point mesh required to accurately sample a square lattice with a spatial extent of length $L_1 \times L_2$), thereby providing an *unbiased* estimate of the order contained within a given discrete pattern by *equally* accounting for contributions across short-, intermediate-, and long-range distances. This salient feature of the τ order metric becomes immediately evident when one attempts to address the following question: what is the degree of order in the *Mona Lisa*, which is arguably one of the most easily recognizable and well-known images in existence to date?

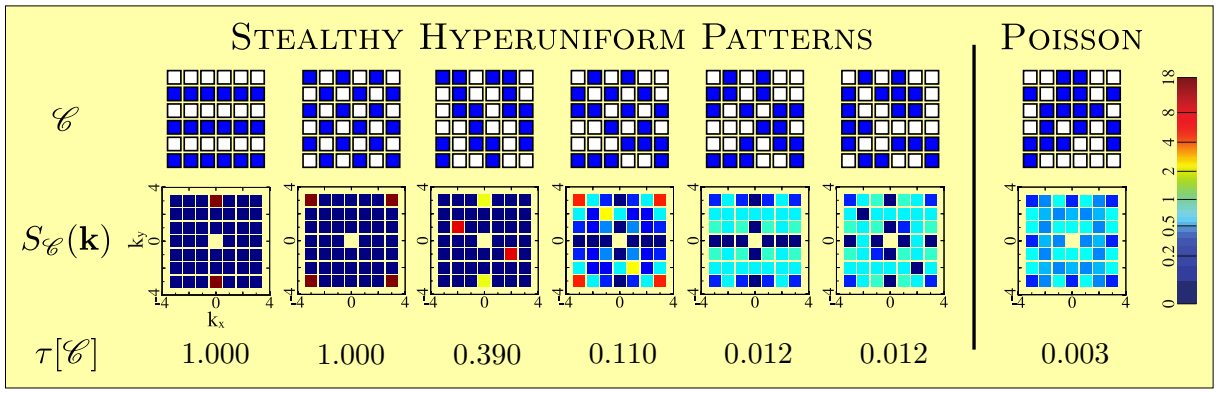

Figure 8.4 (*Top row*) Graphical depiction of a representative series of six stealthy hyperuniform configurations and a single Poisson (random) configuration discretized on a periodic $L \times L$ square lattice (with $L = 6$). Each of these configurations, $\mathscr{C}$, is comprised of $N = 18$ particles (which corresponds to an occupancy of $f = 18/36 = 0.5$) that are represented by blue squares. (*Middle row*) Corresponding structure factors, $S_{\mathscr{C}}(\mathbf{k})$, for each configuration. For the six stealthy hyperuniform configurations, $S_{\mathscr{C}}(\mathbf{k}) = 0$ for some positive exclusion radius, $K \geq 1$ (in units of $2\pi/L$), a property which is not shared by the spatially uncorrelated Poisson pattern on the far right. (*Bottom row*) Corresponding order metric values, $\tau[\mathscr{C}]$, for each configuration as defined by equation (8.3). Note that these patterns have been arranged from *most* ordered to *least* ordered, based on the computed values of $\tau[\mathscr{C}]$.

To quantitatively ascertain the degree of order in this famous portrait, τ was computed for a black & white (or binary) representation of the *Mona Lisa* ($\tau[\mathscr{C}]$) with respect to a *reference* set of configurations that represent (*i*) the most ordered patterns ($\tau[\mathscr{O}]$) and (*ii*) the most disordered patterns ($\tau[\mathscr{P}]$) that can be discretized on a square lattice with the same resolution and number of particles (occupancy) as the black & white image of the *Mona Lisa* (see Fig. 8.2 for more details). In doing so, we determined that τ resolves the degree of order contained in all patterns that can be discretized on this lattice across a span of six orders of magnitude, as defined by the ratio $\tau[\mathscr{O}]/\tau[\mathscr{P}] \approx 10^6$. With $\tau[\mathscr{C}]/\tau[\mathscr{P}] \approx 10^5$, the *Mona Lisa* was found to be significantly *more ordered* than a collection of random spatially uncorrelated Poisson configurations containing the same number of particles—a quantitative finding that is in strong agreement with the general consensus that there is a high relative degree of order contained in this famous portrait. On the same scale, τ for the *Mona Lisa* only differed by one order of magnitude from the most ordered (crystalline) configurations, as given by the computed ratio of $\tau[\mathscr{C}]/\tau[\mathscr{O}] \approx 10^{-1}$. On the surface, this observation again agrees with the general consensus that a portrait of a human subject is intrinsically ordered; however, the relatively close location of the *Mona Lisa* with respect to the most ordered configurations (*e.g.*, the simple checkerboard and striped-phase configurations) is less obvious by visual inspection and seems to be a direct consequence of the fact that τ not only accounts for the presence of order across short-, intermediate-, and long-range distances, but also equally weights each of these contributions in the computation of the overall order metric value.

As such, τ is a sensitive measure of the presence of order across all relevant length scales and is therefore of particular importance in the discrimination of stealthy hyperuniform configurations—patterns which are characterized by the presence of *hidden long-range order* arising from the suppression of number density fluctuations on large length scales. As seen in Fig. 8.3, such patterns are often difficult, if not impossible,

to detect by eye, as the contrast sensitivity of human vision peaks at fairly short distances [42], thereby placing a larger relative weight on observed textural similarities (or lack thereof) in this portion of the distance spectrum. This limitation is overcome by the use of the τ order metric: by quantitatively detecting the presence of order across all length scales, τ can easily discern a disordered stealthy hyperuniform configuration from a random Poisson point pattern.

The strength and utility of τ as a quantitative and unbiased estimator of the degree of order in a given discretized pattern lies in the fact that τ not only agrees with our intuitive definition of order in unambiguous textural comparisons (*i.e.*, by clearly differentiating significantly ordered crystalline structures from disordered Poisson configurations) but can also discriminate subtle textural differences that are not so easily discernible by visual inspection (*i.e.*, by clearly differentiating disordered patterns that contain some degree of hidden order, such as the aforementioned class of stealthy hyperuniform configurations, from truly random spatially uncorrelated Poisson patterns).

In this regard, the defining attributes of τ as an order metric are most clearly illustrated by a detailed consideration of the series of discretized patterns provided in Fig. 8.4. Obtained *via* an exhaustive enumeration of the configurational space corresponding to a periodic 6×6 square lattice, six representative stealthy hyperuniform patterns (in which $S(\mathbf{k}) = 0$ for some positive exclusion radius, $K \geq 1$, in units of $2\pi/L$ throughout the manuscript) are arranged from *most* to *least* ordered according to their respective τ values. From this figure, it is clear that the crystalline striped-phase and simple checkerboard configurations represent the most ordered stealthy hyperuniform patterns that can be discretized on a 6×6 square lattice, a fact that is appropriately reflected in their computed order metric values of $\tau = 1.000$ and relatively large exclusion radii of $K = 3$ and $K = 3\sqrt{2}$, respectively. With an order metric value of $\tau = 0.390$, the staircase configuration is visibly less ordered than the

configurations on the left, and is also accompanied by a smaller exclusion radius of $K = \sqrt{5}$.

More importantly, the success of τ extends well beyond visually detectable ranges of order. For the three remaining stealthy hyperuniform configurations in Fig. 8.4, all of which have an exclusion radius of $K = 1$, it becomes increasingly more difficult to discern the level of order (or lack thereof) in these patterns by eye. In this regard, a careful visual examination of the configuration characterized by $\tau = 0.110$ reveals that this pattern can be constructed *via* the introduction of several defects (*i.e.*, replacements of select occupied sites by vacancies) into the simple checkerboard pattern, a fact which is quantitatively captured by τ. However, the fact that the two remaining stealthy hyperuniform configurations to the right of Fig. 8.4 *appear* as patterns that contain no apparent or discernible order is an inaccurate assessment of these configurations. When compared to the aforementioned crystalline configurations, these two patterns are visibly more disordered, a fact which is again quantitatively reflected by the relatively lower value of $\tau = 0.012$ computed for each of these configurations. In the same breath, these two patterns are indeed stealthy hyperuniform configurations (with $S(\mathbf{k}) = 0$ for $K = 1$), and as such, these patterns contain some degree of hidden long-range order that is not present in a spatially uncorrelated Poisson point pattern, an example of which is given on the far right of Fig. 8.4, wherein $S(\mathbf{k}) \neq 0$ for $K = 1$.

Herein lies the key strength and utility of the τ order metric: by treating contributions to the order of a given configuration that span short-, intermediate-, and long-range distances on an equal footing, τ is able to detect the presence (or absence) of such subtle long-range order. This conjecture is strongly indicative that such an order metric (or appropriate modifications thereof) could be employed in pattern recognition algorithms to identify and quantitatively discern textural similarities and differences that exist across all length scales relevant to the problem of interest, with applications ranging from computer vision and image processing to machine learning.

With such a robust and powerful order metric in hand, we now turn our attention to the measure for "stealthy hyperuniform" digitized patterns, on account of their intrinsic long-range orders that are difficult, if not impossible, for human visual perception to identify. For this purpose, we have devised several algorithms that allow for the systematic identification and generation of disordered stealthy hyperuniform patterns with tunable or prescribed degrees of order as measured by τ. We begin this investigation with an exhaustive enumeration of all possible patterns for small system sizes ($L_1 = L_2 \leq 6$), and then move on to larger and more complicated stealthy hyperuniform patterns generated with stochastic global optimization techniques such as simulated annealing as well as a direct methodology based on superposition of stealthy hyperuniform patterns.

8.2.3 Enumeration of discrete stealthy hyperuniform patterns

In this work, we have explicitly investigated all of the possible patterns that can exist on the 2D square lattice with side lengths, $L_1 = L_2 = L \in \{3, 4, 5, 6\}$, subject to standard periodic boundary conditions along both axes. Unlike the case of continuous point-particle systems, for which the number of configurations that can exist comprises an uncountable infinite set, the systems considered herein have a discrete number of degrees of freedom due to the fact that each lattice site is binary and can either be occupied by a particle or vacant (unoccupied). As such, there exists a finite number of possible patterns that can be discretized on a square lattice of side length L, namely $2^{L \times L}$, and each configuration must be enumerated to obtain an accurate count of the number of stealthy hyperuniform patterns that exist on these underlying lattices. The largest system considered was the 6×6 square lattice, which required explicit enumeration of $2^{36} = 6.9 \times 10^{10}$ configurations. For each configuration, the corresponding structure factor, $S(\mathbf{k})$, was computed for the smallest

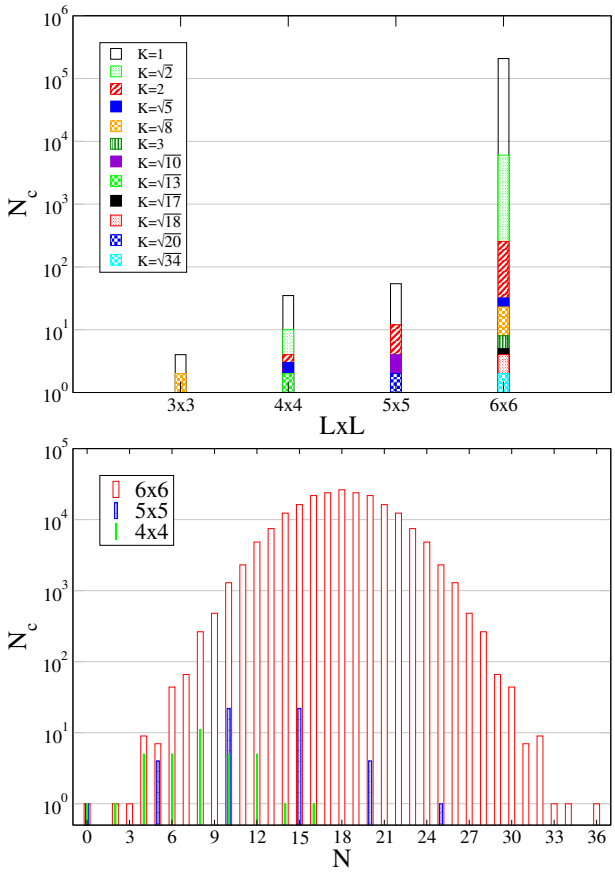

Figure 8.5 The number of distinct stealthy hyperuniform patterns identified by an exhaustive enumeration of the discrete patterns existing on a periodic $L \times L$ square lattice (with $L \in \{3, 4, 5, 6\}$), sorted by (*top*) L and K (in units of $2\pi/L$) and (*bottom*) L and N.

k-vectors contained in the reciprocal-space (k-point) mesh, namely $\mathbf{k}_1 = [1, 0]$ and $\mathbf{k}_2 = [0, 1]$, as $S(\mathbf{k}_1) = S(\mathbf{k}_2) = 0$ is the minimal requirement for classification as a stealthy hyperuniform pattern (with a corresponding exclusion radius of $K = 1$). Each time a configuration met this criteria, it was added to a running list of stealthy hyperuniform configurations (that was maintained throughout the execution of the enumeration algorithm) and explicitly compared against all other structures on the list to remove trivial configurational degeneracies due to symmetrical equivalence (*via* the set of translations, rotations, and reflections defined by the periodicity of the underlying lattice). The final list of non-redundant and symmetry-unique configura-

tions constituted the set of existing stealthy hyperuniform configurations for a given lattice [190].

The results of this enumeration study are summarized in Fig. 8.5. As L increases, the top panel shows that the number of unique configurations that are stealthy up to a certain K also increases, as expected. However, the growth increments are not uniform. For instance, the number of configurations that are stealthy up to $K = 1$ increases dramatically when L increases from 5 to 6, but not as much when L is increased from 4 to 5. This non-uniformity is caused by the underlying relationship between the prime factorization of L and the set of N values that can admit stealthy hyperuniform configurations. As the bottom panel of Fig. 8.5 shows, only the N values that are integer multiples of 5 admit stealthy configurations for $L = 5 = 1 \times 5$. For $L = 4 = 2 \times 2$, only the N values that are multiples of 2 admit stealthy configurations. The $L = 6 = 2 \times 3$ case, however, is much richer. The set of allowed N values not only includes multiples of 2 and 3, but also includes sums of multiples of 2 and 3. As a result, N can have any value between 0 and 6×6, except 1 and 35. Here, the exception for $N = 1$ is due to the fact that 1 is not a sum of a multiple of 2 and 3. The exception for $N = 35$ follows from the fact that this case is the inverse of $N = 1$. Compared to the $L = 5$ case, the $L = 6$ case allows many more N choices and therefore produces a drastically increased number of stealthy patterns. We note in passing that the bottom panel of Fig. 8.5 also shows that the distribution of N in the stealthy hyperuniform configurations is roughly a Gaussian (a parabola in our semi-logarithm plot) centered at $N = L^2/2$.

8.2.4 Stochastic identification of discrete stealthy hyperuniform patterns

In this work, we also utilized the simulated annealing (SA) global optimization scheme [163] in conjunction with classical (Metropolis-Hastings) Monte Carlo (MC)

simulations to generate stealthy hyperuniform configurations discretized on square lattices that were too large for an exhaustive enumeration study. For a given trial configuration, $\mathscr{C}$, the fictitious energy (or objective function) employed in these SA-MC simulations was chosen to be:

$$\theta[\mathscr{C}] = \sum_{\mathbf{k},0<|\mathbf{k}|\leq K} \left[S_{\mathscr{C}}(\mathbf{k}) - S_{\mathscr{T}}(\mathbf{k})\right]^2 = \sum_{\mathbf{k},0<|\mathbf{k}|\leq K} \left[S_{\mathscr{C}}(\mathbf{k})\right]^2, \tag{8.4}$$

in which $S_{\mathscr{C}}(\mathbf{k})$ and $S_{\mathscr{T}}(\mathbf{k})$ are the corresponding structure factors for $\mathscr{C}$ and a *target* ($\mathscr{T}$) configuration, respectively, and the summations are carried out over all $\mathbf{k}$ for which $0 < |\mathbf{k}| \leq K$, based on a pre-defined exclusion radius K. Since our goal is to use SA-MC to stochastically generate stealthy hyperuniform configurations, we take $\mathscr{T}$ to represent a fictitious *target* stealthy hyperuniform configuration that is characterized by $S_{\mathscr{T}}(\mathbf{k}) = 0 \; \forall \; \{\mathbf{k} \mid 0 < |\mathbf{k}| \leq K\}$. Quite interestingly, this objective function is a direct analog of τ, demonstrating the utility of this order metric in the first systematic design of stealthy hyperuniform two-phase digitized patterns with prescribed degrees of order.

The simple quadratic functional form for θ in equation (8.4) is therefore minimized once a configuration $\mathscr{C}$ is located with $S_{\mathscr{C}}(\mathbf{k}) = 0$ for all $\mathbf{k}$-vectors contained

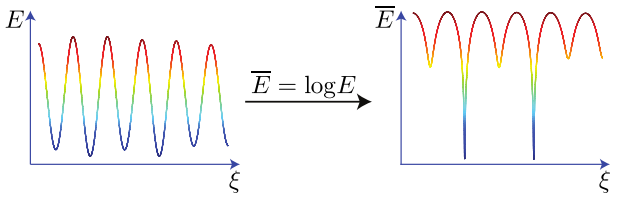

Figure 8.6 Graphical depiction of a one-dimensional slice through a high-dimensional potential energy surface (PES) before (*left*) and after (*right*) the application of a logarithmic transformation on the energy, E, *i.e.*, $\overline{E} = \log(E)$, as a function of the configurational coordinate, ξ. The existence of multiple minima in such high-dimensional PES (depicted here by the presence of two degenerate *global* minima in the vicinity of three low-lying and nearly degenerate *local* minima) plagues global optimization techniques such as simulated annealing (SA) and can be significantly alleviated *via* the application of this logarithmic transformation on the objective function.

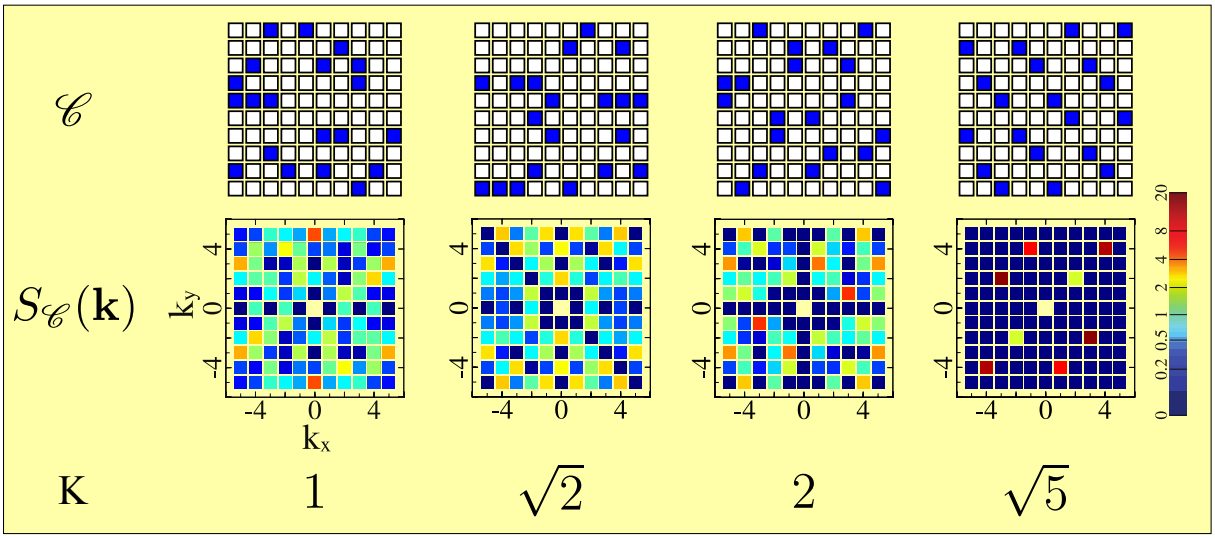

Figure 8.7 (*Top row*) Graphical depiction of a representative series of stealthy hyperuniform patterns generated using our Simulated Annealing-Monte Carlo (SA-MC) approach. Each of these stealthy patterns is discretized on a periodic 10×10 square lattice and comprised of $N = 20$ particles ($f = 0.2$). (*Middle row*) Corresponding structure factors, $S(\mathbf{k})$, for each stealthy pattern in which $S(\mathbf{k}) = 0$ for some positive exclusion radius, $K \geq 1$. (*Bottom row*) Corresponding exclusion radii, K, for each stealthy pattern. Note that these stealthy patterns have been arranged in *increasing* order based on the values of K. The corresponding order metric values, τ, for each of these stealthy patterns were computed as 0.18, 0.19, 0.33, and 2.59, respectively, indicating that τ and K are again positively correlated in these instances.

within the aforementioned exclusion radius, thereby yielding a stealthy hyperuniform configuration with a prescribed degree of order. Due to the presence of "multiple minima" on these high-dimensional potential energy surfaces (PES), which hinders the success rate of global optimization techniques such as SA-MC, we applied a logarithmic transformation on the objective function, *i.e.*, $\overline{\theta} = \log(\theta)$, to clearly differentiate the energy scales associated with global and local minima. As Fig. 8.6 shows, this logarithmic transformation drastically improves the depth of the ground state energy basins, making them much more favorable at lower temperatures. A true ground state (in this case a stealthy hyperuniform pattern) should have $\theta = 0$ or $\overline{\theta} = -\infty$. Due to machine precision (double precision arithmetic was employed throughout this work), the evaluated $\overline{\theta}$ is often around -60. Based on this observation, we considered

Table 8.1 Success rates for generating stealthy hyperuniform configurations *via* Simulated Annealing-Monte Carlo (SA-MC) simulations as a function of N and K on a 10×10 square lattice. For each N and K, 1000 independent SA-MC runs were attempted to determine the final success rate.

f	Success Rate for $K =$					
	1	$\sqrt{2}$	2	$\sqrt{5}$	$\sqrt{8}$	3
0.1	1.000	1.000	0.980	1.000	0.999	0.989
0.2	0.995	0.987	0.158	0.001	0.000	0.000
0.3	0.993	0.771	0.047	0.000	0.000	0.000
0.4	0.993	0.726	0.039	0.000	0.000	0.000
0.5	0.989	0.600	0.007	0.000	0.000	0.000

a SA-MC run to be successful in generating a stealthy hyperuniform configuration once $\overline{\theta}[\mathscr{C}] < -50$ (which corresponds to $\theta[\mathscr{C}] < 10^{-50} \approx 0$).

During the SA-MC optimizations, the temperature T was slowly decreased using an exponential cooling schedule, *i.e.*, $T = \exp(-3 \times 10^{-7} N_t/N)$, in which N_t is the number of trial MC moves attempted (at a given T) and N is the number of particles (or occupied sites), until $T = T_{\min} < 0.1$. To allow for finer refinements of the trial configuration and further minimization of the fictitious energy, an additional $2000 \times N$ trial MC moves were attempted at $T = 0$. Initially, the trial MC moves consist of swapping a randomly chosen occupied site with a randomly chosen unoccupied site. However, the acceptance ratio for this specific type of trial MC move becomes too low as T decreases (*i.e.*, the system is not exploring configurational space and is essentially stuck). To remedy this issue, we switched to "local" trial MC moves once the acceptance ratio dips below a preset threshold of $A_{\min} = 0.1$ (*i.e.*, less than 1,000 accepted moves per 10,000 trial moves). These local trial MC moves involved swapping a randomly chosen occupied site with a randomly chosen unoccupied site that is located within a specified cutoff distance (usually set to approximately 3-4 units in the lattice spacing). Furthermore, we also gradually decrease this cutoff distance thereafter (until it reaches 1 unit in the lattice spacing) to maintain an acceptance ratio above $A_{\min}$.

The success rate for our SA-MC program on a 10×10 lattice ($L = 10$) is summarized in Table 8.1 for $f = N/L^2 \leq 0.5$. Since our numerical method treats occupied sites and unoccupied sites symmetrically, the success rate for $f = x > 0.5$ should be equal to the success rate for $f = 1 - x$. As f approaches 0.5, the observed decrease in the success rate is most likely due to the fact that the search space, *i.e.*, the number of configurations with a particular N, given by $(L^2)!/[N!(L^2 - N)!]$, is largest for $f = 0.5$. In this regard, it would be interesting to find robust alternative methods for overcoming this numerical difficulty and one such approach will be presented below. Four configurations (with $f = 0.2$) identified using this SA-MC method are shown in Fig. 8.7. The annealed configurations are disordered for the smaller three K values, but crystalline for $K = \sqrt{5}$. We note here that this disorder-to-order transition with increasing K was also observed in continuous stealthy hyperuniform systems [328].

8.2.5 Design of stealthy hyperuniform patterns *via* superposition

To find stealthy hyperuniform patterns for a particular system size and N, one can simply enumerate all possible configurations if the system size is small and use SA-MC for larger systems if N is small. That leaves us with the following question: what method should one use if the system size and N are both large? Here we present one such method, which involves a superposition of stealthy hyperuniform patterns with smaller N values. As discussed above, if two patterns $\sigma_1(m, n)$ and $\sigma_2(m, n)$ are both stealthy up to some K and $\sigma_3(m, n) = \sigma_1(m, n) + \sigma_2(m, n)$ is always between 0 and 1 (*i.e.*, there is no overlap in a given phase between thee two configurations), then $\sigma_3(m, n)$ is also stealthy up to K. As such, we simply identify "building block" patterns with relatively small N values and then translate them to eliminate overlaps before superposition.

Fig. 8.8 contains several examples of stealthy hyperuniform patterns (up to $K = 1$) that have been generated using this superposition technique. We chose $L = 6$ for visual clarity, but the method is equally (and particularly) suitable for larger systems. For this system size and K, our enumeration study found 1 stealthy configuration with $N = 2$ and 9 stealthy configurations with $N = 4$. The configuration with $N = 2$ will be denoted as a *doublet* (D) and represents the smallest building block in this superposition scheme. Of the 9 $N = 4$ configurations, 5 of them can be decomposed as superpositions of pairs of doublets, denoted by $D_2 = D \oplus D$ as a *doublet of doublets*. The remaining 4 configurations with $N = 4$ are therefore *quartets* (Q). As Fig. 8.8 illustrates, we can superpose these doublet and quartet building blocks to create complex stealthy hyperuniform patterns. For example, by superposing nine doublets one can create the configuration labeled D_9 in Fig. 8.8 and by superposing three quartets and three doublets, one can create the configuration labeled Q_3D_3. For a configuration generated by this superposition technique to be stealthy up to a given K value, $S(\mathbf{k})$ at two different $\mathbf{k}$-vectors are constrained to be zero. Fig. 8.8 also demonstrates how D and Q building blocks satisfy these constraints.

8.3 Discussion

On account of the daunting range of technical applications, our ability to perceive, analyze, and interpret the wide class of spatial patterns that exist across multiple length scales in matter is a problem of fundamental importance across the physical and biological sciences. Limited aspects of this broad requirement can be attained by human visual capacity as Darwinian evolution of our species has endowed us with a pattern recognition sensitivity that is largely focused on attributes based on short- and intermediate-range order [42]. As a result, it has become increasingly more important to define order metrics that objectively account for pattern attributes that

span all of the relevant distances defined by the system of interest. This chapter accomplishes this objective by defining and analyzing a specific order metric, denoted by τ, which ranks digitized two-phase (binary) images by providing an *unbiased* estimate of the order contained within a given pattern by *equally* accounting for contributions across short-, intermediate-, and long-range distances and therefore fulfills these requirements.

For the sake of simplicity in this initial presentation, τ was defined for square lattices of binary pixels subject to periodic boundary conditions. Inspired by several of our previous works, the central strategy exploited in the definition of τ involves the quantitative comparison of the structure factor ($S_{\mathscr{C}}(\mathbf{k})$) for a given configuration of interest to that of an ensemble of random and spatially-uncorrelated Poisson patterns ($S_{\mathscr{P}}(\mathbf{k})$), which is an obvious standard for the absence of order in a pattern. In this work, special attention has been devoted to the τ measure for two-phase (binary) discretized stealthy hyperuniform patterns, on account of the fact that these disordered systems are characterized by intrinsically hidden long-range order that is difficult, if not impossible, to discern by visual inspection. For this purpose, we have devised a series of novel algorithms that provide the first systematic means to design novel two-phase digitized stealthy hyperuniform patterns with *tunable or prescribed degrees of order*, which is an extremely important and timely advance as these exotic amorphous states of matter are endowed with a number of novel thermodynamic and physical properties that are only starting to be explored in the fields of materials science and engineering.

The findings reported herein demonstrate that τ is a quantitative and unbiased estimator of the degree of order in discrete patterns, and are strongly indicative of the utility of such an order metric across a myriad of fields, including visual perception [233], digital image processing and complex pattern recognition (*e.g.*, facial/voice recognition, linguistics, lexical similarity), information theory (*e.g.*, Shannon entropy,

cryptography, and encoding) [267, 167, 120, 156], as well as data-intensive statistical efforts such as supervised/unsupervised machine learning. In this regard, τ (or appropriate modifications thereof) could be employed in pattern recognition algorithms to identify and quantitatively discern textural similarities and differences that exist across all length scales relevant to the problem at hand.

As an example of the utility of τ in cryptography and encoding [156, 130], binary pixel patterns (*e.g.*, 2D bar codes) produced by useful encoding methods should appear to be similar to random Poisson patterns. Hence their τ measures should numerically be small, *i.e.*, free from easily distinguishable geometric order over a wide range of length scales [156], and thus τ can be a quite sensitive metric when attempting to introduce (or remove) order in a given pattern across different length scales. In this regard, a sensitive order metric like τ that surpasses the capacity of human perception in detecting order across a wide range of length scales can also be useful in the identification of descriptors for machine learning or image classification tasks [130]. Here we note in passing that our visual pattern recognition is even less effective for 3D input (when compared to 2D patterns), whereas τ naturally incorporates changes in dimensionality without diminished capacity for pattern recognition, a feature of τ which becomes increasingly more important when quantifying order in such high-dimensional data-intensive applications. Finally, it would also be interesting to quantitatively compare τ order metric values with the corresponding Shannon entropy and/or Kolmogorov complexity measures for digitized stealthy hyperuniform images [267, 167, 120].

While the Fourier transform is the basic mathematical operation underlying the definition of τ, alternative order metric definitions which utilize different integral transformations should also be considered. One such direction could involve "wavelets" [203]. The central comparison issue here would be whether or not such

an alternative strategy manages to produce equal sensitivity to short-, intermediate-, and long-range patterns or textures.

The famous Mona Lisa portrait by Leonardo da Vinci, reduced to a binary black & white format, has been used in this study to illustrate the sensitivity of τ to spatial order. It is worth pointing out that τ would be unchanged if that portrait was partially translated across its assigned periodic boundaries; in this case, human observation of the resulting pattern would be fundamentally disrupted by contrast. Furthermore, the treatment of this famous portrait as a case study in this work strongly supports the extension of τ to systems with grayscale and/or RGB generalizations of binary pixel states. Such research directions will significantly increase the regime of technological applicability of this order metric while simultaneously enabling further exploration into the complex yet subtle interplay between order and disorder in the structure of matter.

8.4 Methods

8.4.1 Domain of $S(\mathbf{k})$ in discrete patterns

In computing $S(\mathbf{k})$, one only needs to consider a finite number of $\mathbf{k}$-vectors due to the following three reasons. First, the $\mathbf{k}$-vectors need to be consistent with the size of a given pattern, *i.e.*, k_x and k_y must be integer multiples of $2\pi/L_1$ and $2\pi/L_2$, respectively. Second, since $S(\mathbf{k})$ is periodic for the discretized systems considered

herein,

$$
\begin{aligned}
S(k_x + 2\pi, k_y) &= \frac{1}{N} \left| \sum_{m=1}^{L_1} \sum_{n=1}^{L_2} \sigma(m,n) e^{i[(k_x+2\pi)m + k_y n]} \right|^2 \\
&= \frac{1}{N} \left| \sum_{m=1}^{L_1} \sum_{n=1}^{L_2} \sigma(m,n) e^{i(k_x m + k_y n) + i2\pi m} \right|^2 \\
&= \frac{1}{N} \left| \sum_{m=1}^{L_1} \sum_{n=1}^{L_2} \sigma(m,n) e^{i(k_x m + k_y n)} \right|^2 \\
&= S(k_x, k_y), \qquad (8.5)
\end{aligned}
$$

and similarly, $S(k_x, k_y + 2\pi) = S(k_x, k_y)$, thereby reducing the number of $\mathbf{k}$-vectors *via* translational symmetry. Furthermore, $S(\mathbf{k})$ for approximately half of these $\mathbf{k}$-vectors are independent variables since (*cf.* equations (8.1)-(8.2)) $S(\mathbf{0}) = N$ and $S(-\mathbf{k}) = S(\mathbf{k})$.

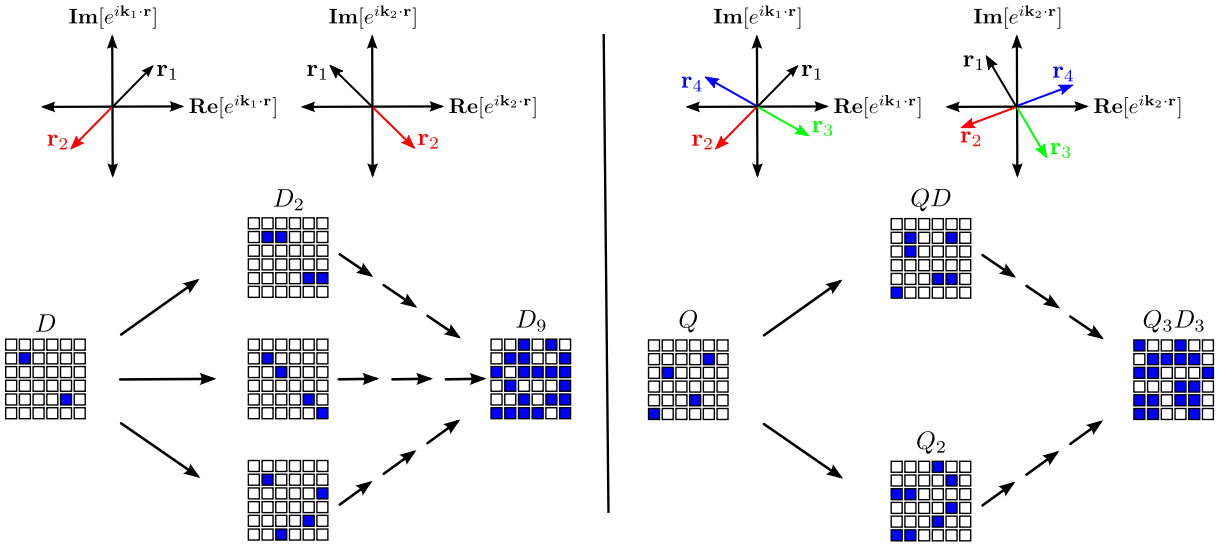

Figure 8.8 (*Upper left*) Vectorial representation of a stealthy pattern comprised of $N = 2$ particles. The corresponding structure factor, $S(\mathbf{k}) = \frac{1}{N}|\sum_{j=1}^{N} \exp[i\mathbf{k}\cdot\mathbf{r}_j]|^2$, will vanish at a given pair of $\mathbf{k}$-vectors, $\mathbf{k}_1$ and $\mathbf{k}_2$, when $\mathbf{r}_1$ and $\mathbf{r}_2$ satisfy the following equations: (1) $\exp[i\mathbf{k}_1\cdot\mathbf{r}_1] + \exp[i\mathbf{k}_1\cdot\mathbf{r}_2] = 0$ and (2) $\exp[i\mathbf{k}_2\cdot\mathbf{r}_1] + \exp[i\mathbf{k}_2\cdot\mathbf{r}_2] = 0$. Any set of $N = 2$ particles whose coordinates satisfy these constraints constitutes a *doublet* (D). (*Lower left*) Graphical depiction of a series of stealthy patterns discretized on a periodic 6×6 square lattice that were constructed *via* superposition of multiple doublets (*i.e.*, $D_2 = D \oplus D$ and $D_9 = D \oplus D \oplus \cdots \oplus D$). Since *each* doublet constitutes a stealthy pattern, the superposition of multiple doublets (without overlap) constitutes a stealthy (or multi-stealthy) hyperuniform pattern as well. (*Upper right*) Vectorial representation of a stealthy pattern comprised of $N = 4$ particles. The corresponding structure factor will vanish at a given pair of $\mathbf{k}$-vectors, $\mathbf{k}_1$ and $\mathbf{k}_2$, when $\mathbf{r}_1$, $\mathbf{r}_2$, $\mathbf{r}_3$, and $\mathbf{r}_4$ satisfy the following equations: (1) $\exp[i\mathbf{k}_1\cdot\mathbf{r}_1] + \exp[i\mathbf{k}_1\cdot\mathbf{r}_2] = 0$, (2) $\exp[i\mathbf{k}_1\cdot\mathbf{r}_3] + \exp[i\mathbf{k}_1\cdot\mathbf{r}_4] = 0$, (3) $\exp[i\mathbf{k}_2\cdot\mathbf{r}_1] + \exp[i\mathbf{k}_2\cdot\mathbf{r}_3] = 0$, and (4) $\exp[i\mathbf{k}_2\cdot\mathbf{r}_2] + \exp[i\mathbf{k}_2\cdot\mathbf{r}_4] = 0$. Any set of $N = 4$ particles whose coordinates satisfy these constraints constitutes a *quartet* (Q). Note here that a quartet is not simply a pair of doublets, *i.e.*, $Q \neq D_2 = D \oplus D$. (*Lower right*) Graphical depiction of a series of stealthy patterns discretized on a periodic 6×6 square lattice that were constructed *via* superposition of multiple doublets and quartets (*i.e.*, $QD = Q \oplus D$, $Q_2 = Q \oplus Q$, and $Q_3D_3 = Q \oplus Q \oplus Q \oplus D \oplus D \oplus D$). Since *each* doublet and *each* quartet constitutes a stealthy pattern, the superposition of multiple doublets and quartets (without overlap) constitutes a stealthy (or multi-stealthy) hyperuniform pattern as well. Hence, this superposition technique can be utilized to directly generate stealthy patterns with both large L and N.

Chapter 9

The Perfect Glass Paradigm: Disordered Hyperuniform Glasses Down to Absolute Zero

9.1 Introduction

Structural glasses are materials made by supercooling liquids below the "glass transition temperature," sufficiently rapidly to avoid crystallization [12]. According to Ref. [45], a qualitative description of a structural glass is "a phase of matter with no long-range order but with a nonzero shear rigidity." It is well known that the glass transition temperature can be reduced by lowering the cooling rate. However, some have postulated that if the glass transition temperature could be postponed down to absolute zero during the supercooling process, then at some low but positive temperature, called the "Kauzmann temperature," the entropy of the supercooled liquid would be equal to and then apparently decline below that of the crystal, resulting in the so-called "Kauzmann paradox" [157, 342], which is schematically depicted in Fig. 9.1. One resolution of this well-known paradox is to assume that supercooled

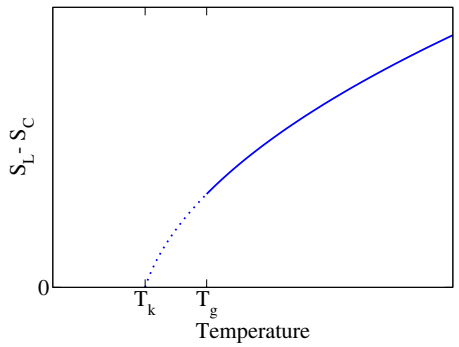

Figure 9.1 Schematic illustration of the so-called Kauzmann paradox. As a liquid is supercooled, the entropy difference between it and crystalline state, $S_L - S_C$, decreases. If the glass transition can be postponed below the Kauzmann temperature, T_k, then the entropy of the liquid would be lower than that of the crystal upon extrapolation. The perfect-glass paradigm introduced in this chapter completely circumvents the Kauzmann paradox.

liquids at the Kauzmann temperature must undergo a thermodynamic phase transition to "ideal glasses". Such glasses identified as ideal would have vanishing extensive configurational entropy [67, 283]. In this chapter, however, we present a completely different model system that we call a "perfect glass." As we will see, one characteristic of the perfect-glass paradigm introduced in the present chapter is the complete circumvention of the Kauzmann paradox.

Various studies have justifiably placed importance on the local environment of each atom in structural glasses [187, 270, 279]. The variations in local motifs and the resulting varying degrees of short-range order have been used to explain the physical properties of glasses. For example, it is believed that atoms in ordered local environments are responsible for thermodynamic properties and kinetic stability of glasses, while atoms in disordered local environments make important contributions to mechanical properties [187]. By contrast, global structural characteristics, such as hyperuniformity, as described below, address key aspects of glass formation that have been unexplored by these local descriptive techniques.

Although the compositions and interactions of experimentally investigated glasses are generally complicated on the atomic scale, many theoretical and computational models with simpler compositions and interactions have been shown to produce glasses under rapid cooling [171, 265]. Moreover, short-range, pairwise additive interactions have been specifically designed to locally frustrate crystallization to create good glass formers [78, 166, 225, 274, 151, 334]. This is often achieved by having two components whose simultaneous existence disrupts crystal nucleation in two dimensions (2D) [166, 225] or three dimensions (3D) [151], or by encouraging pentagonal or icosahedral local geometry [255, 280] that frustrates crystallization [78, 274]. Despite these design goals to strongly inhibit crystal nucleation, the true ground states of these potentials nevertheless turn out to be crystalline [255, 87, 226, 274]. Therefore, liquids with these interactions can still crystallize if cooled slowly enough. Interestingly, there are models that produce amorphous ground states [328, 198, 278], but they cannot resist shear and hence do not behave like glasses, which are mechanically stable. Moreover, in all of these cases, crystalline structures are still part of the ground-state manifold, even if the probability of observing them is extremely small. Therefore, placing such systems in contact with suitable periodic substrates would have the effect of inducing crystallization with an appreciably higher probability. As we will see, the perfect glass paradigm does not even allow this to occur because ordered states (for all temperatures) are completely banished.

Maximally-random jammed (MRJ) packings of hard (nonoverlapping) particles in 2D and 3D are idealized amorphous states of matter that can be regarded to be prototypical glasses [322, 347, 149, 321]. A packing is called "strictly jammed" if no subset of particles may be displaced while allowing uniform volume-preserving deformations of the system boundary [309], implying resistance to both compressive and shear deformations. Among all strictly jammed packings, MRJ states are defined to be the most disordered ones according to suitable order metrics (i.e., measures of the degree

of geometric order). MRJ packings not only exhibit many characteristics that are typical of glasses, but also are extremal in several respects according to the description given in Ref. [45]: They are nonequilibrium, nonergodic many-body systems that are maximally disordered subject to the nonoverlap constraint, non-crystallizable, and mechanically infinitely rigid (both elastic moduli are unbounded) [309]. Indeed, they are perfectly nonergodic, since they are forever trapped in configuration space.

However, there are still two major differences between MRJ packings and molecular glasses. First, MRJ packings are hyperuniform [317, 74, 347, 173, 149], while typical molecular glasses are not [194]. A hyperuniform many-particle system is one in which the structure factor approaches zero in the infinite-wavelength limit [317]. In such systems, density fluctuations are anomalously suppressed at very large lengths scales [317], which imposes strong global structural constraints. All structurally perfect crystals are hyperuniform, but typical disordered many-particle systems, including liquids and molecular glasses, are not. Materials that are simultaneously disordered and hyperuniform can be regarded to be exotic states of matter that lie between a crystal and a liquid; they behave more like crystals in the manner in which they suppress large-scale density fluctuations, and yet they also resemble typical statistically isotropic liquids with no Bragg peaks, and hence have no long-range order. Therefore, disordered hyperuniform states of matter have been the subject of many recent investigations [317, 74, 347, 149, 173, 77, 177, 136, 142, 66, 68, 341, 211, 95].

Second, given sufficiently long observation times at positive temperature, a typical molecular glass will eventually crystallize because the free energy barrier between it and its corresponding stable crystal structure is finite. By contrast, the hard-sphere MRJ state is a singular point that is trapped in a jamming basin in configuration space and hence can never crystallize at constant volume [75].

Geometrically motivated by MRJ extremal glasses, we are interested in constructing molecular-glass analogs (that are not limited to pairwise additive interactions),

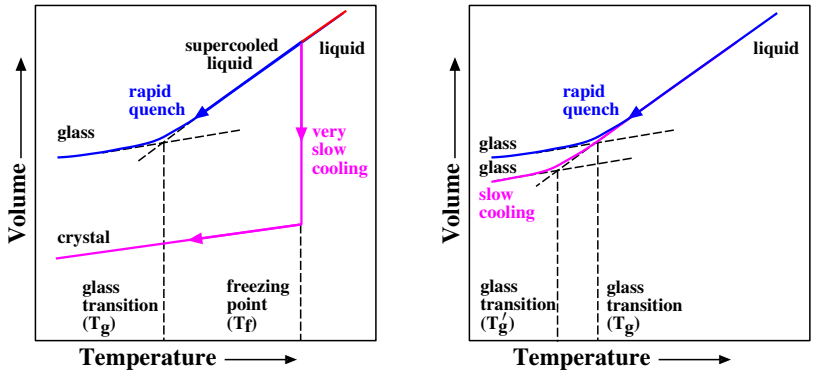

Figure 9.2 Schematic constant-pressure phase diagrams. Left panel: Typical many-particle systems become glasses upon rapid cooling or can crystallize upon slow cooling. Right panel: Our model family creates perfect glasses that by construction cannot crystallize upon quenching to absolute zero temperature.

which we call "perfect glasses"[1]. These analogs should exhibit the following attributes: (1) be disordered and hyperuniform (a global criterion as opposed to the local coordination geometry focus of previous studies); (2) possess no crystalline or quasicrystalline energy minima so that they remain disordered even in the infinite-observation-time limit at positive temperature, implying that they can never crystallize (in contrast to conventional glass formers), as qualitatively shown in Fig. 9.2; and (3) must possess both positive bulk and shear moduli.

In this chapter, we explicitly show that such perfect glasses mathematically exist. Specifically, we demonstrate that a single-component system with a combination of long-ranged two-, three-, and four-body interactions can produce perfect glasses. Our perfect glass interactions are designed in Fourier space which allows us independently to tune the structure factor over the entire range from infinite to intermediate wavelength, including values that will automatically include all possible Bragg peaks, while maintaining hyperuniformity. These global constraints therefore permit the suppression of all possible Bragg peaks, which by definition eliminates any crystal and quasicrystal formation. This attribute of the perfect glass stands in contrast with

[1]Our definition of perfect glass is distinctly different from the "ideal glass former" with reversed T_g and T_m [155].

the ideal glass concept [67, 283] as well as with previous studies that are intended to frustrate crystallization via local coordination preferences [78, 166, 225, 274]. In the case of the former, this means that there is no entropy catastrophe because there is no ordered structure with which to carry out an entropy comparison. Our global approach of preventing crystallization applies to any dimension, in contrast to previously designed interactions that are specifically tailored for a particular space dimension [78, 166, 225, 274].

The major features of perfect glasses is not limited to our three criteria (hyperuniform, possess no crystalline or quasicrystalline energy minima, and possess both positive bulk and shear moduli). We will also see that perfect glasses completely circumvent Kauzmann's paradox. Besides the theoretical existence of perfect glasses, another important finding of our work is that liquid-state configurations of our perfect-glass interaction are hyperuniform and hence possess a zero internal compressibility, implying they have a non-relativistic speed of sound that is infinite. Finally, our results also suggest that up to four-body interactions are necessary to completely avoid crystallization, and thus explains the failure to create such an ideal state of matter heretofore.

9.2 Perfect Glass Potentials

We apply the collective-coordinate optimization scheme [328, 352] to construct interactions that can produce perfect glasses. This procedure involves finding potentials that are given in terms of a targeted form of the structure factor. For a single-component system with N particles in a simulation box of volume V with periodic boundary conditions in d-dimensional Euclidean space $\mathbb{R}^d$, the single-configuration structure factor is defined as $\mathscr{S}(\mathbf{k}) = |\sum_{j=1}^{N} \exp(-i\mathbf{k}\cdot\mathbf{r}_j)|^2/N$, where $\mathbf{k}$ is a d-dimensional wavevector and $\mathbf{r}_j$ is the position of particle j [46, 45]. Many previous

investigations have focused on targeting "stealthy" structure factors, i.e., those in which the structure factor is exactly zero within some sphere of radius K around the origin in Fourier space [328, 286, 325, 352, 353]. When K is large the ground states are crystalline [328, 286, 325, 352]. When K is sufficiently small, however, it has been shown that the ground states of the associated interactions are disordered and highly degenerate [328, 325, 352]. However, although these states are hyperuniform, they are not perfect glasses because they cannot resist shear and crystal structures are part of the ground-state manifold, even if they are sets of zero measure in the infinite-volume limit.

However, the collective-coordinate optimization scheme has also been used to prescribe the potential energy Φ defined by the following more general targeted structure factor [329, 26, 350]:

$$\Phi(\mathbf{r}^N) = \sum_{0<|\mathbf{k}|<K} \tilde{v}(\mathbf{k})[\mathscr{S}(\mathbf{k}) - \mathscr{S}_0(\mathbf{k})]^2, \tag{9.1}$$

where $\mathbf{r}^N = \mathbf{r}_1, \mathbf{r}_2, ..., \mathbf{r}_N$ represents the configurational coordinates, the summation is over all reciprocal lattice vector $\mathbf{k}$'s of the simulation box [45] such that $0 < |\mathbf{k}| < K$, $\mathscr{S}_0(\mathbf{k})$ is a "target" structure factor, $\tilde{v}(\mathbf{k}) > 0$ is a weight function, and K is some cut-off wavenumber that determines the number of constrained wave vectors. At low temperature, this interaction potential attempts to "constrain" the structure factor $\mathscr{S}(\mathbf{k})$ to the target $\mathscr{S}_0(\mathbf{k})$ for all $|\mathbf{k}| < K$, since violating a constraint for any $\mathbf{k}$ will increase the potential energy. The number of independent[2] constraints divided by the total number of degrees of freedom, $d(N-1)$, is a parameter that measures how constrained the system is and is denoted by χ. Previous research has focused on χ values less than 1. In such under-constrained cases, a minimum of the potential energy satisfies all constraints while still having leftover unconstrained degrees of

[2]The definition of $\mathscr{S}(\mathbf{k})$ implies that $\mathscr{S}(\mathbf{k}) = \mathscr{S}(-\mathbf{k})$. Therefore, not all constraints are independent.

freedom. Although this interaction is defined in Fourier space (i.e., in terms of the structure factor), it can be decomposed into a sum of two-body, three-body, and four-body terms in direct space [329]. In Appendix A, we present explicit formulas for each term. In the Appendix G, visualizations of these contributions to the potential energy are provided.

For several reasons, such a model is an excellent starting point for designing perfect glass interactions. First, this model enables one to fulfill the requirement that perfect glasses be hyperuniform because this model constrains $\mathscr{S}(\mathbf{k})$ to a targeted hyperuniform functional form $\mathscr{S}_0(\mathbf{k})$ around the origin. In this chapter, we select the following form for $\mathscr{S}_0(\mathbf{k})$:

$$\mathscr{S}_0(\mathbf{k}) = |\mathbf{k}|^\alpha \quad \text{for } 0 \leq k \leq K, \tag{9.2}$$

where $\alpha > 0$ is an exponent that we are free to prescribe. To ensure that $\mathscr{S}(\mathbf{k})$ has the targeted hyperuniform power-law form of $\mathscr{S}_0(\mathbf{k})$, we choose a weight function that diverges at the origin:

$$\tilde{v}(\mathbf{k}) = \left(\frac{1}{|\mathbf{k}|} - 1\right)^\gamma \quad \text{for } 0 \leq k \leq K, \tag{9.3}$$

where $\gamma \geq 2$ is another exponent to choose. The choices of $\mathscr{S}_0(\mathbf{k})$ and $\tilde{v}(\mathbf{k})$ are not unique: Other target forms of $\mathscr{S}_0(\mathbf{k})$ and other forms of $\tilde{v}(\mathbf{k})$ that diverge to $+\infty$ in the zero wavenumber limit could also result in hyperuniformity. We choose the forms in Eqs. (9.2)-(9.3) for simplicity. Because $\tilde{v}(\mathbf{k})$ goes to zero smoothly as $|\mathbf{k}|$ goes to 1, it is natural to let $K = 1$. Our choice of K and $\tilde{v}(\mathbf{k})$ sets the model's length and energy scales.

Second, this model can completely eliminate crystalline and quasicrystalline energy minima. The structure factor of all crystals and quasicrystals contains "Bragg peaks," i.e., Dirac delta functions [45]. Of all possible periodic and quasiperiodic

configurations, the structures producing the largest-radius zone around $\mathbf{k} = \mathbf{0}$ devoid of Bragg peaks are the triangular and body-centered cubic lattices in 2D and 3D, respectively. However, if we set $\chi > 0.9068\ldots$ in 2D or $\chi > 0.9873\ldots$ in 3D, then even these two structures have some Bragg peaks that fall inside the $|\mathbf{k}| < K$ range; and so do all other crystal and quasicrystal structures [325]. Thus, any crystalline or quasicrystalline configuration will have potential energy diverging to plus infinity and thus cannot be an energy minimum [3].

Third, this model allows us to realize positive shear and bulk moduli. If a structure corresponding to a local minimum in $\Phi(\mathbf{r}^N)$ (called an "inherent structure" in the rest of the chapter) is sheared or compressed at zero temperature, then the set of $\mathbf{k}$ vectors that are consistent with the simulation box changes. A change in these wave vectors then causes a change in $\mathscr{S}_0$ (since $\mathscr{S}_0$ is a function of $\mathbf{k}$), which in turn will change the potential energy. This change is likely positive because the original configuration is an inherent structure. Indeed, in our simulations, we find this perturbation always increases the potential energy and thus the system will resist that perturbation. Therefore, shear and bulk strains cause stresses. However, for an under-constrained system ($\chi < 1$), the unconstrained degrees of freedom allow the system to gradually dissipate the stress over time. Therefore, we always employ $\chi > 1$ to ensure that stresses are sustained.

The qualitative nature of our combination of two-, three-, and four-body potentials has the effect of assigning an impossibly high potential energy to structures that have long-range periodic or quasiperiodic order. Thus when the resulting arrangements of particles are disordered by virtue of the nature of the targeted structure factor, these two-, three-, and four-body contributions to the total energy effectively cancel

[3] This also includes two dimensional crystalline and quasicrystalline states at positive temperature that do not have perfect Dirac-delta-function-like Bragg peaks. Rather, the peaks have an intrinsic broadening characteristic, but the broadening is rather limited in magnitude so our interaction still has the effect of banishing phonon-displaced crystalline and quasicrystalline structures in two dimensions [202].

one another at large distances. Specifically, we show in Appendix B that for perfect glasses, the three- and four-body contributions to the potential energy almost cancel one another in such a way as to produce no infinite-system thermodynamic anomalies: the total energy per particle is an intensive quantity (as quantitatively detailed in Appendix C) and approaches its infinite-system-size very rapidly as N increases.

9.3 Results

9.3.1 Perfect-glass inherent structures

We now quantitatively characterize the structure, elastic moduli, and degree of order of the perfect-glass inherent structures obtained by minimizing the total potential energy, Eq. (9.1), starting from random initial configurations of $N = 2500$ particles for different parameters χ, α, and γ in two and three dimensions. Perfect glasses obtained in this way can be regarded as glasses produced by an infinitely rapid quench from infinite temperature to zero temperature because the random initial configuration is equivalent to the infinite-temperature state, and an energy minimization process may be thought of as evolving the system to a state of zero temperature. Examples of perfect glasses in 2D and 3D are shown in Fig. 9.3.

Pair statistics

The standard pair correlation function [46], $g_2(r)$, and the angular averaged and ensemble-averaged structure factor, $S(k)$, are together effective descriptors for distinguishing crystals, quasicrystals, disordered hyperuniform systems, and nonhyperuniform systems from one another. We will restrict ourselves to $\alpha \geq 1$ because, as we will see, this places a lower bound on the rigidity of a perfect glass and is consistent with the MRJ nature of this ideal amorphous state of matter. These two pair statistics for $\alpha = 2$ and different χ's and γ's are shown in Fig. 9.8. All $g_2(r)$'s and $S(k)$'s are

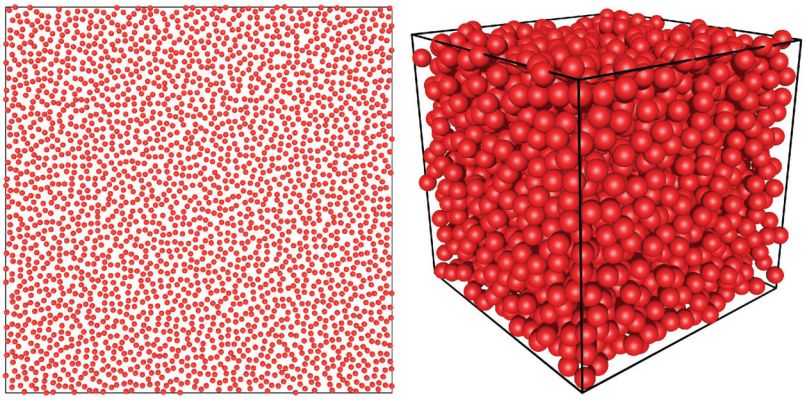

Figure 9.3 Snapshots of perfect glasses with $N = 2500$ with perfect-glass potential with parameters $\chi = 5.10$, $\alpha = 2$, and $\gamma = 3$ in 2D (left) and 3D (right). Both of them are clearly disordered.

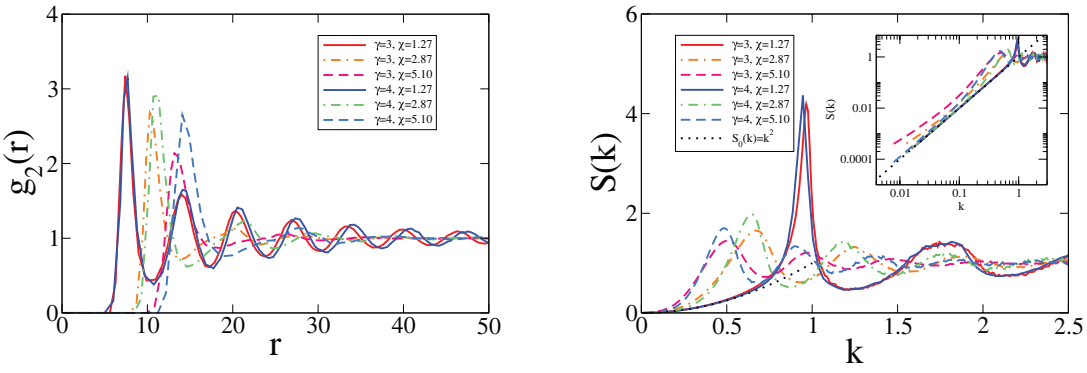

Figure 9.4 Pair correlation functions (left) and structure factors (right) of the perfect glasses in 2D for $\alpha = 2$.

clearly finite and approaches 1 in the $r \to \infty$ or $k \to \infty$ limit, showing that these structures are neither crystalline nor quasicrystalline. Additionally, $S(k)$ follows the target $\mathscr{S}_0(k)$ and approaches 0 as $k \to 0$, demonstrating that these structures are hyperuniform. In Appendix D, we present $S(k)$ for other α and γ values and show that $S(k)$ has the same scaling as $\mathscr{S}_0(k)$ near $k = 0$ only if $\gamma > \alpha$. Otherwise, $S(k)$ will deviate from $\mathscr{S}_0(k)$ and may even appear to saturate at a positive value in the $k \to 0$ limit. If so, the resulting system would not be hyperuniform and conform to our definition of a perfect glass.

Bulk and shear moduli

Here we show the capacity of a perfect glass to resist both compressive and shear deformations. The elastic moduli of the inherent structures for $\gamma = 3$ are presented in Fig. 9.5. Both moduli increase as χ or α increases. In all cases, both moduli are positive, clearly showing that our model meets this criterion for a perfect glass. We only present data for $\gamma = 3$ for simplicity. It is useful to note that we have also calculated these moduli for $\gamma = 2$ or 4 and found the same trend.

Our hyperuniform targeted functional form $\mathscr{S}_0(\mathbf{k}) = |\mathbf{k}|^\alpha$ generally produces substantially higher elastic constants than those for non-hyperuniform forms; see Appendix E for details. This correlation between hyperuniformity and improved mechanical rigidity appropriately reflects the MRJ-like nature of the perfect glass and hence stresses the importance of the hyperuniformity criterion.

Characterizing the degree of disorder

As noted earlier, since perfect glasses are molecular-glass analogs of MRJ sphere packings that are maximally random, we determine here the triplet of parameters (χ, α, γ) that produce the most disordered inherent structures according to two order metrics: the "local" bond-orientational parameter $Q_{6,local}$ [153, 152] (also denoted Ψ_6 in some literature) and the translational order metric τ [325], which are defined in the Methods section. We present the order metrics $Q_{6,local}$ and τ of the inherent structures in Fig. 9.9. Here we want to determine at what value of α is a perfect glass most disordered according to these order metrics. Again, we present data only for $\gamma = 3$ for simplicity, but have found that results for $\gamma = 2$ or 4 behave similarly. The local bond-orientational order $Q_{6,local}$ measures the degree to which the local environments of particles resemble regular hexagons (in 2D) or regular icosahedra (in 3D); it can vary from 0 (disordered) to 1 (perfect hexagonal order) in 2D or from 0 (disordered) to 0.663... (perfect icosahedral order) in 3D. Our relatively low

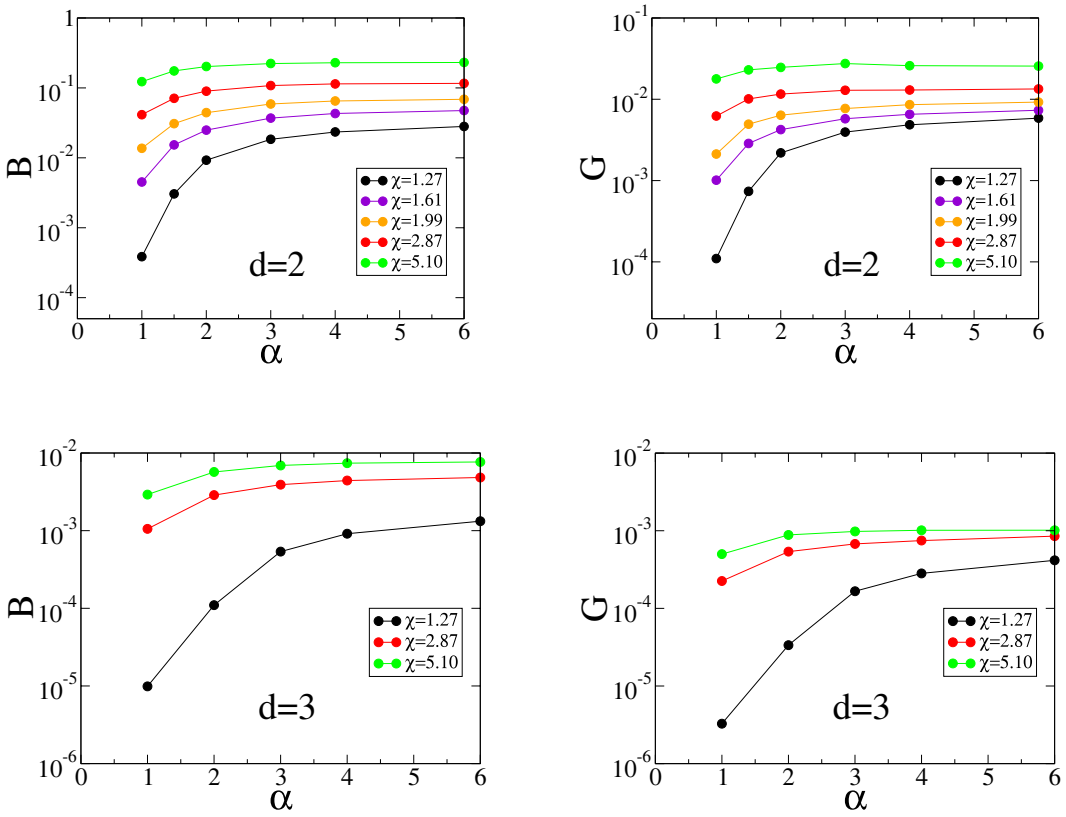

Figure 9.5 Bulk modulus B (left) and shear modulus G (right) versus the exponent α for the inherent structures in 2D (top) and 3D (bottom) for $\gamma = 3$ and selected values of χ.

$Q_{6,local}$ values in 3D indicate that our interaction does not favor icosahedral local configuration. This demonstrates that our approach of frustrating crystallization is fundamentally different from the previous approach of encouraging icosahedral order [78].

As detailed in the Methods section, $Q_{6,local}$ measures only local orientational order, while the translational order metric, τ, takes into account both short-range order and long-range order. Nevertheless, τ shows the same trend as $Q_{6,local}$: Perfect glasses with the lowest α and highest χ have the lowest τ. In fact, we plot τ versus $Q_{6,local}$ for different χ's and α's in 2D and 3D for $\gamma = 3$ in Fig. 9.7 and find that these two order metrics are strongly correlated. Our results for Q_6 and τ are consistent with

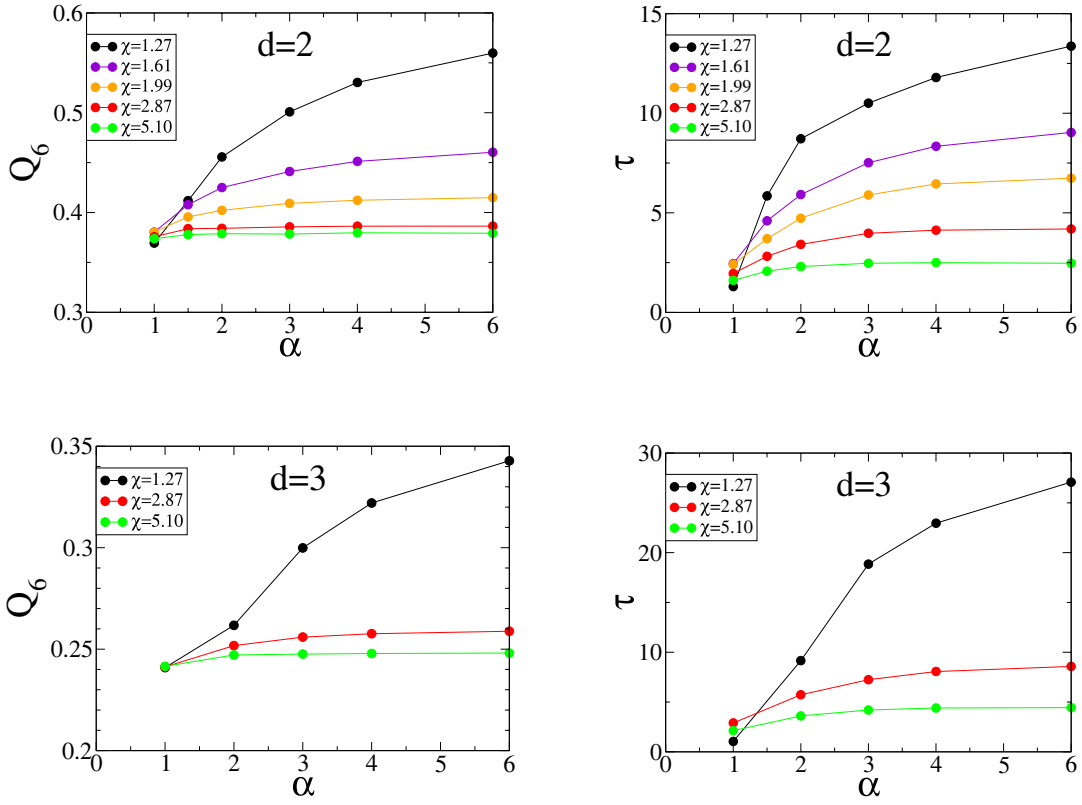

Figure 9.6 Order metrics $Q_{6,local}$ (left) and τ (right) versus the exponent α for the inherent structures in 2D (top) and 3D (bottom) for $\gamma = 3$ and selected values of χ.

the qualitative conclusions of Ref. [329], which reported that increasing α resulted in configurations that increasingly appeared to be more ordered.

While we have shown that the perfect glass is indeed a molecular analog of MRJ, the former is considerably richer. Whereas a perfect glass can have a wide range of degrees of order and elastic moduli, MRJ states, by construction, can only be maximally random subject to the strict jamming condition, which endows them with infinite elastic moduli [309]. We have shown that as α decreases, the elastic moduli decrease. For this reason and to maintain the analogy with MRJ, we restrict the minimum of α to be 1 so as to bound the elastic moduli from below. We also must restrict $\alpha < \gamma$ because $S(k)$ demonstrates indisputable hyperuniformity only in such cases.

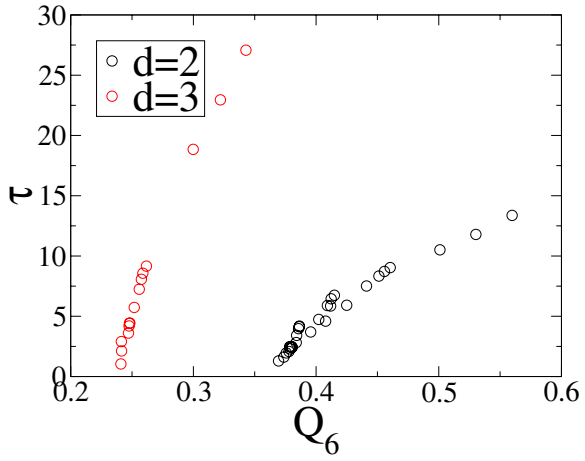

Figure 9.7 Translational order metric τ versus $Q_{6,local}$ for all previously used χ's and α's in 2D and 3D for $\gamma = 3$.

In summary, we have shown that under the two constraints that $\alpha \geq 1$ and $\alpha < \gamma$, the inherent structures of our potential are clearly disordered, hyperuniform, possess positive shear and bulk moduli, and therefore conform to our definition of a perfect glass. We also note that the lowest value of α, equal to unity, produces the lowest order and lowest elastic moduli among all of the cases that we have studied. This behavior is consistent with the fact that MRJ, which are maximally disordered subject to jamming constraint, also have a small-wavenumber scaling of $S(k) \sim k^1$. It has been established that decreasing the exponent α in the small-wavenumber scaling $S(k) \sim k^\alpha$ in many-particle systems is associated with greater disorder and that sublinear scaling ($\alpha < 1$) induces clustering among the particles [350] and is therefore inconsistent with strict jamming in the case of hard spheres [348].

9.3.2 Simulated annealing

The preceding section focused on the inherent structures obtained from random initial configurations, which correspond to glasses produced by an infinitely rapid quench. However, perfect glasses meeting our definition should remain disordered even after

annealing with a finite, slow cooling rate. Here we study the behavior of our system under slow annealing by performing canonical ensemble (constant temperature and volume) molecular dynamics (MD) simulations [100] and gradually decreasing the temperature. We have performed such an annealing for a 2D system of $N = 400$ particles with parameters $\chi = 5.1$, $\alpha = 1$, and $\gamma = 3$. During the annealing process, the potential energy remains continuous with respect to temperature, suggesting that there is no first-order phase transition. As we will mention in the Methods section, the configuration starts to vibrate around a single inherent structure when k_BT drops below 0.3, suggesting that the glass transition temperature, T_g, for this system at this cooling rate is around $0.3/k_B$. The final configuration is disordered, verifying that our system does not crystallize even under slow cooling.

It is worth noting that after slow annealing and a subsequent energy minimization, the final configuration has potential energy per particle $\Phi/N = 2.920$, which is not much lower than that of the previously obtained inherent structures, for which, $\Phi/N = 2.971 \pm 0.014$ at the same system size under the same interaction. This may suggest that most of the local energy minima of the potential energy surface are not much higher than the ground state energy.

9.4 Conclusions and Discussion

We have found a family of interactions that can produce perfect glasses, i.e., hyperuniform glasses with positive bulk and shear moduli, in systems that possess no crystalline or quasicrystalline energy minima. We have demonstrated that the inherent structures (structures obtained by infinitely rapid cooling from infinite temperature to zero temperature) of these interactions are disordered, hyperuniform, and have positive bulk and shear moduli for parameters $1 \leq \alpha < \gamma$ and $\chi > 1$. The lowest α, equal to unity, results in the lowest degree of order, although a priori there was no

reason to expect that maximum disorder would arise when α is minimized. We have also performed a slow simulated annealing on a perfect-glass system and found no first-order phase transition.

Our interactions are designed in Fourier space and completely eliminate crystal and quasicrystal formation. As detailed in Ref. [325], for $\chi > 0.9068\ldots$ in 2D or $\chi > 0.9873\ldots$ in 3D, any crystal or quasicrystal must produce Bragg peaks in the constrained ($|\mathbf{k}| < K$) range. Such Bragg peaks would make the potential energy infinite. Therefore, crystals and quasicrystals cannot be energy minima [4]. Since our perfect glasses are not metastable with respect to a crystal structure, there is no Kauzmann entropy crisis that led to the conjectured existence of "ideal glasses" in the conventional Kauzmann picture [67, 283]. The latter is defined completely differently from the perfect glasses in this work.

All available understanding indicates that with only isotropic two-body interactions, crystalline ground states inevitably occur. However, by adding suitable three- and four-body interactions to appropriate two-body interactions, we show for the first time that crystals and quasicrystals can be completely prevented for any range of temperatures down to absolute zero and thus ensures by construction thermodynamically stable glassy states. The collective-coordinate procedure that we are using to target perfect glass behavior cannot be simplified to the extent of reducing the interaction character below at least four-body interactions. Because the procedure is general, this suggests that a perfect glass cannot be created with two- and three-body interactions depending only on scalar distances alone. This could explain why previous attempts to produce such an ideal state of matter have not been successful. Another observation that suggests the necessity of four-body interactions is that the analytical form of our four-body interaction, Eq. (9.10), appears to strongly penalize

[4] It is interesting to note that our approach to ensure glass formation (eliminating crystals and quasicrystals) is in sharp contrast with the reason why diboron trioxide tends to vitrify. The latter tends to vitrify because of a high energy degeneracy of multiple crystalline structures [86].

long-range bond orientational order, and thus prevent crystallization. Without the four-body interaction, one might be able to design a pair interaction that reproduces the pair correlation function of perfect glasses at a particular temperature (for example, by imitating Ref. [105]). However, crystallization cannot be prevented if the temperature is lowered down to absolute zero.

It is instructive to compare and contrast the perfect-glass potential with the well-known classical rigidity theory of Phillips and Thorpe [295, 204]. This theory applies to glasses with covalent interactions, and states that covalent bonds between atoms in a glass impose constraints on the atomic positions and that the conditions for glass formation will be optimal if the number of constraints is equal to the number of degrees of freedom of the atoms. By contrast, the perfect-glass picture involves overconstraining the system (i.e., having more constraints than the degrees of freedom), which occurs when $\chi > 1$, to ensure positive elastic moduli. Moreover, the Phillips-Thorpe theory states that normal glasses tend to crystallize if the number of constraints is much larger than the number of degrees of freedom, but a perfect glass will never crystallize even for large χ values. Besides these differences, perfect glasses have other important distinctive features, e.g., hyperuniformity and complete prevention of crystallization. Lastly, the isotropic perfect-glass interaction is also very different from the directional covalent-bond interactions that the Phillips-Thorpe theory assumes, and a perfect glass is achievable with identical particles.

It is worth noting that our model systems can maintain hyperuniformity even at positive temperatures. Eqs. (9.1)-(9.3) suggests that, with sufficiently high γ, any nonhyperuniform structure will have infinite energy, and therefore have zero probability of appearing at a finite positive temperature. We analyzed the intermediate configurations from the annealing simulation at $T = 10$ and indeed found hyperuniformity. This feature contrasts with other interactions that have perfect crystalline,

and therefore hyperuniform, ground states but lose hyperuniformity at any positive temperature due to phonon excitations (e.g., Lennard-Jones interaction).

The well-known compressibility relation from statistical mechanics [127] usually provides some insights about the relationship between temperature T and hyperuniformity for equilibrium systems in the infinite-system-size limit at number density $\rho = N/V$:

$$\lim_{k \to 0} S(k) = \rho k_B T \kappa_T. \tag{9.4}$$

We see that in order to have a hyperuniform equilibrium system at positive T that obeys this relation, the isothermal compressibility, $\kappa_T = 1/B$, must be zero; i.e., the system must be incompressible [350, 325] (see Refs. [317] and [315] for some examples). As stated in the previous paragraph, equilibrium systems of particles interacting with the perfect-glass potential at positive temperature (e.g., liquids) are hyperuniform. Does this mean they are also incompressible ($B = \infty$)? Our initial study of perfect glasses in isothermal-isobaric ensembles suggests that they are not incompressible. Thus, the compressibility relation is violated. The reason for this violation is that there are actually two subtly different compressibilities: the "internal" one and the "external" one. If one divides a large system into two halves, compresses one half and decompresses the other half while keeping the total volume constant, the restoring force is related to the internal compressibility. However, if one compresses or decompresses the entire system, causing a volume change, the change in pressure is related to the external compressibility. Normally, the internal compressibility is equal to the external one and thus the compressibility relation holds. However, for perfect glass systems, since the potential energy explicitly penalizes long-wavelength internal density fluctuations but not external volume change, the internal compressibility is zero while the external one is still positive and the compressibility relation no longer holds. A novel consequence of having zero internal compressibility is that the non-relativistic speed of sound is infinite.

Concerning the violation of the compressibility relation, it is interesting to note that we previously have studied Dzugutov glasses and Lennard-Jones glasses, which violate the same relation because they are not in equilibrium, and introduced the following "non-equilibrium index" [194]:

$$X = \frac{\lim_{k\to 0} S(k)}{\rho k_B T \kappa_T} - 1. \tag{9.5}$$

If a system is not in equilibrium and thus violates the compressibility relation, X would be non-zero. However, systems of particles interacting with the perfect-glass potential, even in equilibrium, would still have a non-zero X.

Our perfect-glass model has the unique feature of not being metastable with respect to any crystalline or quasicrystalline states. We believe these features can open up a variety of possibilities. Without the worry of crystallination and with the help of faster computers in the future, one would be able to perform extremely long simulations to study glass dynamics. It would be an interesting future project to study the kinetics of glass formation as a function of temperature and density. It would also be interesting to see whether or not the ground states of the perfect-glass interaction have vanishing configurational entropy per particle. If so, this would be the first example of this conjectured "ideal glass" [283, 67].

Concerning the first criterion of perfect glasses (hyperuniformity), we note in passing that real polymers [135] as well as polymer models [82, 342] have succeeded in approaching hyperuniformity. It remains to be seen whether the remaining two criteria can be approached by novel polymer systems or suitably defined theoretical models of polymers. It is also worth noting that polymer systems are known to involve high-order interactions beyond two-body terms [36, 72, 337], which, as we discussed earlier, are likely required to create perfect glasses.

There is a broader class of mathematical models as those for which $\lim_{\mathbf{k}\to\mathbf{0}} \mathscr{S}_0(\mathbf{k}) \neq 0$ or $\lim_{\mathbf{k}\to\mathbf{0}} \tilde{v}(\mathbf{k}) \neq +\infty$. Generally, they would produce nonhyperuniform glasses and if so, would not conform to our definition of perfect glasses. Nevertheless, such models still completely eliminate crystalline and quasicrystalline energy minima and therefore merit future mathematical analyses and numerical studies. This is in contrast to a study in which a similar type of potential was added to a Lennard-Jones interaction in order to inhibit crystallization [70, 11], but the functional form employed prevented that goal from being accomplished [11].

9.5 Methods

We generate inherent structures of the perfect glass potential by the following procedure: Starting from initial configurations of $N = 2500$ particles in which each particle's position is generated randomly and independently, we minimize the potential energy, Eq. (9.1), first using the low-storage BFGS algorithm [214, 183, 150] and then using the MINOP algorithm [69]. Such a combination of the two minimization algorithms maximizes both efficiency and precision [352]. After energy minimization, the norm of the gradient of potential energy is less than 10^{-13} (in dimensionless units, similarly hereinafter). The simulation box shape is square in 2D and cubic in 3D. Since K and N are fixed, we adjust χ by changing the simulation box size. We choose side lengths L =400, 450, 500, 600, and 800 for χ =1.27, 1.61, 1.99, 2.87, and 5.10, respectively, in 2D and L =104.1, 136.6, and 165.4 for χ =1.27, 2.87, and 5.10, respectively, in 3D. For a 2D case in which $\chi = 5.10$, $\alpha = 2$, and $\gamma = 3$, we also generated inherent structures in a rhombic simulation box with a 60° interior angle and have found no statistically significant difference in the resulting pair correlation function, structure factor, and elastic constants, verifying that our results are not sensitive to the shape of the simulation box. For each combination of χ, α, and γ in both 2D and

3D, we generated between 10 and 100 inherent structures, depending on the energy minimization speed of the specific case.

To demonstrate that our perfect glasses have positive bulk moduli (B) and shear moduli (G), we have also calculated these elastic moduli of the inherent structures by incurring a small (10^{-6}) strain, minimizing the potential energy within the deformed simulation box, and then calculating the stress. The calculated elastic constants are then averaged over different directions of strains and stresses and different configurations.

Since perfect glasses are molecular-glass analogs of hard-sphere MRJ packings that are maximally random, we are interested in finding the triplet of parameters (χ, α, γ) that produce the most disordered inherent structures according to certain order metrics. We have calculated two order metrics: $Q_{6,local}$ and τ. In 2D, Q_6 is defined for a given particle q, as

$$Q_6 = \left| \frac{1}{N_p} \sum_p \exp(6i\theta_{\mathbf{r}_{pq}}) \right|, \tag{9.6}$$

where the summation is over all neighbor particles whose Voronoi cells share an edge with particle q's cell, N_p is the number of such neighbors, and $\theta_{\mathbf{r}_{pq}}$ is the angle between $\mathbf{r}_{pq} = \mathbf{r}_q - \mathbf{r}_p$ and a reference direction. In 3D, Q_6 is defined as

$$Q_6 = \sqrt{\frac{4\pi}{13} \sum_{m=-6}^{6} \left| \frac{1}{N_p} \sum_p Y_{6m}(\theta, \phi) \right|^2}, \tag{9.7}$$

where the summation is over all neighbor particles whose Voronoi cells share a face with particle q's cell, N_p is the number of such neighbors, Y_{lm} is the spherical harmonic function, and θ and ϕ represent colatitude and longitude of $\mathbf{r}_{pq}$. These bond-orientational parameters are the local versions of the ones introduced in Ref. [280]. In both dimensions, $Q_{6,local}$ is an average of Q_6 over all particles in all configurations.

While $Q_{6,local}$ only measures local orientational order, the following translational order metric [325]:

$$\tau = \rho \int_0^\infty [g_2(r) - 1]^2 d\mathbf{r} = \frac{1}{(2\pi)^d \rho} \int_0^\infty [S(k) - 1]^2 d\mathbf{k}, \tag{9.8}$$

takes into account both short-range order and long-range order by measuring the degree to which the pair statistics [$g_2(r)$ and $S(k)$] deviate from those of an ideal gas on all length scales. As Eq. (9.8) shows, τ can be computed from either $g_2(r)$ or $S(k)$. Parseval's theorem guarantees that these two approaches yield the same value of τ in the infinite-system-size limit. However, they can give slightly different results for our finite-sized systems, and hence provide a self-consistency check on its evaluation in a simulation. Although Eq. (9.8) involves infinite integrations, they can be truncated since both $g_2(r)$ and $S(k)$ decay and approach 1 rapidly in the $r \to \infty$ or $k \to \infty$ limit. In our calculation, the integration is truncated at $r_{cut} = 200$ in 2D and $r_{cut} = 50$ in 3D or $k_{cut} = 6$ in both dimensions. As we will show in Appendix F, τ calculated from both approaches agree well, verifying that our $g_2(r)$ and $S(k)$ are consistent and our integration truncation is appropriate.

To demonstrate that perfect glasses cannot crystallize, we have also performed molecular-dynamics-based simulated annealing of the perfect glass potential using the velocity Verlet algorithm [100]. The temperature is controlled by resetting a randomly chosen particle's velocity to a random velocity, drawn from Boltzmann distribution, every 10 time steps. The scaled temperature, k_BT, starts at 10 in dimensionless units and decreases as prescribed by Eq. (6) of Ref. [215]. In evaluating that equation, we use the relaxation time of the potential energy Φ as an estimate of the relaxation time of the system and use the scaling parameter in that Eq. (6) $v_s = 0.6$. The integration time step Δt is adjusted continuously so that the change in total energy every 50 time steps is between 0.0025% and 0.01% when velocity resetting is switched

off. In our simulation Δt changed from 0.05 at $k_BT = 10$ to 0.18 at $k_BT = 0.23$. As k_BT dropped below about 0.3, the configuration started vibrating around a single inherent structure and we thus ended the simulation. The time length of the entire MD simulation is $t = 3.04 \times 10^6$ in dimensionless unit.

9.6 Appendix A: Perfect-Glass Potential in the Direct Space

As we mentioned in the "Perfect Glass Potentials" section, the perfect-glass potential, Eq. (9.1), can be decomposed into a sum of two-, three-, and four-body contributions in the direct space. We present explicit formulas for these contributions here. We provide visulizations of these individual two-, three-, and four-body contributions in the Appendix G.

The total potential energy for N particles in a fundamental cell under periodic boundary condition is given by [329]

$$\Phi(\mathbf{r}^N) = \sum_{0<|\mathbf{k}|<K} \tilde{v}(\mathbf{k})[\mathscr{S}(\mathbf{k}) - \mathscr{S}_0(\mathbf{k})]^2 = \sum_{l<m<n<p} v_4(\mathbf{r}_l, \mathbf{r}_m, \mathbf{r}_n, \mathbf{r}_p) + \sum_{l<m<n} v_3(\mathbf{r}_l, \mathbf{r}_m, \mathbf{r}_n) + \sum_{l<m} v_2(\mathbf{r}_l, \mathbf{r}_m) + v_0, \quad (9.9)$$

where

$$v_4(\mathbf{r}_l, \mathbf{r}_m, \mathbf{r}_n, \mathbf{r}_p) = \frac{8}{N^2} \sum_{0<|\mathbf{k}|<K} \tilde{v}(\mathbf{k})[\cos(\mathbf{k}\cdot\mathbf{r}_{lm})\cos(\mathbf{k}\cdot\mathbf{r}_{np}) + \cos(\mathbf{k}\cdot\mathbf{r}_{ln})\cos(\mathbf{k}\cdot\mathbf{r}_{mp}) + \cos(\mathbf{k}\cdot\mathbf{r}_{lp})\cos(\mathbf{k}\cdot\mathbf{r}_{mn})], \quad (9.10)$$

$$v_3(\mathbf{r}_l, \mathbf{r}_m, \mathbf{r}_n) = \frac{8}{N^2} \sum_{0<|\mathbf{k}|<K} \tilde{v}(\mathbf{k})[\cos(\mathbf{k}\cdot\mathbf{r}_{lm})\cos(\mathbf{k}\cdot\mathbf{r}_{ln}) + \cos(\mathbf{k}\cdot\mathbf{r}_{lm})\cos(\mathbf{k}\cdot\mathbf{r}_{mn}) + \cos(\mathbf{k}\cdot\mathbf{r}_{ln})\cos(\mathbf{k}\cdot\mathbf{r}_{mn})], \quad (9.11)$$

$$v_2(\mathbf{r}_l, \mathbf{r}_m) = \frac{4}{N} \sum_{0<|\mathbf{k}|<K} \tilde{v}(\mathbf{k})\cos(\mathbf{k}\cdot\mathbf{r}_{lm})[1 - \mathscr{S}_0(\mathbf{k}) + \cos(\mathbf{k}\cdot\mathbf{r}_{lm})/N], \quad (9.12)$$

and

$$v_0 = \sum_{0<|\mathbf{k}|<K} \tilde{v}(\mathbf{k})[1 - \mathscr{S}_0(\mathbf{k})]^2. \quad (9.13)$$

9.7 Appendix B: Three- and Four-Body Contributions to the Potential Energy

To produce perfect glasses, we have used a combination of two-, three-, and four-body potentials, as specified by Sec. II in the main text. Interestingly, we also discovered that for perfect glass configurations, the three- and four-body contributions almost cancel each other. We have calculated these contributions for several inherent structures of various potential parameters using the minimum image convention. They are presented in Table 9.1. Because calculating the 4-body contributions in direct space is very expensive, we had to use a relatively small system size, $N = 100$.

Table 9.1 Three-body and four-body contributions to the potential energy for several inherent structures of $N = 100$ particles with $\gamma = 3$ and multiple α's and χ's.

α	χ	total potential energy	3-body contribution	4-body contribution
1	5.10	299.887	-97218.9	89992.4
2	5.10	693.767	-102329.5	100407.8
3	5.10	865.713	-102254.7	100242.6
6	5.10	973.172	-102436.5	100633.4
1	1.27	0.00508	-9361.75	8273.52
2	1.27	0.24845	-10357.32	10257.11

9.8 Appendix C: Energy per Particle for Various System Sizes

To verify that the energy per particle is intensive and to quantify finite-size effects, we have calculated the energy per particle, Φ/N, for various N's for the $\chi = 5.10$, $\alpha = 2$, and $\gamma = 3$ case. We generated 2,000 inherent structures of $N = 100$ particles,

100 inherent structures of $N = 2500$ particles, and 1 inherent structure of $N = 10000$ particles. The average energy per particle, $\langle \Phi/N \rangle$, is 6.99, 6.90, and 6.89, respectively, which strongly suggests the intensivity of the energy per particle in the large-system limit.

9.9 Appendix D: The Conditions Under Which the Structure Factor Follows the Targeted Shape

In the main text, we claim that the structure factor, $S(k)$, follows its target, $\mathscr{S}_0(k)$, and approaches 0 as $k \to 0$ only for $\gamma > \alpha$. Here we provide numerical evidences to support this claim.

In Fig. 9.8 we present $S(k)$ and $\mathscr{S}_0(k)$ for various $1 \leq \alpha \leq 4$ and $2 \leq \gamma \leq 4$. One can see that when $\gamma \leq \alpha$, $S(k)$ deviates from $\mathscr{S}_0(k)$ as k approaches zero and in some cases (e.g. the $\chi = 5.10$, $\alpha = 4$, and $\gamma = 2$ case) even appear to saturate at a positive value instead of approaching zero. However, when $\gamma > \alpha$, $S(k)$ has the same scaling as $\mathscr{S}_0(k)$ in the $k \to 0$ limit except for the $\chi = 5.10$, $\alpha = 1$, and $\gamma = 2$ case. The reason for this exception is unknown.

9.10 Appendix E: Elastic Constants Produced by Non-Hyperuniform Targeted Structure Factors.

As noted in the manuscript, hyperuniform targeted structure factors generally produce much higher elastic constants than their non-hyperuniform counterparts. For $\chi = 5.10$ and $\gamma = 3$, we generated two inherent structures with the non-hyperuniform

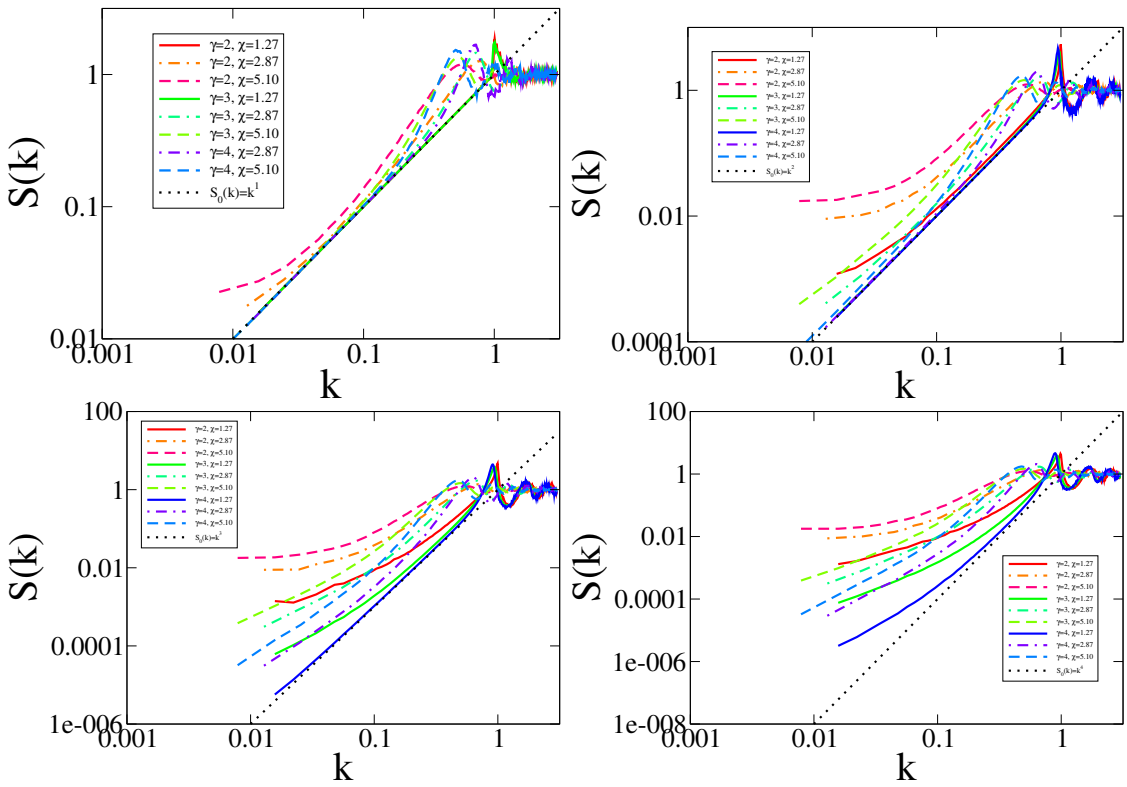

Figure 9.8 Structure factors of inherent structures of the perfect glass interactions in two dimensions for $\alpha = 1$ (top left), $\alpha = 2$ (top right), $\alpha = 3$ (bottom left), and $\alpha = 4$ (bottom right).

targets $\mathscr{S}_0(\mathbf{k}) = (1 + |\mathbf{k}|^2)/2$ and $\mathscr{S}_0(\mathbf{k}) = 1$. They turn out to have elastic constants $B = 0.0363$, $G = 0.0054$ and $B = 0.0174$, $G = 0.0020$, respectively. These elastic constants are to be compared, for example, to $B = 0.2025$, $G = 0.0247$, which are the ensemble-averaged elastic constants with the hyperuniform target $\mathscr{S}_0(\mathbf{k}) = |\mathbf{k}|^2$.

9.11 Appendix F: The Order Metric τ Computed from Direct Space and Fourier Space

As Eq. (6) of the manuscript shows, the order metric τ can be computed from either $g_2(r)$ or $S(k)$. These two approaches should find the same τ in the infinite-system-size limit for an isotropic system, but can give slightly different τ's for our finite-sized

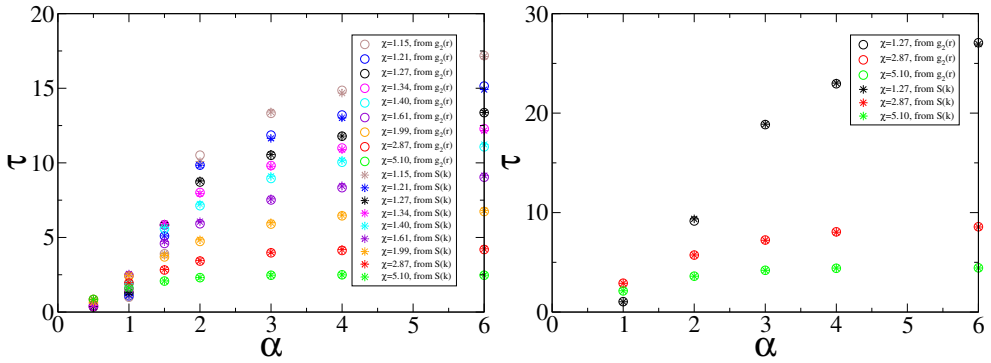

Figure 9.9 Order metric τ versus the exponent α for inherent structures in two (left) and three (right) dimensions for $\gamma = 3$, calculated from $g_2(r)$ or $S(k)$.

systems. In Fig. 9.9 we present τ calculated from both approaches. We see that τ calculated from both approaches are always very close to each other. This indicates that our calculation is accurate.

9.12 Appendix G: Visualizations of the Two-, Three-, and Four-Body Contributions to the Potential Energy

As Appendix A in the main text shows, the perfect-glass potential can be decomposed into a sum of two-, three-, and four-body contributions. We visulize these contributions here for the $d = 2$, $\chi = 5.10$, $\alpha = 3$, and $\gamma = 2$ case. In this case the simulation box side length is $L = 800$. We have experimented with other choices of parameters and found similar results.

The two-body contribution, Eq. (A4) of the main text, is a function of vector $\mathbf{r}_{lm}$. We plot this function versus the x- and y-components of $\mathbf{r}_{lm}$, r_x and r_y, in Fig. 9.10. This contribution of the potential energy is isotropic and repulsive.

The three-body contribution, Eq. (A3) of the main text, is a function three particles' positions and is therefore much harder to visualize. We arrange the three

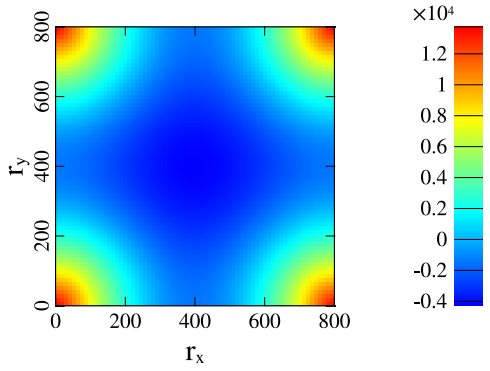

Figure 9.10 The two-body contribution to the perfect-glass potential, Eq. (A4) of the main text, as a function of x- and y-components of $\mathbf{r}_{lm}$

particles as indicated in Fig. 9.11 and plot the three-body contribution to the potential energy for several θ values in Fig. 9.12. It appears that this contribution is large and positive only if all three particles are close to each other.

The four-body contribution, Eq. (A2) of the main text, is a function four particles' positions and is even harder to visulize. To visualize it we have to fix the distance between two particles to the average nearest-neighbor distance between particles. We arrange the four particles as indicated in Fig. 9.13 and plot the four-body contribution to the potential energy for several θ values in Fig. 9.14. It is interesting to note that the four-body contribution becomes very large and positive when just two particles are close to each other.

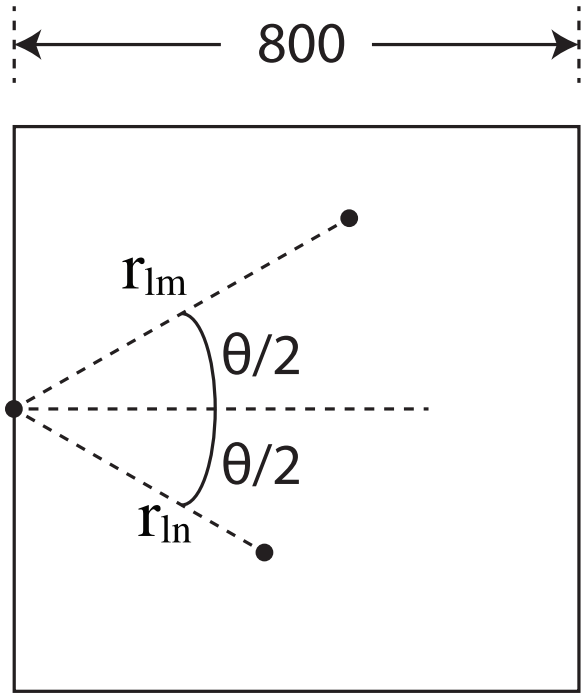

Figure 9.11 Arrangement of the three particles for which we plot the three-body contribution to the potential energy.

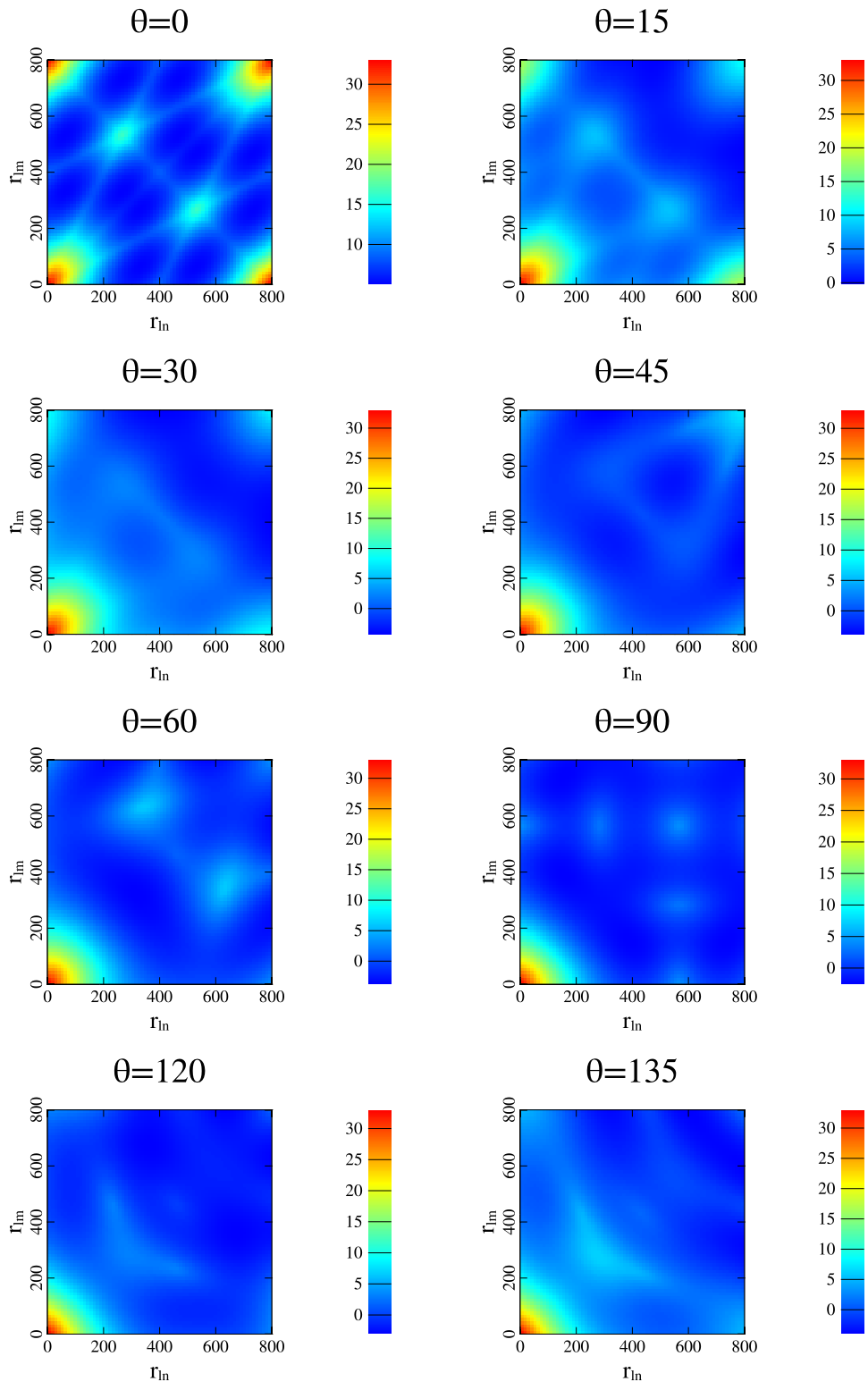

Figure 9.12 The three-body contribution to the perfect-glass potential, Eq. (A3) of the main text, for the three particles shown in Fig. 9.11, as a function of r_{lm} and r_{ln}, for $\theta = 0°$, 15°, 30°, 45°, 60°, 90°, 120°, and 135°, respectively.

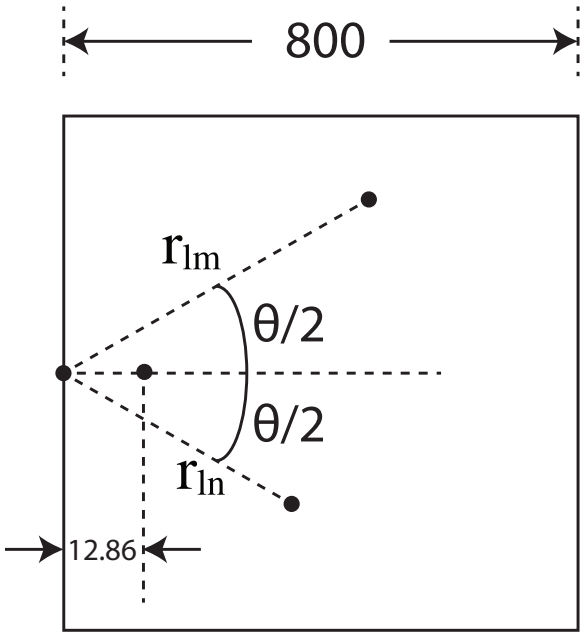

Figure 9.13 Arrangement of the four particles for which we plot the four-body contribution to the potential energy. The distance between two of the particles is fixed at 12.86, the average distance between a particle and its nearest neighbor in the inherent structures in the $d = 2$, $\chi = 5.10$, $\alpha = 3$, and $\gamma = 2$ case.

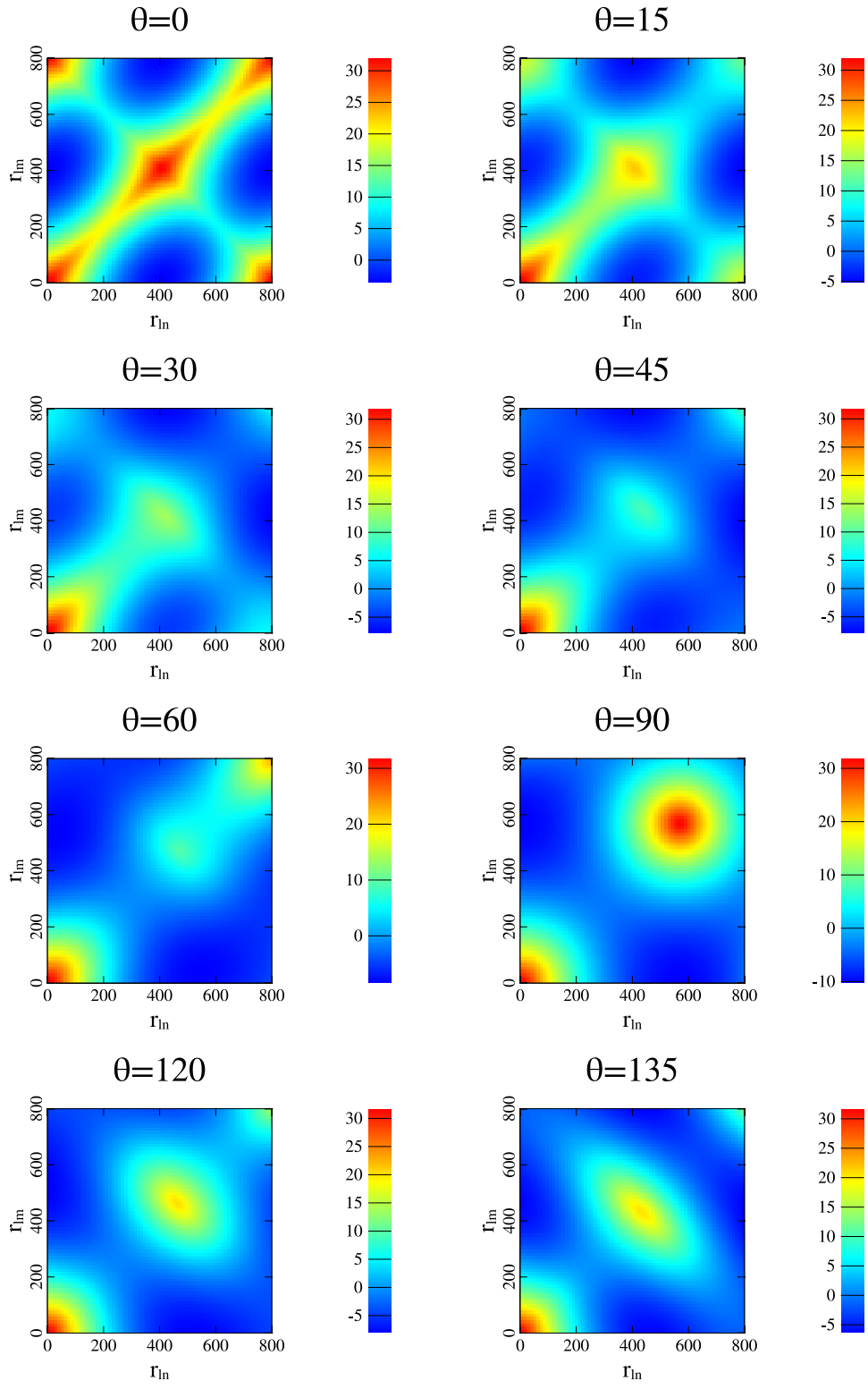

Figure 9.14 The four-body contribution to the perfect-glass potential, Eq. (A2) of the main text, for the four particles shown in Fig. 9.13, as a function of r_{lm} and r_{ln}, for $\theta = 0°$, 15°, 30°, 45°, 60°, 90°, 120°, and 135°, respectively.

Chapter 10

Classical Many-Particle Systems with Unique Disordered Ground States

10.1 Introduction

The classical ground states of many-particle systems are typically crystals consisting of periodically replicated energy-minimizing local geometries with high symmetry. The ability for the particles to attain and display long-range order (Bragg diffraction) becomes the likely procedure for those models to attain their ground state. A specific system at a specific density usually possess a unique crystal ground state, aside from trivial symmetry operations. Therefore, the "enumeration entropy"

$$\mathscr{S}_E = k_B \ln \Omega_E, \tag{10.1}$$

is zero for such ground states. Here Ω_E is the number of *distinct* accessible structures and k_B is the Boltzmann constant.

The fact that ground states of many-body systems can be disordered have intrigued condensed-matter physicists. Although quantum effects are the cause of ground-state disorder in many systems (for example, helium under normal pressure [89] and certain spin systems [158, 259, 212, 49]), classical systems can also have disordered ground states [81, 127, 195, 196, 329, 26, 26, 350, 325]. A ground state of a classical many-particle or spin system is simply a global minimum of the potential energy. For classical many-particle systems in Euclidean spaces, all known examples of disordered ground states possess high enumeration entropy, in the sense that there exists an uncountable collection of geometrically inequivalent ground-state configurations. Here, "inequivalent" configurations are those that are not related to each other by trivial symmetry operations, which includes translations, rotations, and inversions (illustrated in Fig. 10.1). Such examples include equilibrium hard-sphere systems away from jammed states [127] and particles interacting with "stealthy" and related collective-coordinate potentials [329, 26, 26, 350, 325, 352]. While the former situation is trivial in that any nonoverlapping configuration counts as a ground state, the latter systems are less so because certain nonlinear constraints are imposed on the configuration. Depending on the specific constraints, the latter interactions can create "stealthy" systems [325], "super-ideal gases" [26], "equi-luminous materials" [26], as well as other unusual ground states [329, 350].

It it natural to expect that the entropy of these disordered ground states is large and extensive for two reasons. First, entropy has often been associated with the amount of disorder in a system. It was not until 1949 that Onsager realized that entropy and disorder are not always directly related to one another by showing that the entropy of a fluid of hard needles can increase when the needles tend to align with one another, and hence increasing the orientational order of the system [219]. Hard spheres and disks also undergo an entropically driven disorder-order phase transition at sufficiently high densities [8, 99]. Second, as the aforementioned examples illus-

trate, the tendency for ground states to be disordered is caused by the nature of the interactions, which allows certain individual or collective displacements of particles without causing any change in the energy. A ground-state configuration can thus move in these unconstrained directions of the configuration space, and thus become pattern-degenerate with large and extensive entropy. Here we define a set of ground states to be pattern-unique if all of the ground state structures are equivalent, and pattern-degenerate otherwise [1].

In this chapter, we demonstrate that our previously suggested "perfect glass" many-particle system [354] surprisingly possess classical ground states that are counterintuitively disordered with zero enumeration entropy. Perfect glasses are distinguished from normal glasses and other amorphous solids in that they are by construction hyperuniform (anomalously suppress large-scale density fluctuations) [317], as defined by a static structure factor that tends to zero in the infinite-wavelength limit [317]; see Ref. [307] for recent developments. Also, perfect glasses can never crystallize or quasicrystallize at zero or any positive temperature [354], and therefore circumvent the Kauzmann paradox [157]. By contrast, traditional glasses have been venerably understood as liquids kinetically arrested from cooling that are metastable with respect to a crystal [12, 263, 274, 79, 122]. The unique disordered ground states of "perfect glass" models are to be contrasted with zero-entropy crystals and quasicrystals that possess high symmetry and long-range translational and/or rotational

[1]It should be stressed that this chapter focuses on classical many-particle systems. If one includes spin systems (or equivalently, lattice-gas systems), which by definition lack continuous deformations, there are known examples of unique or pattern-unique classical ground states. In the "low-correlation" spin model [195] and a subsequent simplified model [196], the ground state is pattern-unique for a small fraction of system sizes but degenerate for other system sizes, while the degeneracy in the infinite-system-size limit is uncertain. (Although neither Ref. [195] nor Ref. [196] explicitly commented on the ground state degeneracy, we subsequently enumerated all possible spin configurations for 10-20 sites, and found that the ground states of the one-dimensional model described in Ref. [195] are degenerate, even after removing trivial translations and inversions, except for number of sites $N_s = 11$ and $N_s = 15$. Ref. [196] stated that its model has the same ground states as the model described in Ref. [195].) Another example, the well-known spin-glass models, has an unambiguously pattern-unique disordered ground state [81], but does so in a trivial way: the interaction is disordered (different for each pair of neighboring sites), causing the disordered ground state.

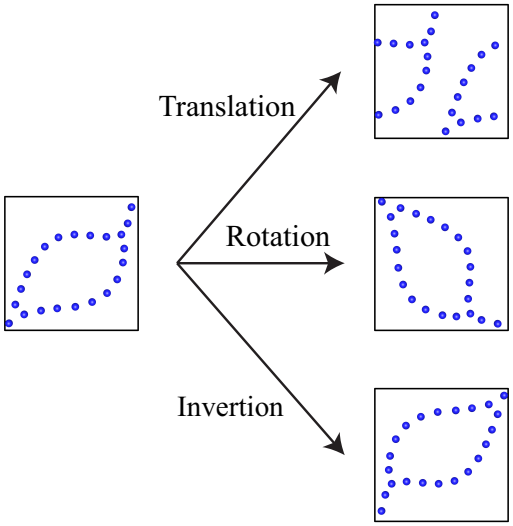

Figure 10.1 Illustration of the three pattern-preserving symmetry operations. Two configurations have the same pattern if they are related to each other through any combination of these three symmetry operations.

order. Thus, these disordered ground states can be fertile area for future research in disciplines beyond physics. Moreover, unlike spin-glass models [81], perfect-glass interactions treat all particles equally and thus does not introduce disorder by the intrinsic random nature of the interactions; unlike the low-correlation spin model [195, 196], the ground state is pattern-unique for all finite system sizes we have studied, and is therefore expected to be pattern-unique in the infinite-system-size limit.

The perfect-glass interaction potential [354] has either a direct-space or Fourier-space representation. In the latter case, we have

$$\Phi(\mathbf{r}_1, \mathbf{r}_2, \cdots, \mathbf{r}_N) = \sum_{0<|\mathbf{k}|<K} \tilde{v}(\mathbf{k})[S(\mathbf{k}) - S_0(\mathbf{k})]^2 \tag{10.2}$$

attempts to constrain the static structure factor, $S(\mathbf{k}) = |\sum_j \exp(i\mathbf{r}_j \cdot \mathbf{k})|^2/N$, to a target function $S_0(\mathbf{k}) = |\mathbf{k}|^\alpha$, for all $\mathbf{k}$ vectors within a certain distance K from the origin; and assigns energy penalties, adjusted by a weight function $\tilde{v}(\mathbf{k}) = (K/|\mathbf{k}| - 1)^3$, if such constraints are violated. Here $\mathbf{r}_j$ is the location of the jth particle, $\mathbf{k}$

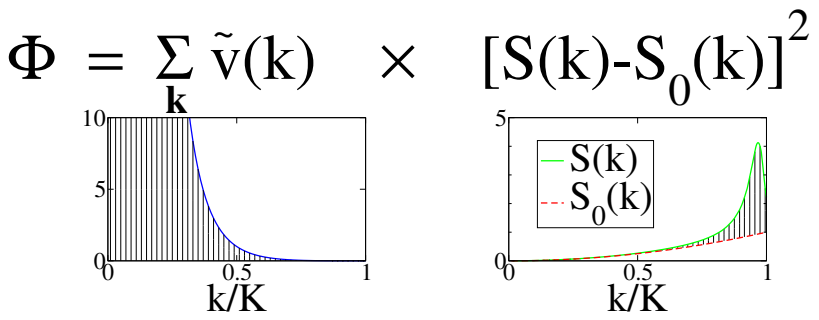

Figure 10.2 Shaded-area illustration of the two multiplicative contributions of the potential energy, defined in Eq. (10.2).

is a wave vector, N is the total number of particles, and α is a positive parameter we can choose freely. The two multiplicative factors in the summand of Eq. (10.2) are illustrated in Fig. 10.2. In general, other forms of $S_0(\mathbf{k})$ and $\tilde{v}(k)$ may also be used, but the particular form was chosen to realize hyperuniformity. The direct-space representation of the perfect-glass potential (10.2) involves a sum of two-body, three-body, and four-body interactions [329].

Define χ as the ratio of the number of constrained degrees of freedom to the number of independent degrees of freedom [354]. We found that when χ is larger than unity, the system runs out of degrees of freedom and becomes glassy, *i.e.,* develops a complex energy landscape with multiple energy minima, and a positive shear modulus [354]. This model completely banishes crystalline structures at any nonnegative temperature, since the existence of Bragg peaks would make the potential energy infinite.

10.2 Simulation Details

While Ref. [354] focused on the non-equilibrium glassy states of this interaction, here we study the classical ground state and demonstrate its pattern uniqueness. We minimize the potential energy, using the low-storage BFGS algorithm [214, 183, 150], starting from random initial configurations, to find local minima of the potential en-

ergy surface. A random local minimum of the potential energy surface is deemed to be reached once the energy minimization routine finishes with a stringent tolerance of $\delta\Phi = 10^{-11}$. Therefore, by repeating this process a sufficient number of times, we expect to find the global minimum of the potential energy surface. After 10^7 to 10^9 independent energy minimization trials, a lowest energy is achieved at least 10 times, but often more than 10^3 times (see the Appendix A for details). Presumably, this is the ground state energy. After that, we compare the ground-state configurations for pattern uniqueness. A particular ground-state configuration is taken to be a comparator, and then we compare it to every other ground-state configuration. Using an algorithm detailed in Appendix B, we attempt to find a translation, a rotation, and/or an inversion so that after these symmetry operations the comparator superposes onto the original ground state. After these symmetry operations are performed, if each particle in the comparator is within $10^{-5}L$ distance to a particle in the other ground state, then the two ground states are deemed to have the same pattern. Here L denotes the side length of the simulation box. The ground state is considered pattern-unique if all of the ground-state configurations have the same pattern as the comparator.

10.3 Results

We studied a total of 60 different combinations of parameters (d, α, χ, and N); see Appendix A for a complete list. These cases cover wide ranges of N (between 10 and 70, including both prime N's and composite N's), α (between 0.5 and 6), and χ (between 1.7 and 2), in one, two, and three dimensions. For all cases, the ground state was found to be disordered and pattern-unique. The discovered ground states of the largest N cases in the first three space dimensions are presented in Fig. 10.3.

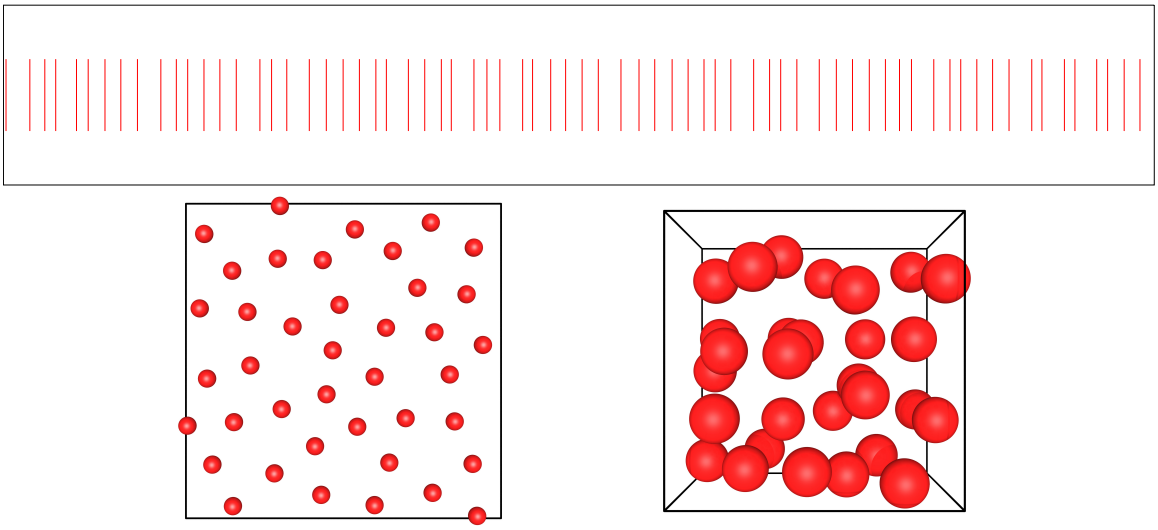

Figure 10.3 The disordered unique ground states of the perfect-glass potential for (top) $d = 1$, $\alpha = 6$, $\chi = 1.75$, and $N = 70$; (bottom left) $d = 2$, $\alpha = 6$, $\chi = 1.87$, and $N = 40$; and (bottom right) $d = 3$, $\alpha = 6$, $\chi = 1.75$, and $N = 30$. These figures illustrate a point presented in Ref. [354], namely, the particles experience a pair repulsion that is clearly observed when one calculates the pair correlation function.

Besides the ground states, we also study other minima of the potential energy surface. As Fig. 10.4 shows, as N increases, the success rate (the probability that one finds the ground state through an energy minimization trial) decreases exponentially, and the number of discovered energy minima increases exponentially. This exponential rise of the number of higher minima is in agreement with what one has topographically for real glass formers [282]. Compared to the $\alpha = 1$ case, the $\alpha = 6$ case possesses a higher success rate and fewer distinct energy levels. This is also expected because as we have discovered earlier, increasing α increases geometrical order in these glasses [354]. Finally, Fig. 10.4 also shows that the ground state energy is roughly proportional to N for both α values we presented.

To further confirm ground-state uniqueness, we have also performed Wang-Landau Monte Carlo (WLMC) simulations on a perfect-glass system with $d = 2$, $\alpha = 1$, $\chi = 1.89$, and $N = 10$. The WLMC algorithm allows one to calculate the density of states $g(E)$ as a function of the potential energy [335] (or equivalently, the hyper-area

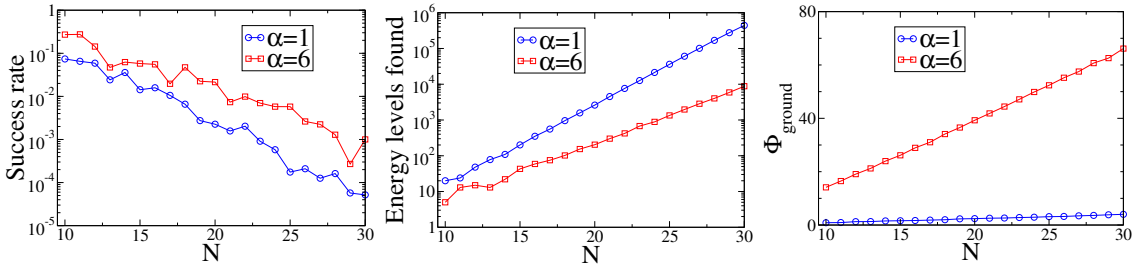

Figure 10.4 (left) The probability of finding the ground states by energy minimization for $d = 1$, $\chi = 2.00$, $\alpha = 1$ and 6, and $10 \leq N \leq 30$. (middle) The number of distinct energy local minima found by 10^7 repeated energy minimizations for the same systems. (right) The ground-state energy of the same systems.

of an iso-energy surface in the configuration space). Alternatively, for energy values very close to the ground state, one could also calculate $g(E)$ from the eigenvalues of the Hessian matrix by treating the system as an harmonic oscillator around the ground state. As detailed in Appendix D, after considering the aforementioned trivial symmetry operations, we find very good agreement between the calculated $g(E)$'s from these two approaches, which differ by less than 12%. If the ground state was 2-fold degenerate, there would be a two-fold difference between the calculated $g(E)$. Therefore, the ground state has to be unique.

From the density of states, we have also calculated the excess isochoric heat capacity C_V of the system, which is given by

$$C_V = \frac{d < \Phi >}{dk_B T}, \tag{10.3}$$

where

$$< \Phi >= \frac{\int E g(E) \exp(-E/k_B T) dE}{\int g(E) \exp(-E/k_B T) dE}. \tag{10.4}$$

The heat capacity, presented in Fig. 10.5, starts at the harmonic value at $T = 0$, and begins to rise because the shape of the potential energy landscape is such that the effective harmonic force constants are reduced in order to produce transition pathways to neighboring minima. The reduction of the local effective force constants

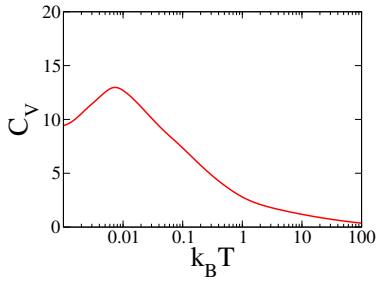

Figure 10.5 Isochoric heat capacity C_V of the perfect-glass system of $d = 2$, $\alpha = 1$, $\chi = 1.89$, and $N = 10$. Here, the constant contribution to the heat capacity from the kinetic energy, $C_{V,\,\text{kinetic}} = dN/2$, is excluded.

increases the amount of configuration spaces associated with that particular level of the potential energy, and therefore increases the heat capacity. Eventually, C_V levels off and decreases because the energy landscape becomes irrelevant at very high temperature.

10.4 Conclusions and Discussion

To summarize, all previously known disordered classical ground states are caused by interactions that allow continuous configurational deformations without energy change. These deformations also cause the ground state to possess large and extensive entropy. Instead of the previous approach, here we create disordered classical ground states by penalizing crystalline order, causing no ground-state degeneracy. These zero-entropy ground states are in sharp contrast with zero-entropy crystalline ground states, since the latter possess very high symmetry and long-range translational and rotational order. Thus, our ground states can be fertile areas for future research in subjects such as mathematics, physics, and cryptography.

Our discovery of unique disordered ground states impinge on the famous Kauzmann glass paradox [157] and the associated "ideal glass" [67] in two ways. First, the perfect-glass model completely circumvents the Kauzmann entropy crisis between the crystal and liquid states, since crystalline and quasicrystalline structures are com-

pletely forbidden in perfect glasses. On the other hand, like "ideal glasses," perfect-glass ground states are disordered while having zero enumeration entropy.

Finally, we also expect our results to be useful in cryptography, where pseudo-random functions with tunable computational complexity are desired; for example, in deriving an encryption key from a password [169]. The task of finding a perfect-glass ground state suits this need, since its complexity can easily be tuned by changing a set of parameters (d, N, α, and χ).

10.5 Appendix A: List of Parameters Tried

We list the parameter combinations (d, α, χ, and N) for which we have carried out enumeration studies as well as several statistics of such studies in Table 10.1.

d	α	χ	N	Number of inherent structures generated	Number of lowest-energy structures generated	Lowest energy	Mean energy (of inherent structures)	Number of distinct energies found
2	1	2.20	6	10^6	97510	0.0534	0.094867	37
2	0.5	1.89	10	3×10^7	1769	0.0059314	0.046363	34719
2	1	1.89	10	3×10^7	14442	0.0512129	0.126145	7398
2	2	1.89	10	3×10^7	1508436	0.835746	0.953847	339
2	6	1.89	10	3×10^7	5178002	2.73031	2.86945	34
2	1	1.87	16	10^8	147	0.0618558	0.178029	2.16×10^7
2	1	1.89	20	10^9	40	0.0664875	0.204629	7.41×10^8
2	6	1.89	20	10^8	265084	5.37199	5.74988	147590
2	6	1.90	30	10^8	1634	8.0647	8.57543	4.08×10^7
2	6	1.87	40	10^8	11	10.6843	11.3862	9.10×10^7
1	1	1.79	20	2×10^7	60490	0.517475	1.015135	3492
1	1	1.74	40	5×10^7	24	0.991197	1.849102	3.06×10^7
1	1	1.79	50	10^9	12	1.68337	2.94643	8.45×10^8
1	6	1.75	60	10^8	28	77.8601	79.7294	5.46×10^7
1	6	1.75	70	10^9	27	93.3095	95.7188	5.94×10^8
1	1	2.00	10	10^7	739724	0.866727	1.31398	20
1	1	2.00	11	10^7	651397	0.929444	1.42011	24
1	1	2.00	12	10^7	589273	1.2673	1.69868	48
1	1	2.00	13	10^7	242182	1.31007	1.87405	78
1	1	2.00	14	10^7	358037	1.53538	2.06303	109
1	1	2.00	15	10^7	142763	1.61837	2.29402	201
1	1	2.00	16	10^7	158544	1.69043	2.50381	351
1	1	2.00	17	10^7	105541	1.85802	2.74284	557
1	1	2.00	18	10^7	65853	1.98903	2.96204	959
1	1	2.00	19	10^7	27438	2.31345	3.17478	1578
1	1	2.00	20	10^7	22617	2.40054	3.4008	2613
1	1	2.00	21	10^7	15771	2.55858	3.64033	4527
1	1	2.00	22	10^7	20318	2.63018	3.85341	7645
1	1	2.00	23	10^7	9110	2.80526	4.06194	12665
1	1	2.00	24	10^7	5778	2.93012	4.289	21383
1	1	2.00	25	10^7	1754	3.1362	4.52102	36116
1	1	2.00	26	10^7	2095	3.21506	4.7385	60728
1	1	2.00	27	10^7	1261	3.45142	4.95513	100960
1	1	2.00	28	10^7	1618	3.60496	5.1805	168599
1	1	2.00	29	10^7	573	3.84163	5.39782	275767
1	1	2.00	30	10^7	518	4.01308	5.60469	442279
1	6	2.00	10	10^7	2715392	14.13106	14.2772	5

1	6	2.00	11	10^7	2749262	16.47931	16.8239	13
1	6	2.00	12	10^7	1432882	19.08413	19.325	15
1	6	2.00	13	10^7	470326	21.22258	21.5804	13
1	6	2.00	14	10^7	624508	23.95933	24.2088	22
1	6	2.00	15	10^7	578671	26.13922	26.7836	43
1	6	2.00	16	10^7	554290	28.93276	29.444	59
1	6	2.00	17	10^7	196175	31.03469	31.902	75
1	6	2.00	18	10^7	471502	34.10818	34.6142	102
1	6	2.00	19	10^7	224480	36.54381	37.2612	154
1	6	2.00	20	10^7	214371	39.26553	39.9763	204
1	6	2.00	21	10^7	73660	41.83513	42.6645	301
1	6	2.00	22	10^7	98901	44.40762	45.3614	422
1	6	2.00	23	10^7	69845	47.1069	48.1436	677
1	6	2.00	24	10^7	57822	49.86945	50.8796	887
1	6	2.00	25	10^7	57726	52.37915	53.5622	1343
1	6	2.00	26	10^7	26194	55.20688	56.4128	1966
1	6	2.00	27	10^7	22438	57.52615	59.1253	2853
1	6	2.00	28	10^7	12874	60.70169	61.9653	4022
1	6	2.00	29	10^7	2699	62.57372	64.6753	5898
1	6	2.00	30	10^7	10039	66.15001	67.5981	8796
3	1	1.70	10	3×10^7	1418	0.0020304	0.0196315	1.04×10^6
3	6	1.77	20	3×10^7	553282	1.05579	1.24064	945314
3	6	1.75	30	3×10^7	518	1.69167	1.88439	2.51×10^7

Table 10.1 List of all the parameter combinations (d, α, χ, and N) we have carried out enumeration study for; and a summary of results for each combination, which includes the number of inherent structures that we generated, the number of times the ground state structure was achieved, the ground-state energy, the mean energy of inherent structures, and the number of distinct energy levels of inherent structures found.

10.6 Appendix B: Details of the Configuration Comparison Algorithm

In the main text, we noted an algorithm that we devised to compare two configurations, and could determine whether one configurations can be superposed onto another after a translation, a rotation, and/or an inversion. We detail this algorithm here.

Let us start with the one-dimensional case for simplicity. For each configuration, we find a "characteristic vector" by the following step:

- Find the closest pair of particles, A and B. Find out their locations, $\mathbf{r}_A$ and $\mathbf{r}_B$.
- Find the distance from particle A to its second closest neighbor particle, d_A; and the same distance for particle B, d_B.
- If $d_A > d_B$, then swap particles A and B.
- The characteristic vector is $\mathbf{v}_1 = \mathbf{r}_B - \mathbf{r}_A$.

The characteristic vector is invariant to configuration translations and particle permutations, and rotates or inverts if the configuration is rotated or inverted. Thus, if the two configurations are indeed related to each other through these trivial symmetry operations, then their characteristic vector must be related to each other by a constant 1 or -1, *i.e.,*

$$\mathbf{v}_1^2 = R\mathbf{v}_1^1, \tag{10.5}$$

where $\mathbf{v}_1^j$ is the characteristic vector of the jth configuration, and R is either 1 or -1. If $R = 1$, then the two configurations are not related to each other by any rotation or inversion. If $R = -1$, then the two configurations are related to each other by a 180° rotation, or equivalently in one dimension, an inversion. The translation relating the two configurations can be found by the difference of the location of particle A: $\mathbf{t} = \mathbf{r}_A^2 - R\mathbf{r}_A^1$, where the superscripts indicate different configurations. Having found the translation and rotation relating these configurations, one can verify that for each particle j in the first configuration, at location $R\mathbf{r}_j^1 + \mathbf{t}$ there is a particle in the second configuration. If so, and if the two configurations have the same number of particles, then these two configurations must be related to each other through symmetry operations.

To generalize this method to $d > 1$ dimensions, one must find d characteristic vectors, derived from d closest particle pairs. Solving the following matrix equation

gives the rotation/inversion matrix between the two configurations, R.

$$\begin{pmatrix} \mathbf{v}_1^2 & \mathbf{v}_2^2 & \cdots & \mathbf{v}_d^2 \end{pmatrix} = R \begin{pmatrix} \mathbf{v}_1^1 & \mathbf{v}_2^1 & \cdots & \mathbf{v}_d^1 \end{pmatrix} \tag{10.6}$$

where $\mathbf{v}_i^j$ is the ith characteristic vector of the jth configuration. The translation relating the two configurations can be found similarly by $\mathbf{t} = \mathbf{r}_A^2 - R\mathbf{r}_A^1$, where $\mathbf{r}_A^j$ denotes the starting particle in finding the first characteristic vector in configuration j. Similar to the 1D case, the jth particle in configuration 1 still corresponds to a particle at $R\mathbf{r}_j^1 + \mathbf{t}$ in configuration 2.

10.7 Appendix C: Density of States $g(E)$ from Harmonic Approximations

In the main text, we mentioned that the density of states, $g(E)$, calculated from harmonic approximations, matches that obtained from Wang-Landau Monte Carlo simulations at low temperatures. Here we detail how one find $g(E)$ using harmonic approximations.

For a d-dimensional configuration of N particles, the configuration space is dN-dimensional. Of these dN directions of the configuration space, d directions correspond to translations of the whole configuration, which cause no energy change. The other $d(N-1)$ directions corresponds to deformations, which generally change the potential energy. Near the classical ground state, such changes can be quantified by the eigenvalues of the Hessian matrix, λ_1, λ_2, $\cdots$, $\lambda_{d(N-1)}$. Let E denote an energy that is slightly above the ground-state energy, E_0, the portion of the configuration space with potential energy $\Phi \leq E$ is given by the equation

$$E \geq E_0 + \frac{\lambda_1}{2}x_1^2 + \frac{\lambda_2}{2}x_2^2 + \cdots + \frac{\lambda_{d(N-1)}}{2}x_{d(N-1)}^2, \tag{10.7}$$

where x_1, x_2, $\cdots$, $x_{d(N-1)}$ are the deformations along each eigenvectors of the Hessian matrix. Equation (10.7) specifies a $d(N-1)$-dimensional ellipsoid, for which the hypervolume is

$$\mathcal{V}_{\text{vibrational}} = \frac{\pi^{d(N-1)/2}}{\Gamma(1+d(N-1)/2)} \prod_{j=1}^{d(N-1)} \sqrt{\frac{2\delta E}{\lambda_j}}, \tag{10.8}$$

where $\frac{\pi^{d(N-1)/2}}{\Gamma(1+d(N-1)/2)}$ is the volume of a $d(N-1)$-dimensional hypersphere of unit radius and $\delta E = E - E_0$.

To obtain the total volume in the configuration space for which $\Phi \leq E$, one need to multiply Eq. (10.8) with a few additional factors to account for trivial symmetry operations. First, there are d independent translations, each contributes a factor of $\sqrt{N}L$, where L is the side length of the simulation box. The factor $\sqrt{N}$ comes from the fact that translations correspond to diagonal movements in the configuration space. An additional factor, f, that depends on the space dimension and the simulation box shape, also needs to be included to account for rotations and inversions. For $d = 2$ with square box, $f = 8$, since such boxes allow rotations of 0°, 90°, 180°, and 270°, and a combination of any rotation with an inversion. Lastly, particle permutations contribute a factor of $N!$. Overall, the total volume in the configuration space is

$$\mathcal{V} = N^{d/2} V f N! \frac{\pi^{d(N-1)/2}}{\Gamma(1+d(N-1)/2)} \prod_{j=1}^{d(N-1)} \sqrt{\frac{2\delta E}{\lambda_j}}, \tag{10.9}$$

where $V = L^d$ is the volume of the simulation box.

The density of states is the surface area of the total volume in the configuration space for which $\Phi \leq E$ to E, and is therefore the derivative of $\mathcal{V}$ to E.

$$g(E) = \frac{d\mathcal{V}}{dE} = N^{d/2} V f N! \frac{\pi^{d(N-1)/2}}{\Gamma(1+d(N-1)/2)} \left(\prod_{j=1}^{d(N-1)} \sqrt{\frac{2}{\lambda_j}} \right) \frac{d(N-1)}{2} \delta E^{d(N-1)/2-1}, \tag{10.10}$$

10.8 Appendix D: Details about Wang-Landau Monte Carlo Simulations

As detailed in the main text, we used Wang-Landau Monte Carlo (WLMC) algorithm to calculate $g(E)$ for a perfect-glass system of $d = 2$, $N = 10$, $\chi = 1.89$, and $\alpha = 1$. To do so, we first divide the energy range $E_0 \leq \Phi < 10^5$ into $N_{\rm bin} = 2 \times 10^4$ bins that are equidistant in a logarithmic scale. Let the minimum and maximum energies of a bin be $E_{\rm min}$ and $E_{\rm max}$, the WLMC algorithm allows one to calculate $g_{\rm bin} = c \int_{E_{\rm min}}^{E_{\rm max}} g(E)dE$ over every bin, where c is an unknown constant independent of the bin [335]. We then determine c by the condition $V^N = \int_{E_0}^{\infty} g(E)dE = \sum g_{\rm bin}$, where the upper limit of the integration can be replaced with 10^5, since $g(E)$ turns out to be negligible for very large E. We finally divide $g_{\rm bin}$ with $(E_{\rm max} - E_{\rm min})$ to find out $g(E)$ at each bin.

We perform a total of 1500 stages of Monte Carlo simulations, each consisting of $N_{\rm trial} = 4 \times 10^7$ trial moves. In each trial move, a random particle is moved by a distance of xyL in every direction, where x is uniformly distributed between -1 and 1, y have 50% probability of being 0.2 and 50% probability of being 0.002, and L is the side length of the simulation box. The WLMC algorithm has a tuning parameter, called the "modification factor" in [335], that affects its efficiency and accuracy. Following Ref. [30], we let this factor be $f = \exp\{\max[2N_{\rm bin}/(N_{\rm trial}i), \exp(-0.1i)]\}$ at the ith stage, where $\max(a, b)$ denotes the maximum value between a and b.

We have performed two independent runs of the simulations detailed above. The resulting $g(E)$ is presented in Fig. 10.6 and compared with the $g(E)$ obtained from the harmonic approximation. At the lowest energies, $g(E)$ from both runs agree very well with that from the harmonic approximation. This verifies the uniqueness of the perfect-glass ground state.

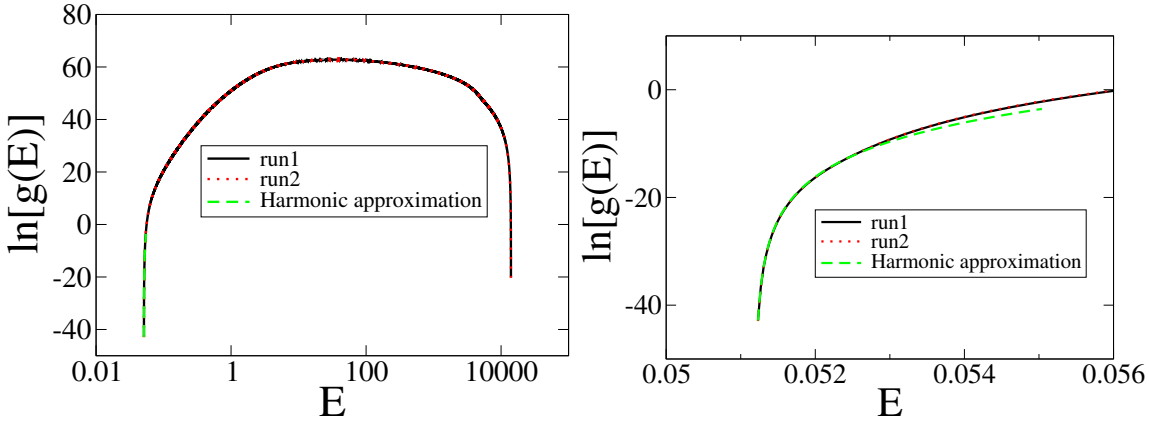

Figure 10.6 (left) Natural logarithm of the density of states, $g(E)$, from two independent runs of WLMC simulations, and from the harmonic approximation. (right) A zoomed-in view near the ground-state energy $E_0 = 0.0512129\ldots$.

Chapter 11

Structure Factor of the Primes

11.1 Introduction

The properties of the prime numbers have been a source of fascination for millenia. Euclid proved that there are infinitely many primes. While the prime numbers are a deterministic subset of the odd integers, they can be viewed, by some measures, as pseudo-random numbers. Given a prime number p_n, the subsequent prime can be found deterministically by sieving [261]. Nonetheless, there is no known deterministic formula that can quickly (polynomial in the number of digits in a prime) generate large numbers that are guaranteed to be prime. (The largest known prime is $2^{43,112,609} - 1$, which is about 13 million digits long.) Let $\pi(n)$ denote the *prime counting function*, which gives the number of primes less than integer n. According to the prime number theorem [124], the prime counting function in the large-n asymptotic limit is given by

$$\pi(n) \sim \frac{n}{\ln(n)} \qquad (n \to \infty). \tag{11.1}$$

This means that for sufficiently large n, the probability that a randomly selected integer not greater than n is prime is very close to $1/\ln(n)$, which can be viewed as position-dependent number density $\rho(n)$ (number of primes up to n divided by the

interval n). This implies that the primes become sparser as n increases and hence can be regarded as a statistically inhomogeneous set of points that are located on a subset of the odd integers.

Let z denote the gap size between any two consecutive primes and $P(z)$ the corresponding *gap probability distribution*. Figure 11.1 compares the *gap probability distribution* $P(z)$ for the primes to the *uncorrelated lattice gas* at the same number density. Here, "uncorrelated lattice gas" refers to a lattice-gas system where each site has a certain probability of being occupied, independent of the occupation of other sites. For an uncorrelated lattice gas at number density $\rho = N/L$ with lattice spacing 2 in the infinite-system-size limit, the gap distribution is exactly given by

$$P(z) = f(1-f)^{z/2-1}, \tag{11.2}$$

where $f = 2\rho$ is the probability that a site is occupied. We see that by the gap distribution, the primes cannot be clearly distinguished from the uncorrelated lattice gas. Indeed, probabilistic methods to treat the primes have yielded fruitful insights about them [111, 104, 210]. For example, based on the assumption that the primes behave like a Poisson process (uncorrelated lattice gas), Cramér (1920) conjectured that [111] for large n

$$g(n) \geq c \ln^2(n) \tag{11.3}$$

where $g(n)$ denotes the *largest prime gap* within an interval $[n, 2n]$. Moreover, there are quick *stochastic* ways to find large primes [205, 237, 228, 23, 16, 7]. Examples are based on variants of Fermat's little theorem [205, 237, 228, 23].

On the other hand, it is known that primes contain unusual patterns. Chebyshev observed in 1853 that primes congruent to 3 modulo 4 seem to predominate over those congruent to 1 [112]. Assuming a generalized Riemann hypothesis, Rubinstein and Sarnak [257] exactly characterized this phenomenon and more general related results.

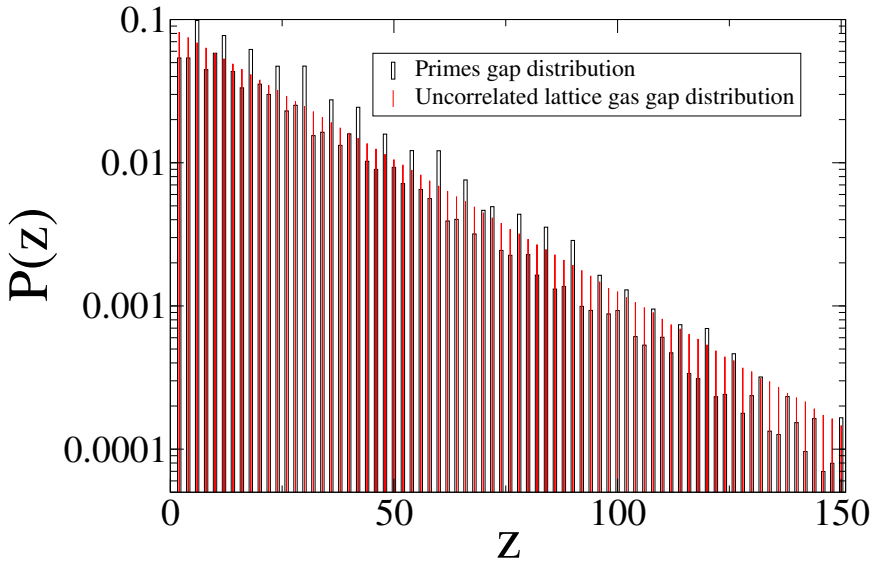

Figure 11.1 Comparison of the gap distribution for the primes and the uncorrrelated lattice gas with the same cardinality (occupation number) as the set of primes. The primes are taken to lie on an integer lattice with a spacing of 2, i.e., a subset of the odd positive integers. We consider N primes in interval $[M, M+L]$ (M large and $M \gg L$). Here $N = 10^7$, $L = 244651480$ with $M = 42151671493$, the 1,800,000,000th prime number.

A computational study on the Goldbach conjecture demonstrates a connection based on a modulo 3 geometry between the set of even integers and the set of primes [197]. In 1934, Vinogradov proved that every sufficiently large odd integer is the sum of three primes [333]. This method has been extended to cover many other types of patterns [116, 117, 115, 292]. Recently it has been shown that there are infinitely many pairs of primes with some finite gap [358] and that primes ending in 1 are less likely to be followed by another prime ending in 1 [176]. Numerical evidence of regularities in the distribution of gaps between primes when these are divided into congruence families have also been reported [200, 64, 340], along with the observation of period-three oscillations in the distribution of increments of the distances between consecutive primes numbers [172].

The present chapter is motivated by some unusual properties of the Riemann zeta function $\zeta(s)$, which is a function of a complex variable s that is intimately related to the primes. The zeta function has many different representations, one of which is

the series formula

$$\zeta(s) = \sum_{n=1}^{\infty} \frac{1}{n^s}, \tag{11.4}$$

which converges for $Re(s) > 1$. However, $\zeta(s)$ has a unique analytic continuation to the entire complex plane, excluding the simple pole at $s = 1$. According to the *Riemann hypothesis*, the nontrivial zeros of the zeta function lie along the *critical line* $s = 1/2 + it$ with $t \in \mathbb{R}$ in the complex plane. The nontrivial zeros tend to get denser the higher on the critical line. When the spacings of the zeros are appropriately normalized so that they can be treated as a homogeneous point process at unity density, the resulting pair correlation function takes on the simple form $1 - \sin^2(\pi r)/(\pi r)^2$ [210]. The corresponding structure factor $S(k)$ (essentially the Fourier transform of $g_2(r)$) tends to zero linearity in the wavenumber k as k tends to zero but is unity for sufficiently large k. This implies that the normalized Riemann zeros possess a remarkable type of correlated disorder at large length scales known as hyperuniformity [315]. A hyperuniform many-particle system is one in which the structure factor approaches zero in the infinite-wavelength limit [317]. In such systems, density fluctuations are anomalously suppressed at very large length scales, a "hidden" order that imposes strong global structural constraints. All structurally perfect crystals and quasicrystals are hyperuniform, but typical disordered many-particle systems, including gases, liquids, and glasses, are not. Disordered hyperuniform many-particle systems are exotic states of amorphous matter that have attracted considerable recent attention [317, 349, 74, 347, 149, 173, 77, 145, 177, 136, 142, 66, 68, 341, 211, 95, 325, 328, 352, 353, 28, 216, 307, 343]. The zeta function is directly related to the primes via the following Euler product formula:

$$\zeta(s) = \Big[\prod_{n=1}^{\infty} [1 - 1/p_n^s] \Big]^{-1}. \tag{11.5}$$

Similarly, there are a variety of *explicit* formulas that link the primes on the one hand to the zeros of the zeta function on the other hand [65, 294, 141]. Thus, one can in principle deduce information about primes from information about zeros of the zeta function. Accordingly, one might expect the primes to encode hyperuniform correlations seen in the Riemann zeros.

In this chapter, we numerically study the pair statistics of the primes, especially the structure factor $S(k)$ in an interval $M \leq p < M+L$ with $M \to \infty$, $L/M \to \beta < 1$. As we will detail in Sec. 11.2.3, this choice of intervals allow us to obtain prime configurations with virtually uniform density. We show that the structure factor exhibits well-defined Bragg-like peaks along with a small "diffuse" contribution. This indicates that the primes are appreciably more correlated than previously thought. Our numerical results definitively suggest an explicit formula for the locations and heights of the peaks, which we prove in [324] using analytic number theory. A simplified proof is also included in this chapter. The formula predicts infinitely many peaks in any non-zero interval, similar to the behavior of quasicrystals. However, primes differ from quasicrystals in that the ratio between the location of any two predicted peaks is rational. We also show numerically that the diffuse part decays slowly as M or L increases. This might indicate that the diffuse part vanishes in an appropriate infinite-system-size limit [324].

11.2 Definitions, Preliminaries, and Simulation Procedure

Given an odd integer $M \geq 3$ and an even integer L, let p_j be jth prime number such that $M \leq p_j < M + L$, where $1 \leq j \leq N$, and N is the number of prime numbers within the interval L such that $M \to \infty$, $L/M \to \beta < 1$. Let us call this set of prime numbers a "configuration." Figure 11.2 illustrates an example of a prime

configuration. We will study the pair correlation function as well as the structure factor of prime-number configurations. For all cases considered in this chapter, $M \geq 3$. Therefore, all of the p_j's are odd integers. We thus treat prime numbers as a lattice-gas system. Each odd integer is a lattice site that can be either occupied (prime) or unoccupied (composite). The rest of this section details mathematical tools we use to treat such systems.

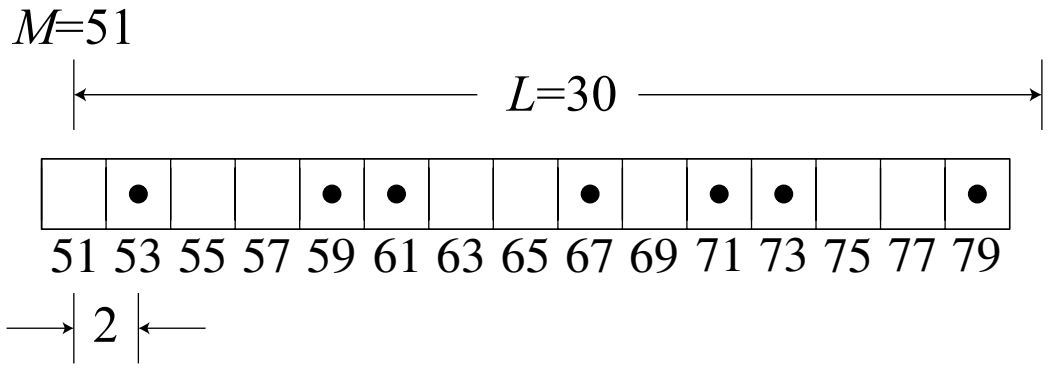

Figure 11.2 Schematic plot of a prime-number configuration with $M = 51$ and $L = 30$. Since we always use $M \geq 3$, any prime number in the interval $[M, M + L)$ is odd. Therefore, a prime-number configuration is a lattice gas with lattice spacing 2 in which the primes are the "occupied" sites and the composites are "unoccupied" sites.

11.2.1 Discrete Fourier transform

For a function $f(r)$ defined on an integer lattice with spacing a that is contained within a periodic box of length L, one may define its Fourier transform as follows:

$$\tilde{f}(k) = \sum_{r=0,a,2a,\cdots,L-a} f(r) \exp(ikr), \tag{11.6}$$

where the parameter k is an integer multiple of $2\pi/L$. The inverse transform is given by

$$f(r) = \frac{1}{N_s} \sum_{j=0}^{N_s-1} \tilde{f}\left(\frac{2\pi j}{L}\right) \exp\left(-i\frac{2\pi j}{L} r\right), \tag{11.7}$$

where $N_s = L/a$ is the number of sites.

11.2.2 Pair statistics and sum rules

Define $\eta(r)$ as the indicator function such that $\eta(r) = 1$ if the site at r is occupied, and $\eta(r) = 0$ if the site at r is not occupied. Define occupation fraction $f =< \eta(r) >$, where $<>$ denotes an average over all r. Let $\tilde{\eta}(r)$ be its Fourier transform. We define the structure factor as

$$S(k) = |\tilde{\eta}(k)|^2/N - N\delta_{k,0}. \tag{11.8}$$

Define the pair correlation function $g_2(r)$ as

$$g_2(r) = \frac{1}{Nf} \sum_{n=0,a,2a,\cdots,L-a} \eta(n)\eta(n+r) - \delta_{r,0}. \tag{11.9}$$

By definition, $g_2(0) = 0$. For $r \neq 0$, $g_2(r)$ can be interpreted as the probability that the site at $p + r$ is occupied given that the site at p is occupied divided by f.

The structure factor and the pair correlation function are related as follows:

$$
\begin{aligned}
N\delta_{k,0} + S(k) &= |\tilde{\eta}(k)|^2/N \\
&= \frac{1}{N} \sum_{m=0,a,2a,\cdots,L-a} \eta(m)\exp(ikm) \sum_{n=0,a,2a,\cdots,L-a} \eta(n)\exp(-ikn) \\
&= \frac{1}{N} \sum_{m=0,a,2a,\cdots,L-a} \quad \sum_{n=0,a,2a,\cdots,L-a} \eta(m)\eta(n)\exp[ik(m-n)] \\
&= \frac{1}{N} \sum_{r=0,a,2a,\cdots,L-a} \quad \sum_{n=0,a,2a,\cdots,L-a} \eta(n+r)\eta(n)\exp(ikr) \\
&= \frac{1}{N} \sum_{n=0,a,2a,\cdots,L-a} \eta(n+0)\eta(n)\exp(ik0) \\
&+ \frac{1}{N} \sum_{r=a,2a,\cdots,L-a} \quad \sum_{n=0,a,2a,\cdots,L-a} \eta(n+r)\eta(n)\exp(ikr) \\
&= \frac{N}{N} + \frac{1}{N} \sum_{r=a,2a,\cdots,L-a} Nfg_2(r)\exp(ikr) \\
&= 1 + f \sum_{r=a,2a,\cdots,L-a} g_2(r)\exp(ikr) \\
&= 1 + f \sum_{r=0,a,2a,\cdots,L-a} g_2(r)\exp(ikr)
\end{aligned}
\tag{11.10}
$$

This equation enables us to obtain a sum rule for both $g_2(r)$ and $S(k)$. For $g_2(r)$, plugging $k = 0$ into Eq. (11.10) yields

$$
\frac{N-1}{f} = \sum_{r=a,2a,\cdots,L-a} g_2(r). \tag{11.11}
$$

The sum rule for $S(k)$ is easily found by invoking the inverse Fourier transform equation:

$$
g_2(r) = \frac{1}{N_s f} \sum_{j=0}^{N_s-1} \left[S\left(\frac{2\pi j}{L}\right) + N\delta_{k,0} - 1 \right] \exp\left(-i\frac{2\pi j}{L} r\right). \tag{11.12}
$$

At $r = 0$, this relation becomes

$$\begin{aligned} 0 &= \sum_{j=0}^{N_s-1} \left[S\left(\frac{2\pi j}{L}\right) + N\delta_{k,0} - 1 \right] \\ &= \sum_{j=1}^{N_s-1} S\left(\frac{2\pi j}{L}\right) + N - N_s, \end{aligned} \tag{11.13}$$

and hence the sum rule for the structure factor is given by

$$\sum_{j=1}^{N_s-1} S\left(\frac{2\pi j}{L}\right) = N_s - N. \tag{11.14}$$

For the primes, $L = 2N_s$, and hence the sum rule is specifically

$$\sum_{j=1}^{N_s-1} S\left(\frac{\pi j}{N_s}\right) = N_s - N. \tag{11.15}$$

11.2.3 Simulation procedure

The fact that all primes greater than 3 are odd integers lead to a few important properties of $S(k)$. First, $N\delta_{k,0} + S(k)$ is a periodic function of period π ,since

$$\begin{aligned} N\delta_{k+\pi,0} + S(k+\pi) &= \frac{|\sum_{j=1}^{N} \exp[-i(k+\pi)(p_j - M)]|^2}{N} \\ &= \frac{|\sum_{j=1}^{N} \exp[-ik(p_j - M)] \exp(-i\pi(p_j - M)]|^2}{N} \\ &= \frac{|-\exp(i\pi M) \sum_{j=1}^{N} \exp[-ik(p_j - M)]|^2}{N} \\ &= \frac{|\sum_{j=1}^{N} \exp[-ik(p_j - M)]|^2}{N} \\ &= N\delta_{k,0} S(k), \end{aligned} \tag{11.16}$$

Second, from Eqs. (11.6) and (11.8), one can see that when $k = m\pi$, where m is any non-zero integer, $S(k) = N$ achieves the global maximum of this function. The function $S(k)$ therefore displays strong peaks at such k values. Third, from

Eqs. (11.6) and (11.8), one can see the function $S(k)$ has reflection symmetry $S(k) = S(-k)$. This reflection symmetry, combined with the periodicity [Eq. (11.16)], implies another reflection symmetry, $S(\pi/2+k) = S(\pi/2-k)$. With these properties in mind, we only need to study $S(k)$ in the $0 < k \leq \pi$ range in this chapter.

One can similarly define the structure factor of uncorrelated lattice gases by replacing the N prime numbers, p_j, with N random odd integers. The resulting structure factor also has a period of π, displays a peak when k is a multiple of π, and has reflection symmetry $S(\pi/2 + k) = S(\pi/2 - k)$.

In statistical mechanics, the study of $S(k)$ often focuses on statistically homogeneous systems. However, the prime numbers are not homogeneous. Instead, in the vicinity of x, the density of prime numbers scales as $1/\ln(x)$. To overcome this difference, we focus on large M values and let L/M be a constant less than unity. This implies that the prime numbers in the interval $[M, M + L)$ are nearly uniformly distributed. For example, we will study a system of $M = 10^{10}$ and $L = 10^7$. As x changes from M to $M + L$, $1/\ln(x)$ only changes from $0.043429\cdots$ to $0.043427\cdots$.

We minimize the problem of inhomogeneity by requiring sufficiently large M. Instead, one might think an even better way to this problem is to rescale the configuration such that it is homogeneous. The natural scaling is to replace each prime number p with $p/\ln(p)$. However, it turns out that after performing such rescaling, the structure factor becomes not interesting. We present $S(k)$ of such a rescaled configuration in Fig. 11.3. The structure factor appears to be completely noisy, with no obvious peaks with heights comparable to N. This is to be contrasted with our findings reported in the rest of the chapter, in which we choose to study the primes in the interval $M \leq p \leq M + L$ with $M \to \infty$, $L/M \to \beta < 1$.

We obtain a list of prime numbers from Ref. [2], and calculate $S(k)$ of prime numbers and ideal uncorrelated lattice gases with the fast Fourier transform (FFT) algorithm using the kissFFT software [3]. This algorithm has the advantage of not

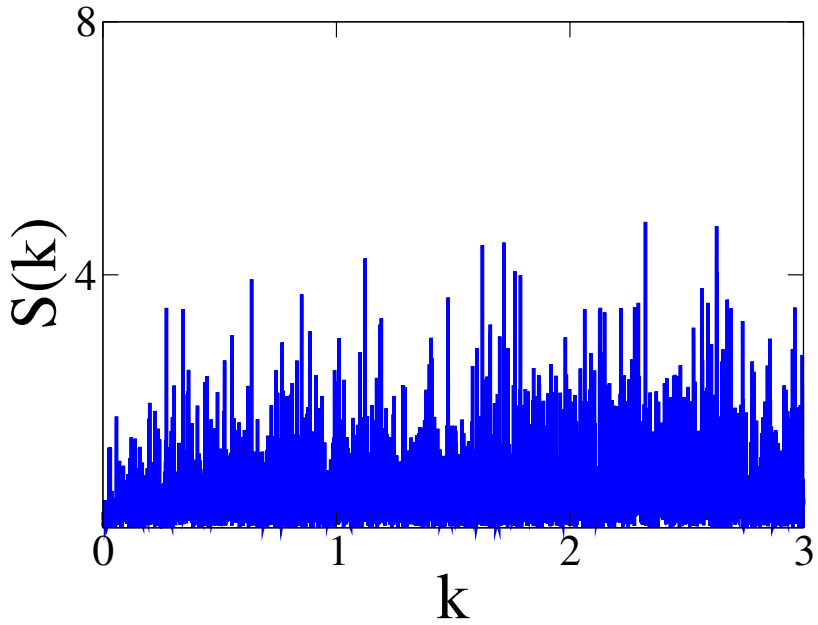

Figure 11.3 Structure factor $S(k)$ associated with $p/\ln(p)$ for all prime number p's in the interval $[3, 3+10^5)$.

only being "fast" [1], but also being accurate, as the upper bound on the relative error scales as $\epsilon \log(L)$, where ϵ is the machine floating-point relative precision. We use double-precision numbers to further minimize ϵ.

More precisely, FFT allows one to efficiently calculate

$$X(q) = \sum_{n=0}^{T-1} x_n \exp(-2\pi i q n/T) \tag{11.17}$$

for arbitrary x_0, x_1, $\cdots$, x_{T-1}. Here, we simply let $T = L/2$, and let $x_j = 1$ if $M + 2j$ is a prime number and $x_j = 0$ if $M + 2j$ is composite. The structure factor is then calculated from:

$$S(2\pi q/L) = |X(q)|^2/N. \tag{11.18}$$

[1] The time complexity of calculating $S(k)$ for all k's using FFT algorithm scales as $L\log(L)$, while the time complexity of doing so using Eq. (11.10) scales as LN.

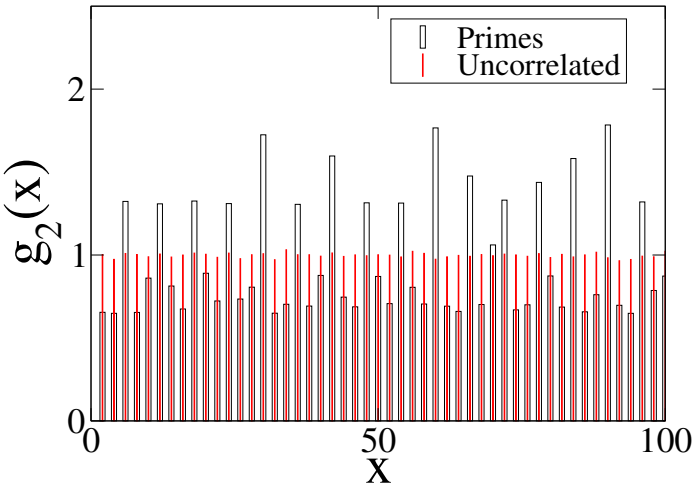

Figure 11.4 Pair correlation function $g_2(x)$, as defined in Eq. (11.9), for a prime number configuration of $M = 10^{10} + 1$, $L = 10^6$, and $N = 43427$, compared with $g_2(x)$ of a uncorrelated lattice gas configuration of the same L and N.

11.3 Results for the Pair Statistics of the Prime Numbers

The pair correlation function as defined in Eq. (11.9), $g_2(x)$, of prime numbers is presented in Fig. 11.4 and compared with $g_2(x)$ of uncorrelated lattice gases. This quantity for uncorrelated lattice gas is simply

$$g_2(x) = \frac{N-1}{f(N_s-1)} \tag{11.19}$$

for any $x \neq 0$. This is because after one site is occupied, out of the remaining $N_s - 1$ sites, exactly $N - 1$ sites are occupied. We see that by this measure, the prime numbers appear to be distinctly different from lattice gases. We see that $g_2(x)$ for primes is higher than $g_2(x)$ of the uncorrelated lattice gas if and only if x is divisible by 3. However, we will see that the difference in pair statistics is much more obvious when we study $S(k)$ below.

We present and study numerically calculated structure factors of prime numbers for various M's and L's in this section. At first, let us examine $S(k)$ for $M = 10^6 + 1$ and $L = 5000$, which is presented in Fig. 11.5. At a larger scale, $S(k)$ appears to consist of many well-defined Bragg-like peaks of various heights, with the highest peak occurring at $k = \pi$. As we zoom in, it becomes evident that besides those peaks, $S(k)$ also has a random, noisy contribution that is often below 1. We will call the latter contribution the "diffuse part" in the rest of the chapter. Figure 11.5 also includes $S(k)$ for uncorrelated lattice gases, which consists of a diffuse part and a single peak at the trivial value of $k = \pi$. Away from the peak, $S(k)$ for uncorrelated lattice gases has an average value of $\frac{N_s - N}{N_s - 1}$. This is because the sum rule, Eq. (11.14), requires that $S(k)$ average to this value. A major conclusion is that the structure factor of the primes is characterized by a substantial amount of order across length scales, relative to the uncorrelated lattice gas, as evidenced by the appearance of many Bragg-like peaks.

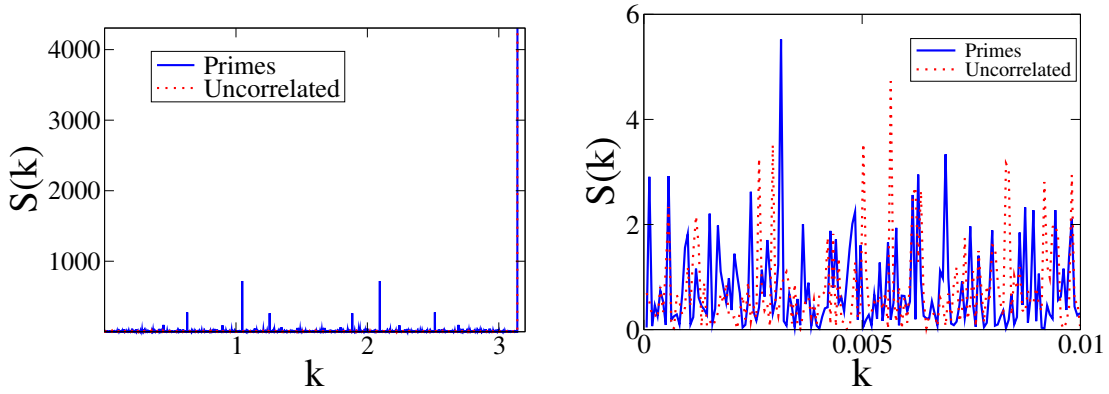

Figure 11.5 Left: $S(k)$ for prime numbers for $M = 10^{10} + 1$ and $L = 10^5$ contains many well-defined Bragg-like peaks of various heights, creating a type of self-similarity. Right: A zoomed-in view revealing the existence of a small, noisy "diffuse part" besides the peaks. We also plot $S(k)$ for uncorrelated lattice gases for comparison. As we have discussed in Sec. 11.2, we only show $S(k)$ in the range $0 < k \leq \pi$, and therefore omit the peak at $k = 0$.

At this stage, the distinction between the peaks and the "diffuse part" is somewhat unclear. Since $S(k)$ contains peaks of various heights, is it possible that the diffuse

part is actually made of many smaller peaks? We can only answer this question after we study the peaks and the diffuse part more deeply later in this section.

11.3.1 Peaks

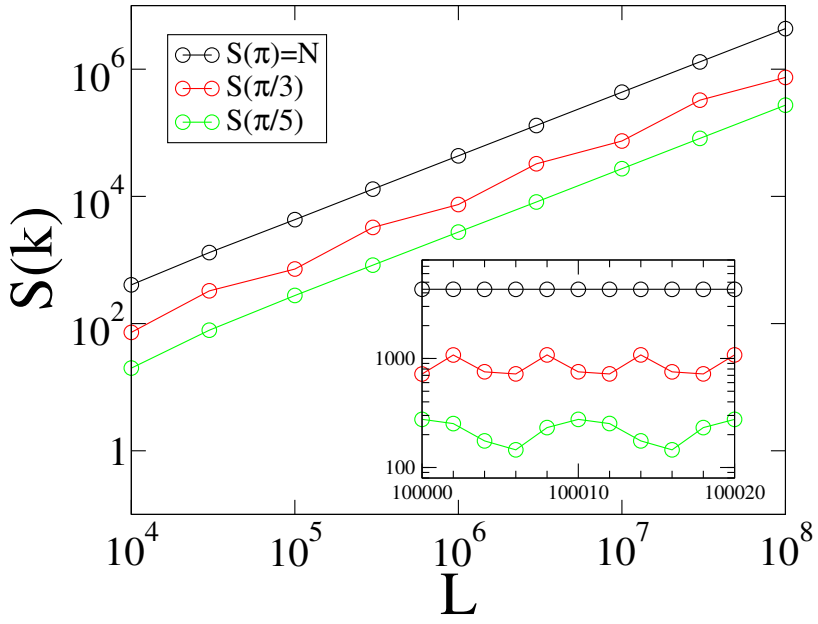

Figure 11.6 The structure factor $S(k)$ at $k = \pi$, $k = \pi/3$, and $k = \pi/5$, as a function of L at $M = 10^{10} + 1$. The inset presents more data for $10^5 \leq L \leq 10^5 + 20$.

We move on to study the peaks. From Fig. 11.5, one sees that the highest peak is at $k = \pi$, which is trivially caused by the periodicity of the underlying lattice. The next highest two peaks are at $k = \pi/3$ and $k = 2\pi/3$ [2]. Even lower peaks occur at $k = \pi/5$, $2\pi/5$, $3\pi/5$, and $4\pi/5$. Still lower peaks occur at $k = \pi/7$, $2\pi/7$, $3\pi/7$, $4\pi/7$, $k = 5\pi/7$, and $6\pi/7$. Examining $S(k)$ of a much larger system ($M = 10^{10} + 1$ and $L = 10^7$) revealed that there are even more peaks. Using analytic number theory, we have shown elsewhere [324] that the peaks indeed become Dirac-delta-like functions (in the infinite-size limit) with locations that obey the formula $k = m\pi/n$, where m

[2] It should be noted that since k has to be integer multiples of $2\pi/L$, for $L = 10^5$, $k = \pi/3$ and $k = 2\pi/3$ cannot be chosen. The actually observed peaks occur at the closest allowed k points instead.

is any integer coprime with n and n is any square-free odd integer and hence has a distinct prime factorization, i.e., $n = \prod_{j=1}^{J} p_j$, where J is a positive integer, and p_1, p_2, $\cdots$, p_J are non-repeating prime numbers larger than 2. If n is even or is not square-free, then we observe no peak at $k = m\pi/n$. We verified the existence of such peaks for n up to 300. As n increases beyond 300, however, the peaks become too weak to be distinguishable from the diffuse part.

Having an analytical formula of the peak locations, we move on to study the peak heights. As we have shown earlier, the height of the peak at $k = \pi$ is simply N. What can we say about the heights of the other peaks? In Fig. 11.6 we present computed peak heights at $k = \pi/3$ and $k = \pi/5$ for $M = 10^{10} + 1$ and various L's. We see that as L grows, the heights of the peaks at $k = \pi/3$ and $k = \pi/5$ also grow and remain being roughly proportional to N. Looking at the inset, we see that both $S(\pi/3)$ and $S(\pi/5)$ oscillates periodically as L increases: $S(\pi/3)$ attains a maximum when L is divisible by 3, and $S(\pi/5)$ attains a maximum when L is divisible by 5. Examining the heights of other peaks, we find that the height of a peak at $k = m\pi/n$ is indeed highest when L is divisible by n.

Since the divisibility of L with n affects the peak heights and hence will introduce unintended errors if not chosen properly, we desire an L that is divisible by as many prime numbers as possible. We therefore chose $L = 2 \times 3 \times 5 \times 7 \times 11 \times 13 \times 17 \times 19 = 9699690$ and recomputed the heights of several peaks. The results are summarized in Table 11.1. We find that when L is divisible by n, the height of the peak at $k = m\pi/n$ is very close to $N \prod_{j=1}^{J} (p_j - 1)^{-2}$, where p_j are the distinct prime factors of n. Indeed, this result is proved elsewhere [324].

Do these numerically generated peaks have finite or infinitesimal width? To answer this question, we present a close view of the peak at $k = \pi/3$ for three different L's in Fig. 11.7. It turns out that, if L is divisible by n, the peak at $k = m\pi/n$ has infinitesimal width, in the sense that $S(k)$ at one k value attains the local maximum

Table 11.1 Peak heights at several different n and m's for $M = 2.5 \times 10^8 + 1$ and $L = 9699690$ and comparison with the predicted height from the analytical formula.

n	m	$S(m\pi/n)/N$	Postulated analytical formula
3	1	0.2500000003	$(3-1)^{-2} = 0.25$
5	1	0.06268293536	$(5-1)^{-2} = 0.0625$
	2	0.06231833526	
7	1	0.02764696627	$(7-1)^{-2} = 0.02777\cdots$
	2	0.02783423055	
	3	0.02785282486	
15= 3×5	1	0.01564115190	$[(3-1)(5-1)]^{-2} = 0.015625$
	2	0.01583266309	
	4	0.01551814312	
	7	0.01550964066	
105= $3 \times 5 \times 7$	1	0.0004096963803	$[(3-1)(5-1)(7-1)]^{-2} = 0.00043402777\cdots$
	2	0.0004418025682	
	4	0.0004305924622	
	8	0.0003879974866	
	11	0.0004203223484	
	13	0.0004411107279	
	16	0.0004191249498	
	17	0.0003893716268	
	19	0.0004388128207	
	22	0.0004193036024	
	23	0.0004375599695	
	26	0.0004203613535	
	29	0.0004418187004	
	31	0.0004457650582	
	32	0.0004237635619	
	34	0.0004500979160	
	37	0.0004466597486	
	38	0.0004663304920	
	41	0.0004255673779	
	43	0.0004845933410	
	44	0.0004679589962	
	46	0.0004572985410	
	47	0.0004095637658	
	52	0.0004521962772	

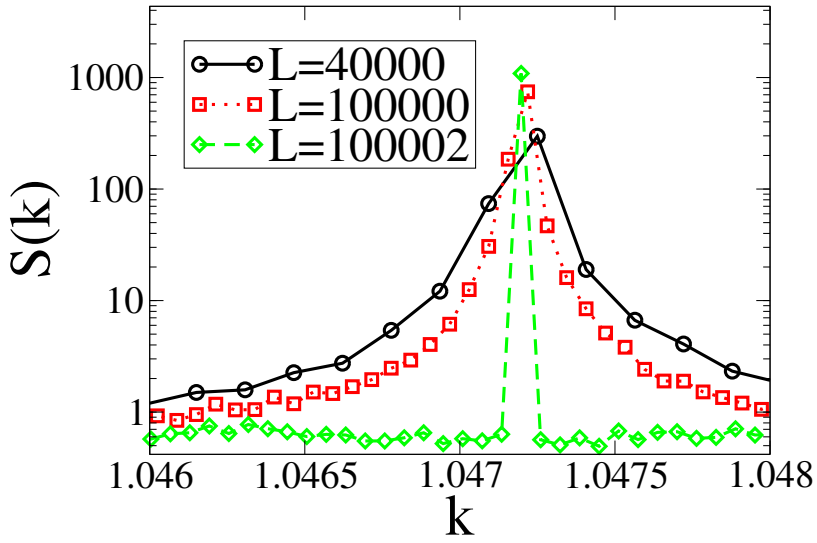

Figure 11.7 $S(k)$ near $k = \pi/3$ for three different L's. Each curve is averaged over 100 prime-number configurations, with the jth configuration consists of all prime numbers in the range $[10^{10} + (j-1)L + 1, 10^{10} + jL + 1)$.

and $S(k)$ at all adjacent k values are as low as the typical diffuse part. However, if L is not divisible by n, then the peak has a finite width, as $S(k)$ of all k values very close to $m\pi/n$ rises and become much higher than the typical diffuse part. In Fig. 11.7 one can also see that when peak widths are finite, a lower L results in a more broadly spread peaks. Therefore, all of the peaks may have infinitesimal width in the infinite-L limit. However, in a finite-L simulation, choosing an L that is divisible by as many prime numbers as possible provides a better estimate of $S(k)$ in the infinite-L limit. As n increases, one finds an increasing number of lower peaks, resulting in a statistical self-similarity.

11.3.2 The diffuse part

The above analysis suggest that the structure factor of the primes possesses infinitely many Dirac-delta-function peaks of various heights.. Therefore, one might naturally ask, could the random, noisy "diffuse part" be simply a superposition of many small peaks? Unfortunately, the answer is no. In Fig. 11.8 we present $S(k)$ of two different

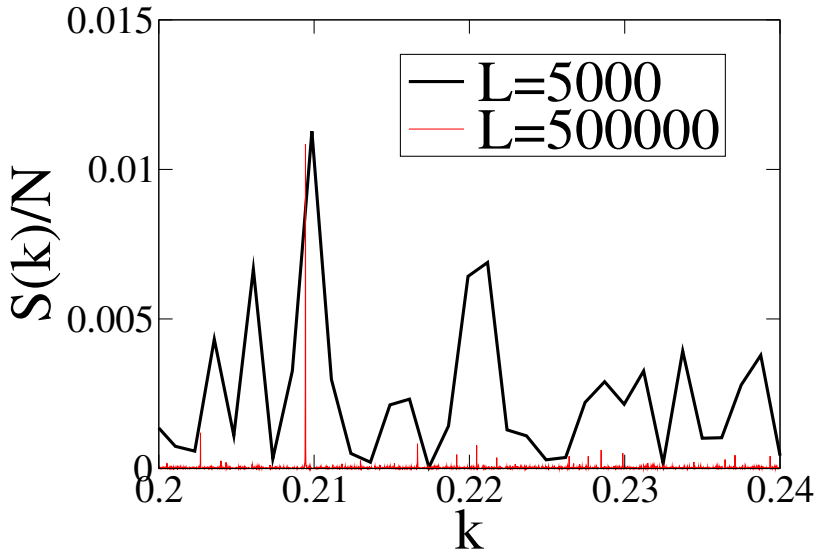

Figure 11.8 The structure factor, $S(k)$, normalized by N, for two different L's and $M = 10^6 + 1$.

L's in the range $0.2 \leq k \leq 0.24$. For $L = 5000$, $S(k)$ in this range appeared completely random and noisy, matching our definition of the diffuse part. To see if this diffuse part is actually a superposition of many small peaks, we compare it to the structure factor for $L = 500000$. The larger L allows more k points to be chosen, and therefore improves the k resolution, and reveals some peaks in this k range. We see that although $S(k)$ of the smaller L appeared to be entirely random, the maximum at $k \approx 0.21$ corresponds to a strong peak of the larger system, and is therefore actually a peak. However, other maxima for the smaller system do not correspond to peaks for the larger system, and can only be explained by assuming the existence of a noisy contribution to $S(k)$ which we call the "diffuse part." To summarize, in Fig. 11.8 we show that there is clearly a noisy contribution to $S(k)$ other than the peak contribution. However, it is difficult to completely distinguish these two components of $S(k)$.

Therefore, the diffuse part indeed exists but it is difficult to distinguish. Nevertheless, we can quantify the diffuse part using the median of $S(k)$ for all possible choices of k in the range $0 < k \leq \pi$. We present these medians in Fig. 11.9. As L

increases, the median of $S(k)$ generally decreases. However, with our current data, it is unclear if the median of $S(k)$ approaches zero in the $L \to \infty$ limit.

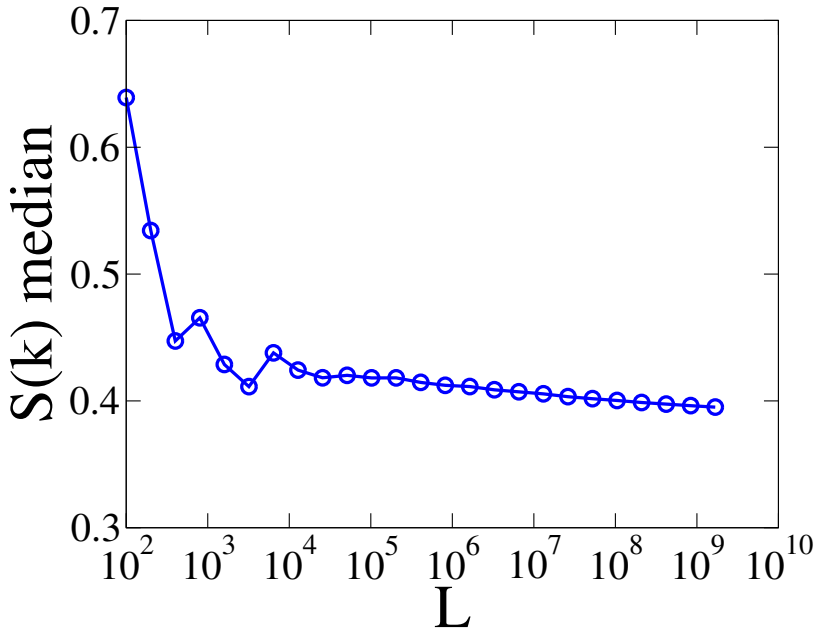

Figure 11.9 The median of the structure factor, $S(k)$, for all possible choices of k, as a function of L. Here M is chosen to be $10L$. The diffuse part of primes appears to be slowing decreasing as L increases. This is to be contrasted with the uncorrelated lattice gas with an appreciably larger predictable diffuse part in which there is no dependence on system size.

The diffuse part contributes to not only k points where there are no peaks, but also to k points where there are peaks. In Fig. 11.10, we compare numerical peak heights, averaged over all allowed m for a particular n, with our analytical formula. It turns out that the numerical average is always slightly higher than the formula, and their difference is of the same order of magnitude as the diffuse part. Thus, $S(k)$ at predicted peak locations is actually the sum of the peak and diffuse contributions.

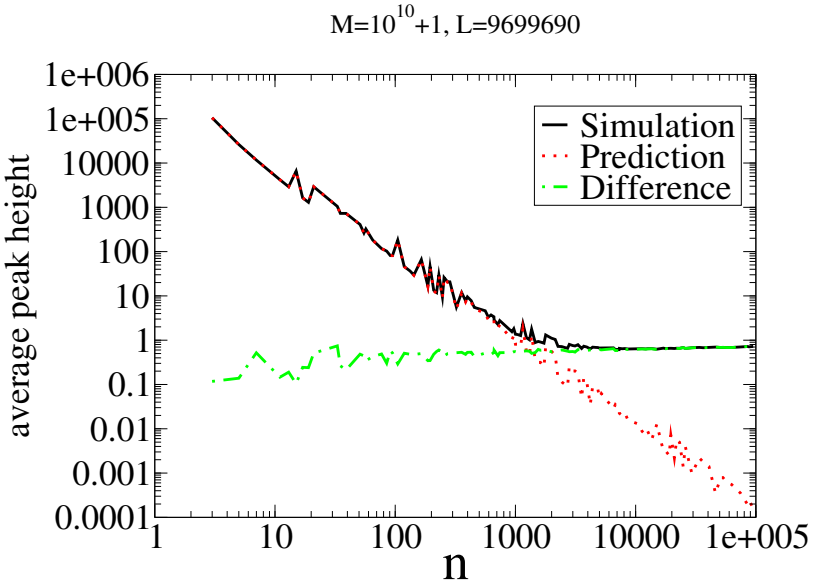

Figure 11.10 Average peak height of all peaks of a given n, the predicted peak heights, and their difference for all $n < 10^5$ that are odd, square-free, and divide L evenly. Here $M = 10^{10} + 1$ and $L = 9699690$. For each n, we find all m's that are coprime with n, and average the heights of peaks at $m\pi/n$. The average turns out to be always greater than the prediction, $N \prod_{j=1}^{J} (p_j - 1)^{-2}$. Their difference is between 0.1 and 1, which is of the same order of magnitude as the diffuse part.

11.4 Theoretical Explanation of the Peak Properties

In this section, we present a theoretical explanation of the observed peak locations, peak heights, and peak shapes of the structure factor in the range $0 < k \leq \pi$. The observations are

- peaks with heights $N \prod_{j=1}^{J} (p_j - 1)^{-2}$ appear at $k = m\pi/n$, where $n = \prod_{j=1}^{J} p_j$, and $p_1, p_2, \cdots, p_J$ are odd, distinct prime numbers; and
- peaks have finite width if L is not divisible by n and infinitesimal width otherwise.

The location, height and shape of the peak at $k = \pi$ ($m = 1$, $n = 1$ case) is trivially explained as already noted in Sec. 11.2, and so we focus on $n > 1$ cases here. The explanation for peak locations and heights is a simplification of the analysis presented in a theoretical study [324]. The explanation for peak shapes is not published elsewhere.

For concreteness, we first consider the cases $n = 3$, $m = 1$ and $n = 3$, $m = 2$. The combination of two facts explains these peaks. The first fact is simply that for every prime number $p > 3$, $p = 1$ or 5 (mod 6). Let $N_{a,b}$ be the number of prime number p's in the interval $[M, M + L)$ such that $p = b \pmod{a}$. Here, we will always consider even a's, and since p is odd, b also have to be odd. The first fact can then be reformulated as $N_{6,3} = 0$. The second fact, a stronger form of Dirichlet's theorem on arithmetic progressions [13], states that for large prime number p's, calculating p modulo a may give any integer b that is co-prime with a. Moreover, all of the possible b's are equally likely to appear. Therefore, in the infinite-L limit, both $N_{6,1}$ and $N_{6,5}$ asymptotically approach $N/2$. By definition,

$$\begin{aligned} S(\pi/3) &= \frac{|\sum_{j=1}^{N} \exp[-i\pi(p_j - M)/3]|^2}{N} \\ &= \frac{|\sum_{j=1}^{N} \exp(-i\pi p_j/3)|^2}{N}. \end{aligned} \tag{11.20}$$

For any p_j, if $p_j = 1 \pmod 6$, then we always have $\exp(-i\pi p_j/3) = \exp(-i\pi/3)$. On the other hand, if $p_j = 5 \pmod 6$, then $\exp(-i\pi p_j/3) = \exp(-i5\pi/3)$. Thus

$$\begin{aligned} S(\pi/3) &= \frac{|N_{6,1} \exp(-i\pi/3) + N_{6,5} \exp(-i5\pi/3)|^2}{N} \\ &\approx \frac{N}{4} |\exp(-i\pi/3) + \exp(-i5\pi/3)|^2 \\ &= \frac{N}{4}. \end{aligned} \tag{11.21}$$

Similarly,

$$\begin{aligned} S(2\pi/3) &= \frac{|\sum_{j=1}^{N} \exp[-i2\pi(p_j - M)/3]|^2}{N} \\ &= \frac{|N_{6,1}\exp(-i2\pi/3) + N_{6,5}\exp(-i4\pi/3)|^2}{N} \\ &\approx \frac{N}{4}. \end{aligned} \tag{11.22}$$

In fact, for any odd prime n, one have $N_{2n,n} = 0$. For large L, Dirichlet's theorem then gives $N_{2n,1} = N_{2n,3} = \cdots = N_{2n,n-1} = N_{2n,n+1} = N_{2n,n+3} = \cdots = N_{2n,2n-1} = N/(n-1)$. Plugging in these equations into Eqs. (11.8) yields $S(m\pi/n) = N(n-1)^{-2}$.

Similarly, for a generally non-prime odd n, one can find all b's that are co-prime with $2n$, distribute a total of N primes evenly among all allowed b values, and then calculate $S(m\pi/n)$ from Eqs. (11.8). If the prime factorization of n is $n = \prod_j p_j$, one will find $S(m\pi/n) = 0$ if any of the two p_j's are the same and $S(m\pi/n) = N\prod(p_j - 1)^{-2}$ otherwise.

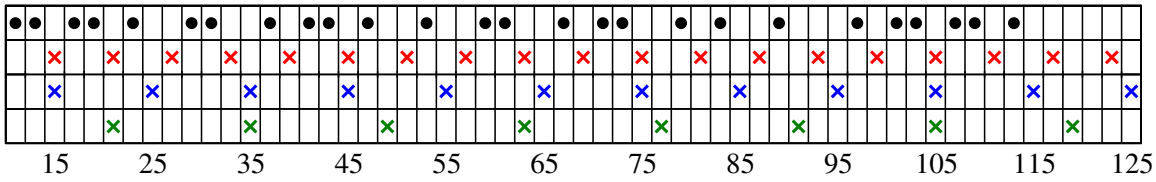

Figure 11.11 Illustration of the superposition of multiple periodicities for prime numbers. Black dots indicate occupied sites, crosses indicate sites that cannot be occupied because of a certain periodicity. For example, when one divides three consecutive odd integers by 3, the remainders are 0, 2, and 1. The site with a remainder of 0 is divisible by 3, and cannot be prime (red crosses). The other two sites may or may not be prime, but generally, prime numbers are evenly distributed between $3n + 1$ sites and $3n + 2$ sites. Thus, prime numbers statistically exhibit periodicities of 6. Similarly, prime numbers show statistical periodicity of 10 (blue crosses), 14 (green crosses), and even larger periods (not shown in the figure).

We have thus explained the peak locations and heights. We now move on to explain the peak shapes. In particular, why does a peak at $k = m\pi/n$ appear to have infinitesimal width if and only if L is divisible by n. Our previous success at explaining peak locations and peak heights suggest that, for the purpose of studying

a peak at $k = m\pi/n$, the prime number configuration may be considered as a one-dimensional periodic configuration of period $2n$. Within each period, there are some numbers that have certain probability of being prime and other numbers that are definitely not prime. For example, to study the peak at $k = \pi/3$, we can divide a prime configuration of an arbitrary length L into $\lfloor L/6 \rfloor$ periods of length 6, where $\lfloor x \rfloor$ denotes the largest integer less than or equal to x [3]. Within each period, odd number q's such that $q = 1$ or 5 (mod 6) have a certain probability to be a prime number, while the other odd number q such that $q = 3$ (mod 6) cannot be prime. Such a division of a configuration is schematically shown in Fig. 11.11.

Roughly speaking, when L is not divisible by n, the broadening of the peak is caused by the incommensurability of the simulation box of size L and the period $2n$. A more quantitative explanation is presented below: Let us study the contribution to $\tilde{\rho}(k)$ from each period. Define the contribution from the jth period be c_j, the periodicity gives the following relationship between c_j and c_1

$$c_j = c_1 \exp[-ik2n(j-1)]. \tag{11.23}$$

If $k = m\pi/n$, then $c_j = c_1$. There are a total of $\lfloor L/2n \rfloor$ such periods, thus

$$\tilde{\rho}(k) = \lfloor L/2n \rfloor c_1. \tag{11.24}$$

To study the peak shape, we have to also consider k close to but not equal to $m\pi/n$. Let $f = \exp(-ik2n)$, we have $c_j = c_1 f^{j-1}$. Summing over all $\lfloor L/2n \rfloor$ contributions

[3] More precisely, the configuration is divided into $\lfloor L/2n \rfloor$ periods and up to $n-1$ remaining sites. However, the remaining sites can be neglected in the following calculations for sufficiently large systems.

to $\tilde{\rho}(k)$ yields

$$\begin{aligned}\tilde{\rho}(k) &= c_1 + c_1 f + c_1 f^2 + \cdots + c_1 f^{\lfloor L/2n \rfloor - 1} \\ &= c_1 \left(\frac{1 - f^{\lfloor L/2n \rfloor}}{1 - f} \right).\end{aligned} \tag{11.25}$$

Therefore,

$$\begin{aligned}S(k) &= \frac{|\tilde{\rho}(k)|^2}{N} \\ &= \frac{|c_1|^2}{N} \frac{|1 - f^{\lfloor L/2n \rfloor}|^2}{|1 - f|^2} \\ &= \frac{|c_1|^2}{N} \frac{|1 - \exp(-ik2n\lfloor L/2n \rfloor)|^2}{|1 - \exp(-ik2n)|^2} \\ &= \frac{|c_1|^2}{N} \frac{|1 - \cos(2n\lfloor L/2n \rfloor k) + i \sin(2n\lfloor L/2n \rfloor k)|^2}{|1 - \cos(2nk) + i \sin(2nk)|^2} \\ &= \frac{|c_1|^2}{N} \frac{\sin^2(n\lfloor L/2n \rfloor k)}{\sin^2(nk)}.\end{aligned} \tag{11.26}$$

Since we are studying the shape of a peak at $m\pi/n$, it is natural to let $\Delta k = k - m\pi/n$:

$$\begin{aligned}S(k) &= \frac{|c_1|^2}{N} \frac{\sin^2(n\lfloor L/2n \rfloor k)}{\sin^2(nk)} \\ &= \frac{|c_1|^2}{N} \frac{\sin^2(n\lfloor L/2n \rfloor \Delta k)}{\sin^2(n\Delta k)}\end{aligned} \tag{11.27}$$

Since Δk is very small, we can assume $n\Delta k$ is very small and that $n\lfloor L/2n \rfloor \Delta k \approx L\Delta k/2$. Thus

$$\begin{aligned}S(k) &\approx \frac{|c_1|^2}{N} \frac{\sin^2(L\Delta k/2)}{(n\Delta k)^2} \\ &= \frac{|c_1|^2 L^2}{4Nn^2} \left(\frac{\sin(L\Delta k/2)}{L\Delta k/2} \right)^2\end{aligned} \tag{11.28}$$

We see that the peak shape is a cardinal sine function squared and that the peak width is inversely proportional to L. This result shows that all peaks have infinitesimal width in the $L \to \infty$ limit. However, why did we observe an infinitesimal peak width even for

finite L's that are divisible by n? This is caused by the discrete nature of the possible choices of k. As we have stated earlier, k has to be an integer multiple of $2\pi/L$. When L is an even number that is divisible by an odd number n, $\Delta k = k - m\pi/n$ is also an integer multiple of $2\pi/L$. Plugging such a Δk into Eq. (11.28), one will find $S(k) = 0$ unless $\Delta k = 0$. Therefore, the peak at $k = m\pi/n$ appears to have infinitesimal width.

11.5 Reconstruction of Prime Number Configurations

The above analysis suggest that, ignoring the diffuse part, we have analytical formula not only for $S(k)$, which is related to the modulus to the complex $\tilde{\rho}(k)$, but also for the phase of $\tilde{\rho}(k)$. This allows us to reconstruct a prime-number configuration, i.e., predict all prime numbers in an arbitrary interval $[M, M + L)$, by performing inverse Fourier transformation on $\tilde{\rho}(k)$. Unfortunately, since we ignore the diffuse part, the prediction cannot be completely accurate. In this section, we will describe our attempt at reconstructing prime number configurations and report its accuracy. These results are to be published in Ref. [324].

We reconstruct a prime-number configuration in an interval $[M, M + L)$ by the following steps:

1. Calculate $N = (M + L)/\ln(M + L) - M/\ln(M)$. Since the prime number theorem states that the number of prime numbers below a certain number x is approximately $x/\ln(x)$, N is the expected number of prime numbers in this interval.

2. Initialize $\tilde{\rho}(k)$ at all $k \neq 0$ to be zero. Set $\tilde{\rho}(0) = N$.

3. Find all n's such that $n = \prod_j p_j$, where p_j are distinct, odd prime numbers, below a threshold n_{max}.

4. For each n, find all integer m's such that $0 < m < n$ and is co-prime with n.

5. For each n and m, we need to reconstruct a peak at $k = m\pi/n$. As we have demonstrated in the previous section, for the purpose of reconstructing this peak, the prime-number configuration can be treated as a periodic system of period $2n$. We then find whether each number in the first period can be a prime number or not and calculate c_1.

6. If L is divisible by n, then the peak at $k = m\pi/n$ should have infinitesimal width. We therefore increase $\tilde{\rho}(m\pi/n)$ by $(L/n)c_1$, which is the predicted value of $\tilde{\rho}(m\pi/n)$ given in Eq. (11.24).

7. If L is not divisible by n, then the peak at $k = m\pi/n$ should have a finite width. We therefore have to increase $\tilde{\rho}(k)$ of all k points adjacent to $m\pi/n$ by the value predicted by Eq. (11.25). Here, the criteria for an "adjacent" k point is that the absolute value of the result from Eq. (11.25) is larger than $\sqrt{N}$.

8. Perform an inverse Fourier transform of $\tilde{\rho}(k)$ to find $\rho(x)$.

9. If we had a completely accurate prediction of $\tilde{\rho}(k)$, the resulting $\rho(x)$ would be exactly one for each prime number and exactly zero for each composite number. Unfortunately, the predicted $\tilde{\rho}(k)$ is not completely accurate because of two reasons. First, there should be infinitely many peaks, but we only consider a finite number of peaks for which $n < n_{max}$. Second, we are not considering the diffuse part. Therefore, the resulting $\rho(r)$ is not exactly zero or one. We find N numbers with the highest predicted $\rho(x)$ and predict those numbers to be prime.

We have performed such reconstruction process for $L = 510510$ and several different M's and n_{max}'s. The accuracy of our prediction is summarized in Fig. 11.12. We see that for smaller M's and larger n_{max}'s, this reconstruction process can have

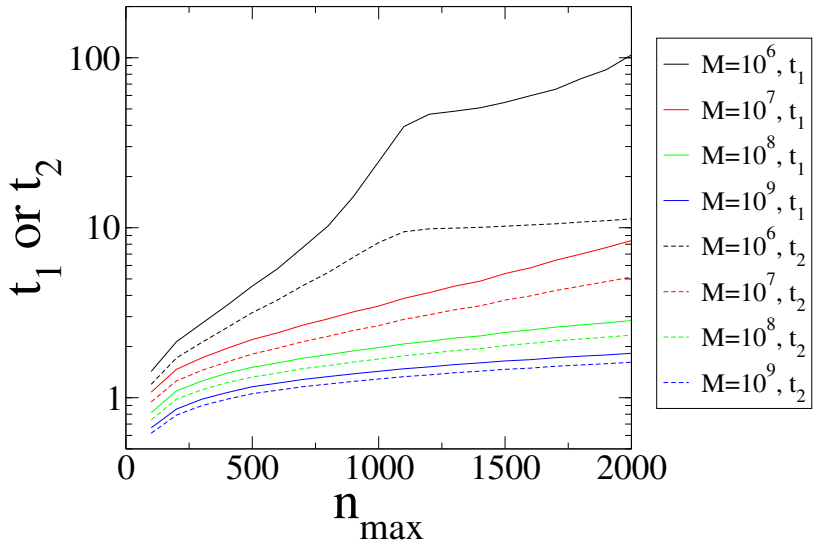

Figure 11.12 Two measures of the accuracy of the predicted prime numbers, correct predictions divided by incorrect predictions, and correct predictions divided by prime numbers that are not predicted, of our prime-number reconstruction process.

excellent accuracy. With $M = 10^6$ and $n_{max} = 2000$, more than 99% of the predicted prime numbers turn out to be correct. Unfortunately, as M increases, the accuracy drops. For any M, increasing n_{max} improves the accuracy, but also increases the computational cost.

In the above reconstruction process, we have neglected the diffuse part. It turns out that if one introduces a random, independent noise to $\tilde{\rho}(k)$, with magnitude corresponding to the diffuse part contribution, $S_{diffuse} = 0.4$, the prediction accuracy actually becomes much worse. In Fig. 11.13 we present such results. Compared to the prediction without this random noise, all ratios here becomes much lower. This seems to indicate that the existence of the diffuse part is due to numerical limitations, for example, we could not use infinite M and L in simulations.

It it interesting to comment on the computational complexity of this reconstruction process. If n^{max} is negligible compared to L, then the slowest step is the inverse Fourier transform of $\tilde{\rho}(k)$. This step scales as $\mathcal{O}(L \log L)$, which is slightly worse than the best known method to deterministically find prime numbers below a certain

limit L. The latter method is called "segmented sieve of Eratosthenes with wheel factorization," and scales as $\mathcal{O}(L \log \log L)$ [232].

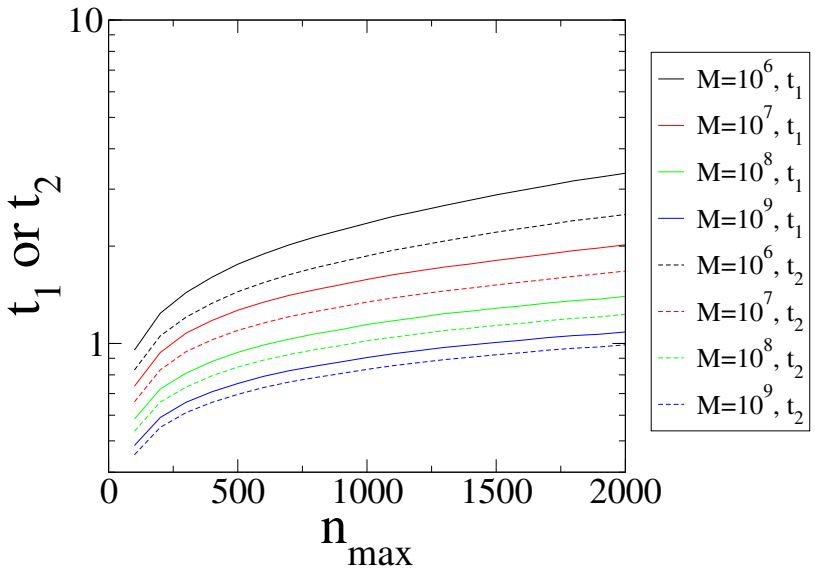

Figure 11.13 Two measures of the accuracy of the predicted prime numbers, correct predictions divided by incorrect predictions, and correct predictions divided by prime numbers that are not predicted, of our prime-number reconstruction process.

11.6 Conclusions

In summary, we numerically show that the structure factor of the primes in certain intervals exhibit well-defined Bragg-like peaks together with a small diffuse contribution. We show that the peaks persist as system size increases. Therefore, we have shown that the primes are characterized by a substantial amount of order, especially relative to the uncorrelated lattice gas, which does not possess such peaks. More detailed theoretical analysis on several aspects of the primes will be presented in Ref. [324], including estimates of the diffuse contribution as a function of the system size, the evaluation of the τ order metric, $S(k)$ at irrational multiples of π, and the analytical evaluation of the pair correlation function. We also show there that the

primes in certain intervals are not only hyperuniform but also exhibit dense Bragg peaks in the sense of limit-periodic systems.

Bibliography

[1] http://codeblue.umich.edu/hoomd-blue.

[2] http://www.primos.mat.br/2T_en.html.

[3] https://sourceforge.net/projects/kissfft/.

[4] https://www.gnu.org/software/gsl/manual/html_node/multimin-algorithms-with-derivatives.html.

[5] CGAL, Computational Geometry Algorithms Library. http://www.cgal.org.

[6] Z. Adamczyk, B. Siwek, M. Zembala, and P. Weronski. Influence of polydispersity on random sequential adsorption of spherical particles. *J. Colloid Interface Sci.*, 185(1):236–244, 1997.

[7] M. Agrawal, N. Kayal, and N. Saxena. Primes is in p. *Annals Math.*, pages 781–793, 2004.

[8] B. J. Alder and T. E. Wainwright. Phase transition for a hard sphere system. *J. Chem. Phys.*, 27(5):1208–1209, 1957.

[9] H. C. Andersen. Molecular dynamics simulations at constant pressure and/or temperature. *J. Chem. Phys.*, 72(4):2384–2393, 1980.

[10] J. A. Anderson, C. D. Lorenz, and A. Travesset. G.neral purpose molecular dynamics simulations fully implemented on graphics processing units. *J. Comput. Phys.*, 227(10):5342–5359, 2008.

[11] L. Angelani, R. Di Leonardo, G. Ruocco, A. Scala, and F. Sciortino. Quasisaddles as relevant points of the potential energy surface in the dynamics of supercooled liquids. *The Journal of chemical physics*, 116(23):10297–10306, 2002.

[12] C. A. Angell. Perspective on the glass transition. *J. Phys. Chem. Solids*, 49(8):863–871, 1988.

[13] T. M. Apostol. *Introduction to analytic number theory*. Springer Science & Business Media, 2013.

[14] N. W. Ashcroft and N. D. Mermin. *Solid State Physics*. HRW international editions. Holt, Rinehart and Winston, 1976.

[15] J. C. Ashworth, M. Mehr, P. G. Buxton, S. M. Best, and R. E. Cameron. Cell invasion in collagen scaffold architectures characterized by percolation theory. *Adv. Healthc. Mater.*, 4(9):1317–1321, 2015.

[16] A. O. L. Atkin and F. Morain. Elliptic curves and primality proving. *Math. Computation*, 61(203):29–68, 1993.

[17] S. Atkinson, F. H. Stillinger, and S. Torquato. Static structural signatures of nearly jammed disordered and ordered hard-sphere packings: Direct correlation function. *Phys. Rev. E*, 94(3):032902, 2016.

[18] S. Atkinson, G. Zhang, A. B. Hopkins, and S. Torquato. Critical slowing down and hyperuniformity on approach to jamming. *Phys. Rev. E*, 94(1):012902, 2016.

[19] F. Attneave. Some informational aspects of visual perception. *Psychological Rev.*, 61(3):183, 1954.

[20] M. Avellaneda and S. Torquato. Rigorous link between fluid permeability, electrical conductivity, and relaxation times for transport in porous media. *Phys. Fluids A*, 3(11):2529–2540, 1991.

[21] Á. Bácsi and A. Virosztek. Local density of states and friedel oscillations in graphene. *Phys. Rev. B*, 82(19):193405, 2010.

[22] A. Baiker. Supercritical fluids in heterogeneous catalysis. *Chem. Rev.*, 99(2):453–474, 1999.

[23] R. Baillie and S. S. Wagstaff. Lucas pseudoprimes. *Math. Computation*, 35(152):1391–1417, 1980.

[24] J. R. Banavar and L. M. Schwartz. Magnetic resonance as a probe of permeability in porous media. *Phys. Rev. Lett.*, 58(14):1411, 1987.

[25] R. D. Batten, D. A. Huse, F. H. Stillinger, and S. Torquato. Novel ground-state crystals with controlled vacancy concentrations: From kagomé to honeycomb to stripes. *Soft Matter*, 7(13):6194–6204, 2011.

[26] R. D. Batten, F. H. Stillinger, and S. Torquato. Classical disordered ground states: Super-ideal gases and stealth and equi-luminous materials. *J. Appl. Phys.*, 104(3):033504–033504, 2008.

[27] R. D. Batten, F. H. Stillinger, and S. Torquato. Interactions leading to disordered ground states and unusual low-temperature behavior. *Phys. Rev. E*, 80(3):031105, 2009.

[28] R. D. Batten, F. H. Stillinger, and S. Torquato. Novel low-temperature behavior in classical many-particle systems. *Phys. Rev. Letters*, 103(5):050602, 2009.

[29] R. D. Batten, F. H. Stillinger, and S. Torquato. Inherent structures for soft long-range interactions in two-dimensional many-particle systems. *J. Chem. Phys.*, 135(5):054104, 2011.

[30] R. E. Belardinelli and V. D. Pereyra. Wang-Landau algorithm: A theoretical analysis of the saturation of the error. *J. Chem. Phys.*, 127(18):184105, 2007.

[31] J. D. Bernal. Geometry of the structure of monatomic liquids. *Nature*, 185:68–70, 1960.

[32] E. P. Bernard and W. Krauth. Two-step melting in two dimensions: First-order liquid-hexatic transition. *Phys. Rev. Lett.*, 107(15):155704, 2011.

[33] L. Berthier, P. Chaudhuri, C. Coulais, O. Dauchot, and P. Sollich. Suppressed compressibility at large scale in jammed packings of size-disperse spheres. *Phys. Rev. Lett.*, 106(12):120601, 2011.

[34] L. Bindi, P. J. Steinhardt, N. Yao, and P. J. Lu. Natural quasicrystals. *Science*, 324(5932):1306–1309, 2009.

[35] M. Blander and J. L. Katz. Bubble nucleation in liquids. *AIChE J.*, 21(5):833–848, 1975.

[36] P. G. Bolhuis, A. A. Louis, and J. P. Hansen. Many-body interactions and correlations in coarse-grained descriptions of polymer solutions. *Phys. Rev. E*, 64(2):021801, 2001.

[37] R. B. Brahim and A. Chehaidar. Small-angle x-ray scattering of two-phase atomistic models for amorphous silicon–germanium alloys. *J. Non-Cryst. Solids*, 416:4–13, 2015.

[38] B. J. Brosilow, R. M. Ziff, and R. D. Vigil. Random sequential adsorption of parallel squares. *Phys. Rev. A*, 43(2):631, 1991.

[39] S. G. Brush. History of the lenz-ising model. *Rev. Mod. Phys.*, 39(4):883, 1967.

[40] I. C. Kim and S. Torquato. Effective conductivity of suspensions of hard spheres by brownian motion simulation. *J. Appl. Phys.*, 69(4):2280–2289, 1991.

[41] A. Cadilhe, N. Araújo, and V. Privman. Random sequential adsorption: from continuum to lattice and pre-patterned substrates. *J. Phys. Condens. Matter*, 19(6):065124, 2007.

[42] T. Caelli. On discriminating visual textures and images. *Percept. Psychophys.*, 31(2):149–159, 1982.

[43] L. C. Campos, C. C. de Souza Silva, and S. Apolinario. Structural phases of colloids interacting via a flat-well potential. *Phys. Rev. E*, 86(5):051402, 2012.

[44] B. Capone, I. Coluzza, F. LoVerso, C. N. Likos, and R. Blaak. Telechelic star polymers as self-assembling units from the molecular to the macroscopic scale. *Phys. Rev. Lett.*, 109(23):238301, 2012.

[45] P. M. Chaikin and T. C. Lubensky. *Principles of Condensed Matter Physics*. Cambridge University Press, 2000.

[46] D. Chandler. *Introduction to Modern Statistical Mechanics*. Oxford University Press, 1987.

[47] S. Chandrasekhar. *Liquid Crystals*. Cambridge University Press, 1992.

[48] P. Charbonneau, A. Ikeda, G. Parisi, and F. Zamponi. Glass transition and random close packing above three dimensions. *Phys. Rev. Lett.*, 107(18):185702, 2011.

[49] C.-C. Chen, L. Muechler, R. Car, T. Neupert, and J. Maciejko. Fermionic symmetry-protected topological phase in a two-dimensional Hubbard model. *Phys. Rev. Lett.*, 117(9):096405, 2016.

[50] D. Chen, Y. Jiao, and S. Torquato. Equilibrium phase behavior and maximally random jammed state of truncated tetrahedra. *J. Phys. Chem.*, 118(28):7981–7992, 2014.

[51] E. Chertkov, R. A. DiStasio Jr, G. Zhang, R. Car, and S. Torquato. Inverse design of disordered stealthy hyperuniform spin chains. *Phys. Rev. B*, 93(6):064201, 2016.

[52] M. Cieśla. Random sequential adsorption of polymer. *Phys. Rev. E*, 87(5):052401, 2013.

[53] M. Cieśla and J. Barbasz. Random sequential adsorption on fractals. *J. Chem. Phys.*, 137:044706, 2012.

[54] M. Cieśla and J. Barbasz. Modelling of interacting dimer adsorption. *Surf. Sci.*, 612:24, 2013.

[55] M. Cieśla and J. Barbasz. Random packing of spheres in menger sponge. *J. Chem. Phys.*, 138:214704, 2013.

[56] H. Cohn and N. Elkies. New upper bounds on sphere packings i. *Ann. Math.*, 157:689–714, 2003.

[57] H. Cohn and A. Kumar. Algorithmic design of self-assembling structures. *Proc. Natl. Acad. Sci.*, 106(24):9570–9575, 2009.

[58] H. Cohn and A. Kumar. Optimality and uniqueness of the leech lattice among lattices. *Ann. Math.*, 170:1003–1050, 2009.

[59] W. D. Comper. *Extracellular Matrix*. Number v. 1 in Extracellular Matrix. Taylor & Francis, 1996.

[60] J. H. Conway and N. J. A. Sloane. On lattices equivalent to their duals. *J. Number Theor.*, 48(3):373–382, 1994.

[61] J. H. Conway and N. J. A. Sloane. *Sphere Packings, Lattices and Groups*. Springer, Berlin, G.rmany, 1998.

[62] D. W. Cooper. Parking problem (sequential packing) simulations in two and three dimensions. *J. Colloid Interface Sci.*, 119(2):442–450, 1987.

[63] D. W. Cooper. Random-sequential-packing simulations in three dimensions for spheres. *Phys. Rev. A*, 38:522–524, 1988.

[64] S. R. Dahmen, S. D. Prado, and T. Stuermer-Daitx. Similarity in the statistics of prime numbers. *Physica A*, 296:523–528, 2001.

[65] H. Davenport and H. L. Montgomery. *Multiplicative number theory*, volume 74. Springer, New York, 1980.

[66] C. De Rosa, F. Auriemma, C. Diletto, R. Di Girolamo, A. Malafronte, P. Morvillo, G. Zito, G. Rusciano, G. Pesce, and A. Sasso. Toward hyperuniform disordered plasmonic nanostructures for reproducible surface-enhanced raman spectroscopy. *Phys. Chem. Chem. Phys.*, 17(12):8061–8069, 2015.

[67] P. G. Debenedetti and F. H. Stillinger. Supercooled liquids and the glass transition. *Nature*, 410(6825):259–267, 2001.

[68] R. Degl'Innocenti, Y. D. Shah, L. Masini, A. Ronzani, A. Pitanti, Y. Ren, D. S. Jessop, A. Tredicucci, H. E. Beere, and D. A. Ritchie. Thz quantum cascade lasers based on a hyperuniform design. In *SPIE OPTO*, page 93700A. International Society for Optics and Photonics, 2015.

[69] J. Dennis and H. Mei. Two new unconstrained optimization algorithms which use function and gradient values. *J. Optim. Theory Appl.*, 28(4):453–482, 1979.

[70] R. Di Leonardo, L. Angelani, G. Parisi, and G. Ruocco. Off-equilibrium effective temperature in monatomic lennard-jones glass. *Phys. Rev. Lett.*, 84(26):6054, 2000.

[71] M. Dijkstra, D. Frenkel, and J.-P. Hansen. Phase separation in binary hard-core mixtures. *J. Chem. Phys*, 101(4):3179–3189, 1994.

[72] M. Dijkstra and R. van Roij. Entropic wetting and many-body induced layering in a model colloid-polymer mixture. *Phys. Rev. Lett.*, 89(20):208303, 2002.

[73] R. A. DiStasio Jr, É. Marcotte, R. Car, F. H. Stillinger, and S. Torquato. Designer spin systems via inverse statistical mechanics. *Phys. Rev. B*, 88(13):134104, 2013.

[74] A. Donev, F. H. Stillinger, and S. Torquato. Unexpected density fluctuations in jammed disordered sphere packings. *Phys. Rev. Lett.*, 95(9):090604, 2005.

[75] A. Donev, S. Torquato, F. H. Stillinger, and R. Connelly. A linear programming algorithm to test for jamming in hard-sphere packings. *J. Compu. Phys.*, 197(1):139–166, 2004.

[76] T. Dotera, T. Oshiro, and P. Ziherl. Mosaic two-lengthscale quasicrystals. *Nature*, 506(7487):208–211, 2014.

[77] R. Dreyfus, Y. Xu, T. Still, L. A. Hough, A. G. Yodh, and S. Torquato. Diagnosing hyperuniformity in two-dimensional, disordered, jammed packings of soft spheres. *Phys. Rev. E*, 91(1):012302, 2015.

[78] M. Dzugutov. Glass formation in a simple monatomic liquid with icosahedral inherent local order. *Phys. Rev. A*, 46(6):R2984, 1992.

[79] M. D. Ediger and P. Harrowell. Perspective: Supercooled liquids and glasses. *J. Chem. Phys.*, 137(8):080901, 2012.

[80] E. Edlund, O. Lindgren, and M. N. Jacobi. Designing isotropic interactions for self-assembly of complex lattices. *Phys. Rev. Lett.*, 107(8):85503, 2011.

[81] S. F. Edwards and P. W. Anderson. Theory of spin glasses. *J. Phys. F*, 5(5):965, 1975.

[82] J. Eilhard, A. Zirkel, W. Tschöp, O. Hahn, K. Kremer, O. Schärpf, D. Richter, and U. Buchenau. Spatial correlations in polycarbonates: Neutron scattering and simulation. *J. Chem. Phys.*, 110(3):1819–1830, 1999.

[83] Y. Fan, J. K Percus, D. K Stillinger, and F. H. Stillinger. Constraints on collective density variables: one dimension. *Phys. Rev. A*, 44(4):2394, 1991.

[84] J. Feder. Random sequential adsorption. *J. Theor. Biol.*, 87(2):237–254, 1980.

[85] J. Feder and I. Giaever. Adsorption of ferritin. *J. Colloid Interface Sci.*, 78(1):144–154, 1980.

[86] G. Ferlat, A. P. Seitsonen, M. Lazzeri, and Mauri F. Hidden polymorphs drive the vitrification in b2o3. *Nat. Mater.*, 11:925–929, 2012.

[87] J. R. Fernández and P. Harrowell. Crystal phases of a glass-forming Lennard-Jones mixture. *Phys. Rev. E*, 67(1):011403, 2003.

[88] R. P. Feynman. Atomic theory of the two-fluid model of liquid helium. *Phys. Rev.*, 94(2):262, 1954.

[89] R. P. Feynman. Application of quantum mechanics to liquid helium. *Prog. Low Temperature Phys.*, 1:17–53, 1955.

[90] R. P. Feynman and M. Cohen. Energy spectrum of the excitations in liquid helium. *Phys. Rev.*, 102(5):1189, 1956.

[91] A. Filipponi, A. Di Cicco, M. Benfatto, and C. R. Natoli. The three-body correlation function in amorphous silicon probed by x-ray absorption spectroscopy. *Europhys. Lett.*, 13(4):319, 1990.

[92] L. Finegold and J. T. Donnell. Maximum density of random placing of membrane particles. *Nature*, 278:443–445, 1979.

[93] R. Finken, M. Schmidt, and H. Löwen. Freezing transition of hard hyperspheres. *Phys. Rev. E*, 65(1):016108, 2001.

[94] M. Florescu, P. J Steinhardt, and S. Torquato. Optical cavities and waveguides in hyperuniform disordered photonic solids. *Phys. Rev. B*, 87(16):165116, 2013.

[95] M. Florescu, S. Torquato, and P. J Steinhardt. Designer disordered materials with large, complete photonic band gaps. *Proc. Natl. Acad. Sci.*, 106(49):20658–20663, 2009.

[96] P. J. Flory. Intramolecular reaction between neighboring substituents of vinyl polymers. *J. Am. Chem. Soc.*, 61(6):1518–1521, 1939.

[97] S. Franz, H. Jacquin, G. Parisi, P. Urbani, and F. Zamponi. Quantitative field theory of the glass transition. *Proc. Nat. Acad. Sci.*, 109(46):18725–18730, 2012.

[98] S. Franz and G. Parisi. Local spin glass order in 1d. *Europhys. Lett.*, 75(3):385, 2006.

[99] D. Frenkel. Entropy-driven phase transitions. *Physica A*, 263(1-4):26–38, 1999.

[100] D. Frenkel and B. Smit. *Understanding Molecular Simulation: From Algorithms to Applications*. Academic Press, 1996.

[101] D. Frenkel and B. Smit. *Understanding molecular simulation: from algorithms to applications*, volume 1. Academic press, London, UK, 2001.

[102] H. L. Frisch and J. K. Percus. High dimensionality as an organizing device for classical fluids. *Phys. Rev. E*, 60(3):2942, 1999.

[103] A. Gabrielli and S. Torquato. Voronoi and void statistics for superhomogeneous point processes. *Phys. Rev. E*, 70(4):041105, 2004.

[104] P. X. Gallagher. On the distribution of primes in short intervals. *Mathematika*, 23:4–9, 1976.

[105] V. Gerold and J. Kern. The determination of atomic interaction energies in solid solutions from short range order coefficients-an inverse monte carlo method. In *Atomic Transport and Defects in Metals by Neutron Scattering*, pages 17–21. Springer, 1986.

[106] J. L. Gevertz and S. Torquato. A novel three-phase model of brain tissue microstructure. *PLoS Comput. Biol.*, 4(8):e1000152, 2008.

[107] S. Ghosh and A. Nishry. Gaussian complex zeros on the hole event: the emergence of a forbidden region. *arXiv preprint arXiv:1609.00084*, 2016.

[108] L. Gibiansky and S. Torquato. Link between the conductivity and elastic moduli of composite materials. *Phys. Rev. Lett.*, 71(18):2927, 1993.

[109] L. Gibiansky and S. Torquato. Connection between the conductivity and bulk modulus of isotropic composite materials. 452(1945):253–283, 1996.

[110] C. J. Gommes, Y. Jiao, and S. Torquato. Microstructural degeneracy associated with a two-point correlation function and its information content. *Phys. Rev. E*, 85(5):051140, 2012.

[111] A. Granville. Harald cramér and the distribution of prime numbers. *Scandinavian Actuarial Journal*, 1995(1):12–28, 1995.

[112] A. Granville and G. Martin. Prime number races. *Amer. Math. Monthly*, 113:1, 2006.

[113] J. J. Gray, D. H. Klein, B. A. Korgel, and R. T. Bonnecaze. Microstructure formation and kinetics in the random sequential adsorption of polydisperse tethered nanoparticles modeled as hard disks. *Langmuir*, 17(8):2317–2328, 2001.

[114] P. O. Gray. *Psychology, Fourth Edition*. Worth Publishers, 2002.

[115] B. Green and T. Tao. The mobius function is asymptotically orthogonal to nilsequences. *arXiv:0807.1736 [math.NT]*, 2008.

[116] B. Green and T. Tao. The primes contain arbitrarily long arithmetic progressions. *Annals of Math.*, 167, 2008.

[117] B. Green and T. Tao. Linear equations in primes. *Annals Math.*, pages 1753–1850, 2010.

[118] L. Grippo and S. Lucidi. A globally convergent version of the polak-ribiere conjugate gradient method. *Math. Programming*, 78(3):375–391, 1997.

[119] O. Gromenko and V. Privman. Random sequential adsorption of oriented superdisks. *Phys. Rev. E*, 79(4):042103, 2009.

[120] P. Grunwald and P. Shannon Vitanyi. Shannon information and kolmogorov complexity. *arXiv preprint arXiv:cs.0410002*, 2004.

[121] M. Guenza and K. S Schweizer. Local and microdomain concentration fluctuation effects in block copolymer solutions. *Macromolecules*, 30(14):4205–4219, 1997.

[122] S. Gupta, J. Stellbrink, E. Zaccarelli, C. N. Likos, M. Camargo, P. Holmqvist, J. Allgaier, L. Willner, and D. Richter. Validity of the stokes-einstein relation in soft colloids up to the glass transition. *Phys. Rev. Lett.*, 115(12):128302, 2015.

[123] J. Haberko, N. Muller, and F. Scheffold. Direct laser writing of three-dimensional network structures as templates for disordered photonic materials. *Phys. Rev. A*, 88(4):043822, 2013.

[124] J. Hadamard. Sur la distribution des zéros de la fonction $\zeta(s)$ et ses conséquences arithmétiques. *Bulletin de la Societé mathematique de France*, 24:199–220, 1896.

[125] T. C. Hales. A proof of the kepler conjecture. *Ann. Math.*, 162:1065–1185, 2005.

[126] C. Hanel, C. N. Likos, and R. Blaak. Effective interactions between multilayered ionic microgels. *Materials*, 7(12):7689–7705, 2014.

[127] J.-P. Hansen and I. R. McDonald. *Theory of simple liquids*. Elsevier, 1990.

[128] Z. Hashin. The elastic moduli of heterogeneous materials. *J. Appl. Mech.*, 29(1):143–150, 1962.

[129] Z. Hashin and S. Shtrikman. A variational approach to the theory of the elastic behaviour of multiphase materials. *J. Mech. Phys. Solids*, 11:127–140, April 1963.

[130] K. He, X. Zhang, S. Ren, and J. Sun. Delving deep into rectifiers: Surpassing human-level performance on imagenet classification. In *Proc. IEEE Intl. Conf. Comput. Vision*, pages 1026–1034, 2015.

[131] M. Hejna, P. J. Steinhardt, and S. Torquato. Nearly hyperuniform network models of amorphous silicon. *Phys. Rev. B*, 87(24):245204, 2013.

[132] P. C. Hemmer, E. Velasco, L. Mederos, G. Navascués, and G. Stell. Solid-solid transitions induced by repulsive interactions. *J. Chem. Phys.*, 114:2268, 2001.

[133] H. Hentschel, V. Ilyin, N. Makedonska, I. Procaccia, and N. Schupper. Statistical mechanics of the glass transition as revealed by a voronoi tesselation. *Phys. Rev. E*, 75(5):050404, 2007.

[134] S. Hert and M. Seel. dD convex hulls and Delaunay triangulations. In *CGAL User and Reference Manual*. CGAL Editorial Board, 4.3 edition, 2014.

[135] B. Hess, S. León, N. Van Der Vegt, and K. Kremer. Long time atomistic polymer trajectories from coarse grained simulations: bisphenol-a polycarbonate. *Soft Matter*, 2(5):409–414, 2006.

[136] D. Hexner and D. Levine. Hyperuniformity of critical absorbing states. *Phys. Rev. Lett.*, 114(11):110602, 2015.

[137] E. L. Hinrichsen, J. Feder, and T. Jøssang. Geometry of random sequential adsorption. *J. Stat. Phys.*, 44(5):793–827, 1986.

[138] J. B. Hough, M. Krishnapur, Y. Peres, and B. Virág. *Zeros of Gaussian analytic functions and determinantal point processes*, volume 51. American Mathematical Society, Providence, RI, 2009.

[139] A.-P. Hynninen, C. G. Christova, R. Van Roij, A. Van Blaaderen, and M. Dijkstra. Prediction and observation of crystal structures of oppositely charged colloids. *Phys. Rev. Lett.*, 96(13):138308, 2006.

[140] E. Ising. Beitrag zur theorie des ferromagnetismus. *Zeitschrift für Physik A Hadrons and Nuclei*, 31(1):253–258, 1925.

[141] H. Iwaniec and E. Kowalski. *Analytic number theory*, volume 53. American Mathematical Society, 2004.

[142] R. L Jack, I. R Thompson, and P. Sollich. Hyperuniformity and phase separation in biased ensembles of trajectories for diffusive systems. *Phys. Rev. Lett.*, 114(6):060601, 2015.

[143] A. Jain, J. R. Errington, and T. M. Truskett. Inverse design of simple pairwise interactions with low-coordinated 3d lattice ground states. *Soft Matter*, 9:3866–3870, 2013.

[144] S. Ji, U. Nagpal, W. Liao, C.-C. Liu, J. J. de Pablo, and P. F. Nealey. Three-dimensional directed assembly of block copolymers together with two-dimensional square and rectangular nanolithography. *Adv. Mater.*, 23(32):3692–3697, 2011.

[145] Y. Jiao, T. Lau, H. Hatzikirou, M. Meyer-Hermann, J. C. Corbo, and S. Torquato. Avian photoreceptor patterns represent a disordered hyperuniform solution to a multiscale packing problem. *Phys. Rev. E*, 89(2):022721, 2014.

[146] Y. Jiao, F. H. Stillinger, and S. Torquato. Modeling heterogeneous materials via two-point correlation functions: Basic principles. *Phys. Rev. E*, 76(3):031110, 2007.

[147] Y. Jiao, F. H. Stillinger, and S. Torquato. A superior descriptor of random textures and its predictive capacity. *Proc. Nat. Acad. Sci.*, 106(42):17634–17639, 2009.

[148] Y. Jiao, F. H. Stillinger, and S. Torquato. Gometrical ambiguity of pair statistics: Point configurations. *Phys. Rev. E*, 81(1):011105, 2010.

[149] Y. Jiao and S. Torquato. Maximally random jammed packings of platonic solids: hyperuniform long-range correlations and isostaticity. *Phys. Rev. E*, 84(4):041309, 2011.

[150] S. G. Johnson. The nlopt nonlinear-optimization package. http://ab-initio.mit.edu/nlopt.

[151] H. Jonsson and H. C. Andersen. Icosahedral ordering in the Lennard-Jones liquid and glass. *Phys. Rev. Lett.*, 60(22):2295, 1988.

[152] A. R. Kansal, S. Torquato, and F. H. Stillinger. Diversity of order and densities in jammed hard-particle packings. *Phys. Rev. E*, 66(4):041109, 2002.

[153] A. R. Kansal, T. M. Truskett, and S. Torquato. Nonequilibrium hard-disk packings with controlled orientational order. *J. Chem. Phys.*, 113(12):4844–4851, 2000.

[154] S. C. Kapfer and W. Krauth. Two-dimensional melting: From liquid-hexatic coexistence to continuous transitions. *Phys. Rev. Lett.*, 114(3):035702, 2015.

[155] V. Kapko, Z. Zhao, D. V. Matyushov, and C. A. Angell. Ideal glassformers vs ideal glasses: Studies of crystal-free routes to the glassy state by potential tuning molecular dynamics, and laboratory calorimetry. *J. Chem. Phys.*, 138(12):12A549, 2013.

[156] V. Katos. A randomness test for block ciphers. *Appl. Math. Comput.*, 162(1):29–35, 2005.

[157] W. Kauzmann. The nature of the glassy state and the behavior of liquids at low temperatures. *Chem. Rev.*, 43(2):219–256, 1948.

[158] T. Kennedy, E. H. Lieb, and H. Tasaki. A two-dimensional isotropic quantum antiferromagnet with unique disordered ground state. *J. Stat. Phys.*, 53(1):383–415, 1988.

[159] I. C. Kim and S. Torquato. Determination of the effective conductivity of heterogeneous media by brownian motion simulation. *J. Appl. Phys.*, 68(8):3892–3903, 1990.

[160] I. C. Kim and S. Torquato. Diffusion of finite-sized brownian particles in porous media. *J. Chem. Phys.*, 96(2):1498–1503, 1992.

[161] I. C. Kim and S. Torquato. Effective conductivity of suspensions of overlapping spheres. *J. Appl. Phys.*, 71(6):2727–2735, 1992.

[162] T. Kinjo, K. Ohguchi, K. Yasuoka, and M. Matsumoto. Computer simulation of fluid phase change: vapor nucleation and bubble formation dynamics. *Comput. Mater. Sci.*, 14(1):138–141, 1999.

[163] S. Kirkpatrick, C. D. Gelatt, M. P. Vecchi, et al. Optimization by simulated annealing. *Science*, 220(4598):671–680, 1983.

[164] C. Kittel. *Introduction to Solid State Physics*. Wiley, Hoboken, New Jersey, 8th edition, 2005.

[165] M. A. Klatt and S. Torquato. Characterization of maximally random jammed sphere packings: Voronoi correlation functions. *Phys. Rev. E*, 90(5):052120, 2014.

[166] W. Kob and H. C. Andersen. Scaling behavior in the β-relaxation regime of a supercooled Lennard-Jones mixture. *Phys. Rev. Lett.*, 73(10):1376, 1994.

[167] A. N. Kolmogorov. On tables of random numbers. *Theor. Comput. Sci.*, 207:387–395, 1998.

[168] J. M. Kosterlitz and D. J. Thouless. Ordering, metastability and phase transitions in two-dimensional systems. *J. Phys. C*, 6(7):1181, 1973.

[169] H. Krawczyk. Cryptographic extraction and key derivation: The hkdf scheme. In *Advances in Cryptology-Crypto 2010*, pages 631–648. Springer, 2010.

[170] W. P. Krekelberg, M. J. Pond, G. Goel, V. K. Shen, J. R. Errington, and T. M. Truskett. Generalized rosenfeld scalings for tracer diffusivities in not-so-simple fluids: Mixtures and soft particles. *Phys. Rev. E*, 80(6):061205, 2009.

[171] W. D. Kristensen. Computer-simulated amorphous structures (i). quenching of a Lennard-Jones model system. *J. Non-Cryst. Solids*, 21(3):303–318, 1976.

[172] P. Kumar, P. C. Ivanov, and H. E. Stanley. Information entropy and correlations in prime numbers. *arXiv:cond-mat/0303110 [cond-mat.stat-mech]*, 2003.

[173] R. Kurita and E. R. Weeks. Incompressibility of polydisperse random-close-packed colloidal particles. *Phys. Rev. E*, 84(3):030401, 2011.

[174] P. Laurin, M. Girard, A. Markov, and M. Skorobogatiy. Hollow core terahertz optical fibers with hyperuniform disordered dielectric reflectors. In *Infrared, Millimeter, and Terahertz waves (IRMMW-THz), 2014 39th International Conference on*, pages 1–2. IEEE, 2014.

[175] V. Lemaire, J. Belair, and P. Hildgen. Structural modeling of drug release from biodegradable porous matrices based on a combined diffusion/erosion process. *Int. J. Pharm.*, 258(1):95–107, 2003.

[176] R. J. Lemke Oliver and K. Soundararajan. Unexpected biases in the distribution of consecutive primes. *arXiv:1603.03720 [math.NT]*, 2016.

[177] I. Lesanovsky and J. P. Garrahan. Out-of-equilibrium structures in strongly interacting rydberg gases with dissipation. *Phys. Rev. A*, 90(1):011603, 2014.

[178] O. Leseur, R. Pierrat, and R. Carminati. High-density hyperuniform materials can be transparent. *Optica*, 3:763, 2016.

[179] D. Levine and P. J. Steinhardt. Quasicrystals: a new class of ordered structures. *Phys. Rev. Lett.*, 53(26):2477, 1984.

[180] D. Levine and P. J. Steinhardt. Quasicrystals. i. definition and structure. *Phys. Rev. B*, 34(2):596, 1986.

[181] C. N. Likos, A. Lang, M. Watzlawek, and H. Löwen. Criterion for determining clustering versus reentrant melting behavior for bounded interaction potentials. *Phys. Rev. E*, 63(3):031206, 2001.

[182] C. N. Likos, M. Schmidt, H. Löwen, M. Ballauff, D. Pötschke, and P. Lindner. Soft interaction between dissolved flexible dendrimers: theory and experiment. *Macromolecules*, 34(9):2914–2920, 2001.

[183] D. C. Liu and J. Nocedal. On the limited memory bfgs method for large scale optimization. *Math. Programming*, 45(1-3):503–528, 1989.

[184] C. D. Lorenz and R. M. Ziff. Precise determination of the critical percolation threshold for the three-dimensional swiss cheese model using a growth algorithm. *J. Chem. Phys.*, 114(8):3659–3661, 2001.

[185] H. Löwen. Melting, freezing and colloidal suspensions. *Physics Reports*, 237(5):249–324, 1994.

[186] L. Lue, M. Bishop, and P. A. Whitlock. The fluid to solid phase transition of hard hyperspheres in four and five dimensions. *J. Chem. Phys.*, 132:104509, 2010.

[187] E. Ma. Tuning order in disorder. *Nat. Mater.*, 14(6):547–552, 2015.

[188] W. Man, M. Florescu, K. Matsuyama, P. Yadak, G. Nahal, S. Hashemizad, E. Williamson, P. Steinhardt, S. Torquato, and P. Chaikin. Photonic band gap in isotropic hyperuniform disordered solids with low dielectric contrast. *Optics express*, 21(17):19972–19981, 2013.

[189] W. Man, M. Florescu, E. P. Williamson, Y. He, S. R. Hashemizad, B. Y. C. Leung, D. R. Liner, S. Torquato, P. M. Chaikin, and P. J. Steinhardt. Isotropic band gaps and freeform waveguides observed in hyperuniform disordered photonic solids. *Proc. Natl. Acad. Sci.*, 110(40):15886–15891, 2013.

[190] É. Marcotte, R. A. DiStasio Jr, F. H. Stillinger, and S. Torquato. Designer spin systems via inverse statistical mechanics. ii. ground-state enumeration and classification. *Phys. Rev. B*, 88(18):184432, 2013.

[191] É. Marcotte, F. H. Stillinger, and S. Torquato. Optimized monotonic convex pair potentials stabilize low-coordinated crystals. *Soft Matter*, 7(6):2332–2335, 2011.

[192] É. Marcotte, F. H. Stillinger, and S Torquato. Unusual ground states via monotonic convex pair potentials. *J. Chem. Phys.*, 134:164105, 2011.

[193] É. Marcotte, F. H. Stillinger, and S. Torquato. Designed diamond ground state via optimized isotropic monotonic pair potentials. *J. Chem. Phys.*, 138:061101, 2012.

[194] É. Marcotte, F. H. Stillinger, and S. Torquato. Nonequilibrium static growing length scales in supercooled liquids on approaching the glass transition. *J. Chem. Phys.*, 138(12):12A508, 2013.

[195] E. Marinari, G. Parisi, and F. Ritort. Replica field theory for deterministic models: I. binary sequences with low autocorrelation. *J. Phys. A*, 27(23):7615, 1994.

[196] E. Marinari, G. Parisi, and F. Ritort. Replica field theory for deterministic models. ii. a non-random spin glass with glassy behaviour. *J. Phys. A*, 27(23):7647, 1994.

[197] F. Martelli. Dealing with primes i.: On the goldbach conjecture. *arXiv:1309.5895 [math.NT]*, page 2013.

[198] F. J. Martinez-Veracoechea, B. M. Mladek, A. V. Tkachenko, and D. Frenkel. Design rule for colloidal crystals of dna-functionalized particles. *Phys. Rev. Lett.*, 107(4):045902, 2011.

[199] S. Martis, É. Marcotte, F. H. Stillinger, and S. Torquato. Exotic ground states of directional pair potentials via collective-density variables. *J. Stat. Phys.*, 150(3):414–431, 2013.

[200] J. Maynard. Small gaps between primes. *Annals of Math.*, 181:383–413, 2015.

[201] A. Mejdoubi and C. Brosseau. Numerical calculations of the intrinsic electrostatic resonances of artificial dielectric heterostructures. *J. Appl. Phys.*, 101(8):084109–084109, 2007.

[202] N. D. Mermin. Crystalline order in two dimensions. *Phys. Rev.*, 176(1):250, 1968.

[203] Y. Meyer. *Wavelets and Operators*. Cambridge Studies in Advanced Mathematics. Cambridge University Press, 1992.

[204] M. Micoulaut. Concepts and applications of rigidity in non-crystalline solids: a review on new developments and directions. *Adv. Phys. X*, 1(2):147–175, 2016.

[205] G. Miller. Riemann's hypothesis and tests for primality. *Journal of Computer and System Sciences*, 13:300–317, 1976.

[206] H. Minkowski. Diskontinuitätsbereich für arithmetische äquivalenz. *J. Reine Angew. Math*, 129:220–274, 1905.

[207] P. P. Mitra and P. N. Sen. Effects of microgeometry and surface relaxation on nmr pulsed-field-gradient experiments: Simple pore geometries. *Phys. Rev. B*, 45(1):143, 1992.

[208] B. M. Mladek, P. Charbonneau, C. N. Likos, D. Frenkel, and G. Kahl. Multiple occupancy crystals formed by purely repulsive soft particles. *J. Phys. Condens. Matter*, 20(49):494245, 2008.

[209] B. M. Mladek, D. Gottwald, G. Kahl, M. Neumann, and C. N. Likos. Formation of polymorphic cluster phases for a class of models of purely repulsive soft spheres. *Phys. Rev. Lett.*, 96(4):045701, 2006.

[210] H. L. Montgomery. The pair correlation of zeros of the zeta function. In *Proc. Symp. Pure Math*, volume 24, pages 181–193, 1973.

[211] N. Muller, J. Haberko, C. Marichy, and F. Scheffold. Silicon hyperuniform disordered photonic materials with a pronounced gap in the shortwave infrared. *Adv. Opt. Mater.*, 2(2):115–119, 2014.

[212] M. Nakamura and S. Todo. Order parameter to characterize valence-bond-solid states in quantum spin chains. *Phys. Rev. Lett.*, 89(7):077204, 2002.

[213] M. Newman and R. M. Ziff. Efficient monte carlo algorithm and high-precision results for percolation. *Phys. Rev. Lett.*, 85(19):4104, 2000.

[214] J. Nocedal. Updating quasi-newton matrices with limited storage. *Math. Comp.*, 35(151):773–782, 1980.

[215] Y. Nourani and B. Andresen. A comparison of simulated annealing cooling strategies. *J. Phys A*, 31(41):8373, 1998.

[216] D. S. Novikov, J. H. Jensen, J. A. Helpern, and E. Fieremans. Revealing mesoscopic structural universality with diffusion. *Proc. Nat. Acad. Sci.*, 111(14):5088–5093, 2014.

[217] E. G. Noya and J. P. K. Doye. Structural transitions in the 309-atom magic number lennard-jones cluster. *J. Chem. Phys.*, 124:104503, 2006.

[218] A. Okabe, B. Boots, K. Sugihara, and S. N. Chiu. *Spatial tessellations: concepts and applications of Voronoi diagrams*, volume 501. John Wiley & Sons, 2009.

[219] L. Onsager. The effects of shape on the interaction of colloidal particles. *Ann. NY Acad. Sci.*, 51(1):627–659, 1949.

[220] G. Ortiz and P. Ballone. Correlation energy, structure factor, radial distribution function, and momentum distribution of the spin-polarized uniform electron gas. *Phys. Rev. B*, 50(3):1391, 1994.

[221] N. Otsu. A threshold selection method from gray-level histograms. *IEEE Trans. Syst. Man. Cybern.*, 9(1):62–66, 1979.

[222] G. Parisi and F. Slanina. Toy model for the mean-field theory of hard-sphere liquids. *Phys. Rev. E*, 62:6554–6559, Nov 2000.

[223] G. Parisi and F. Zamponi. Amorphous packings of hard spheres for large space dimension. *J. Stat. Mech. Theor. Exp.*, 2006(03):P03017, 2006.

[224] G. Parisi and F. Zamponi. Mean-field theory of hard sphere glasses and jamming. *Rev. Mod. Phys.*, 82(1):789, 2010.

[225] D. N. Perera and P. Harrowell. Relaxation dynamics and their spatial distribution in a two-dimensional glass-forming mixture. *J. Chem. Phys.*, 111(12):5441–5454, 1999.

[226] D. N. Perera and P. Harrowell. Stability and structure of a supercooled liquid mixture in two dimensions. *Phys. Rev. E*, 59(5):5721, 1999.

[227] Y. Pomeau. Some asymptotic estimates in the random parking problem. *J. Phys. A*, 13(6):L193, 1980.

[228] C. Pomerance, J. L. Selfridge, and S. S. Wagstaff. The pseudoprimes to $25 \cdot 10^9$. *Math. Computation*, 35(151):1003–1026, 1980.

[229] S. Prestipino, F. Saija, and P. V. Giaquinta. Hexatic phase in the two-dimensional gaussian-core model. *Phys. Rev. Lett.*, 106(23):235701, 2011.

[230] S. Prestipino, F. Saija, and G. Malescio. The zero-temperature phase diagram of soft-repulsive particle fluids. *Soft Matter*, 5(14):2795–2803, 2009.

[231] D. Priour Jr. Percolation through voids around overlapping spheres: a dynamically based finite-size scaling analysis. *Phys. Rev. E*, 89(1):012148, 2014.

[232] P. Pritchard. Linear prime-number sieves: A family tree. *Sci. comput. programming*, 9(1):17–35, 1987.

[233] E. D. Protonotarios, A. Johnston, and L. D. Griffin. Difference magnitude is not measured by discrimination steps for order of point patterns. *J. Vis.*, 16(9):2–2, 2016.

[234] J. A. Quintanilla, S. Torquato, and R. M. Ziff. Efficient measurement of the percolation threshold for fully penetrable discs. *J. Phys. A*, 33(42):L399, 2000.

[235] J. A. Quintanilla and R. M. Ziff. Asymmetry in the percolation thresholds of fully penetrable disks with two different radii. *Phys. Rev. E*, 76(5):051115, 2007.

[236] E. Rabani, D. R. Reichman, P. L. Gissler, and L. E. Brus. Drying-mediated self-assembly of nanoparticles. *Nature*, 426(6964):271–274, 2003.

[237] M. Rabin. Probabilistic algorithm for testing primality. *J. Number Theory*, 12:128–138, 1980.

[238] A. P. Ramirez, A. Hayashi, R. J. Cava, R. Siddharthan, and B. S. Shastry. Zero-point entropy in spin ice. *Nature*, 399(6734):333–335, 1999.

[239] M. C. Rechtsman, F. H. Stillinger, and S. Torquato. Optimized interactions for targeted self-assembly: Application to a honeycomb lattice. *Phys. Rev. Lett.*, 95(22):228301, 2005.

[240] M. C. Rechtsman, F. H. Stillinger, and S. Torquato. Designed interaction potentials via inverse methods for self-assembly. *Phys. Rev. E*, 73(1):011406, 2006.

[241] M. C. Rechtsman, F. H. Stillinger, and S. Torquato. Self-assembly of the simple cubic lattice with an isotropic potential. *Phys. Rev. E*, 74(2):021404, 2006.

[242] M. C. Rechtsman, F. H. Stillinger, and S. Torquato. Negative thermal expansion in single-component systems with isotropic interactions. *J. Phys. Chem. A*, 111(49):12816–12821, 2007.

[243] M. C. Rechtsman, F. H. Stillinger, and S. Torquato. Synthetic diamond and wurtzite structures self-assemble with isotropic pair interactions. *Phys. Rev. E*, 75(3):031403, 2007.

[244] M. C. Rechtsman, F. H. Stillinger, and S. Torquato. Negative poisson ratio materials via isotropic interactions. *Phys. Rev. Lett.*, 101(8):85501, 2008.

[245] R. A. Reck and S. Prager. Diffusion-controlled quenching at higher quencher concentrations. *J. Chem. Phys.*, 42(9):3027–3032, 1965.

[246] C. J. O. Reichhardt, C. Reichhardt, and A. R. Bishop. Structural transitions, melting, and intermediate phases for stripe-and clump-forming systems. *Phys. Rev. E*, 82(4):041502, 2010.

[247] A. Renyi. On a one-dimensional problem concerning random space filling. *Sel. Trans. Math. Stat. and Prob.*, 4:203–218, 1963.

[248] M. D. Rintoul. Precise determination of the void percolation threshold for two distributions of overlapping spheres. *Phys. Rev. E*, 62(1):68, 2000.

[249] M. D. Rintoul and S. Torquato. Metastability and crystallization in hard-sphere systems. *Phys. Rev. Lett.*, 77(20):4198, 1996.

[250] M. D. Rintoul and S. Torquato. Precise determination of the critical threshold and exponents in a three-dimensional continuum percolation model. *J. Phys. A*, 30(16):L585, 1997.

[251] M. D. Rintoul, S. Torquato, and G. Tarjus. Nearest-neighbor statistics in a one-dimensional random sequential adsorption process. *Phys. Rev. E*, 53(1):450, 1996.

[252] R. A. Rohde and P. B. Price. Diffusion-controlled metabolism for long-term survival of single isolated microorganisms trapped within ice crystals. *Proc. Nat. Acad. Sci.*, 104(42):16592–16597, 2007.

[253] R. D. Rohrmann and A. Santos. Structure of hard-hypersphere fluids in odd dimensions. *Phys. Rev. E*, 76(5):051202, 2007.

[254] E. Roman and N. Majlis. Computer simulation model of the structure of ion implanted impurities in semiconductors. *Solid State Commun.*, 47(4):259–261, 1983.

[255] J. Roth and A. R. Denton. Solid-phase structures of the Dzugutov pair potential. *Phys. Rev. E*, 61(6):6845, 2000.

[256] T. H. Rowan. Functional stability analysis of numerical algorithms. *Ph.D. thesis, University of Texas at Austin*, 1990.

[257] M. Rubinstein and P. Sarnak. Chebyshev's bias. *Experiment. Math.*, 3:173–197, 1994.

[258] V. S. Kumar and V. Kumaran. Voronoi cell volume distribution and configurational entropy of hard-spheres. *J. Chem. Phys.*, 123(11):114501, 2005.

[259] S. Sachdev. Kagomé-and triangular-lattice Heisenberg antiferromagnets: Ordering from quantum fluctuations and quantum-disordered ground states with unconfined bosonic spinons. *Phys. Rev. B*, 45(21):12377, 1992.

[260] G. Sakai, N. Matsunaga, K. Shimanoe, and N. Yamazoe. Theory of gas-diffusion controlled sensitivity for thin film semiconductor gas sensor. *Sensor. Actuat. B Chem.*, 80(2):125–131, 2001.

[261] F. R. S. Samuel. The sieve of eratosthenes. being an account of his method of finding all the prime numbers. *Philo. Trans.*, 62:327–347, 1772.

[262] D. E. Sands. *Introduction to Crystallography*. Dover Books on Chemistry. Dover Publications, 2012.

[263] S. Sastry. The relationship between fragility, configurational entropy and the potential energy landscape of glass-forming liquids. *Nature*, 409(6817):164–167, 2001.

[264] G. E. Schröder-Turk, W. Mickel, S. C. Kapfer, M. A. Klatt, F. M. Schaller, M. J. F. Hoffmann, N. Kleppmann, P. Armstrong, A. Inayat, D. Hug, et al. Minkowski tensor shape analysis of cellular, granular and porous structures. *Adv. Mater.*, 23(22-23):2535–2553, 2011.

[265] F. Sciortino, S. Mossa, E. Zaccarelli, and P. Tartaglia. Equilibrium cluster phases and low-density arrested disordered states: the role of short-range attraction and long-range repulsion. *Phys. Rev. Lett.*, 93(5):055701, 2004.

[266] A. K. Sen and S. Torquato. Effective conductivity of anisotropic two-phase composite media. *Phys. Rev. B*, 39(7):4504, 1989.

[267] C. E. Shannon. A mathematical theory of communication. *Bell Syst. Tech. J.*, 27:379–423, 1948.

[268] R. D. Shannon. Revised effective ionic radii and systematic studies of interatomic distances in halides and chalcogenides. *Acta. Crystallogr. A*, 32(5):751–767, 1976.

[269] D. Shechtman, I. Blech, D. Gratias, and J. W Cahn. Metallic phase with long-range orientational order and no translational symmetry. *Phys. Rev. Lett.*, 53(20):1951, 1984.

[270] H. W. Sheng, W. K. Luo, F. M. Alamgir, J. M. Bai, and E. Ma. Atomic packing and short-to-medium-range order in metallic glasses. *Nature*, 439(7075):419–425, 2006.

[271] P. Sheng and R. V. Kohn. Geometric effects in continuous-media percolation. *Phys. Rev. B*, 26(3):1331, 1982.

[272] J. D. Sherwood. Packing of spheroids in three-dimensional space by random sequential addition. *J. Phys. A*, 30(24):L839, 1999.

[273] J. D. Sherwood. Random sequential adsorption of lines and ellipses. *J. Phys. A*, 23(13):2827, 1999.

[274] H. Shintani and H. Tanaka. Frustration on the way to crystallization in glass. *Nat. Phys.*, 2(3):200–206, 2006.

[275] M. Skoge, A. Donev, F. H. Stillinger, and S. Torquato. Packing hyperspheres in high-dimensional euclidean spaces. *Phys. Rev. E*, 74(4):041127, 2006.

[276] N. J. Sloane. Kepler's conjecture confirmed. *Nature*, 395(6701):435–436, 1998.

[277] S. Slotterback, M. Toiya, L. Goff, J. F Douglas, and W. Losert. Correlation between particle motion and voronoi-cell-shape fluctuations during the compaction of granular matter. *Phys. Rev. Lett.*, 101(25):258001, 2008.

[278] F. Smallenburg and F. Sciortino. Liquids more stable than crystals in particles with limited valence and flexible bonds. *Nature Physics*, 9(9):554–558, 2013.

[279] F. W. Starr, S. Sastry, J. F. Douglas, and S. C. Glotzer. What do we learn from the local geometry of glass-forming liquids? *Phys. Rev. Lett.*, 89(12):125501, 2002.

[280] P. J. Steinhardt, D. R. Nelson, and M. Ronchetti. Bond-orientational order in liquids and glasses. *Phys. Rev. B*, 28(2):784, 1983.

[281] F. H. Stillinger. Phase transitions in the gaussian core system. *J. Chem. Phys.*, 65(10):3968–3974, 1976.

[282] F. H. Stillinger. *Energy Landscapes, Inherent Structures, and Condensed-Matter Phenomena*. Princeton University Press, 2016.

[283] F. H. Stillinger and P. G. Debenedetti. Glass transition thermodynamics and kinetics. *Annu. Rev. Condens. Matter Phys.*, 4(1):263–285, 2013.

[284] C. Straley, A. Matteson, S. Feng, L. M. Schwartz, W. E. Kenyon, and J. R. Banavar. Magnetic resonance, digital image analysis, and permeability of porous media. *Appl. Phys. Lett.*, 51(15):1146–1148, 1987.

[285] T. Strutz. *Data Fitting and Uncertainty: A Practical Introduction to Weighted Least Squares and Beyond*. Vieweg and Teubner Verlag, Wiesbaden, Germany, 2010.

[286] A. Sütő. Crystalline ground states for classical particles. *Phys. Rev. Lett.*, 95:265501, Dec 2005.

[287] A. Sütő. From bcc to fcc: Interplay between oscillating long-range and repulsive short-range forces. *Phys. Rev. B*, 74:104117, Sep 2006.

[288] R. H. Swendsen. Dynamics of random sequential adsorption. *Phys. Rev. A*, 24(1):504, 1981.

[289] D. Tabor. *Gases, Liquids and Solids: And Other States of Matter*. Cambridge University Press, 1991.

[290] J. Talbot, P. Schaaf, and G. Tarjus. Random sequential addition of hard spheres. *Mol. Phys.*, 72(6):1397–1406, 1991.

[291] J. Talbot, G. Tarjus, and P. Schaaf. Unexpected asymptotic behavior in random sequential adsorption of nonspherical particles. *Phys. Rev. A*, 40(8):4808, 1989.

[292] T. Tao and T. Ziegler. The inverse conjecture for the gowers norm over finite fields in low characteristic. *Annals of Combinatorics*, 16(1):121–188, 2012.

[293] G. Tarjus, P. Schaaf, and J. Talbot. Random sequential addition: a distribution function approach. *J. Stat. Phys.*, 63(1):167–202, 1991.

[294] G. Tenenbaum and G. Tenenbaum. *Introduction to analytic and probabilistic number theory*, volume 46. Cambridge University Press, Cambridge, 1995.

[295] M. F. Thorpe. Continuous deformations in random networks. *J. Non-Cryst. Solids*, 57(3):355–370, 1983.

[296] S. Torquato. Microstructure characterization and bulk properties of disordered two-phase media. *J. Stat. Phys.*, 45(5):843–873, 1986.

[297] S. Torquato. Relationship between permeability and diffusion-controlled trapping constant of porous media. *Phys. Rev. Lett.*, 64(22):2644, 1990.

[298] S. Torquato. Nearest-neighbor statistics for packings of hard spheres and disks. *Phys. Rev. E*, 51(4):3170, 1995.

[299] S. Torquato. Effective stiffness tensor of composite media: Ii. applications to isotropic dispersions. *J. Mech. Phys. Solids*, 46(8):1411–1440, 1998.

[300] S. Torquato. Exact conditions on physically realizable correlation functions of random media. *J. Chem. Phys.*, 111(19):8832–8837, 1999.

[301] S. Torquato. *Random heterogeneous materials: microstructure and macroscopic properties*, volume 16. Springer Science & Business Media, 2002.

[302] S. Torquato. Inverse optimization techniques for targeted self-assembly. *Soft Matter*, 5(6):1157–1173, 2009.

[303] S. Torquato. Reformulation of the covering and quantizer problems as ground states of interacting particles. *Phys. Rev. E*, 82(5):056109, 2010.

[304] S. Torquato. Effect of dimensionality on the continuum percolation of overlapping hyperspheres and hypercubes. *J. Chem. Phys.*, 136:054106, 2012.

[305] S. Torquato. *Random Heterogeneous Materials: Microstructure and Macroscopic Properties*. Interdisciplinary Applied Mathematics. Springer New York, 2013.

[306] S. Torquato. Disordered hyperuniform heterogeneous materials. *J. Phys.: Condens. Matter*, 28(41):414012, 2016.

[307] S. Torquato. Hyperuniformity and its generalizations. *Phys. Rev. E*, 94(2):022122, 2016.

[308] S. Torquato and M. Avellaneda. Diffusion and reaction in heterogeneous media: Pore size distribution, relaxation times, and mean survival time. *J. Chem. Phys.*, 95(9):6477–6489, 1991.

[309] S. Torquato, A. Donev, and F. H. Stillinger. Breakdown of elasticity theory for jammed hard-particle packings: conical nonlinear constitutive theory. *Int. J. Solids Struct.*, 40(25):7143, 2003.

[310] S. Torquato and Y. Jiao. Effect of dimensionality on the continuum percolation of overlapping hyperspheres and hypercubes. ii. simulation results and analyses. *J. Chem. Phys.*, 137:074106, 2012.

[311] S. Torquato and Y. Jiao. Organizing principles for dense packings of nonspherical hard particles: Not all shapes are created equal. *Phys. Rev. E*, 86(1):011102, 2012.

[312] S. Torquato and I. C. Kim. Efficient simulation technique to compute effective properties of heterogeneous media. *Appl. Phys. Lett.*, 55(18):1847–1849, 1989.

[313] S. Torquato, I. C. Kim, and D. Cule. Effective conductivity, dielectric constant, and diffusion coefficient of digitized composite media via first-passage-time equations. *J. Appl. Phys.*, 85(3):1560–1571, 1999.

[314] S. Torquato, B. Lu, and J. Rubinstein. Nearest-neighbor distribution functions in many-body systems. *Phys. Rev. A*, 41(4):2059, 1990.

[315] S. Torquato, A. Scardicchio, and C. E. Zachary. Point processes in arbitrary dimension from fermionic gases, random matrix theory, and number theory. *J. Stat. Mech. Theor. Exp.*, (11):P11019, 2008.

[316] S. Torquato and F. H. Stillinger. Controlling the short-range order and packing densities of many-particle systems. *J. Phys. Chem. B*, 106(33):8354–8359, 2002.

[317] S. Torquato and F. H. Stillinger. Local density fluctuations, hyperuniformity, and order metrics. *Phys. Rev. E*, 68(4):041113, 2003.

[318] S. Torquato and F. H. Stillinger. Exactly solvable disordered sphere-packing model in arbitrary-dimensional euclidean spaces. *Phys. Rev. E*, 73(3):031106, 2006.

[319] S. Torquato and F. H. Stillinger. New conjectural lower bounds on the optimal density of sphere packings. *Exp. Math.*, 15(3):307–331, 2006.

[320] S. Torquato and F. H. Stillinger. Toward the jamming threshold of sphere packings: Tunneled crystals. *J. Appl. Phys.*, 102(9):093511–093511, 2007.

[321] S. Torquato and F. H. Stillinger. Jammed hard-particle packings: From Kepler to Bernal and beyond. *Rev. Mod. Phys.*, 82(3):2633, 2010.

[322] S. Torquato, T. M. Truskett, and P. G. Debenedetti. Is random close packing of spheres well defined? *Phys. Rev. Lett.*, 84(10):2064, 2000.

[323] S. Torquato, O. U. Uche, and F. H. Stillinger. Random sequential addition of hard spheres in high euclidean dimensions. *Phys. Rev. E*, 74(6):061308, 2006.

[324] S. Torquato, G. Zhang, and M. de Courcy-Ireland. Hidden multiscale order in the primes. to be published.

[325] S. Torquato, G. Zhang, and F. H. Stillinger. Ensemble theory for stealthy hyperuniform disordered ground states. *Phys. Rev. X*, 5(2):021020, 2015.

[326] T. M. Truskett, S. Torquato, and P. G. Debenedetti. Towards a quantification of disorder in materials: Distinguishing equilibrium and glassy sphere packings. *Phys. Rev. E*, 62(1):993, 2000.

[327] D. S. Tuch, V. J. Wedeen, A. M. Dale, J. S. George, and J. W. Belliveau. Conductivity tensor mapping of the human brain using diffusion tensor mri. *Proc. Nat. Acad. Sci.*, 98(20):11697–11701, 2001.

[328] O. U. Uche, F. H. Stillinger, and S. Torquato. Constraints on collective density variables: Two dimensions. *Phys. Rev. E*, 70(4):046122, 2004.

[329] O. U. Uche, S. Torquato, and F. H. Stillinger. Collective coordinate control of density distributions. *Phys. Rev. E*, 74(3):031104, 2006.

[330] J. A. Van Meel, D. Frenkel, and P. Charbonneau. Geometrical frustration: A study of four-dimensional hard spheres. *Phys. Rev. E*, 79(3):030201, 2009.

[331] R. D. Vigil and R. M. Ziff. Random sequential adsorption of unoriented rectangles onto a plane. *J. Chem. Phys.*, 91(4):2599, 1989.

[332] R. D. Vigil and R. M. Ziff. Kinetics of random sequential adsorption of rectangles and line segments. *J. Chem. Phys.*, 93:8270, 1990.

[333] I. M. Vinogradov. The method of trigonometrical sums in the theory of numbers (russian). *Trav. Inst. Math. Steklo*, 10, 1937.

[334] D. Wales. *Energy Landscapes: Applications to Clusters, Biomolecules and Glasses*. Cambridge Molecular Science. Cambridge University Press, 2003.

[335] F. Wang and D. P. Landau. Efficient, multiple-range random walk algorithm to calculate the density of states. *Phys. Rev. Lett.*, 86:2050–2053, Mar 2001.

[336] E. B. Watson and T. Müller. Non-equilibrium isotopic and elemental fractionation during diffusion-controlled crystal growth under static and dynamic conditions. *Chem. Geol.*, 267(3):111–124, 2009.

[337] M. Watzlawek, C. N. Likos, and H Löwen. Phase diagram of star polymer solutions. *Phys. Rev. Lett.*, 82(26):5289–5292, 1999.

[338] J. D. Weeks, D. Chandler, and H. C. Andersen. Role of repulsive forces in determining the equilibrium structure of simple liquids. *J. Chem. Phys.*, 54:5237, 1971.

[339] B. Widom. Random sequential addition of hard spheres to a volume. *J. Chem. Phys.*, 44:3888, 1966.

[340] M. Wolfll. Unexpected regularities in the distribution of prime numbers. *Proc. of the 8th Joint EPS - APS Int. Conf. Physics Computing*, 1996.

[341] R. Xie, G. G. Long, S. J. Weigand, S. C. Moss, T. Carvalho, S. Roorda, M. Hejna, S. Torquato, and P. J. Steinhardt. Hyperuniformity in amorphous silicon based on the measurement of the infinite-wavelength limit of the structure factor. *Proc. Natl. Acad. Sci.*, 110(33):13250–13254, 2013.

[342] W.-S. Xu, J. F. Douglas, and K. F. Freed. Entropy theory of polymer glass-formation in variable spatial dimension. *Adv. Chem. Phys.*, 161:443–497, 2016.

[343] W.-S. Xu, J. F. Douglas, and K. F. Freed. Influence of cohesive energy on the thermodynamic properties of a 2 model glass-forming polymer melt. *Macromolecules*, 49(21):8341–8354, 2016.

[344] W. X. Xu and H. S. Chen. Numerical investigation of effect of particle shape and particle size distribution on fresh cement paste microstructure via random sequential packing of dodecahedral cement particles. *Comput. Struct.*, 114:35–45, 2013.

[345] J. L. Yarnell, M. J. Katz, R. G. Wenzel, and S. H. Koenig. Structure factor and radial distribution function for liquid argon at 85 k. *Phys. Rev. A*, 7(6):2130, 1973.

[346] S. Yu, X. Piao, J. Hong, and N. Park. Bloch-like wave dynamics in disordered potentials based on supersymmetry. *arXiv preprint arXiv:1501.02591*, 2015.

[347] C. E. Zachary, Y. Jiao, and S. Torquato. Hyperuniform long-range correlations are a signature of disordered jammed hard-particle packings. *Phys. Rev. Lett.*, 106(17):178001, 2011.

[348] C. E. Zachary, Yang Jiao, and S. Torquato. Hyperuniformity, quasi-long-range correlations, and void-space constraints in maximally random jammed particle packings. i. polydisperse spheres. *Phys. Rev. E*, 83(5):051308, 2011.

[349] C. E. Zachary and S. Torquato. Hyperuniformity in point patterns and two-phase random heterogeneous media. *J. Stat. Mech. Theor. Exp.*, (12):P12015, 2009.

[350] C. E. Zachary and S. Torquato. Anomalous local coordination, density fluctuations, and void statistics in disordered hyperuniform many-particle ground states. *Phys. Rev. E*, 83(5):051133, 2011.

[351] N. Zamel, N. G. C. Astrath, X. Li, J. Shen, J. Zhou, F. B. G. Astrath, H. Wang, and Z.-S. Liu. Experimental measurements of effective diffusion coefficient of oxygen–nitrogen mixture in pem fuel cell diffusion media. *Chem. Engi. Sci.*, 65(2):931–937, 2010.

[352] G. Zhang, F. H. Stillinger, and S. Torquato. Ground states of stealthy hyperuniform potentials: I. Entropically favored configurations. *Phys. Rev. E*, 92(2):022119, 2015.

[353] G. Zhang, F. H. Stillinger, and S. Torquato. Ground states of stealthy hyperuniform potentials: II. Stacked-slider phases. *Phys. Rev. E*, 92(2):022120, 2015.

[354] G. Zhang, F. H. Stillinger, and S. Torquato. The perfect glass paradigm: Disordered hyperuniform glasses down to absolute zero. *Sci. Rep.*, 6, 2016.

[355] G. Zhang, F. H. Stillinger, and S. Torquato. Transport, geometrical, and topological properties of stealthy disordered hyperuniform two-phase systems. *J. Chem. Phys.*, 145(24):244109, 2016.

[356] G. Zhang and S. Torquato. Precise algorithm to generate random sequential addition of hard hyperspheres at saturation. *Phys. Rev. E*, 88(5):053312, 2013.

[357] K. Zhang, P. Charbonneau, and B. M. Mladek. Reentrant and isostructural transitions in a cluster-crystal former. *Phys. Rev. Lett.*, 105(24):245701, 2010.

[358] Y. Zhang. Bounded gaps between primes. *Annals of Math.*, 3:1121–1174, 2014.

[359] H. J. Zhao, V. R. Misko, and F. M. Peeters. Analysis of pattern formation in systems with competing range interactions. *New J. Phys.*, 14(6):063032, 2012.

[360] R. Ziff and S. Torquato. Percolation of disordered jammed sphere packings. *J. Phys. A Math. Theor.*, 50(8):085001, 2017.

[361] T. I. Zohdi. On the optical thickness of disordered particulate media. *Mech. Mater.*, 38(8):969–981, 2006.